Nanoscale Josephson devices

Christopher Bell
St. John's College
Cambridge

A dissertation submitted for the degree of Doctor of Philosophy at the University of Cambridge

December 2003

The best way to have a good idea is to have lots of ideas

- Linus Pauling

Declaration

This dissertation is a result of my own work and includes nothing which is the outcome of work done in collaboration except where specifically indicated in the text. This work has been carried out in the Department of Materials Science and Metallurgy, University of Cambridge, U.K. since October 2000. No part of this dissertation has been submitted previously at Cambridge or any other University for a degree, diploma or other qualification. This dissertation does not exceed $60,000$ words.

Christopher Bell
December 2003

Summary

This thesis describes the development and applications of sub-micron current-perpendicular-to-plane devices fabricated by three-dimensional etching with a focused ion beam microscope. This technique was applied to a range of materials, including the study of *c*-axis Josephson junctions in the high temperature superconductor $Tl_2Ba_2CaCu_2O_8$, the fabrication of superconducting quantum interference devices with sub-micron loop areas, and GaN light emitting diodes. The main body of research was carried out in the study of Nb based Josephson junctions working at a temperature of 4.2 K. Junctions with normal metal, insulating and ferromagnetic barriers were characterised, as well as the first metallic antiferromagnetic Josephson junctions using γ-$Fe_{50}Mn_{50}$ as the barrier. 'Pseudo-spin-valve' Josephson junctions were also created using a Co/Cu/$Fe_{20}Ni_{80}$ barrier. In this case the relative orientation of the magnetic moments of the Co and $Fe_{20}Ni_{80}$ could be changed with an applied magnetic field. The magnetoresistance and critical current of the device showed a strong correlation, implying a direct influence of the magnetic structure of the device on the critical current.

Parts of this thesis have been published, or submitted for publication as detailed below.

C. Bell, G. Burnell, C. W. Leung, E. J. Tarte, D.-J. Kang, M. G. Blamire
Controllable Josephson current through a pseudo-spin-valve structure
Appl. Phys. Lett. **84**, 1153 (2004)

C. Bell, E. J. Tarte, G. Burnell, C. W. Leung, D.-J. Kang, M. G. Blamire
Proximity and Josephson effects in superconductor - antiferromagnetic Nb / γ-$Fe_{50}Mn_{50}$ heterostructures
Phys. Rev. B **68**, 144517 (2003)

P. A. Warburton, A. R. Kuzhakhmetov, C. Bell, G. Burnell, M. G. Blamire, H. Wu, C. R. M. Grovenor and H. Schneidewind
Sub-Micron Thin Film Intrinsic Josephson Junctions
IEEE Trans. Appl. Supercond. **13**, 821 (2003)

C. Bell, G. Burnell, D.-J.Kang, R. H. Hadfield, M. J. Kappers, and M. G. Blamire
Fabrication of nanoscale heterostructure devices with a focused ion beam microscope
Nanotechnology, **14**, 630 (2003)

These papers are reproduced in Appendix B.

Acknowledgments

What is essential is invisible to the eye

- Antoine de Saint-Exupéry

At the top of the list, I thank my supervisor Dr. Mark Blamire for letting my thesis grow in the way that it did, while at the same time asking many incisive questions which cut through a great deal of woolly thinking, to get to the important points. Also I express my gratitude to Prof. Jan Evetts and the whole of the Device Materials group, many of whom I have worked directly with over the years, for creating such a diverse mixture of people and research. Within that list, special mentions go to my offices mates: Debbie, Laura, Brian, Sibe and, when he was ever there, Ugi, for putting up with me, and also Rumen for telling me to go home. Thanks also to Nadia for a huge amount of technical help from turbo pumps to dicing saws, Karen for her help after persuading me to use LaTeX 2_ε, José for many useful tutorials on magnetism and ear popping, and more recently Antonio for his friendship as well as his novel 'stick' approach to mass-flow control.

Within the list of close collaborators, I am indebted to Ed Tarte for his patience in the face of my repeated questions and random ideas concerning superconductors and junctions, Dae-Joon Kang for his continuing help with all FIB related issues, and Gavin Burnell, not only as a sounding board for ideas but also for his innumerable Dualscope patches (in particular the ones that meant I didn't have to stop in the lab all night). In the early years of my thesis Robert Hadfield provided endless hours of entertainment and useful discussion for which I am very grateful, and similarly Dennis Leung for his insights into spintronics, and many other ideas and advice.

Outside of the lab, I thank the London enclave of Dude and Lucy for the repeated use of their drink and floor, as well as their efforts to keep me entertained outside of Cambridge. In Cambridge I must say a profound thank you to Nagulan, Sarah and Alix for making my graduate days what they were. I hope the future holds even better times. Finally I come to my family: thanks to Graham and Helen in Cambridge, and my parents and everyone else up North for all of their support, and for letting me get away with being a student for three more years.

I acknowledge the Engineering and Physical Sciences Research Council, U.K. for funding me for three years. I am also grateful for additional funding and money for travel and conferences from the Barber Trust and Superconductivity group of the Institute of Physics, the 'π-shift' network of the European Science Foundation, the Cambridge Philosophical Society, and St. John's College, Cambridge.

Following my viva, I would also like to express my thanks to Prof. Mark Welland and Dr. Hans Hilgenkamp for their many interesting questions and comments on my work. I hope that the adjustments I have made in the text, following their remarks, helps to make some of the results and discussion clearer to the reader.

CB

Contents

Symbols

a, b, c	Crystallographic axes
$a_{k\downarrow}, a^{\dagger}_{k\uparrow}$	Single electron creation / annihilation operators
A	Device area
$A, \mathbf{A}$	Magnetic vector potential
$B, \mathbf{B}$	Flux density
B_C	Critical flux density
C	Capacitance
d	Film thickness
D	Electronic diffusion constant
e	Electronic charge
E	Energy
E_{Ex}	Exchange energy
E_F	Fermi energy
f	Frequency
f, F	Free energy
$F(x)$	Electron correlation parameter
h	Planck's constant
$\hbar$	Planck's constant / 2π
$H, \mathbf{H}$	Magnetic field strength
H_{bias}	Exchange bias field
H_C	Coercive field
H_{Ex}	Exchange field
H_S	Saturation field
I	Current
I_C	Critical current
I_S	Stoner potential energy
J	Current density
J_C	Critical current density
J_{ij}	Exchange integral
$k, \mathbf{k}$	Momentum
K	Wavevector
k_B	Boltzmann's constant
k_F	Fermi wavevector
ℓ	Electronic mean free path
ℓ_s	Spin diffusion length
ℓ_t	Thermal healing length
L	Inductance
m_e	Electronic mass
$M, \mathbf{M}$	Magnetisation
M_R	Remanent magnetisation
M_S	Saturation magnetisation
$\mathcal{N}$, $\mathcal{N}(E_F)$	Density of states at Fermi level
n	Integer
$\mathbf{n}$	Film normal
n_s	Superelectron number density
n_p	Superelectron pair density
N	Number (of electrons)
P	Polarisation
P_{max}	Maximum power dissipation
q	Nesting vector
q	Wavevector
Q	Centre of mass momentum
r	Distance
R	Resistance
R_N	Normal state resistance
$\mathbf{S}$	Spin
t	Time
T	Temperature
T_B	Blocking temperature
T_C	Superconducting critical temperature
T_{C0}	Saturation T_C
T_{CS}	Plain superconductor T_C
T_M	Curie temperature
T_N	Néel temperature
T_0	Bulk clean limit T_C
u_k, v_k	Occupation amplitudes
v_F	Fermi velocity
V	Voltage
$V_{k,-k}$	BCS interaction parameter
V_s	Shapiro step voltage
$x, \mathbf{x}$	Distance, position vector
x, y, z	Junction dimensions
Y	Thermal boundary resistance

α, β	Ginzburg-Landau parameters	ν	Ginzburg-Landau parameter
β_c	McCumber parameter	ξ_0	Clean limit coherence length
β_L	Screening parameter	ξ_{AF}	Antiferromagnetic coherence length
β, γ	Spin asymmetry coefficients	ξ_{BCS}	BCS coherence length
γ	Electronic specific heat capacity	ξ_F	Ferromagnetic coherence length
Δ	Gap function	ξ_{GL}	Ginzburg-Landau coherence length
ε	Reduced temperature	ξ_N	Normal metal coherence length
ϵ_k	Reservoir energy	ξ_S	Superconducting coherence length
η	Ginzburg-Landau parameter	ρ	Electrical resistivity
θ	Superconducting phase	σ	Electrical conductivity
θ	Ga^+ beam angle with film normal	τ	Normalised time
κ	Ginzburg-Landau ratio λ_{GL}/ξ_{GL}	ϕ	Gauge invariant phase difference
λ	Wavelength	Φ	Flux density
λ	London penetration depth	Φ_{ex}	External flux
$\lambda^{\pm}$	Critical exponents	Φ_J	Junction flux
λ_{GL}	Ginzburg-Landau penetration depth	Φ_0	Flux quantum
λ_J	Josephson penetration depth	Φ_s	SQUID flux
Λ	London parameter	$\psi(x)$	Ginzburg-Landau order parameter
μ_0	Permeability of vacuum	Ψ	London superfluid wave function

Abbreviations

AD	Analogue to Digital
AF	Antiferromagnet, antiferromagnetic, antiferromagnetically (aligned ferromagnetic layers)
AFM	Atomic Force Microscope
BCS	Bardeen, Cooper and Schrieffer
CIP	Current In Plane
CPP	Current Perpendicular to Plane
DAQ	Data Acquisition
DoS	Density of States
EDX	Energy Dispersive X-ray
EE	Enhanced Etch
EFSE	Exchange-Field Supercurrent Enhancement
F	Ferromagnet, ferromagnetic, ferromagnetically (aligned ferromagnetic layers)
FIB	Focused Ion Beam
GL	Ginzburg-Landau
GPIB	General Purpose Interface Bus
GMR	Giant Magnetoresistance
HTS	High Temperature Superconductor
I	Insulator
LED	Light Emitting Diode
LTS	Low Temperature Superconductor
MR	Magnetoresistance
N	Normal metal
NIST	National Institute of Standards
PSV	Pseudo-Spin-Valve
RCSJ	Resistively and Capacitively Shunted Junction
RRR	Resistance or resistivity ratio
RSJ	Resistively Shunted Junction
S	Superconductor
SEM	Scanning Electron Microscope
SQUID	Superconducting Quantum Inference Device
SV	Spin-Valve
TEM	Transmission Electron Microscope
UHV	Ultra High Vacuum
UV	Ultra-Violet
VSM	Vibrating Sample Magnetometer

List of Figures

List of Tables

Introduction

Although the magnetic properties of lodestone have been known of for thousands of years, and superconductivity is less than 100 years old [1], the two phenomena are both examples of essentially similar physics: the interaction of electrons in solid via quantum mechanical exchanges on the microscopic level to form an ordered macroscopically coherent system.

Ferromagnetism is a complimentary phase transition to superconductivity. In the BCS theory of superconductivity the electron-electron *attraction* around the Fermi surface forms Cooper pairs of electrons with *anti-parallel* spins. In the case of ferromagnetism it is an electron *repulsion*, (due to Hund's rule) that forms *parallel* aligned spins. In both cases the effects are only understandable on a microscopic level within the framework quantum mechanics.

The antagonism between parallel spin ferromagnetism and anti-parallel Cooper pairs in (most) superconductors has attracted more and more interest in recent years. Ternary and borocarbide compounds display an intermixing of superconducting and magnetic ordering across the phase diagrams [2]. Ferromagnetism and superconductivity exist simultaneously in different layers of the high temperature superconducting cuprate $RuSr_2GdCu_2O_8$ [3]. More recently the heavy fermion materials such as UGe_2 [4] and perhaps also $ZrZn_2$ [5] are becoming accepted as ferromagnetic superconductors [6].

Equally however, much interest is still generated by the behaviour of simple metallic superconductors, themselves understood for many years, which can show essentially the same inhomogeneous superconductivity as exhibited by the more complex materials, when grown as heterostructures with ferromagnetic interlayers. Recent interest has been enhanced by the potential application of such devices in the development of solid state Quantum Computers, which will out-perform conventional computers by orders of magnitude [7, 8]. The so-called π-junction is an important logic element in this scheme, and can be realised in several ways, utilising for example the *d*-wave nature of the cuprates [9], the controllable properties of normal metal barriers with metallic superconducting electrodes [10], as well as junctions with ferromagnetic barriers [11]. Part of the present work seeks to realise a further possibility: a magnetically controllable π-junction, fabricated by means of a spin active barrier.

The outline of the thesis is as follows. The basic theory of magnetism is dealt with first, with an emphasis on ferromagnetism. This allows the inclusion of the effect of ferromagnetism into the theories of low temperature superconductors and the Josephson effect in chapters 2 and 3. The film growth and fabrication stages are outlined in chapter 4, as well as details of the measurement systems. The new three dimensional device fabrication technique using the focused ion beam (FIB) is presented in chapter 5. The fabrication of intrinsic Josephson junctions in the high temperature superconductor $Tl_2Ba_2CaCu_2O_8$ will then be discussed, as well as $Nb/MoSi_2/Nb$ junctions, superconducting quantum interference devices, and finally GaN light emitting diodes. The work on $Tl_2Ba_2CaCu_2O_8$ was carried out in collaboration with P. A. Warburton and A. R. Kuzhakhmetov (University College London), who measured the devices; H. Wu and C. R. M. Grovenor (Oxford University) who grew the thin films and G. Burnell

who helped produce many of the devices with the FIB. For the GaN devices the films were grown by M. J. Kappers, and I also acknowledge the help of D. Robson. For the case of the Nb/$MoSi_2$/Nb junctions, the films were grown by Y. Chong, (National Institute of Standards, Boulder, Colorado), and some devices were made in the FIB by G. Burnell. A range of different Josephson junctions are then considered: insulating barriers, normal metal, and ferromagnetic metals. Chapter 8 describes the fabrication of spin-active Josephson junctions, beginning with giant magnetoresistive multilayers, antiferromagnetic metallic barriers, and finally the spin-valve junctions. The directions of possible future work are presented in chapter 9.

This thesis is a collection of many ideas, some of them 'proof of principle' for the FIB fabrication technique, rather than an in-depth study of a single type of junction. For this reason, the theoretical chapters are broad and lacking any detail in addition to that directly relevant to the present work, although I have tried to give both microscopic and phenomenological models for all of the physics discussed. For that I offer no apology - but I hope that the references presented, in particular those given at the start of the chapters, will allow further investigation by the reader if required.

Units & terminology

Throughout this work SI units have been used in all but the most pathological of cases. This was done despite the continuing use in the literature of non-SI units, such as mbar for vacuum systems, Oersteds, Gauss and emu for magnetic measurements, and Ångström for distances. This thesis strongly overlaps the magnetic and superconducting fields of research, the literature of the latter would seem to be less resistant to using SI units. To avoid confusion when switching between the discussions on magnetism and superconductivity the SI system is therefore used throughout.

The abbreviations F (AF), as well as meaning (anti)ferromagnet(ic), will also refer to (anti)-parallel alignment of individual ferromagnetic layers within a thin film multilayer structure. It should be clear from the context which meaning should be taken, otherwise the full term is used. Other common symbols used in the literature have been changed to avoid confusion with other terms, however some symbols do retain multiple meanings. Again, the context of their use should be clear.

Finally, the term 'electron' is used in several ways, for brevity, and refers to 'bare' electrons in a vacuum in the discussion of SEMs and FIBs for example, as well as the Fermi liquid 'quasi-particle' excitation at low temperatures in a solid.

References

[1] H. K. Onnes, Commun. Phys. Lb. Univ. Leiden No 124c (1911).

[2] L. N. Bulaevskiĭ, A. I. Buzdin, M.L.Kulić, and S. V. Panjukov, Adv. Phys. **34**, 175 (1985).

[3] J. Tallon, C. Bernhard, M. Bowden, P. Gilberd, T. Stoto, and D. Pringle, IEEE Trans. Appl. Supercond. **9**, 1696 (1999).

[4] S. S. Saxena, P. Agarwal, K. Ahilan, F. M. Grosche, R. K. W. Haselwimmer, M. J. Steiner, E. Pugh, I. R. Walker, S. R. Julian, P. Monthoux, G. G. Lonzarich, A. Huxley, I. Sheikin, D. Braithwaite, and J. Flouquet, Nature **406**, 587 (2000).

[5] C. Pfleiderer, M. Uhlarz, S. M. Hayden, R. Vollmer, H. von Lohneysen, N. R. Bernhoeft, and G. G. Lonzarich, Nature **412**, 58 (2001).

[6] T. He, Q. Huang, A. P. Ramirez, Y. Wang, K. A. Regan, N. Rogado, M. A. Hayward, M. K. Haas, J. S. Slusky, K. Inumara, H. W. Zandbergen, N. P. Ong, and R. J. Cava, Nature **411**, 54 (2001).

[7] V. V. Ryazanov, Usp. Fiz. Nauk **169**, 920 (1999), [Phys. Usp. **42** 825 (1999)].

[8] G. Blatter, Nature **421**, 796 (2003).

[9] C. C. Tsuei and J. R. Kirtley, Rev. Mod. Phys. **72**, 969 (2000).

[10] J. J. A. Baselmans, B. J. van Wees, and T. M. Klapwijk, Phys. Rev. B **65**, 224513 (2002).

[11] V. V. Ryazanov, A. V. Veretennikov, V. A. Oboznov, A. Y. Rusanov, A. A. Golubov, and J. Aarts, Usp. Fiz. Nauk **171**, 81 (2001).

Chapter 1

Ferromagnetism

The phenomenological and microscopic theories of ferromagnetism are reviewed [1, 2, 3, 4], this is followed by a discussion of magnetically active (thin film) device structures [5].

1.1 Ferromagnetism

1.1.1 Ginzburg-Landau phenomenological theory

The philosophy of the Ginzburg-Landau theory of second order phase transitions exploits the fact that near the phase transition, some 'correlation length' ξ diverges, and the microscopic details of the system can be summed over (it is therefore a *mean-field* theory), and treated purely phenomenologically. The only remaining important elements are then the dimensionality and symmetries of the system. The transition is defined in terms of some 'order parameter' which is zero in the higher symmetry state. At the phase transition this symmetry is broken, the system falls into a lower symmetry state, and the order parameter acquires a non-zero value.

An example of the application of this theory is ferromagnetism. A material cooled below its Curie temperature T_M, becomes ferromagnetic (T_M is used to avoid confusion with the superconducting transition temperature T_C). Above T_M, in zero applied field, the spins are randomly orientated (in a state of high symmetry). The 'order parameter' $\mathbf{M}$, (the net magnetisation) is zero. Below T_M the spins break the rotational symmetry of the system (choosing a particular direction to point in), and are correlated over a macroscopically large area: the size of the magnetic domain (section 1.1.5). $\mathbf{M}$ is now non-zero. A phenomenological Hamiltonian for the system in terms of the magnetisation per unit volume $\mathbf{M}$ is

$$f(\mathbf{M},T) = f_0(T) + \frac{\varepsilon(T)}{2}\mathbf{M}^2 + \eta(T)\mathbf{M}^4 + \nu(T)(\nabla\mathbf{M})^2 + ... - \mathbf{H}\cdot\mathbf{M}\,, \tag{1.1}$$

where the ... represents higher orders terms. $\mathbf{H}$ is the applied field, and ε, η and ν are phenomenological parameters. The shape of $f(\mathbf{M},\mathbf{T})$ for various parameter values is shown in figure 1.1. For $\varepsilon > 0$, the minimum of f is no longer at $\mathbf{M} = 0$. Clearly ε must be related to T_M. It is easy to show that $\varepsilon = (T - T_M)/T_M$. For $\nu > 0$ uniform $\mathbf{M}$ minimises f. ν is therefore a phenomenological term related to the microscopic exchange energy which aligns the spins. It is clear from the $\nabla\mathbf{M}$ term that the lowest energy excitations of the system will be ones with large spatial wavelengths, where $\mathbf{M}$ changes slowly from one point to the next. These collective modes are known as *magnons*[1], (see section 1.2.5).

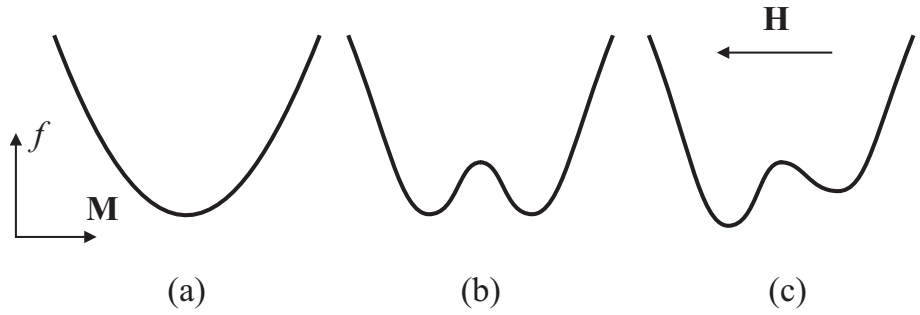

Figure 1.1: Ginzburg-Landau free energy for a ferromagnet, with $\eta > 0$: (a) $\varepsilon > 0$, (b) $\varepsilon < 0$, (c) with an applied field $\mathbf{H}$.

[1] Analogous to e.g. phonons, which occur as a result of the broken *spatial* symmetry of a crystal.

1.1.1.1 Critical behaviour near T_M

The 'correlation length' ξ, over which fluctuations in $\mathbf{M}$ are correlated, diverges near T_M. Many of the physical properties ('response functions') of the ferromagnet (F) also diverge, among them the susceptibility, $\mathrm{d}M/\mathrm{d}H$, and specific heat capacity. Of relevance in this work $\mathrm{d}\rho/\mathrm{d}T$, the first derivative of the temperature dependent resistivity, also diverges. This can be understood by considering the increased electron scattering by scale-invariant fluctuating domains. Fisher [6] proposed the functional form

$$\frac{1}{\rho_M}\left(\frac{\mathrm{d}\rho}{\mathrm{d}T}\right) = \left(\frac{A^{\pm}}{\lambda^{\pm}}\right)\left(\left|\frac{T_M - T}{T_M}\right|^{-\lambda^{\pm}} - 1\right) + B^{\pm}\,, \tag{1.2}$$

to describe the behaviour. The $\pm$ signs refer to the values above and below T_M respectively, and ρ_M is the resistivity at T_M. $A^{\pm}$ and $B^{\pm}$ are constants, $\lambda^{\pm}$ is the 'critical exponent' which should be a constant for systems with the same symmetry and dimensionality. Cu_xNi_{1-x} alloys have been investigated in the case of $x = 0.3$ by Sousa *et al* [7]. In that case λ^{+} (above T_M) ≈ 0.07, was consistent with measurements of elemental ferromagnets [8]. However, the value of λ was found to be strongly dependent on the choice of T_M, with the best fit to equation 1.2 found for a value of T_M nearly 10 K greater than $T_{\max}$ (the peak in the $(\mathrm{d}\rho/\mathrm{d}T)$) [7]. Rossiter [9, 10] has also pointed out that composition inhomogeneities and clustering in alloy systems gives spatially varying T_M that will tend to blur the transition. In the present work it was not possible to achieve $\varepsilon < 10^{-2}$ required to examine the critical behaviour in detail. Electrical measurements of $R(T)$ were used to give a measure of T_M in $Cu_{0.4}Ni_{0.6}$ films too thin to obtain $M(T)$ data. As will be seen in section 7.4.1, it was difficult to reduce the error in T_M to less than a few tens of K, but this was accurate enough to show some variation of T_M with film thickness.

1.1.2 Microscopic exchange interaction

It is possible to write down a simple effective Hamiltonian[2] describing the interaction of a lattice of N spins:

$$\mathcal{H}_{\text{eff}} = -2\sum_{i>j}^{N} J_{ij}\mathbf{S}_i.\mathbf{S}_j\,. \tag{1.3}$$

Conventionally the $-$ sign is chosen so that $J_{ij} > 0$ gives ferromagnetic coupling. The exchange integral

$$J_{ij} \propto \int \phi_i^*(\mathbf{r}_1)\phi_j^*(\mathbf{r}_2)\frac{e^2}{|\mathbf{r}_1 - \mathbf{r}_2|}\phi_i(\mathbf{r}_2)\phi_j(\mathbf{r}_1)\,\mathrm{d}\mathbf{r}_1\,\mathrm{d}\mathbf{r}_2 \tag{1.4}$$

describes the Coulomb interaction due to the overlap of the wavefunctions ϕ_1 and ϕ_2. Considering a simple argument for the H_2 molecule: the two electrons would prefer, (due to the Coulomb term) to both be near to the nuclei. Pauli exclusion forbids parallel spins occupying the same space, therefore the anti-parallel state is lower in energy. More generally, inter-atom

[2] The Heisenberg Hamiltonian.

wavefunctions are not orthogonal, and a first principles calculation using equation 1.4 is not possible for more complex materials [1]. Ferromagnetism can only be explained by a complex balance of energies, which are strongly dependent on the band-structure of a given material. From experiment ferromagnetism is found in for example the $3d$ transition metals Co, Ni and Fe. Stoner's criterion, which ignores the first principles calculations and *assumes* $J_{ij} > 0$, can be used to give a phenomenological justification for the appearance of ferromagnetism.

1.1.3 Stoner's criterion

Co, Ni and Fe are the three most common 'itinerant' $3d$ transition metals that are ferromagnetic at room temperature. Their outer electrons are delocalised[3] and shared between the $4s$ and $3d$ orbitals, with the unfilled $3d$ shell being responsible for the net magnetic moment. To explain the ferromagnetism of these materials, Stoner's criterion considers an unpolarised metal with N electrons. The number of up ($\uparrow$) and down ($\downarrow$) spins are equal: $2N_\uparrow = 2N_\downarrow = N$. If there is a shift in the $\uparrow$ and $\downarrow$ Fermi seas the kinetic energy cost is

$$\Delta E_1 = \frac{(N_\uparrow - N_\downarrow)^2}{2\mathcal{N}(E_F)} = \frac{N^2 P^2}{2\mathcal{N}(E_F)}\,, \tag{1.5}$$

where the electron polarisation $P = (N_\uparrow - N_\downarrow)/N$, and $\mathcal{N}(E_F)$ is the density of states (DoS), at the Fermi energy E_F. This is balanced by a gain in potential energy due to the electrons

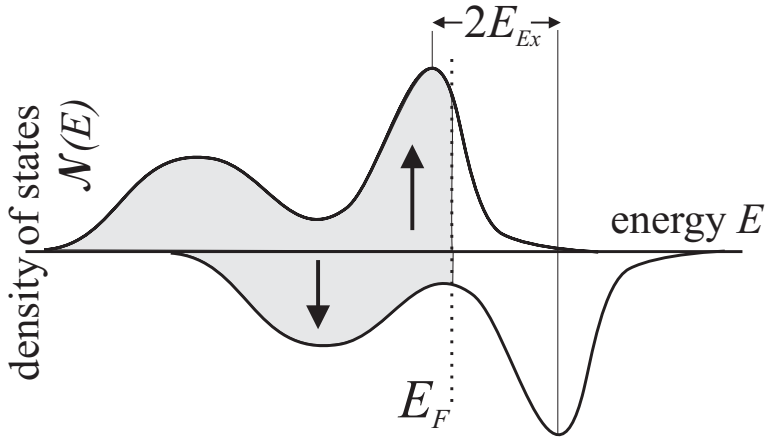

Figure 1.2: Schematic of the splitting of the density of states about the Fermi surface in a $3d$ ferromagnet.

involved in the exchange interaction. This exchange is a scattering process, and therefore only electrons near the Fermi surface take part. If I_S (the phenomenological version of J_{ij}), is the potential energy gain when a spin is flipped due to the exchange interaction, then the potential energy gain is

$$\Delta E_2 = -\frac{I_S}{2}(N_\uparrow - N_\downarrow)^2 = -\frac{N^2 I_S}{2}P^2. \tag{1.6}$$

[3]This is of course an over-simplification: see for example [11].

The Stoner criterion for a ferromagnetic instability is then

$$\Delta E_1 + \Delta E_2 < 0 \quad \Rightarrow \quad I_S \mathcal{N}(E_F) > 1 \; . \tag{1.7}$$

$\mathcal{N}(E_F)$ can be thought of as some 'bandwidth': Co, Fe and (particularly) Ni all have relatively sharp peaks in the DoS near E_F, (as the schematic in figure 1.2), which means a large number of electrons contribute to the criterion given by equation 1.7.

The bands are split by an amount $2E_{Ex}$. By analogy with the splitting of the DoS by an applied field in Pauli paramagnetism, the *exchange field* (some internal field holding the spins together) can be defined by the relation

$$E_{Ex} = H_{Ex} M_S \; , \tag{1.8}$$

where M_S is the saturation magnetisation. E_{Ex} and H_{Ex} are often used interchangeably in the literature concerning the S/F proximity effect (see section 2.4), but it is the exchange splitting E_{Ex} that is the relevant energy scale in these systems.

1.1.3.1 Nesting

The shape of the DoS near E_F is important for Stoner's criterion to be met. However the argument neglected the shape and structure of the Fermi surface itself. In particular 'nesting' was ignored. Nesting occurs when large section of occupied (electron) bands can be connected to unoccupied (hole) bands via a wavevector q in momentum space (figure 1.3). The electrons and holes can form bound states (the pairing is analogous to the BCS superconducting state - section 2.2), and generate antiferromagnetic (AF) order (a spin density wave), before the

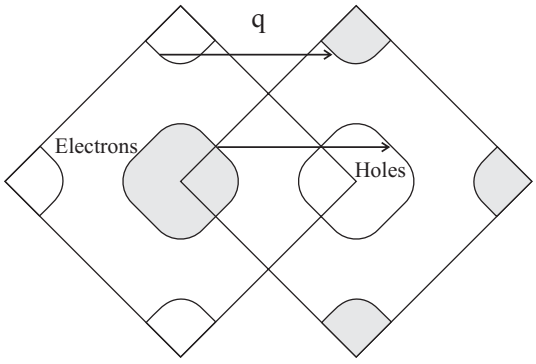

Figure 1.3: Nesting vector q in the band structure of Cr projected onto the (100) plane. Taken from [4] and [12].

Stoner criterion can be met. The property of nesting will be returned to in the study of the superconductor / AF proximity effect (section 2.5), since the symmetry breaking on the Fermi surface due to the nesting has a profound effect on superconductivity.

1.1.4 Magnetic anisotropy

In the thin films used in this work, there are a large number of competing energies as well as the exchange coupling, that finally determine the behaviour of the magnetic moments in the sample. Although the exchange coupling between spins is the strongest interaction, and determines the magnitude of M_S, the magnetisation *direction* can be determined by the weaker energies. These terms are generally not isotropic in space. The anisotropies most relevant to the present work are listed in table 1.1.

Energy	Preferred spin alignment
Exchange	Ferromagnetic
Zeeman	With applied field
Magnetostatic	Antiferromagnetic
Crystallographic anisotropy	With certain crystal axes
Induced anisotropy	Direction of applied field during deposition
Shape anisotropy	Parallel to interface (thin films / patterned structures)
Exchange bias	Uni-directional (field-cool direction)

Table 1.1: Different energies in a ferromagnet important for this work.

1.1.4.1 Induced anisotropy

Induced anisotropy can be achieved by depositing a thin film in a magnetic field [13]. Various other means such as annealing in a field, or angled depositions are possible, but not relevant to this work. The induced anisotropy will be considered further in chapter 4.

1.1.4.2 Shape anisotropy in thin films

The magnetic moment, with all other things equal, will tend to lie in the plane of a thin film. This is due to the energy cost of the relatively large field produced by magnetic 'charges' on the surface in figure 1.4 (a) compared to (b). The case of perpendicular magnetisation is neglected

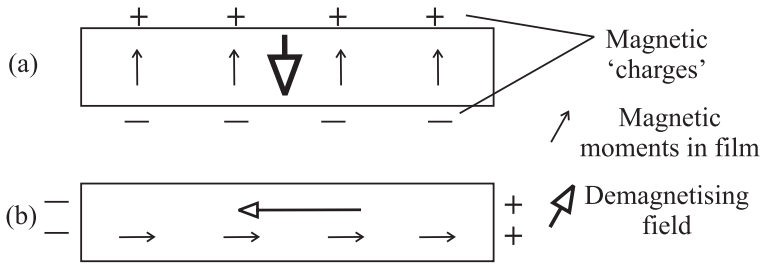

Figure 1.4: Demagnetising field for magnetic moments (a) out of plane (b) in plane, for a thin ferromagnetic film.

in the present discussion - see [14] for more information.

1.1.5 Domain walls

From the above discussion, the balance of the different anisotropies determines the final direction of **M**. This assumes that there is no further energy cost for spatially uniform **M**. The stray field of such a uniform magnetisation must also be considered. There are several ways of representing the total magnetostatic energy of a ferromagnetic system[4]. One version is given by

$$E_M = -\frac{\mu_0}{2} \int \mathbf{H}'^2 \, \mathrm{d}V \; . \tag{1.9}$$

The sum is over all space [2], and $\mathbf{H}'$ is the field at a given point due to all the moments. The integral is always positive, and for macroscopic systems this term can become the dominant energy - the result being the preference for flux closure rather than perfect ferromagnetic alignment, as shown in figure 1.5. This is the so-called pole-avoidance principle. This can be understood since the 'overlap integral' of equation 1.4 means that the exchange interaction between F moments is a short-range force[5]; whereas the magnetostatic (dipole) interaction is long-ranged, and integrated over the whole sample. Different domains within the ferromagnet therefore form to achieve this flux closure.

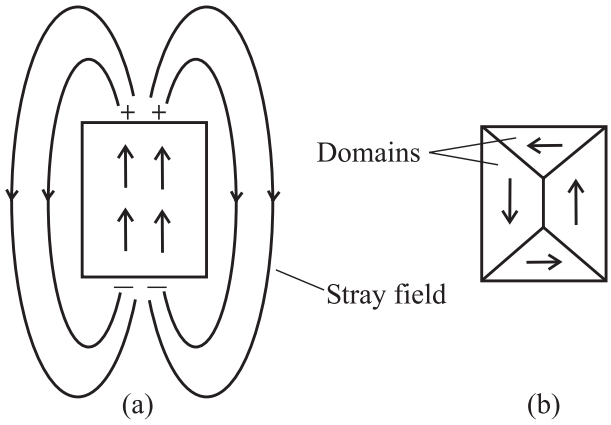

Figure 1.5: Magnetic moment alignment in zero applied field with (a) exchange term dominant and (b) one possible arrangement of domains to produce flux closure with the magnetostatic term dominant.

1.1.5.1 Bloch and Néel domain walls

The exchange coupling makes it unfavourably for the direction of the moments to switch suddenly between domains. Figure 1.6 (a) shows a Bloch *domain wall* [15] containing smoothly rotating moments which minimises the energy cost due to the exchange interaction.

For the case of the thin film, the 'magnetic charges' formed by the Bloch wall moments rotating out of plane means that it is more favourable for the moments to rotate in the plane of the film. A Néel wall [16] (figure 1.6 (b)) is formed in preference to a Bloch wall in this way. The width of the domain wall is strongly dependent on the material and its anisotropies, but

[4] For example see section 7.2 in [1].
[5] Details of the actual range (nearest or next-nearest exchange) is not important.

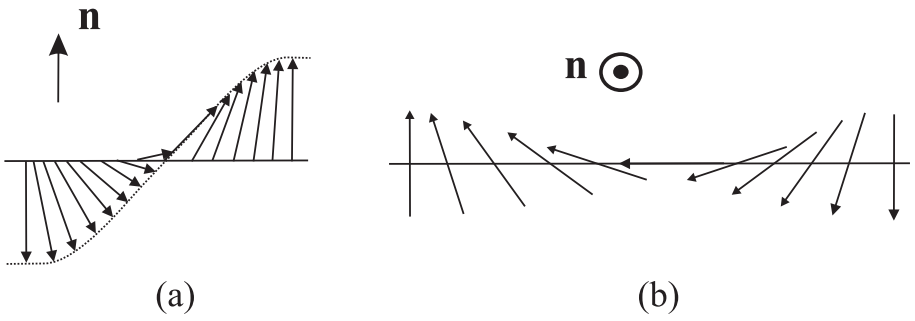

Figure 1.6: Spiraling magnetic moments for (a) a Bloch wall, and (b) a Néel domain wall for thin films. **n** is the film normal. Adapted from Chikazumi [2].

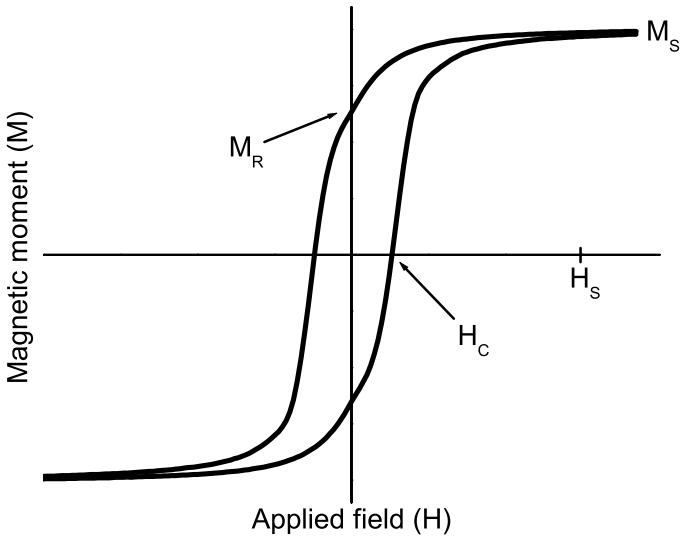

Figure 1.7: Saturation magnetisation (M_S), remanent magnetisation (M_R), coercive field (H_C) and saturation field (H_S) determined by a $M(H)$ measurement.

is typically of the order of tens to 100 nm. Nucleating and moving domains around over defect pinning sites takes energy, and is a hysteretic process. This gives a generic explanation to the shape of the $M(H)$ loop in figure 1.7. The $M(H)$ loop is characterised by a saturation moment M_S, obtained above an applied field H_S; a remanent moment M_R, present after applying a field H_S and reducing it to zero; and the coercive field H_C: the field required to change the sign of M. An initial magnetisation curve (rising from $H = 0, M = 0$), is also observed if the sample is demagnetised. This can be done by sweeping the applied field through a series of minor hysteresis loops with decreasing amplitude until $M = 0$.

1.2 Magnetically active devices

1.2.1 Giant magnetoresistance

A Giant Magnetoresistance (GMR) change with applied field was discovered by Baibich *et al* [17] in multilayers of Fe/Cr grown by molecular beam epitaxy. In that case the MR = 100% $\times$ $(R_{\max} - R_{\min})/R_{\max} = \Delta R/R_{\max}$ was nearly 50 % at 4.2 K. GMR was subsequently found in sputtered multilayer films and granular alloys. This can be understood in a simple picture by considering the change in electron scattering as the ferromagnetic moments are moved around from the antiferromagnetically (AF) aligned state to ferromagnetic (F) alignment by the applied field. The scattering rate of an electron is given via Fermi's Golden rule as $\propto \mathcal{N}(E_F)$ [18]. Hence there is more scattering when there are more states available for the electrons to be scattered into.[6] If the shape of the density of states near E_F is assumed to be the same as in figure 1.2, the down spin electrons in figure 1.8 (a) (F alignment) experience a much larger scattering than the up spins; whereas the situation is equal in the AF case. Considering the two spin channels as parallel resistors, (figure 1.8 (c) and (d)), the change of resistance between the F and AF states is then clear.

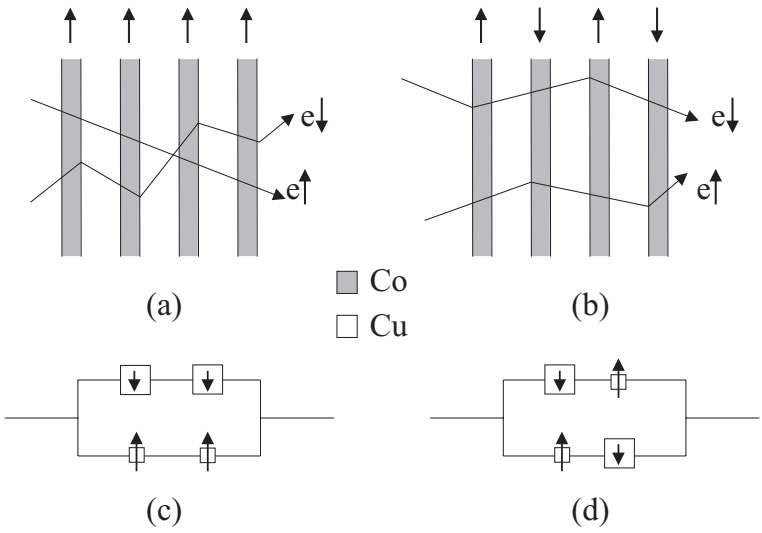

Figure 1.8: Paths of majority and minority spin electrons through a GMR multilayer: (a) F alignment, (b) AF alignment, and equivalent circuits (c) and (d).

It was later found that the strength of the GMR effect oscillated as a function of the thickness of the spacer between the ferromagnetic layers (figure 1.9). For many materials (other than Cr), the '1$^{\text{st}}$ AF peak' - where the alternate ferromagnetic layers are coupled antiferromagnetically occurs at $\sim$ 1 nm spacer thickness, followed by a region of F coupling and a '2$^{\text{nd}}$ AF peak' at $\sim$ 2 nm thickness [19]. The strength of the AF coupling, (the field required to align the anti-parallel moments), decreases with spacer thickness (3$^{\text{rd}}$ order peaks have only seen for materials with strong coupling). A detailed discussion of the theoretical explanation for the oscillation

[6] Due to Pauli expulsion only electrons near the Fermi surface can be scattered.

will not be presented. However a simple model of oscillatory and decaying coupling due to spin dependent electron confinement in the spacer leads to a good qualitative picture [20]. The phenomena of GMR will be returned to in section 8.2, as diagnostic tool in the development of the fabrication technique described in section 5.1.

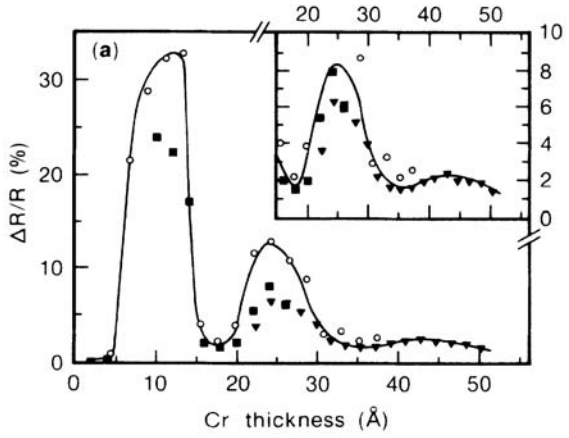

Figure 1.9: Oscillation of the GMR with Cr spacer in a [(2 nm)Fe / (t_{Cr})Cr]$_N$ multilayer, for $N = 20$ (open circles) and 30 (closed symbols). Taken from Parkin *et al* [21].

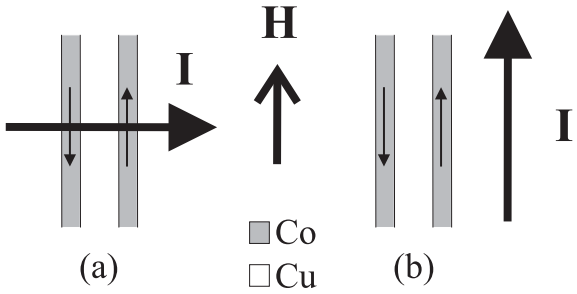

Figure 1.10: Current direction through thin film layers for (a) CPP and (b) CIP measurement, with an applied field **H**.

It is possible to measure the GMR in either the *Current-In-Plane* (CIP) or *Current-Perpendicular-to-Plane* (CPP) configuration, as shown in figure 1.10. The CIP measurement requires no patterning and is therefore easier to perform on thin films. The CIP geometry has the disadvantage of a lower GMR relative to the equivalent CPP measurement. The theoretical description is also more complex. The CPP configuration gives easier access to many of the fundamental parameters of the system [22], but is more complex to achieve experimentally. Various methods have been developed to produce the preferred CPP configuration with micron-scale superconducting contacts [23], (these require sensitive resistance measurements due to the low resistance) and sub-micron length scales accessed using including deposition through nanowires formed in an insulating polycarbonate matrix [24], or *e*-beam lithography [25], as well as the technique discussed in section 5.1.

1.2.2 Spin-valves

The fields required to rotate the magnetic moments from parallel to anti-parallel in section 1.2.1 are relatively large and unsuited for use in magnetic memory applications. A simple spin-valve (SV) consists of two F layers which rotate from anti-parallel to parallel alignment, and show a MR for the same reason as the GMR multilayers. If the two layers are made of different materials (a pseudo-spin-valve (PSV)) the different coercive fields can be exploited: the softer F layer aligns with a relatively small applied field, with the harder material not switched. The higher resistance anti-parallel state is achieved. In this case the spacer layer is relatively thick, and is used to decouple the ferromagnetic layers to prevent them from switching at the same field. For a CIP configuration the Cu spacer cannot be too thick, since the %MR will be decreased

due to the Cu shunting the current. This is not a restriction in the CPP case. A review of CPP SVs can be found in reference [26].

1.2.3 Exchange bias

As an alternative to a PSV, exchange bias can be used to change the properties of one of the ferromagnetic layers. In this case an antiferromagnet is grown next to the ferromagnetic layer. The exchange bias coupling between the AF and F layers causes a *uni-directional* anisotropy to be formed. The centre of the $M(H)$ loop is shifted from $H = 0$ by an amount H_{bias}.[7] This effect was discovered over 40 years ago [27], (for recent reviews see [28, 29]). In addition to the shift of the hysteresis loop, the H_C of the biased F layer is also increased. This can be understood qualitatively by considering the schematic in figure 1.11 (a). The surface spins of the AF and F couple together as shown. This coupling gives the preferred direction, (the bias), but also increases the energy required to move the ferromagnetic domains around, i.e. H_C is increased. This very simplified picture hugely overestimates the strength of the coupling: $H_{bias} \sim$ a few T, compared to tens of mT typically obtained experimentally.

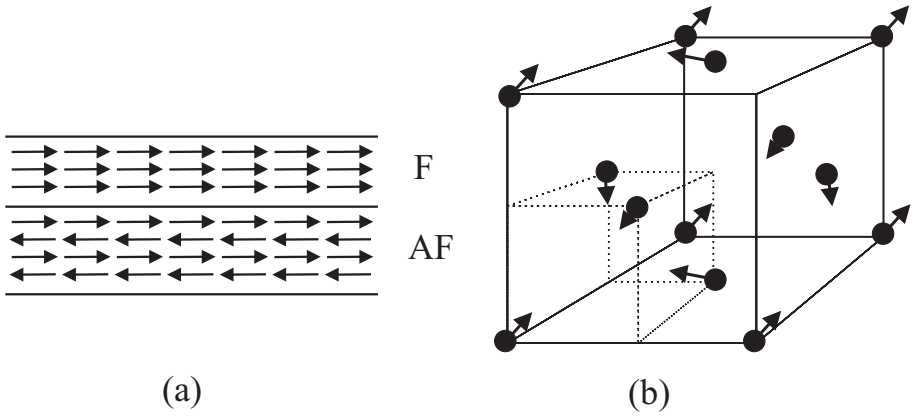

Figure 1.11: (a) Naïve picture of exchange bias effect: spins at the surface of the AF align and pin the spins in the F layer (b) γ-FeMn 3Q spin structure for an f.c.c. unit cell, taken from Schulthess *et al* [30].

In practice exchange bias can be set by field cooling through the blocking temperature T_B of the AF, ($T_B \leq T_N$, where T_N is the Néel temperature: the antiferromagnetic equivalent of T_M), or by growing an F/AF bilayer in an applied field $H > H_S$. This field saturates the F layer before the AF is grown. T_B and H_{bias} both decrease as the AF thickness is decreased below $\sim 6 - 7$ nm [31].

1.2.3.1 Antiferromagnetic γ-FeMn

The f.c.c. disordered AF γ-$Fe_{50}Mn_{50}$ has a bulk $T_N = 490$ K [28], and has been frequently used in the study of exchange bias. Although its magnetic / exchange bias properties have been intensively studied, the crystal structure is complex and difficult to probe. The precise nature

[7] H_{ex} is commonly used in the literature, but avoided here to prevent confusion with the exchange field.

of the magnetic structure of this material is still under debate [32, 33]. The 3Q structure is one possibility considered in the literature, as shown in figure 1.11. In this case, the Fe and Mn atoms are randomly distributed around the lattice sites, with the moments in figure 1.11 pointing in the four $< 111 >$ directions. The nature of the groundstate is not clear however. Simulations imply that a more complex '3Q-R' structure may have a lower energy [32] - the question still remains open.

The electronic properties are less well studied, and there have not been any experimental studies of properties such as the Fermi velocity, electronic heat capacity of FeMn thin films.

1.2.3.2 Interface spin compensation

The nature of the F/AF interface is critical to understand the exchange bias properties. The spins in the AF can be uncompensated, i.e. a section is taken through one of the sublattices such that the surface moments are aligned ferromagnetically. Alternatively the surface can be compensated, and resemble the bulk AF. In this case the exchange bias may also form via a 'spin-flop' with the F moments at 90° to both AF sublattices [34].

Clearly such detail is very dependent on the sample treatment and growth, (see [29] for more details). This may have implications for boundary conditions set on S/AF interfaces, to restrain possible theoretical models of the work discussed in section 8.3.

1.2.4 MR *vs* ferromagnetic thickness

If the magnetic layers are made thinner, the GMR decreases [35]. This is found for SVs and GMR multilayers. To examine the MR in the general case, the CPP PSV in figure 1.12 is considered. Following the work of Valet and Fert [22, 36], in the limit that the spin diffusion length $\ell_S \gg$ total F thickness, a simple 'two-resistor' model can be used. The spin diffusion length - the length scale over which the electron is spin-flip scattered - is dominated by spin-orbit coupling and magnetic impurity scattering at low temperatures, and is estimated as > 100 nm [22]. Throughout this work this limit will be assumed.

Yang *et al* [37] assumed spin independent Nb/F interfaces such that $R^{\uparrow}_{\mathrm{Nb}/F} = R^{\downarrow}_{\mathrm{Nb}/F} = 2R_{\mathrm{Nb}/F}$. Similarly for the normal metal (Cu) $\rho^{\uparrow}_{N} = \rho^{\downarrow}_{N} = 2\rho_N$. The bulk F resistivity and N/F interface resistance have different values dependent on the spin direction. Going from left to right in figure 1.12, for thicknesses t_{X} of the layer X, the resistance area product in the AF configuration for the up spin electron is

$$\begin{aligned} AR^{\mathrm{AF}\uparrow} = \; & 2AR_{\mathrm{Nb/Co}} + \rho^{\uparrow}_{\mathrm{Co}} t_{\mathrm{Co}} + AR^{\uparrow}_{\mathrm{Co/Cu}} + 2\rho_{\mathrm{Cu}} t_{\mathrm{Cu}} \\ & + AR^{\downarrow}_{\mathrm{Py/Cu}} + \rho^{\downarrow}_{\mathrm{Py}} t_{\mathrm{Py}} + 2AR_{\mathrm{Nb/Py}}. \end{aligned} \tag{1.10}$$

By appropriate swapping of $\uparrow$ and $\downarrow$ in equation 1.10, the value of $AR^{\mathrm{AF}\downarrow}$ can be found, as well as those for the parallel configuration: $AR^{\mathrm{F}\uparrow}$ and $AR^{\mathrm{F}\downarrow}$. The total AR and $A\Delta R$ can now be found, and therefore the % MR.

1.2.5 Temperature dependence

Figure 1.13 shows the $R(H)$ behaviour of a CIP GMR multilayer, (with t_{Cu} near to the 2nd AF peak), measured at 298 K and 77 K. The hysteresis indicates non-ideal and weak AF coupling in this case, but this does not detract from the generic T dependence. Both the % MR and H_S are increased as T is decreased. The increase in H_S can be attributed to two effects. Thermal activation of domain wall movement over pinning sites is decreased at lower temperatures [38], (as is the case in other F materials). The GMR interlayer coupling is also known to increase [39] at lower temperatures - this has been attributed to the Fermi-Dirac statistics in the N spacer, or the decrease in magnon scattering. The increase in the MR is also attributed to a decrease in spin-flip electron-magnon scattering [40, 41].

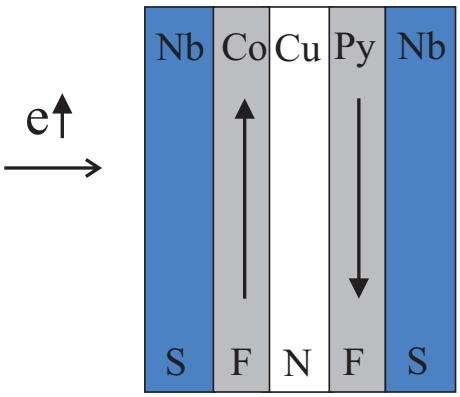

Figure 1.12: Cross section of a CPP PSV structure, with an 'up' spin electron moving from left to right.

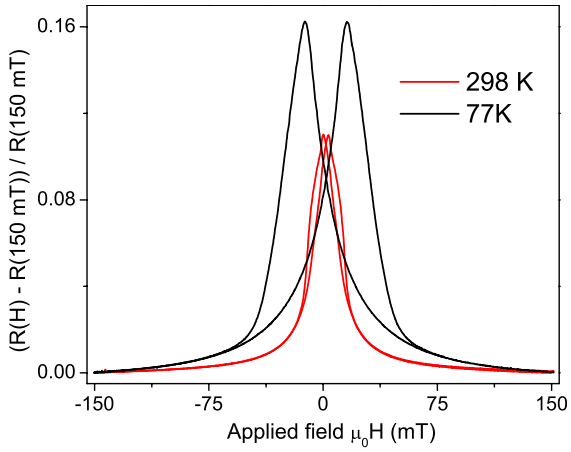

Figure 1.13: $R(H)$ for a $[Cu/Co]_6$ multilayer ($d_{Cu} \sim 2$ nm) at 298 K and 77 K.

1.2.6 Effect of film roughness

The comparison between two Nb/GMR/Nb multilayers with nominally identical GMR layers is shown in figure 1.14. One has thin, ($\sim$ 5 nm) Nb layers above and below the GMR multilayer, the other with thicker (150 nm) Nb. The increased roughness of the Nb underlayer has lead to an increased H_C. This has been explained (figure 1.15) in terms of magnetostatic coupling between the 'charges' of two finite thickness F layers, due to the conformal roughness of the film. The charges act as barriers reducing the mobility of domain walls, increasing H_C, and also increases the tendency for F coupling, making the MR response weaker. This will be a consideration returned to in section 8.2.

1.2.7 Effect of lateral size

The domains in section 1.1.5, which reduced the stray flux, cost energy. For small enough samples this energy is too large, and the patterned magnetic element is single domain.[8] For

[8] Although this does not necessarily imply *uniform* magnetisation [44].

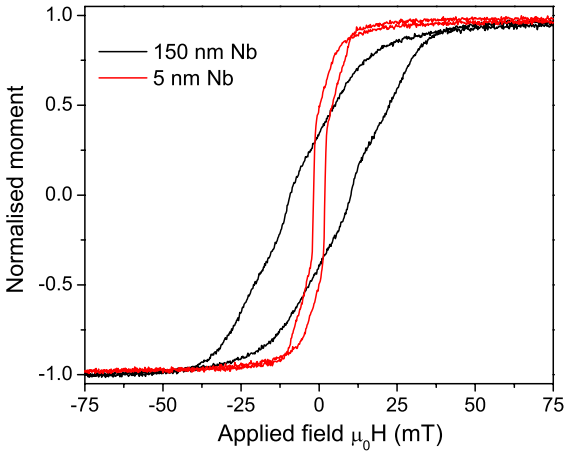

Figure 1.14: Nb/GMR/Nb $M(H)$ loops with the same GMR layers, and thin and thick Nb layers, (see section 8.2 for film details).

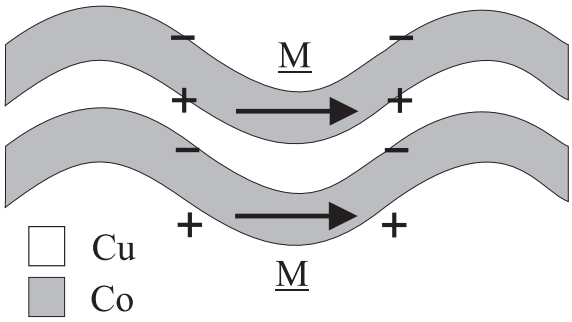

Figure 1.15: Ferromagnetic coupling of magnetic layers due to conformal roughness. After Néel [42] and Kools *et al* [43].

a high aspect ratio ferromagnetic wire, it is energetically favourable for the moments to point along the length of the wire to reduce the demagnetising field, (using the same argument as the thin films in section 1.1.4.2). The coercive and saturation fields of the wire in that direction is therefore increased as the width is decreased [45]. Edge roughness due to the milling may also increase H_C [46]. These are just two possible outcomes of lateral patterning of thin F films. The physics of this type of patterning is important technologically and intensively studied. For a very thorough and recent review see [44].

The GMR of sub-micron high aspect ratio shapes is affected only weakly or not at all [47]. Although this would seem surprising, it may be that patterning induced defects / roughness mask the increase in MR. The reduction in the number of domains with size can also change the shape of the $R(H)$ response ([48] and section 8.4.3). This is due to the fact that the complex reversal mechanisms in these cases are no longer averaged over many domains. The resistance of individual domains can therefore be a significant fraction of the total value.

References

[1] A. Aharoni, *Introduction to the Theory of Ferromagnetism* (Oxford Science Publications, 1996).
[2] S. Chikazumi, *Physics of Ferromagnetism* (Oxford Science Publications, 1996).
[3] C. Kittel, *Introduction to Solid State Physics* (Wiley & Sons Inc., 1996).
[4] L.-P. Lévy, *Magnetism and Superconductivity* (Springer, 2000).
[5] M. Ziese and M. J. Thornton, eds., *Spin Electronics* (Springer-Verlag, 2001).
[6] M. E. Fisher, Rep. Prog. Phys. **30**, 615 (1967).
[7] J. B. Sousa, M. R. Chaves, R. S. Pinto, and M. F. Pinheiro, J. Phys. F: Met. Phys. **2**, L83 (1972).
[8] P. P. Craig, W. I. Goldburg, T. A. Kitchens, and J. I. Budnick, Phys. Rev. Lett. **19**, 1334 (1967).
[9] P. L. Rossiter, *The Electrical Resistivity of Metals and Alloys* (Cambridge University Press, 1991).
[10] P. L. Rossiter, J. Phys. F: Met. Phys. **11**, 2105 (1981).
[11] C. G. Shull and H. A. Mook, Phys. Rev. Lett. **16**, 184 (1966).
[12] E. Fawcett, Rev. Mod. Phys. **60**, 209 (1988).
[13] R. F. Soohoo, *Magnetic Thin Films* (Harper and Row, 1965).
[14] M. T. Johnson, P. J. H. Bloemen, F. J. A. den Broeder, and J. J. de Vries, Rep. Prog. Phys. **59**, 1409 (1996).
[15] F. Bloch, Z. Physik **74**, 295 (1932).
[16] L. Néel, Comptes. Rendus **241**, 533 (1955).
[17] M. N. Baibich, J. M. Broto, A. Fert, F. Nguyen Van Dau, F. Petroff, P. Etienner, G. Creuzet, A. Friederich, and J. Chazelas, Phys. Rev. Lett. **61**, 2472 (1988).
[18] J. J. Sakurai, *Modern Quantum Mechanics* (Addison Wesley, 1994).
[19] S. S. P. Parkin, Phys. Rev. Lett. **67**, 3598 (1991).
[20] P. Bruno, J. Phys.: Condens. Matter **11**, 9403 (1999).
[21] S. S. P. Parkin, N. More, and K. P. Roche, Phys. Rev. Lett. **64**, 2304 (1990).
[22] T. Valet and A. Fert, Phys. Rev. B **48**, 7099 (1993).
[23] R. D. Slater, J. A. Caballero, R. Loloee, and W. P. Pratt Jr., J. Appl. Phys. **90**, 5242 (2001).
[24] L. Piraux, J. M. George, J. F. Despres, C. Leroy, E. Ferain, R. Legras, K. Ounadjela, and A. Fert, Appl. Phys. Lett. **65**, 2484 (1994).
[25] F. J. Albert, N. C. Emley, E. B. Myers, D. C. Ralph, and R. A. Buhrman, Phys. Rev. Lett. **89**, 226802 (2002).
[26] J. Bass and W. P. Pratt Jr., J. Magn. Magn. Mater. **200**, 274 (1999).
[27] W. H. Meiklejohn and C. P. Bean, Phys. Rev. **102**, 1413 (1956).
[28] J. Nogués and I. K. Schuller, J. Magn. Magn. Mater. **192**, 203 (1999).
[29] A. E. Berkowitz and K. Takano, J. Magn. Magn. Mater. **200**, 552 (1999).
[30] T. C. Schulthess, W. H. Butler, and G. M. Stocks, J. Appl. Phys. **85**, 4842 (1999).

[31] R. Jungblut, R. Coehoorn, M. T. Johnson, J. aan de Stegge, and A. Reinders, J. Appl. Phys. **75**, 6659 (1994).
[32] G. M. Stocks, W. A. Shelton, T. C. Schulthess, B. Újfalussy, W. H. Butler, and A. Canning, J. Appl. Phys. **91**, 7355 (2002).
[33] K. Nakamura, T. Ito, and A. J. Freeman, Phys. Rev. B **67**, 014405 (2003).
[34] N. C. Koon, Phys. Rev. Lett. **78**, 4865 (1997).
[35] D. J. Kubinski and H. Holloway, J. Appl. Phys. **79**, 7395 (1996).
[36] T. Valet and A. Fert, J. Magn. Magn. Mater. **121**, 378 (1993).
[37] Q. Yang, P. Holody, R. Loloee, L. L. Henry, W. P. Pratt Jr., P. A. Schroeder, and J. Bass, Phys. Rev. B **51**, 3226 (1995).
[38] P. Gaunt, Philos. Mag. B **48**, 261 (1983).
[39] J. Lindner, C. Rüdt, E. Kosubek, P. Poulopoulos, K. Baberschke, P. Blomquist, R. Wäppling, and D. L. Mills, Phys. Rev. Lett. **88**, 167206 (2002).
[40] M. A. M. Gijs, S. K. J. Lenczowski, and J. B. Giesbers, Phys. Rev. Lett. **70**, 3343 (1993).
[41] M. A. M. Gijs, S. K. J. Lenczowski, R. J. M. van de Veerdonk, J. B. Giesbers, M. T. Johnson, and J. B. F. aan de Stegge, Phys. Rev. B **50**, 16733 (1994).
[42] L. Néel, Comptes. Rendus **255**, 1676 (1962).
[43] J. C. S. Kools, W. Kula, D. Mauri, and T. Lin, J. Appl. Phys. **85**, 4466 (1999).
[44] J. I. Martín, J. Nogués, K. Liu, J. L. Vicent, and I. K. Schuller, J. Magn. Magn. Mater. **256**, 449 (2003).
[45] A. O. Adeyeye, J. A. C. Bland, C. Daboo, J. Lee, U. Ebels, and H. Ahmed, J. Appl. Phys. **79**, 6120 (1996).
[46] L. Kong, Q. Pan, B. Cui, M. Li, and S. Y. Chou, J. Appl. Phys. **85**, 5492 (1999).
[47] J. A. Katine, A. Palanisami, and R. A. Buhrman, Appl. Phys. Lett. **74**, 1883 (1999).
[48] K. Nordquist, S. Pendharkar, M. Durlam, D. Resnick, S. Tehrani, D. Mancini, T. Zhu, and J. Shi, J. Vac. Sci. Technol. B **15**, 2274 (1997).

Chapter 2

Superconductivity

The basic theory of low temperature superconductors is introduced [1, 2, 3]. The proximity effect between superconductors, normal [4], ferromagnetic [5] and antiferromagnetic metals is then examined, with the relationship to Andreev reflection [6]. Following this there is a brief discussion of the 'high temperature' superconducting cuprates.

2.1 Principal features

After the discovery of the sudden drop in resistivity in Hg at liquid helium temperatures [7], many other materials were subsequently found to show a similar transition at a variety of temperatures. The d.c. resistivity below this superconducting transition temperature was zero to within experimental error. Bulk niobium has the highest transition temperature $T_C = 9.25$ K, of the naturally occurring elements at atmospheric pressure. When the transition to the superconducting state occurs, the material does not simply become a perfect conductor. Meissner and Ocshenfeld [8] showed that magnetic flux is expelled from a superconductor when cooled below T_C. This perfect diamagnetism is in contrast to the trapping of flux expected on the basis of Faraday's law for a perfect conductor.

The phase transition that occurs at T_C provides the energy required to expel flux. The 'Meissner effect' therefore can only occur up to a certain critical magnetic field. Type I superconductors are no longer superconducting above this critical flux density B_C, (the flux density B is used in place of the field H to avoid confusion with the coercive field H_C). Type II superconductors are no longer perfect diamagnets above a flux density B_{C1}, and the flux enters the bulk as quantised vortices, (section 2.1.3). Only at the higher flux density B_{C2} is superconductivity totally suppressed.[1]

2.1.1 Two-Fluid model and London theory

As a phenomenological model of superconductivity, the Two-Fluid model [9] assumes a certain fraction of the normal electrons become dissipationless superelectrons. This fraction is temperature dependent, ranging from zero just above T_C, to one at 0 K. This model gives a simple explanation of why the critical field changes with temperature, and provided limited quantitative agreement with experiment.

F. London and H. London [10] adopted the diamagnetic property as being most fundamental and assumed a superfluid wavefunction with effective superelectron *pair* density n_p of the form $\Psi = \sqrt{n_p}\, e^{i\theta}$ that was rigid to the 'vorticity' imparted by a magnetic field, (the pair density is used as a convenience, second guessing the result of the microscopic theory in section 2.2). Using the standard gauge invariant [1] quantum mechanical form for current density in the presence of a vector potential $\mathbf{A}$, the supercurrent density $\mathbf{J}$ is then

$$\Lambda \mathbf{J} = -\left(\frac{\hbar}{2e}\nabla\theta + \mathbf{A}\right) . \tag{2.1}$$

$\Lambda = m_e/n_s e^2$, and the superelectron density $n_s = 2n_p$. With the addition of Maxwell's equations the Londons were able to account for the zero resistivity and also show that magnetic flux does penetrate the superconductor, but decays exponentially into the bulk. The characteristic decay length is the London penetration depth $\lambda = (\Lambda/\mu_0)^{\frac{1}{2}}$ which is of the order of 44 nm for Nb - a typical value for a metallic low T_C superconductor. The surface supercurrent $\mathbf{J}$ provides an equal and opposite magnetic field which cancels the applied field.

[1] Other fields such as the surface critical field B_{C3} are ignored for simplicity.

Integrating equation 2.1 around a closed loop, the phase θ must be single valued to within a factor of 2π.

$$\oint (\mathbf{A} + \Lambda \mathbf{J}) \cdot \mathrm{d}\mathbf{x} = \frac{\hbar}{2e} 2\pi n, \tag{2.2}$$

where n is an integer. For the case of a bulk superconductor a contour can be chosen inside the material where $\mathbf{J} = 0$. The integral $\oint \mathbf{A} \cdot \mathrm{d}\mathbf{x}$ is the flux Φ through the loop. Defining the *flux quantum* $\Phi_0 = \frac{h}{2e}$, equation 2.2 leads to $\Phi = n\Phi_0$. The flux through the loop of superconductor is quantised in units of Φ_0.

2.1.2 Ginzburg-Landau theory

The Ginzburg-Landau (GL) theory allows the number density of superelectrons to vary in space. At T_C a more subtle symmetry is broken compared to the rotational symmetry of a ferromagnet (section 1.1.1). The superfluid wavefunction, now written as $\psi(x)$, breaks the gauge symmetry and chooses a definite quantum mechanical phase, which is rigid (as in the London model) over macroscopic length scales. The phenomenological free energy density is written in terms of ψ which is complex, and can be position dependent:

$$f(\psi, T) = f_0(T) + \varepsilon(T)|\psi|^2 + \frac{1}{2}\alpha\,|\psi|^4 + \beta\,|(-i\hbar\nabla + e^*A)\psi|^2 + ... \tag{2.3}$$

Where α, β and ε are phenomenological terms, and e^* some effective charge, (which turns out to be twice the electronic charge). Conventionally β is taken as $1/2m^*$ where $m^* = 2m_e$ - the mass of a pair, and $\varepsilon \propto (T - T_C)/T_C$, analogous to the ferromagnetic case. Minimizing over all space:

$$\frac{1}{2m^*}(-i\hbar\nabla + 2eA)^2\psi + (\varepsilon + \alpha|\psi|^2)\psi = 0\,. \tag{2.4}$$

Equation 2.4 allows ψ to be found for any given A. With suitable boundary conditions [1] the GL penetration depth and coherence lengths can be derived from equation 2.4:

$$\lambda_{GL} = \sqrt{m^*\alpha/4\mu_0 e^2|\varepsilon|}\,, \tag{2.5}$$

$$\xi_{GL} = \sqrt{\hbar^2/2m^*|\varepsilon|}\,. \tag{2.6}$$

$\xi_{GL}(T)$ is the characteristic length scale over which $\psi(x)$ varies. Using the microscopic theory (section 2.2) ξ_{GL} in the dirty limit can be shown to be

$$\xi_{GL} = 0.855\sqrt{\xi_0 \ell}\left(\frac{T_C - T}{T_C}\right)^{-\frac{1}{2}}. \tag{2.7}$$

Where, (in the clean limit: $\ell \gg \xi_0$), $\xi_0 \approx \hbar v_F/k_B T_C$. v_F is the Fermi velocity, ℓ the electronic mean free path and k_B Boltzmann's constant (also see section 2.2).

2.1.3 Abrikosov vortices

Using the GL theory, Abrikosov [11] considered a superconductor in a magnetic field, and showed that when the ratio $\kappa = \lambda_{GL}(T)/\xi_{GL}(T)$ was large enough ($\kappa > 1/\sqrt{2}$) the superconductor / normal interface was unstable, and broke up into normal and superconducting regions. This is the case of type II superconductors above B_{C1}, where flux enters the bulk as quantised vortices, (type I have $\kappa < 1/\sqrt{2}$). These vortices are characterised by a core of size $\sim \xi_{GL}(T)$ in which $|\psi|$ is suppressed, and a circulating supercurrent which shields the flux line from the bulk, extending a distance $\sim \lambda_{GL}$(T) from centre of the core (figure 2.1).

If these vortices move, voltages are generated and the superconductor can no longer carry current without dissipation [12]. However it is energetically favourable for the normal core of the vortex to sit on an impurity or damaged region which is not superconducting. Vortices can be pinned at such sites, and prevented from moving. This pinning is important both technologically [13] and in the present work (section 7.1).

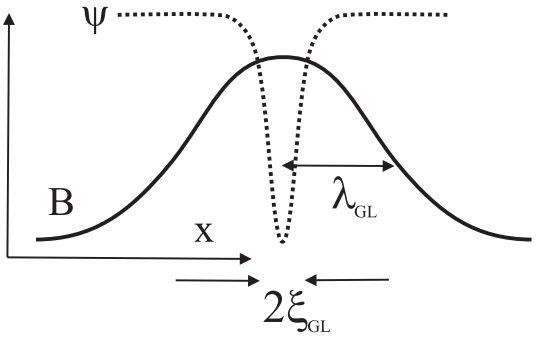

Figure 2.1: Schematic of the behaviour of the flux density **B** (solid line), and the wavefunction ψ (dashed line) around a vortex. Taken from Waldram [1].

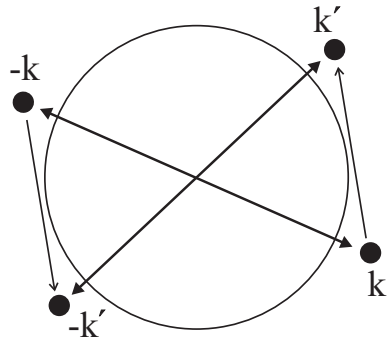

Figure 2.2: Scattering transition of paired electrons (with zero net momentum), around the Fermi surface in the Cooper model.

2.2 Microscopic theory

The prediction by Fröhlich [14] and experimental verification of the 'isotope effect' showed that lattice phonons were important in coupling electrons to form the superconducting state. Cooper showed that for a small attractive potential $V_{k,k'} = \langle \mathbf{k}, -\mathbf{k}|V|\mathbf{k}', -\mathbf{k}'\rangle$ (figure 2.2) a pair of electrons in contact with the Fermi sea is unstable with respect to condensation into a bound pair [15]. This provided a mechanism of bonding electrons together involving phonon coupling. The theoretical model was not simple, since the coupled state cannot be derived by a perturbation of the uncoupled state [16, 17].

The Bardeen-Cooper-Schrieffer (BCS) theory [18] followed from the work of Cooper, and was able to account for the properties of superconductors in terms of the condensation of 'Cooper' electron pairs into a macroscopically occupied groundstate. The calculation of parameters such as the penetration depth, coherence length and critical fields could be then made from first principles. Lattice phonons interacting with the electrons provide the attractive potential energy

V required by the Cooper theory. In a very basic model, an electron distorts the crystal lattice producing a local region of low potential energy. As long as the interaction is not too strong, (i.e. the momentum transfer is small compared to the phonon frequency), the electron moves off in a time much faster than the lattice relaxes, (so-called *overscreening*) enabling another electron to take advantage of the potential well, which effectively couples the two electrons together.

The superconducting groundstate $|\psi_G\rangle$ can be written as

$$|\psi_G\rangle = \prod_k (u_k + e^{i\theta} v_k a^\dagger_{k\uparrow} a^\dagger_{-k\downarrow})|0\rangle \ , \tag{2.8}$$

with

$$|u_k^2| + |v_k^2| = 1 \ . \tag{2.9}$$

Here $|0\rangle$ is the vacuum state, $e^{i\theta}$ is an arbitrary phase factor associated with all of the Cooper pairs. The $a^\dagger_{ks}$ operators obey the fermionic commutation rules, (which embody Pauli's exclusion principle), and create an electron with spin $\mathbf{s}$ and momentum $\mathbf{k}$. $|u_k|^2$ gives the probability of the momentum pair state being empty, and $|v_k|^2$ it being full. Using this groundstate the energy of an electron with momentum $\mathbf{k}$ is given by

$$E_k^2 = \epsilon_k^2 + \Delta_k^2 \ . \tag{2.10}$$

ϵ_k is the reservoir energy, from which the electron is excited, and Δ_k is the superconducting gap

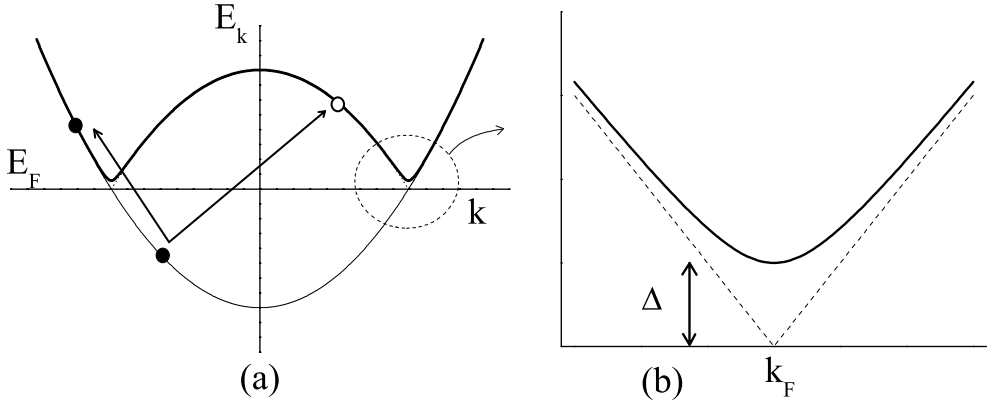

Figure 2.3: (a) Excitation spectrum for a normal metal measured relative to the Fermi energy. The excitation above E_F can be considered as electron-like (•) or hole-like (◦). (b) Detail of the gap in the superconductor spectrum (solid line) compared to the normal case (dashed line) near the Fermi wavevector k_F, according to equation 2.10.

in the energy spectrum (figure 2.3). An energy of $2\Delta_k$ must therefore be supplied to break up a Cooper pair, and produce excitations. Since the gap has blurred the Fermi energy above *and* below k_F, these excitations can have electron-like and hole-like properties, and will be referred to as quasi-particles. In addition to the intra-pair attraction it is the strong overlap and pair-pair correlations which cause the gap to open. The pairs are immune to scattering due to these pair-pair correlations caused by Pauli exclusion.

The gap Δ_k is determined using

$$\Delta_k = -\sum_{k'} \frac{V_{k,k'}\Delta_{k'}}{2E_{k'}} \, . \tag{2.11}$$

In the weak-coupling limit V can be approximated as a (negative) constant. In this simplest case, the most energetically favourable state is an s-wave symmetry (Δ independent of $\mathbf{k}$) with the Cooper pairs having overall zero momentum, and spin singlet ($-\mathbf{k}\uparrow, +\mathbf{k}\downarrow$). The singlet ensures the overall fermionic anti-symmetry of the wavefunction.

The coherence length can now be understood in BCS theory as the 'size' of a Cooper pair. In the clean limit $\xi_0 = \hbar v_F/\pi\Delta(0)$. Where $\Delta(0) \approx 1.76 k_B T_C$, (this is valid for many metals). Given the electron density in most metals, and the size of ξ_0, Cooper pairs spatially overlap in conventional BCS superconductors.

It is important to note that for the formulation used in equation 2.8, the number operator is not an eigenstate. The distribution of N is strongly peaked around the actual value, but its value is uncertain. This is important for the Josephson effect (chapter 3). In fact it is possible to show that the N and θ are conjugate variables such that

$$\Delta N \, \Delta\theta \geq 1 \, . \tag{2.12}$$

2.3 The proximity effect

When a superconductor is placed in good electrical contact with another material it is clear that the gap parameter Δ must change with position. The standard mean field approach of BCS theory is inapplicable in this situation. Gor'kov [19] was able to show that the GL theory could be derived from a limiting case of the BCS microscopic model, and used position dependent gap $\Delta(x)$ as an order parameter [20]:

$$\Delta(x) = V(x)F(x) \, . \tag{2.13}$$

$|F|^2$ gives the probability of finding a Cooper pair at position x. The effective electron-electron interaction is given by $V(x)$, which is attractive in the superconductor, but can be zero in the other material. In the superconductor / normal metal (S/N) bilayer with $V = 0$ in the N layer, $\Delta = 0$ in the normal metal, but $F(x)$ is non-zero close to the interface.[2]

A simple model of the interface with no current is shown below in figure 2.4. Werthamer and de Gennes [21] theory extended Gor'kov's work assuming thick layers in the dirty limit: such that the microscopic details at the interface become less important.

The characteristic decay length in the normal metal ξ_N in the clean and dirty limits is given by

$$\xi_N^0 = \hbar v_F/2\pi k_B T \, , \tag{2.14}$$

[2]The case $V < 0$ for a normal metal is the case that it is a superconductor with $T > T_C$.

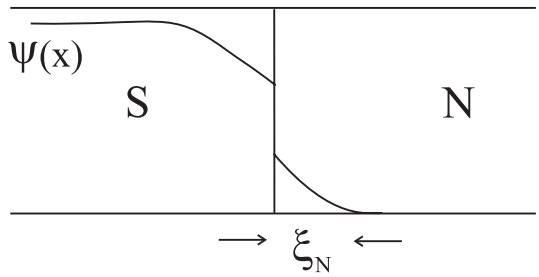

Figure 2.4: Behaviour of $\psi(x)$ near a S/N interface.

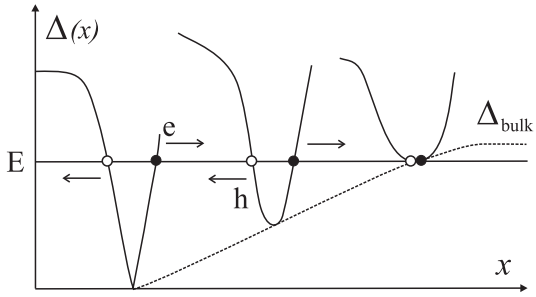

Figure 2.5: Andreev reflection of an quasi-electron (•) as a quasi-hole (○) at an S/N interface. After Zagoskin [6].

and

$$\xi_N = \sqrt{\frac{\hbar v_F \ell}{6\pi k_B T}} \,. \tag{2.15}$$

respectively. In figure 2.4 the boundary conditions at the interface are such that not only is there some 'leakage' of the Cooper pair density into the normal metal, but also the proximity of the metal reduces the Cooper pair density in the superconductor. In thin films this weakening of the superconductivity near the boundary leads to suppression of T_C.

In the one frequency approximation for film thickness $d_{S,(N)} > \xi_{S,(N)}$ in the dirty limit the T_C of an S/N bilayer is given as

$$q \tan(q\, d_S) = \frac{D_N \mathcal{N}_N(E_F)}{D_S \mathcal{N}_S(E_F)} K \tanh(K d_N) \,. \tag{2.16}$$

q and K are the wavevectors in the S and N layers, $D_X = \frac{1}{3} v_F \ell$ and $\mathcal{N}_X(E_F)$ are respectively the electronic diffusion constant and density of states at the Fermi level in the X layer.

2.3.1 Andreev reflection

Current can flow from a normal metal into a superconductor with an applied voltage $< \Delta$. Since single particle excitations cannot exist in the superconductor with sub-gap energies, the incoming electrons must be converted into Cooper pairs. This process is known as Andreev reflection [22], and is shown schematically in figure 2.5. The magnitude of $\Delta(x)$ steadily increases upon passing into the bulk superconductor. When the energy of the electron $E = \Delta(x)$ the quasi-electron's momentum is near perfectly *reversed*,[3] the spin flipped, and a quasi-hole returns from right to left in the figure. To conserve charge, spin and momentum a Cooper pair enters the superconductor.

In clean structures where Andreev reflection is the dominant process, (in the absence of normal reflection due to e.g. Fermi velocity mismatch), interference of the quasi-electrons and holes can lead to oscillatory transport properties. These effects will not be discussed - see [23] for a review. Importantly for the present case, Andreev reflection is strongly altered in the case of an S/F boundary. This will be discussed in section 2.4.1.

[3] Not specularly reflected.

2.4 Ferromagnetic proximity effect

The orbital motion of electrons in an applied magnetic field causes the break up of Cooper pairs. This effect is present when a ferromagnetic layer is considered in proximity to a superconductor. However, more important in this case is the so-called paramagnetic effect, in which a relatively strong magnetic field suppresses superconductivity by aligning the spins of the electrons in a Cooper pair. On a microscopic level following Demler *et al* [24], a Cooper pair is considered adiabatically transferred from a superconductor into a ferromagnet, in the absence of significant spin-orbit coupling. Electrons with spin parallel to the exchange field in the Cooper pairs are decreased in potential energy, the spins anti-parallel to the exchange field are increased in energy by the same amount. In order for the total electron energy to remain constant the momenta change by an amount $\pm\Delta k = \pm E_{Ex}/\hbar v_F$. Fermionic antisymmetry requires that the pair must also be described with the spin up and spin down electrons interchanged in momentum space, (figure 2.6 (a)(i) and (ii)).

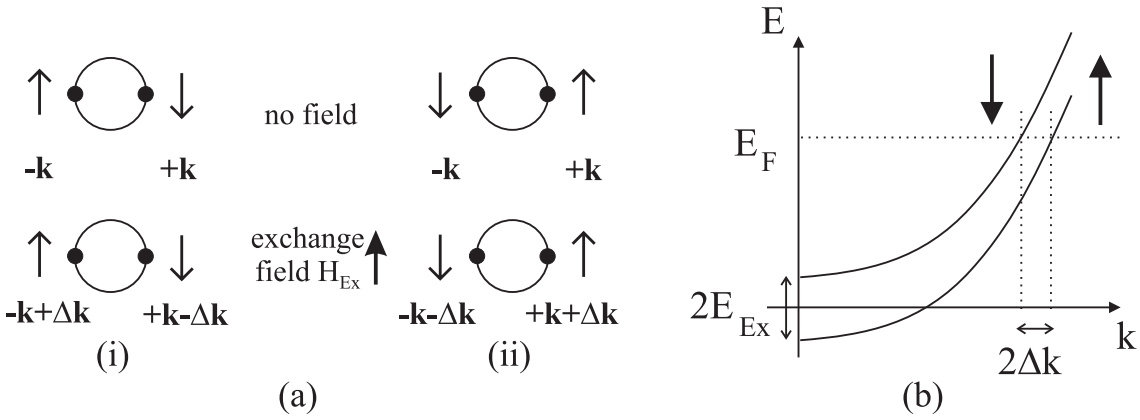

Figure 2.6: (a) Two possible configurations (i) and (ii) for the momentum change of electrons in a Cooper pair due to (b) band splitting in the presence of exchange field. After Demler *et al* [24].

Combining the two possibilities into a singlet produces a wavefunction of the form $\cos(Q(x_1+x_2))\Psi(x_1-x_2)$, where $\Psi(x_1-x_2)$ is the original wave function of the Cooper pair in the superconductor, (with electrons at x_1 and x_2), and Q is the centre of mass momentum $2E_{Ex}/\hbar v_F$. The amplitude and phase of the order parameter spatially oscillates. This type of spatially inhomogeneous superconductivity with a non-zero centre of mass momentum is formally the same as the Fulde-Ferrel-Larkin-Ovchinnikov (FFLO) state [25, 26] predicted for type II materials in high applied magnetic fields.[4] The FFLO state occurs in a relatively small region of the $(\mathbf{H}, T)$ phase diagram [28]. In this case the superconductivity is induced in the ferromagnet by the superconductor, with H_{Ex} analogous to the high applied field in the FFLO case, and the 'bulk' multilayer is a combination of BCS and FFLO states in the S and F layers respectively. However the Cooper pair is not an eigenstate in the F layer. Hence the order parameter decays exponentially away from the S/F interface, as in the S/N case. The S/F proximity effect is

[4]Experimental observations of the FFLO state in bulk samples have been made only recently [27].

characterised by an decaying, but oscillating order parameter.

The two characteristic length scales in the ferromagnetic layer, the decay length ξ_{F1}, and the oscillation period ξ_{F2} arise from the general form given by [29]:

$$\xi_F = \left[\frac{\hbar D}{2(\pi k_B T + iE_{Ex})}\right]^{\frac{1}{2}} . \tag{2.17}$$

For a strong ferromagnet $E_{Ex} \gg k_B T$, and $\xi_{F1} = \xi_{F2}$. Other limits of equation 2.17 will be discussed in section 3.2.

2.4.1 Implications for Andreev reflection

Quasi-particles have their spin flipped when they undergo Andreev reflection (section 2.3.1). In the S/F case a majority (up) spin quasi-electron is reflected as a minority (down) spin. Assuming the up and down spin channels do not mix, the conductance is then controlled by the *minority* band density of states, if magnon assisted spin-flip scattering is ignored [30]. In such cases a non-equilibrium accumulation of spins may build up at the S/F interface [31].

This may have important consequences in the measurement of CPP GMR multilayers discussed in section 1.2.1. Several experiments [32, 33], (as well as the present work: section 8.2), use superconducting Nb electrodes. Theoretical modelling by Taddei *et al* [34] found a large suppression in the CPP GMR for structures with superconducting electrodes in the clean limit, due to Andreev reflection at the S/F interface. As shown in their schematic (figure 2.7), because the up spin quasi-electrons are reflected as down spin quasi-holes, in total they 'see' the same resistance in the anti-parallel (AF) and parallel (F) orientations of the GMR stack, (compare with figure 1.8). Taddei *et al* initially concluded that spin-flip scattering was the only cause of the GMR observed experimentally [34], but later added the possibility that spin orbit coupling could reduce the difference between the theory and experiment [35]. Other models using semi-infinite S layers (rather than the finite thicknesses of the work of Taddei *et al*), showed a similar suppression to zero MR in the diffusive limit, but recovered the MR in the ballistic / quasi-ballistic limit [36, 37]. The Andreev conductance of domain walls near the S/F interface

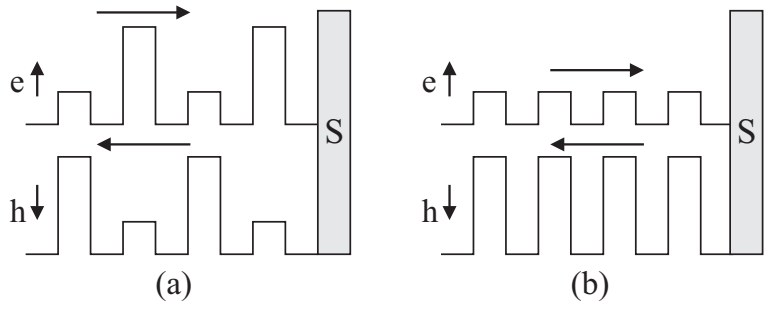

Figure 2.7: Schematic diagram of the scattering potentials experienced by Andreev reflected quasiparticles in a GMR multilayer due to an S/F interface in the (a) AF and (b) F alignments. Taken from Taddei *et al* [34].

has also been considered by Chtchelkatchev *et al* [38]. In this case, in the limit of full polarisation

in the ferromagnetic layer, the sub-gap Andreev conductance is proportional to the total length of domain walls at the S/F interface.

2.4.2 Multilayer studies

It was noted by de Gennes that ξ_F would typically be < 10 nm due to the pair breaking exchange field, and that films of that thickness were 'very difficult to prepare' [39]. Advances in thin film growth now allow the preparation of high quality S/F structures within this thickness range.

The oscillations of ξ_F mean that for a suitable thickness of ferromagnetic d_F, the groundstate phase difference between consecutive S layers in a S/F multilayer can be π, instead of 0 [40, 41] (also see section 3.2).[5] This was predicted to give a non-monotonic dependence of the transition temperature vs ferromagnetic thickness $T_C(d_F)$, in S/F multilayers.

Wong *et al* [42] initiated the renewed theoretical and experimental interest in the field when they studied the critical field B_{C2} parallel to the plane, in V/Fe superlattices. A crossover in the field dependence from two-dimensional to three-dimensional was found when $d_V \sim \xi_{BCS}$ and $d_{\mathrm{F}e} \sim$ a few atomic planes, implying coexistence of superconductivity and ferromagnetism for the three-dimensional case. Similar behaviour was then found in V/Ni [43] and Mo/Ni structures [44].

Following this work, an array of different multilayer systems have since been examined. Recent reviews can be found in [5, 45]. Many different systems were studied, showing oscillating $T_C(d_F)$ [46, 47, 48]. Many however found no such behaviour [49, 50, 51, 52], other than a strong decoupling effect of the superconducting layers by only a few nm of ferromagnetic material. Evidence for π coupling was cast into further doubt when oscillatory $T_C(d_F)$ was found in F/S/F trilayers [53, 54]. In these cases π-coupling must be ruled out, since there is only one superconducting layer.

Various theoretical models of trilayer and multilayer systems have developed predicting oscillatory $T_C(d_F)$ [22, 41, 55, 56]. The interface roughness and alloying for such thin F layers is crucial [54]. These factors, along with spin-orbit coupling can wash out the oscillatory behaviour [45]. The different results have been attributed to changes in the S/F interface transparency at the onset of ferromagnetism, which is dependent on the system studied [57, 58], making clear evidence for a π shift difficult to prove. As shall be seen in section 3.2 it has only been with the use of *weak* F layers, (alloys with low T_M), that ξ_F is large enough that π phase shifts can be controllably demonstrated using tunnel and Josephson junctions.

2.4.3 'Spin-valve' structures

Various designs have been put forward to use the ferromagnetic layer - the orientation of which can be changed with an applied field - to controllable alter the superconducting layer in proximity to it. In the simplest case of an S/F bilayer, the transport properties can be varied in accordance

[5] The 0-π transition was found to be continuous with stable states between 0 and π but only "in a narrow range" [41].

with the hysteresis of the ferromagnet. This has been interpreted in terms of domain structure in the F layer [59] or spontaneous vortices in the S layer [60].

Other 'spin-valve' devices using multiple ferromagnetic layers (figure 2.8) have been examined theoretically, [61, 62, 63]. These structures are predicted to show a strong variation of T_C with the relative orientation of the ferromagnetic layers. In the case of the F/S/F structure, only a small change in T_C has been found experimentally [64] compared to the theoretical value.

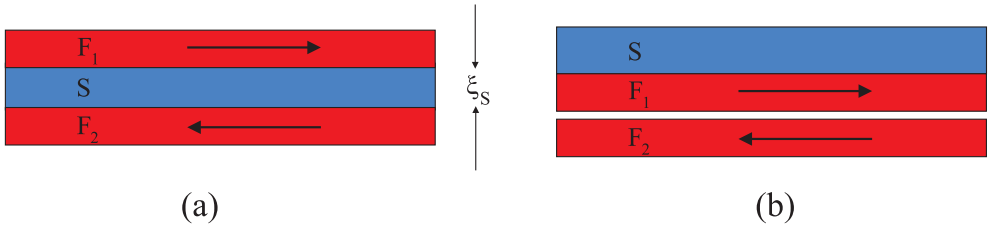

Figure 2.8: Schematics of (a) the F/S/F spin-valve as suggested by Tagirov [62] and (b) the S/F_1/F_2 structure of Oh *et al* [63].

2.4.3.1 Anomalous proximity effect

There is increasing evidence for coupling through ferromagnetic materials over a length scale two orders of magnitude greater than the typical values of ξ_F above [65, 66, 67, 68]. This surprising result may be explained due to the presence of domain walls in the ferromagnetic layer. The rotating magnetic moment may turn the singlet Cooper pair into a triplet state, which can penetrate the ferromagnet to a similar distance as the singlet state in the normal metal case [69, 70, 71]. Currently this possibility has not been confirmed.

2.5 Antiferromagnetic proximity effect

Krivoruchko has considered the superconductor / antiferromagnet (S/AF) system, where the same charge carriers take part in the superconductivity and antiferromagnetism [72, 73]. In the case of band antiferromagnetism due to nesting of the Fermi surfaces (section 1.1.3.1), the symmetry in momentum space is destroyed, similar to the splitting of the Fermi surface in the ferromagnetic case. Therefore a band antiferromagnet heavily suppresses superconductivity. In the dirty limit (for both S and AF), assuming that the characteristic frequencies of the system are such that $\hbar\omega \sim T_C \ll T_N$ then the AF wavevector has the form $k_{AF} = 2/\xi_{AF}$ (rather than the complex form $k_F = 2(1+i)/\xi_F$ which gives rise to the oscillating order parameter in the ferromagnetic case - section 2.4). This leads to a coherence length ξ_{AF}, of the form

$$\xi_{AF} = \left[\frac{2\hbar D}{E_{Ex}}\right]^{\frac{1}{2}} . \tag{2.18}$$

$E_{Ex} \sim k_B T_N$ is now the exchange coupling energy between the AF spins [72].

As seen in section 2.4, there is a large body of experimental and theoretical work concerning the S/F proximity effect. This is not the case for the S/AF system. Cr is a good example known to have a variety of spin density wave phases [74], and has attracted some investigation in Nb/Cr multilayers [75], and Cr/V/Cr trilayers [76]. Nb/CuMn (spin-glass) systems have also been studied [77], but very few other systems (see references in [73]). In the absence of a large theoretical literature, much of the theory presented in this section and section 3.3 uses a simplified model to give a generic understanding of the S/AF system.

The T_C of S/AF bilayers with varying d_S and d_{AF} are presented in section 8.3.2. In reference [76] the data was analysed in terms of the Werthamer theory [78], which considers the case that the metals are identical in the normal state - i.e. the Fermi velocities, residual resistivity and Debye temperatures are the same, and uses a single effective coherence length. In the present case however the Nb and FeMn films are significantly different, and the coherence lengths of the S and AF should be considered separately. Hence the de Gennes theory in the one frequency approximation is used [79] (section 2.3).

The AF is taken to have $T_C = 0$ K. Using

$$\frac{1}{q} \approx \xi_S \sqrt{2} \left(\frac{T - T_C}{T_C} \right)^{-\frac{1}{2}} \tag{2.19}$$

and $K = k_{AF} = 2/\xi_{AF}$ in equation 2.16 above, the T_C of the S/AF bilayer satisfies

$$\frac{1}{\sqrt{2}\,\xi_S} \sqrt{\left(\frac{T_{CS}}{T_C} - 1 \right)} \tan \left[\frac{d_S}{\sqrt{2}\,\xi_S} \sqrt{\left(\frac{T_{CS}}{T_C} - 1 \right)} \right] = \frac{2}{\xi_{AF}} \frac{D_{AF} \mathcal{N}_{AF}(E_F)}{D_S \mathcal{N}_S(E_F)} \tanh \left[\frac{2 d_{AF}}{\xi_{AF}} \right], \tag{2.20}$$

where $\xi_S = 0.855(\xi_0 \ell)^{\frac{1}{2}}$. $1/q$ is within 20 % of ξ_{GL} in this approximation [80]. The largest root of this equation gives T_C, the transition temperature of the bilayer. Here $\mathcal{N}_{S,AF}(E_F)$ are the density of states at the Fermi level of the S and AF respectively, and T_{CS} the transition temperature of the plain S layer, (without the AF next to it).

A more complex Green's function method, which goes beyond the one frequency approximation, used by Krivoruchko [73] will not be presented here, but will be compared to the experimental data in section 8.3.2.

2.6 Superconductivity in the cuprates

The first member of the family of 'High Temperature Superconductors' (HTS) to be discovered was $La_{2-x}Ba_xCuO_4$ [81]. Many different cuprates were subsequently discovered, all based around the layered perovskite structure, with superconductivity strongly sensitive to the stoichiometry [82]. At present $HgBa_2Ca_2Cu_3O_8$ has the highest $T_C = 157$ K at a pressure of 23.5 GPa [83], with $Tl_2Ba_2CaCu_2O_8$ (Tl-2212), having $T_C \sim 100$ K [84], (see figure 2.9 (a) and section 6.1).

Of most relevance to this work is the layered and anisotropic electrical properties of the cuprates both above and below T_C. For example, above T_C, values of the resistivity ratio ρ_c/ρ_{ab} for the different crystallographic direction a, b and c vary from 10 for optimally doped

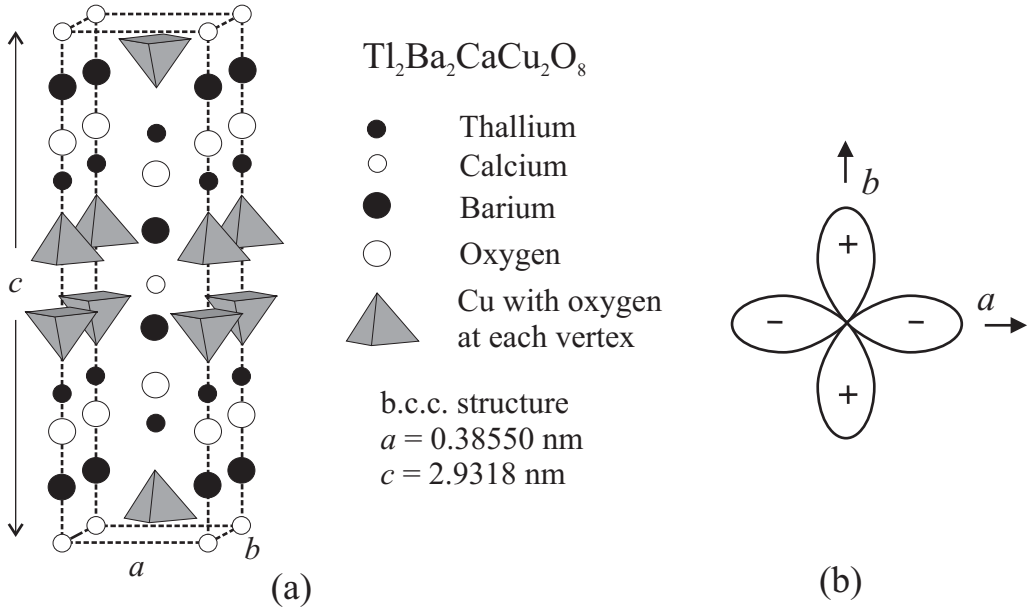

Figure 2.9: (a) The crystal structure of Tl-2212 from Poole [82] after Subramanian *et al* [85]. (b) Amplitude and phase of the gap parameter $\Delta(\mathbf{k})$ with $d_{x^2-y^2}$ symmetry relative to the crystallographic directions a and b ($a = b$ in this case).

$YBa_2Cu_3O_{6+x}$ (YBCO) to 10^5 for $Bi_2Sr_2CaCu_2O_{8+x}$ [1]. The superconductivity is thought to preside in the CuO_2 planes, with the other layers acting as a combination of spacer and charge reservoir. The coherence length ξ is relatively short in both the a-b plane and c directions (of the order of 2 nm and 0.5 nm respectively [1]). Hence the superconductivity in neighbouring CuO_2 planes can be only weakly coupled. Due to the weak interplane coupling intrinsic Josephson junctions are observed when current is passed in the c-direction of the more anisotropic cuprates (see section 3.6 for further theory and section 6.1.5.1 for measurements of Tl-2212 junctions).

There is currently no full theoretical description of the superconducting and normal state properties of the HTS. The superconductivity is based on Cooper pairs [86], and Knight shift measurements and symmetry arguments [87] mean that the Cooper pairs are singlet, but the microscopic mechanism is not clear. The determination of the symmetry of the gap parameter Δ was one of the key experimental results which constrains the possible theories of the HTS [87]. After several crucial *phase sensitive* experiments [88, 89] using YBCO it was generally agreed that the symmetry is dominated by a $d_{x^2-y^2}$ component. The amplitude of Δ varies in k-space, and the phase changes sign across nodal lines at 45° to the a and b directions (figure 2.9 (b)). The work in YBCO has been repeated with similar results for compounds in the different groups of the HTS family [90], but the universality of the d-wave symmetry is not confirmed.

For device physics the result of d-wave symmetry is somewhat similar to the oscillating phase of the order parameter in the ferromagnet. The π shift for example in S/F multilayers, can be mirrored by arranging that the two lobes of the d-wave with different sign should meet, or by using d-wave / s-wave junctions [91, 92], (see figure 3.10 in section 3.6.2).

References

[1] J. R. Waldram, *Introduction to Superconductivity in Metals and Cuprates* (Institute of Physics Publising, 1996).
[2] M. Tinkham, *Introduction to Superconductivity, (2nd Edition)* (McGraw-Hill, 1996).
[3] J. R. Schrieffer, *Theory of Superconductivity* (Perseus Books, 1983).
[4] P. G. de Gennes, *Superconductivity of Metals and Alloys* (Perseus Books, 1965).
[5] Y. A. Izyumov, Y. N. Proshin, and M. G. Khusainov, Usp. Fiz. Nauk **172**, 113 (2002), [Phys. Usp. **45** 109 (2002)].
[6] A. M. Zagoskin, *Quantum Theory of Many-Body Systems* (Springer, 1998).
[7] H. K. Onnes, Commun. Phys. Lb. Univ. Leiden No 124c (1911).
[8] W. Meissner and R. Ochsenfeld, Naturwissenschaften **21**, 787 (1933).
[9] C. J. Gorter and H. G. B. Casimir, Phys. Z. **35**, 963 (1934).
[10] F. London and H. London, Proc. R. Soc. **A149**, 71 (1935).
[11] A. A. Abrikosov, Zh. Éksp. Teor. Fiz. **32**, 1442 (1957), [JETP **5** 1174 (1957)].
[12] J. Bardeen and M. J. Stephen, Phys. Rev. **140**, A1197 (1965).
[13] J. E. Evetts, ed., *Critical Currents* (Supercond. Sci. Technol. **5**, 1992), Proceeding of the 6$^{\text{th}}$ International Workshop on Critical Currents.
[14] H. Fröhlich, Phys. Rev. **79**, 845 (1950).
[15] L. N. Cooper, Phys. Rev. **104**, 1189 (1956).
[16] M. R. Schafroth, Helv. Phys. Acta **24**, 645 (1951).
[17] A. B. Migdal, Zh. Éksp. Teor. Fiz. **34**, 1438 (1958), [JETP **7** 996 (1957)].
[18] J. Bardeen, L. N. Cooper, and J. R. Schrieffer, Phys. Rev. **108**, 1175 (1957).
[19] L. P. Gor'kov, Zh. Éksp. Teor. Fiz. **36**, 1918 (1959), [JETP **9** 1364 (1959)].
[20] L. P. Gor'kov, Zh. Éksp. Teor. Fiz. **34**, 735 (1958), [JETP **7** 505 (1958)].
[21] P. G. de Gennes, Phys. Lett. **5**, 22 (1963).
[22] A. F. Andreev, Zh. Éksp. Teor. Fiz. **46**, 1823 (1964), [JETP **19** 1228 (1964)].
[23] C. J. Lambert and R. Raimondi, J. Phys.: Condens. Matter **10**, 901 (1998).
[24] E. A. Demler, G. B. Arnold, and M. R. Beasley, Phys. Rev. B **55**, 15174 (1997).
[25] P. Fulde and A. Ferrel, Phys. Rev. **135**, A550 (1964).
[26] A. Larkin and Y. Ovchinnikov, Zh. Éksp. Teor. Fiz. **47**, 1136 (1964), [JETP **20** 762 (1965)].
[27] J. Singleton, J. A. Symington, M.-S. Nam, A. Ardavan, M. Kurmoo, and P. Day, J. Phys.: Condens. Matter **12**, L641 (2000).
[28] D. Saint-James, G. Sarma, and E. J. Thomas, *Type II Superconductivity* (Pergamon, New York, 1969).
[29] V. V. Ryazanov, A. V. Veretennikov, V. A. Oboznov, A. Y. Rusanov, A. A. Golubov, and J. Aarts, Usp. Fiz. Nauk **171**, 81 (2001).
[30] M. J. M. de Jong and C. W. J. Beenakker, Phys. Rev. Lett. **74**, 1657 (1995).
[31] G. Tkachov, E. McCann, and V. Fal'ko, Phys. Rev. B **65**, 024519 (2001), and references therein.
[32] W. P. Pratt Jr., S.-F. Lee, J. M. Slaughter, R. Loloee, P. A. Schroeder, and J. Bass, Phys.

Rev. Lett. **66**, 3060 (1991).
[33] P. Holody, W. C. Chiang, R. Loloee, J. Bass, W. P. Pratt, and P. A. Schroeder, Phys. Rev. B **58**, 12230 (1998).
[34] F. Taddei, S. Sanvito, J. H. Jefferson, and C. J. Lambert, Phys. Rev. Lett. **82**, 4938 (1999).
[35] F. Taddei, S. Sanvito, and C. J. Lambert, Phys. Rev. B **63**, 012404 (2001).
[36] N. Ryzhanova, B. Dieny, C. Lacroix, N. Strelkov, D. Bagrets, and A. Vedyayev, J. Phys.: Condens. Matter **13**, 4001 (2001).
[37] A. Vedyayev, D. Bagrets, A. Bagrets, N. Ryzhanova, N. Strelkov, B. Dieny, and C. Lacroix, J. Magn. Magn. Mater. **242**, 453 (2002).
[38] N. M. Chtchelkatchev and I. S. Burmistrov, Phys. Rev. B **68**, 140501R (2003).
[39] P. G. de Gennes, Rev. Mod. Phys. **36**, 225 (1964).
[40] L. N. Bulaevkiĭ, V. V. Kuziĭ, A. A. Sobyanin, and P. N. Lebedev, Solid State Comm. **25**, 1053 (1978).
[41] Z. Radović, M. Ledvij, L. Dobrosavljević-Grujić, A. I. Buzdin, and J. R. Clem, Phys. Rev. B **44**, 759 (1991).
[42] H. K. Wong, B. Y. Jin, H. Q. Yang, J. B. Ketterson, and J. E. Hilliard, J. Low Temp. Phys. **63**, 307 (1986).
[43] H. Homma, C. S. L. Chun, G.-G. Zheng, and I. K. Schuller, Phys. Rev. B **33**, 3562 (1986).
[44] C. Uher, J. L. Cohn, and I. K. Schuller, Phys. Rev. B **34**, 4906 (1986).
[45] I. A. Garifullin, J. Magn. Magn. Mater. **240**, 571 (2002).
[46] J. S. Jiang, D. Davidovic, D. H. Reich, and C. L. Chien, Phys. Rev. Lett. **74**, 314 (1995).
[47] C. L. Chien, J. S. Jiang, J. Q. Xiao, D. Davidovic, and D. H. Reich, J. Appl. Phys. **81**, 5358 (1997).
[48] F. Y. Ogrin, S. L. Lee, A. D. Hillier, A. Mitchell, and T.-H. Shen, Phys. Rev. B **62**, 6021 (2000).
[49] S. Kaneko, U. Hiller, J. M. Slaughter, C. M. Falco, C. Coccorese, and L. Maritato, Phys. Rev. B **58**, 8229 (1998).
[50] J. E. Mattson, C. D. Potter, M. J. Conover, C. H. Sowers, and S. D. Bader, Phys. Rev. B **55**, 70 (1997).
[51] P. Koorevaar, Y. Suzuki, R. Coehoorn, and J. Aarts, Phys. Rev. B **49**, 441 (1994).
[52] G. Verbank, C. D. Potter, R. Schad, P. Belien, V. V. Moshchalkov, and Y. Bruynseraede, Physica C **235-240**, 3295 (1994).
[53] T. Mühge, K. Westerholt, H. Zabel, N. N. Garif'yanov, Y. V. Goryunov, I. A. Garifullin, and G. G. Khaliullin, Phys. Rev. B **55**, 8945 (1997).
[54] L. Lazar, K. Westerholt, H. Zabel, L. R. Tagirov, Y. V. Goryunov, N. N. Garif'yanov, and I. A. Garifullin, Phys. Rev. B **61**, 3711 (2000).
[55] I. Baladié, A. Buzdin, N. Ryzhanova, and A. Vedyayev, Phys. Rev. B **63**, 054518 (2001).
[56] C. A. R. S. de Melo, Phys. Rev. Lett. **79**, 1933 (1997).
[57] J. Aarts, J. M. E. Geers, E. Brück, A. A. Golubov, and R. Coehoorn, Phys. Rev. B **56**, 2779 (1997).
[58] L. R. Tagirov, Physica C **307**, 145 (1998).
[59] R. J. Kinsey, Ph.D. Thesis, University of Cambridge (2002).
[60] V. V. Ryazanov, V. A. Oboznov, A. S. Prokof'ev, and S. V. Dubonos, Pis'ma Zh. Éksp. Teor. Fiz. **77**, 43 (2003), [JETP Lett. **77** 39 (2003)].
[61] S. Takahashi, H. Imamura, and S. Maekawa, Phys. Rev. Lett. **82**, 3911 (1999).
[62] L. R. Tagirov, Phys. Rev. Lett. **83**, 2058 (1999).
[63] S. Oh, D. Youm, and M. R. Beasley, Appl. Phys. Lett. **71**, 2376 (1997).
[64] J. Y. Gu, C.-Y. You, J. S. Jiang, J. Pearson, Y. B. Bazaliy, and S. D. Bader, Phys. Rev. Lett. **89**, 267001 (2002).

[65] M. D. Lawrence and N. Giordano, J. Phys.: Cond. Matter **8**, 563 (1996).
[66] V. T. Petrashov, V. N. Antonov, S. V. Maksimov, and R. S. Sahikhaidarov, Pis'ma Zh. Éksp. Teor. Fiz. **59**, 523 (1994), [JETP Lett. **59** 523 (1994)].
[67] M. Giroud, H. Courtois, K. Hasselbach, D. Mailly, and B. Pannetier, Phys. Rev. B **58**, 11872 (1998).
[68] V. T. Petrashov, I. A. Sosnin, I. Cox, A. Parsons, and C. Troadec, Phys. Rev. Lett. **83**, 3281 (1999).
[69] A. Kadigrobov, R. I. Shekhter, and M. Jonson, Europhys. Lett. **54**, 394 (2001).
[70] F. S. Bergeret, A. F. Volkov, and K. B. Efetov, Phys. Rev. B **64**, 134506 (2001).
[71] F. S. Bergeret, V. V. Pavlovskii, A. F. Volkov, and K. B. Efetov, Int. J. Mod. Phys. B **16**, 1459 (2002).
[72] V. N. Krivoruchko, Zh. Éksp. Teor. Fiz **109**, 649 (1995), [JETP **82**, 347 (1995)].
[73] V. N. Krivoruchko, Zh. Éksp. Teor. Fiz **111**, 547 (1997), [JETP **84**, 300 (1997)].
[74] E. Fawcett, Rev. Mod. Phys. **60**, 209 (1988).
[75] Y. Cheng and M. B. Stearns, J. Appl. Phys. **67**, 5038 (1990).
[76] M. Hübener, D. Tikhonov, I. A. Garifullin, K. Westerholt, and H. Zabel, J. Phys.: Condens. Matter **14**, 8687 (2002).
[77] C. Attanasio, C. Coccorese, L. V. Mercaldo, M. Salvato, L. Maritato, S. L. Prischepa, C. Giannini, L. Tapfer, L. Ortega, and F. Comin, Physica C **312**, 112 (1999).
[78] N. R. Werthamer, Phys. Rev. **132**, 2440 (1963).
[79] P. G. de Gennes, Rev. Mod. Phys. **36**, 225 (1964).
[80] E. J. Tarte, Ph.D. Thesis, University of Cambridge (1992).
[81] J. G. Bednorz and K. A. Müller, Z. Phys. B **64**, 189 (1986).
[82] C. Poole, *Handbook of Superconductivity* (Academic Press, 2000).
[83] M. Nuñez Regueiro, J. L. Tholence, E. V. Antipov, J. J. Capponi, and M. Marezio, Science **262**, 5130 (1993).
[84] R. M. Hazen, L. W. Finger, R. J. Angel, C. T. Prewitt, N. L. Ross, C. G. Hadidiacos, P. J. Heaney, D. R. Veblen, Z. Z. Sheng, A. E. Ali, and A. M. Hermann, Phys. Rev. Lett. **60**, 1657 (1988).
[85] M. A. Subramanian, J. C. Calabrese, C. C. Torardi, J. Gopalakrishnan, T. R. Askew, R. B. Flippin, K. J. Morrissey, U. Chowdhry, and A. W. Slight, Nature **332**, 420 (1988).
[86] C. E. Gough, M. S. Colclough, E. M. Forgan, R. G. Jordan, M. Keene, C. M. Muirhead, A. I. M. Rae, N. Thomas, J. S. Abell, and S. Sutton, Nature **326**, 855 (1987).
[87] J. F. Annett, N. Goldenfeld, and A. J. Leggett, *Physical Properties of High-Temperature Superconductors V* (World Scientific, 1996), chap. 6, p. 375.
[88] D. A. Wollman, D. J. Van Harlingen, W. C. Lee, D. M. Ginsberg, and A. J. Leggett, Phys. Rev. Lett. **71**, 2134 (1993).
[89] C. C. Tsuei, J. R. Kirtley, C. C. Chi, L. S. Yu-Jahnes, A. Gupta, T. Shaw, J. Z. Sun, and M. B. Ketchen, Phys. Rev. Lett. **73**, 593 (1994).
[90] C. C. Tsuei and J. R. Kirtley, Rev. Mod. Phys. **72**, 969 (2000).
[91] H. Hilgenkamp, Ariando, H. J. H. Smilde, D. H. A. Blank, G. Rijnders, H. Rogalla, J. R. Kirtley, and C. C. Tsuei, Nature **422**, 50 (2003).
[92] D. J. Van Harlingen, Rev. Mod. Phys. **67**, 515 (1995).

Chapter 3

Josephson Effect

The theory of the Josephson effect for insulating, normal metal [1, 2], antiferromagnetic, ferromagnetic, and inhomogeneous ferromagnetic barriers is outlined. SQUIDs [3] and cuprate junctions [4] are then considered.

3.1 The Josephson effect

The Josephson effect occurs when Cooper pairs pass through a 'weak-link'. It was theoretically predicted [5] and verified experimentally soon afterwards in single junctions [6], and loops with two junctions [7]. The initial prediction was for the case of an S/I/S (I = insulator) tunnel junction. Cooper pairs were shown to be able to tunnel through the barrier with a rate of the same order of magnitude as 'normal', single particle excitations. Initially it was thought that the probability of two electrons tunnelling at the same time would be much less than single particle tunnelling, and that the effect would therefore be too small to observe.

To understand why the Josephson effect is observable, it is noted from the previous chapter that macroscopic phase coherence is a crucial requirement for superconductivity, but also that there is a number-phase uncertainty (equation 2.12). For an isolated system $\Delta N = 0$ and hence θ is not determined: the phase is rigid, but the *absolute* value is arbitrary. When two coupled systems are considered the *relative* phase is important, (consider for example equation 2.1). Now that $\Delta\theta$ is restrained,[1] N is uncertain in the two superconducting banks. This uncertainty can be seen as the decaying 'tail' of the wavefunction ψ having some finite value in the other S electrode. The Josephson effect is therefore not the same as two single electrons tunnelling at the same time. The electrons are not independent: they both come from the same phase coherent reservoir, which has some finite probability of existing in the other electrode. The phase coherence plays the crucial rôle in allowing the measurement of the Josephson current. In fact the ubiquity of the Josephson effect is such that this weak coupling limit can be applied to any macroscopic wavefunction [8].

The 'weak-link' is defined such that when a phase difference of 2π (or integer multiples) is applied across the weak-link, it returns reversibly to its original state. This is in contrast to the application of a phase gradient in a bulk superconductor, (equation 2.1) which leads to a supercurrent, and does not return to its original state. From this definition, a 'weak-link' has a 2π-periodic free energy. The free energy is written as $F = -F_0 \cos\phi$ where $F_0 > 0$, such that F is minimal for $\phi = \theta_1 - \theta_2 = 0$ in zero magnetic field. The phase difference of the two superconducting banks is measured in the direction of the momentum change, and therefore opposite to the conventional current. Using $\hbar\partial\phi/\partial t = 2eV$, and identifying $\mathrm{d}F/\mathrm{d}t$ with the power IV, the Josephson relation

$$I = I_C \sin\phi \tag{3.1}$$

is obtained, where $I_C = 2eF_0/\hbar$. At zero voltage the 'd.c. Josephson effect' gives supercurrent flowing through the junction whose amplitude depends only on the phase difference across it, so long as $|I| < I_C$. An applied voltage causes the phase difference and hence the supercurrent to oscillate at a frequency of $2eV/h \sim 480$ GHz/mV: the so-called 'a.c. Josephson effect'. This high frequency oscillation is averaged to zero over a normal measurement time. Shapiro [9] showed that the application of microwaves to a junction can lock-in to this high frequency a.c. current, generating spikes in a voltage biased $I - V$ characteristic, (or steps if the junction is current

[1] The fact that $\Delta\theta$ is fixed is not completely trivial - see [1].

biased - as in the present work), at voltages determined only by the frequency of the microwave signal and fundamental ratio e/h. This can be used to generate voltage standards (section 6.2), and is known as the 'inverse a.c. Josephson effect'.

It is important to note that equation 3.1 is only a first order term, and departures from sinusoidal behaviour are often found [2].

3.1.1 S/I/S junctions

When $I > I_C$ in an S/I/S junction at $T = 0$ K, no current flows until a voltage $2\Delta/e$ is dropped across the junction, (assuming Δ in the two S electrodes is the same). Above this voltage Cooper pairs are split up, and a resistive quasi-particle branch is seen, (figure 3.1). Calculating F_0 from the BCS theory, the $I_C R_N$ product for an S/I/S junction is [10] :

$$I_C(T)R_N = \left(\frac{\pi\Delta(T)}{2e}\right)\tanh\left(\frac{\Delta(T)}{2k_BT}\right) \ . \tag{3.2}$$

For the RCSJ model discussed in section 3.1.5 it is important to note that S/I/S junctions can

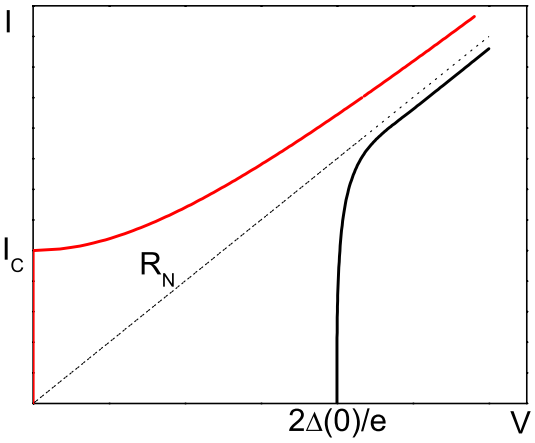

Figure 3.1: Positive quadrant of $I-V$ characteristic at $T = 0$ K for an S/I/S (black) and S/N/S (red) junction.

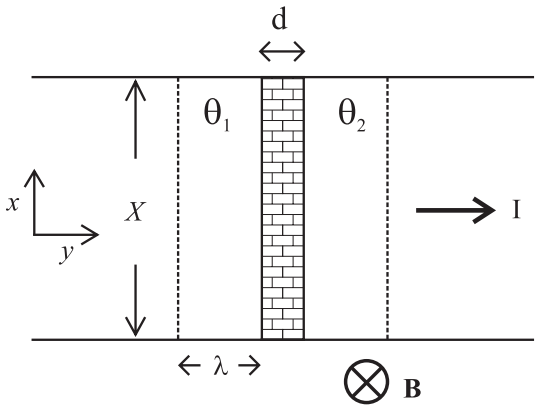

Figure 3.2: Josephson junction of width X with barrier thickness d. Current I flows as shown. A flux density **B** is applied out of plane.

have significant capacitance compared to metallic junctions, leading to significant hysteresis in the $I-V$ curves.

3.1.2 S/N/S junctions

The S/N/S case can be considered as two S/N bilayers. From the proximity effect discussed in section 2.3 it is clear that an S/N/S Josephson junction can be formed. For a long ($d_N \gg \xi_N$) S/N/S junction in the dirty limit:

$$I_C(T)R_N = \left(\frac{3\pi\Delta_s^2}{2ek_BT_c}\right)\frac{d_N/\xi_N}{\sinh(d_N/\xi_N)} \ . \tag{3.3}$$

Δ_s is the value of $\Delta(x)$ just next to the S/N interface [11]. Likharev [2] considered the rigid boundary condition $\Delta_s = \Delta_{bulk} = \Delta$ and obtained

$$I_C(T)R_N = \left(\frac{2|\Delta^2|}{\pi e k_B T_c}\right) \frac{d_N/\xi_N}{\sinh(d_N/\xi_N)} \tag{3.4}$$

in the long limit, but also calculated $I_C(T)R_N$ for a range of d_N/ξ_N ratios. Near T_C the T dependence of Δ_s means that $I_C \propto (T - T_C)$ for rigid boundary conditions, and $(T - T_C)^2$ for soft boundary conditions [12].

The normal state resistance is determined largely through $R_N = (\rho_N d_N + 2R_{S/N})/A$ where ρ_N is the N layer resistivity, $R_{S/N}$ is the specific contact resistance, and A the junction area, (although in equation 3.3 $R_N = \rho_N L$, [11]).

3.1.3 Response to magnetic field

When a flux B threads a Josephson junction, the gauge invariant phase is given by

$$\phi = \theta_1 - \theta_2 - \frac{2e}{\hbar}\int_1^2 \mathbf{A} \cdot d\mathbf{y} \; . \tag{3.5}$$

This causes the phase to vary across the junction width according to

$$\phi(x) = \phi(0) - 2\pi B x \tilde{d}/\Phi_0 \; . \tag{3.6}$$

$\tilde{d} = d + 2\lambda$, where d is the barrier thickness (figure 3.2). As long as the junction width is short compared to the Josephson penetration depth λ_J then the field generated by the current can be neglected, and the current flows uniformly across the junction. λ_J is given by

$$\lambda_J = (\hbar/2e\mu_0 J_C \tilde{d})^{\frac{1}{2}} \; . \tag{3.7}$$

$J_C = I_C/XZ$ is the junction critical current density, with Z the junction dimension normal to the page in figure 3.2. In this case the critical current as a function of applied field, $I_C(H)$, is analogous to the diffraction of light, and can be found by Fourier transforming the junction 'aperture'. For a 'single slit' junction with uniform current

$$I_C = XZ\, J_C \left|\frac{\sin(\pi B X \tilde{d}/\Phi_0)}{\pi B X \tilde{d}/\Phi_0}\right| \tag{3.8}$$

as shown in figure 3.3. $I_C(H)$ can be modelled for non-uniform current flow [3]. An important case is when the junction dimensions $\geq \lambda_J$. The flux is screened from the centre of the junction, and the self field of the current cannot be neglected. The $I_C(H)$ becomes triangular and can be asymmetric, depending on the geometry (figure 3.4) [3].

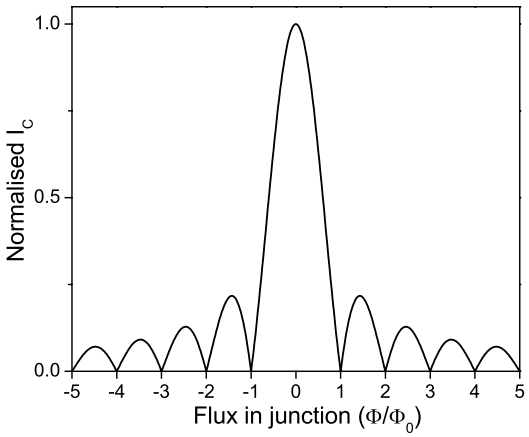

Figure 3.3: Josephson junction I_C vs flux in the barrier, showing the ideal 'Fraunhofer diffraction'.

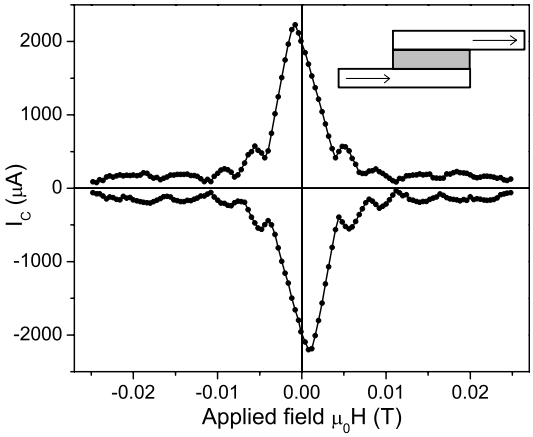

Figure 3.4: A Nb/Mo/Nb junction $I_C(H)$ in the long limit (see section 7.2). Inset: Geometry of the 'in-line' junction.

3.1.4 Finite S thickness

In the derivation of the 'Fraunhofer' modulation $I_C(H)$ in section 3.1.3 it was assumed that the electrode thickness was large compared to λ, and a contour could be taken where no screening current flowed. In the present work the Nb electrodes are of the order of 150 - 180 nm thick. Due to geometrical effects [13] λ in a thin film can be much larger than the bulk value. The condition $d_{\mathrm{Nb}} > \lambda$ is therefore not guaranteed. Following Weihnacht [14] if the current flowing is negligible, and the barrier thickness d is ignored, applying the London theory to figure 3.2:

$$H(y) = H_A \frac{\coth\left(\frac{y \pm d_S/2}{\lambda}\right)}{\coth\left(\frac{d_S}{2\lambda}\right)} \tag{3.9}$$

The + sign is for $y > 0$ and − for $y < 0$ as measured from the barrier. H_A is the external field. It has been assumed that the electrode thickness d_S and λ are the same on both sides of the junction. The distance between the minima of the 'Fraunhofer' is now given by

$$\mu_0 \Delta H = \frac{\Phi_0}{2\lambda X \tanh\frac{d_S}{2\lambda}} \ . \tag{3.10}$$

When the currents flowing are significant the Josephson penetration depth is modified to

$$\lambda_J^{-2} = \frac{4e}{\hbar}\mu_0 J_C \lambda \coth\left(\frac{d_S}{\lambda}\right) \ . \tag{3.11}$$

3.1.5 RCSJ model

The Resistively and Capacitively Shunted Junction model, (RCSJ) considers an idealised Josephson element, in parallel with some resistance for $I > I_C$, as well as a capacitance C, due to the

area of the weak link between the electrodes. The $I(V,\phi)$ relation is then

$$I = I_c \sin\phi + \frac{V}{R} + C\frac{\mathrm{d}V}{\mathrm{d}t} \ . \tag{3.12}$$

Using $\tau = t(2eI_C/C\hbar)^{1/2}$ equation 3.12 can be rewritten [13] as

$$\frac{\mathrm{d}^2\phi}{\mathrm{d}\tau^2} + \frac{1}{\beta_c^2}\frac{\mathrm{d}\phi}{\mathrm{d}\tau} + \sin\phi = \frac{I}{I_c} \ . \tag{3.13}$$

The parameter $\beta_c = R(2eI_CC/\hbar)^{1/2}$, and is known as the McCumber parameter [15]. This is a measure of the damping in the junction. For $\beta_c = 0$ equation (3.13) can be solved analytically for $I > I_C$ to give the average voltage $\bar{V}$

$$\bar{V} = R(I^2 - I_C^2)^{\frac{1}{2}} \tag{3.14}$$

as shown in figure 3.1. The 'RSJ' fit is usually reasonable for many S/N/S junctions (section 7.2), where C is negligible.

3.2 S/F/S junctions

The π state discussed in section 2.4.2 is realised in a Josephson junction when $F_0 < 0$ (section 3.1). The groundstate minimum is now at π, and $J_C < 0$. The original prediction of a π-junction made by Bulaevskiĭ *et al* [16] considered magnetic impurities in a tunnel barrier, which affected the individual electrons of a Cooper pair in turn as they crossed the barrier. Using equation 3.5 the π-junction in a loop of S then has a groundstate with a spontaneous current, and flux of $\Phi_0/2$ through the loop.

Metallic F barriers in the dirty limit were first considered by Buzdin and Kupriyanov [17]. Near T_C they used the GL equations to obtain

$$I_CR_N = \left(\frac{\pi\Delta^2 d_F^2}{8e\xi_F T_C}\right) \frac{|\sinh(d_F/\xi_F)\cos(d_F/\xi_F) + \cosh(d_F/\xi_F)\sin(d_F/\xi_F)|}{\sinh^2(d_F/\xi_F)\cos^2(d_F/\xi_F) + \cosh^2(d_F/\xi_F)\sin^2(d_F/\xi_F)} \tag{3.15}$$

as shown in figure 3.5. When the term inside the $||$ is negative the π contact is obtained.

In terms of the oscillating order parameter, the π-junction is formed with the ferromagnet thickness $d_F \sim \pi\xi_{F2}$ - half a period of the oscillation of the order parameter. Equation 2.17 can be approximated for $E_{Ex} \geq k_BT$ by [19]:

$$\xi_{F1,(2)} = \left[\frac{\hbar D}{\left[E_{Ex}^2 + (\pi k_BT)^2\right]^{\frac{1}{2}} + (-)k_BT}\right]^{\frac{1}{2}} \ . \tag{3.16}$$

ξ_{F1} increases with decreasing temperature, whereas ξ_{F2} decreases. Hence a crossover as a function of T from 0 to π coupling is possible, in the range of thicknesses as shown in figure 3.6. Crucially, when compared to the multilayer T_C measurements (section 2.4.2) measuring a single

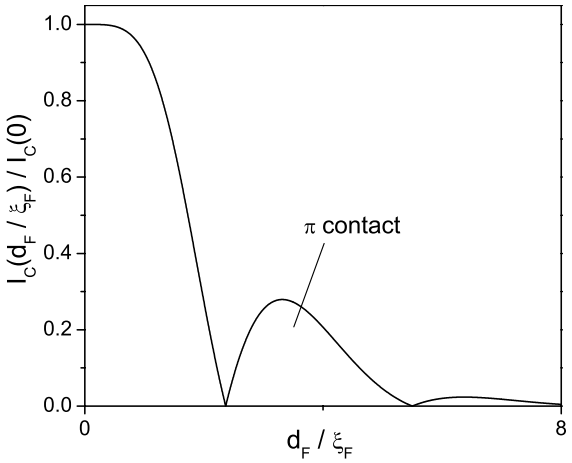

Figure 3.5: Re-entrant $I_C(d_F)$ for a S/F/S junction. Taken from Buzdin *et al* [17].

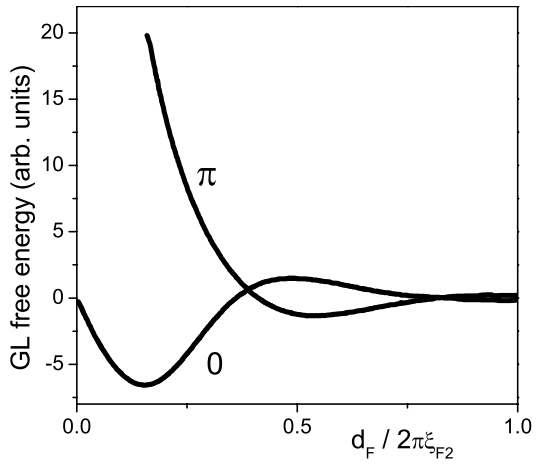

Figure 3.6: Free energies for 0 and π junctions. A crossover from 0 to π with T can be observed in the range $0.4 < d_F/2\pi\xi_{F2} < 0.8$. Taken from Ryazanov *et al* [18].

junction removes the issue of the changing F properties with thickness when many different S/F samples are grown.

This temperature crossover was observed in $Nb/Cu_xNi_{1-x}/Nb$ junctions by Ryazanov *et al* [18], as a cusp in the $I_C(T)$. In the case of the π phase shift for a single junction, the $I_C(H)$ is *not* shifted, (the π shift adds to the constant term ϕ_0 in equation 3.6). A shift is only observed in two junction loop with one '0'-junction and one π-junction, or more complex arrangements such as the frustrated five junction loop used by Ryazanov *et al* [20]. Kontos *et al* have measured the superconducting density of states in the F layer (Pd_{1-x} Ni_x) using an N/I/F/S structure [21], finding the change from the 0 to π phase. They have also measured the re-entrant $I_CR_N(d_F)$ in S/I/F/S structures [22], as predicted by equation 3.15 (figure 3.5). Sellier *et al* have also examined CuNi alloys [23, 24], and were able to quantitatively fit the I_CR_N product using the spin-flip scattering length as an adjustable parameter.

Junctions with Gd [25] and Ni [26] have also been fabricated, with the latter claiming double re-entrance in the $J_C(d_F)$, but with a relatively small number of data points. Shadow deposition has also been used to create sub-micron Co junctions [27, 28], with distorted $I_C(H)$ patterns: their importance will be discussed in section 8.4.

3.3 S/AF/S junctions

No measurements have ever been made of antiferromagnetic Josephson junctions other than one system which studied YBCO / magnetic oxide / YBCO junctions [29] with the barrier near the ferromagnetic-antiferromagnetic transition. In that case however there was not strong evidence of true Josephson coupling. In section 8.3 the results of S/AF/S junctions with the AF γ-$Fe_{50}Mn_{50}$ are presented. There is no present theory for such junctions. Following de Gennes theory for a dirty S/N/S junction (section 3.1.2) $J_C \propto \exp(-k_{AF}d_{AF})$. Using $k_{AF} = 2/\xi_{AF}$ this

leads to

$$J_C(d_{AF}) \propto \exp(-2d_{AF}/\xi_{AF}) \; . \tag{3.17}$$

Although it is not clear if this is a justified equation, it will be used as a generic model, assuming that any corrections will only be of the order of unity when a fuller theory of AF junctions is developed.

3.4 Non-homogeneous F devices

3.4.1 S/F/X/F/S

The initial work on S/F/S junctions assumed a homogeneous exchange field. More recent theory has been concerned with inhomogeneous barriers, in which the magnetism can be actively controlled. Bergeret *et al* [30] first considered the S/F/I/F/S case with $d_{S,F} < \xi_{S,F}$. They demonstrated a formal (logarithmic) divergence of I_C with an anti-parallel alignment of the two F layers as $H_{Ex} \rightarrow \Delta$. The I_C for anti-parallel alignment was always larger than the parallel case - the Exchange Field Supercurrent Enhancement (EFSE).

This created much interested in this system. Golubov *et al* [31] considered Bergeret's work in the dirty limit for both the S and F layers, for arbitrary thickness of the F layer and barrier transparency. It was found that for the parallel alignment of the F layers the $0-\pi$ transition should be observed, as well as EFSE for the anti-parallel case with thin F layers, again with $H_{Ex} \approx \Delta$. The qualitative reasoning for this effect is that the energy shift due to the exchange field is equal to the local gap induced in the F. In this case the peak in the local DoS is shifted to zero energy, (i.e. the Fermi level) giving the divergence of I_C at $T = 0$.[2] This is analogous to the Riedel singularity of the a.c. Josephson supercurrent when $eV = 2\Delta$ [32]. The $0-\pi$ crossover however is not the same as that in section 3.2 due to the oscillating order parameter, ($d_F < \xi_F$). A $\pi/2$ jump in phase occurs at each S/F interface. By swapping between the F and AF alignments, Golubov *et al* pointed out that it was possible to switch from the 0 to π state.

More generally, the case of S_F/X/S_F junctions were considered by Chtchelkatchev *et al* [33], (S_F is either a superconducting ferromagnet, or a S/F bilayer). They considered the case where the exchange field $|H_{Ex}| \leq \Delta$. An enhancement of the I_C was found for the AF alignment of the two F layers as before. For X=I (insulator) the EFSE effect is seen if the transparency is small, but as the transparency increases, the EFSE effect decreases. For the case that X is a dirty normal metal there is no EFSE, and only a weak (10%) enhancement of the I_C for the S_FINIS_F case. In the ballistic limit for the F/N/F structure Zaitsev [34] has predicted an enhanced I_C in the AF state, with the ratio $(I_C^F - I_C^{AF})/I_C^F$ of the order of unity, much larger than the corresponding MR, for the case that $H_{Ex} > \Delta$. It is not clear in this case how the mechanism differs from the other limits discussed above.

[2] A BCS DoS was used in [31].

3.4.2 Other inhomogeneous structures

Three other systems are also relevant to the present work. Clinton and Johnson [35] used the destruction of superconductivity by the inhomogeneous stray field from the end of a 'line charge' of magnetic moment in the planar geometry to create a Josephson junction. Although the Josephson current does not pass through the F layer, this idea is important for the later analysis (section 8.4). There is also the possibility of triplet components in the Josephson junctions, as referred to in section 2.4.3.1. This has been considered by Bergeret *et al* [36]. Depending on the choice of parameters, (in particular the wavevector of the magnetic modulation), the π state could be made not to occur, and the $I_C(T)$ behaviour change from S/N/S-like, to strongly non-monotonic. Finally Gor'kov and Kresin [37] considered a multilayer GMR system, and predicted giant magneto-oscillations of the Josephson current as the F layers are canted from AF alignment. In this case the microscopic mechanism was not outlined, and the half metal limit is considered, without taking account of possible triplet correlations [38, 39].

3.5 SQUIDs

3.5.1 Single junction in a loop

Consider the superconducting loop containing a single junction (known as an r.f. SQUID), as shown in figure 3.7 (a). The junction has a phase difference ϕ across it, and flux Φ threading it. Following equation 3.5, with the contour such that $\mathbf{J} = 0$, then $2\pi n = (2e/\hbar)\Phi + \phi$. Ignoring multiples of 2π, which just give periodic behaviour:

$$\phi = -2\pi \frac{\Phi}{\Phi_0} \, . \tag{3.18}$$

The flux is given by

$$\Phi = \Phi_{ex} + IL \, , \tag{3.19}$$

which is the sum of the applied flux Φ_{ex}, and that due to the current in the loop of inductance L.

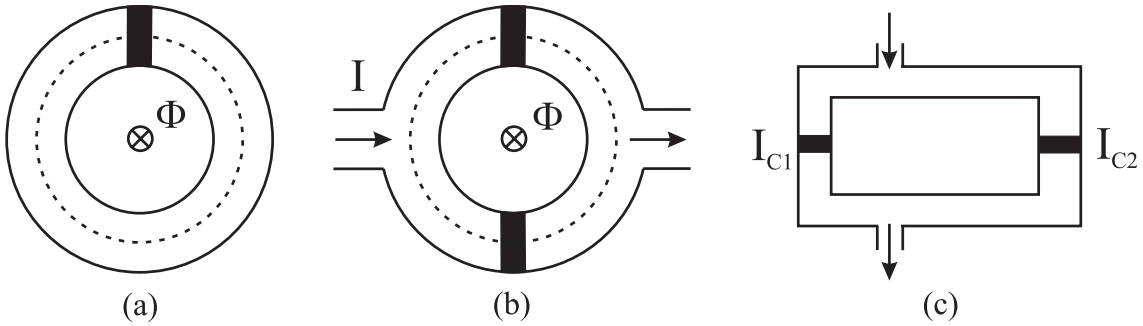

Figure 3.7: Superconducting loop linked by flux Φ with (a) one junction and (b) two junctions in the loop. (c) Asymmetric biasing of a d.c. SQUID with different junction critical currents.

3.5.2 The d.c. SQUID

In the case of the d.c. SQUID with two junctions, (figure 3.7 (b)) the flux Φ linking the junction produces phase differences ϕ_1 and ϕ_2 across each junction. In the most general case, (following Barone and Paterno [3]) the case of an asymmetric loop is considered, with the two junctions having different I_Cs: I_{C1} and I_{C2}, (figure 3.7 (c)). The unequally divided current around the SQUID links net flux through the loop. The current in the device is given by

$$I = I_{C1} \sin \phi_1 + I_{C2} \sin \phi_2 \ . \tag{3.20}$$

By analogy with equation 3.18,

$$\phi_2 - \phi_1 = 2\pi \frac{\Phi_{ex}}{\Phi_0} + \beta_1 \sin \phi_1 - \beta_2 \sin \phi_2 \ . \tag{3.21}$$

Where $\beta_i = 2\pi L_i I_{Ci}/\Phi_0$, and the total loop inductance $L = L_1 + L_2$. The critical current of the junction is then found by maximising I in equation 3.20, subject to the constraint of equation 3.21. It is straightforward to show that this can be done by solving for ϕ_2 in the relation

$$\phi_2 = \cos^{-1}\left[\frac{-I_{C1}\cos\phi_1}{I_{C2}(1+\beta_1\cos\phi_1)+\beta_2 I_{C1}\cos\phi_1}\right] \ . \tag{3.22}$$

With ϕ_1 and ϕ_2 known, I_C and Φ_{ex} can then be found using equations 3.20 and 3.21. Figure 3.8 shows the ϕ_2 vs ϕ_1 plot, and the resulting I_C vs Φ_{ex}/Φ_0. In this case the ratios I_{C2}/I_{C1} and L_2/L_1 were chosen to be the same. The $I_C(\Phi_{ex}/\Phi_0)$ plot is characterised by a non-zero $I_C^{\min}$, and an anti-symmetric response ($I_C(-\Phi_{ex}) = -I_C(\Phi_{ex})$).

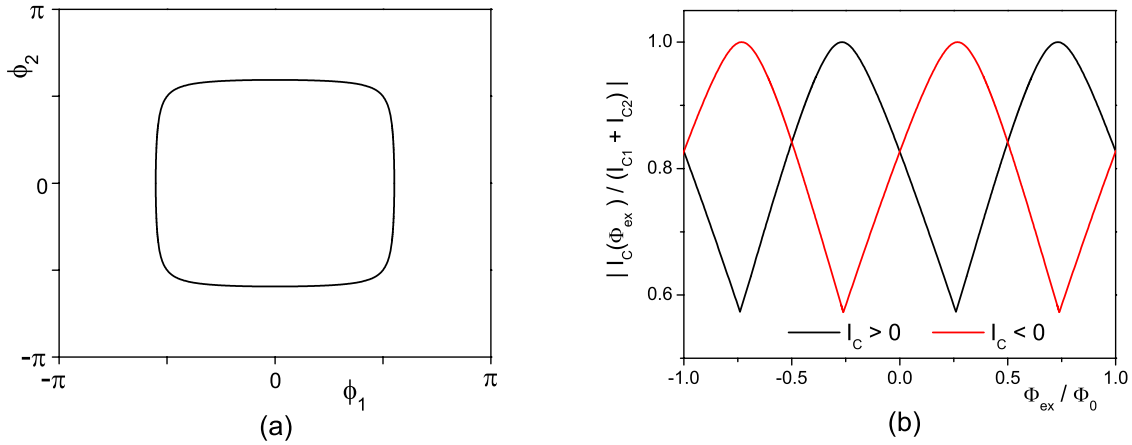

Figure 3.8: (a) Numerical model of ϕ_2 vs ϕ_1 and (b) corresponding $|I_C(\Phi_{ex}/\Phi_0)|$ normalised to $I_{C1}+I_{C2}$, showing the anti-symmetry between positive and negative I_Cs, and asymmetric peak shape. In this case $I_{C2}/I_{C1} = L_2/L_1 = 0.63$.

For the simpler case of negligible inductance, $L \to 0$, $\Phi = \Phi_{ex}$, and analytical solutions for the above relations can be found. Following the same method as section 3.1.3, the analogy with

diffraction leads us to a 'Young's double slit' $I_C(H)$:

$$I_C(\Phi) = [(I_{C1} - I_{C2})^2 + 4I_{C1}I_{C2}\cos^2(\pi\Phi/\Phi_0)]^{\frac{1}{2}} \ . \tag{3.23}$$

When the junction I_Cs are equal, ($I_{C1} = I_{C2} = I_0$), this reduces to

$$I_C(\Phi) = 2I_0 \left|\cos\left(\frac{\pi\Phi}{\Phi_0}\right)\right| \ . \tag{3.24}$$

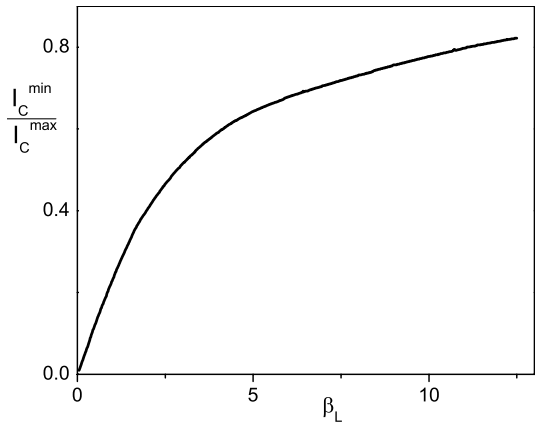

Figure 3.9: Dependence of $I_C^{\min}/I_C^{\max}$ on the screening parameter β_L (black) for $I_{C1} = I_{C2}$, taken from Peterson *et al* [40].

A screening parameter β_L, is defined analogously to the β_is above:

$$\beta_L = \frac{2\pi I_0 L}{\Phi_0} = \frac{\pi I_C^{\max} L}{\Phi_0} \ . \tag{3.25}$$

As can be seen from figure 3.9, the minimum I_C obtained ($I_C^{\min}$) by modulating the SQUID with a field is strongly dependent on β_L. This is clear from the above general numerical analysis, as well as the analytical cases described above. The value of β_L is also an important parameter in the noise performance of a SQUID (see [41] for a review). In many applications it is the *voltage* modulation rather than ΔI_C that is measured by biasing the SQUID at constant $I > I_C$, (section 6.3).

Finally it is important to consider the effect of the single junctions in the SQUID loop. Using the diffraction analogy, if the size of the loop becomes comparable to the individual junction dimensions, then the amplitude of the SQUID $I_C(\Phi)$ oscillation is modulated by the Fraunhofer pattern of the single junctions, (see section 6.3.2).

3.6 Josephson junctions in the cuprates

3.6.1 Intrinsic junctions

The short coherence lengths and layered structure of the cuprates (section 2.6) gives rise to intrinsic junctions in the c direction in the more anisotropic materials. Intrinsic junctions were first found in $Bi_2Sr_2CaCu_2O_{8+\delta}$ (Bi-2212) by Kleiner *et al* [42]. These have aroused much interest since they give access to important parameters describing the c-axis transport used in the theories of the HTS, without the problems of surface effects introduced in for example tunnelling spectroscopy [4].

Various methods for making c-axis measurements are used. Mesas can be etched in single crystals or thin films to controllably create tens to thousands of junctions. This process can be done in parallel, (using two cleaved Bi-2212 lamellae which are annealed together) to create many thousands of junctions in series [43, 44]. Also step-edge junctions and vicinal films have been used (see section 6.1.3).

By careful ramping of the current it is possible to trace out the different branches of the $I-V$. Each branch corresponds to one (or a small number) of atomic plane Josephson junctions. The hysteresis and multiple branches of the $I-V$ curves seen in intrinsic junctions imply an S/I/S character to the individual junctions (figure 6.2). A sub-gap current is always observed, unlike the LTS case. This is consistent with the d-wave scenario in which quasi-particles are always present for $T > 0$ K. In the HTS however, the gap is less well defined than the analogous artificial LTS stack. Sub-gap resonant structures have also been observed, (first in Bi-2212 single crystal junctions [45] and later in other systems, including Tl-2212 - section 6.1.5.1). The n^{th} resistive branch is split into two hysteretic regions, each with n branches, (i.e. a total of $2n+1$ branches). This has been ascribed to resonances between the Josephson oscillations and c-axis optical phonons [46]. The $2n+1$ multiplicity is a consequence of each of the n junctions switching between the three possible resistance branches which can be occupied [47].

Early measurements created much interest in the so-called 'back-bending' (negative differential resistance) of the $I-V$s at high bias. This was initially attributed to a variety of non-equilibrium effects, but it later became clear that heating was the cause of the distortions [48, 49]. Heating is significant in single crystals and even the micron sized mesas made with optical lithography. The sub-micron method using a focused ion beam introduced by Kim *et al* for whiskers and thin films [50, 51], and developed in the present work ([52, 53] and chapters 5 and 6), seem to suffer less from heating effects. This is presumably due to the reduced I_C, meaning that the power generated is easier to remove.

3.6.2 Other HTS junctions

Unlike the LTS technologies, epitaxial growth is required for HTS thin film to avoid grain boundaries which can form weak links. This strongly restricts circuit design. Using bicrystal substrates grain boundary growth can be controlled: the common [001] tilt grain boundaries for example show S/N/S-like Josephson coupling for tilt angles between $15° - 45°$ [54]. Electron

beam writing [55] and proton damage [56] have also been used to fabricate planar junctions, but these are time consuming and/or expensive. Ramp edge junctions (see for example [57]) are perhaps the best way to integrate HTS with standard multilevel processing, but still not ideal.

Grain boundary junctions enable the investigation of the d-wave symmetry in the $a-b$ plane. In this way π-SQUIDs can be made, as shown in figure 3.10, by exploiting the change of sign of the order parameter between neighbouring 'lobes' in k-space. Finally c-axis HTS/LTS junctions

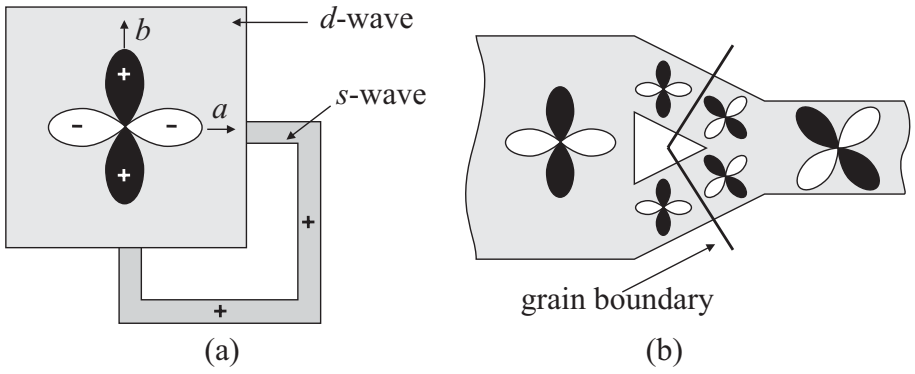

Figure 3.10: Two methods of generates π-SQUIDs: using (a) a d-wave / s-wave combination [58] or (b) an all d-wave (grain boundary) case [59].

(e.g. YBCO/Pb [60]) and [001] *twist* junctions [61, 62] have been studied. Both of which have argued for an order parameter in the HTS which is a combination of d and s-wave [63, 64, 65]. This developing area will not be discussed in detail.

References

[1] J. R. Waldram, Rep. Prog. Phys. **39**, 751 (1976).
[2] K. K. Likharev, Rev. Mod. Phys. **51**, 101 (1979).
[3] A. Barone and G. Paterno, *Physics and Applications of the Josephson Effect* (Wiley, New York, 1982).
[4] A. A. Yurgens, Supercond. Sci. Technol. **13**, R85 (2000), (and references therein).
[5] B. D. Josephson, Phys. Lett. **1**, 251 (1962).
[6] P. W. Anderson and J. M. Rowell, Phys. Rev. Lett. **10**, 230 (1963).
[7] R. C. Jaklevic, J. Lambe, A. H. Silver, and J. E. Mercereau, Phys. Rev. Lett. **12**, 159 (1964).
[8] R. P. Feynman, R. B. Leighton, and M. Sands, *The Feynman Lectures on Physics: Volume III* (Addison-Wesley Publishing, 1966).
[9] S. Shapiro, Phys. Rev. Lett. **11**, 80 (1963).
[10] V. Ambegaokar and A. Baratoff, Phys. Rev. Lett. **10**, 486 (1963).
[11] P. G. de Gennes, Phys. Lett. **5**, 22 (1963).
[12] K. A. Delin and A. W. Kleinsasser, Supercond. Sci. Technol. **9**, 227 (1996).
[13] M. Tinkham, *Introduction to Superconductivity, (2nd Edition)* (McGraw-Hill, 1996).
[14] M. Weihnacht, Phys. Status Solidi **32**, K169 (1969).
[15] D. E. McCumber, J. Appl. Phys. **39**, 3113 (1968).
[16] L. N. Bulaevkiĭ, V. V. Kuziĭ, A. A. Sobyanin, and P. N. Lebedev, Solid State Comm. **25**, 1053 (1978).
[17] A. I. Buzdin and M. Y. Kupriyanov, Pis'ma Zh. Éksp. Teor. Fiz. **53**, 308 (1991), [JETP Lett. **53** 321 (1991)].
[18] V. V. Ryazanov, V. A. Oboznov, A. Y. Rusanov, A. V. Veretennikov, A. A. Golubov, and J. Aarts, Phys. Rev. Lett. **86**, 2427 (2001).
[19] V. V. Ryazanov, A. V. Veretennikov, V. A. Oboznov, A. Y. Rusanov, A. A. Golubov, and J. Aarts, Usp. Fiz. Nauk **171**, 81 (2001).
[20] V. V. Ryazanov, V. A. Oboznov, A. V. Veretennikov, and A. Y. Rusanov, Phys. Rev. B **65**, 020501(R) (2001).
[21] T. Kontos, M. Aprili, J. Lesueur, and X. Grison, Phys. Rev. Lett. **86**, 304 (2001).
[22] T. Kontos, M. Aprili, J. Lesueur, F. Genêt, B. Stephanidis, and R. Boursier, Phys. Rev. Lett. **89**, 137007 (2002).
[23] H. Sellier, Ph.D. Thesis, Université Joseph-Fourier, Grenoble (2002).
[24] H. Sellier, C. Baraduc, F. Lefloch, and R. Calemczuk, Phys. Rev. B **68**, 054531 (2003).
[25] O. Bourgeois, P. Gandit, J. Lesueur, A. Sulpice, X. Grison, and J. Chaussy, Eur. Phys. J. B **21**, 75 (2001).
[26] Y. Blum, A. Tsukernik, M. Karpovski, and A. Palevski, Phys. Rev. Lett. **89**, 187004 (2002).
[27] C. Sürgers, T. Hoss, C. Schönenburger, and C. Strunk, J. Magn. Magn. Mater. **240**, 598 (2002).
[28] T. Hoss, C. Strunk, C. Sürgers, and C. Schönenburger, Physica E **14**, 341 (2002).

[29] M. Kasai, Y. Kanke, T. Ohno, and Y. Kozono, J. Appl. Phys. **72**, 5344 (1992).
[30] F. S. Bergeret, A. F. Volkov, and K. B. Efetov, Phys. Rev. Lett. **86**, 3140 (2001).
[31] A. A. Golubov, M. Y. Kupriyanov, and Y. V. Fominov, Pis'ma Zh. Éksp. Teor. Fiz. **75**, 223 (2002), [JETP Lett. **75** 190 (2002)].
[32] E. Riedel, Z. Naturforsch. A **19**, 1634 (1964).
[33] N. M. Chtchelkatchev, W. Belzig, and C. Bruder, Pis'ma Zh. Éksp. Teor. Fiz. **75**, 772 (2002), [JETP Lett. **75** 646 (2002)].
[34] A. V. Zaitsev, Physica B **329-333**, 1498 (2003).
[35] T. W. Clinton and M. Johnson, J. Appl. Phys. **85**, 1637 (1999).
[36] F. S. Bergeret, A. F. Volkov, and K. B. Efetov, Phys. Rev. B **64**, 134506 (2001).
[37] L. P. Gor'kov and V. Kresin, Appl. Phys. Lett. **78**, 3657 (2001).
[38] V. N. Krivoruchko, (personal communication).
[39] M. Eschrig, J. Kopu, J. C. Cuevas, and G. Schön, Phys. Rev. Lett. **90**, 137003 (2003).
[40] R. L. Peterson and C. A. Hamilton, J. Appl. Phys. **50**, 8135 (1979).
[41] D. Koelle, R. Kleiner, F. Ludwig, E. Dantsker, and J. Clarke, Rev. Mod. Phys. **71**, 631 (1999).
[42] R. Kleiner, F. Steinmeyer, G. Kunkel, and P. Müller, Phys. Rev. Lett. **68**, 2394 (1992).
[43] H. B. Wang, P. H. Wu, and T. Yamashita, Appl. Phys. Lett. **78**, 4010 (2001).
[44] H. B. Wang, P. H. Wu, T. Yamashita, and P. Müller, Proc. ISEC 2003 **1**, ITh2 (2003).
[45] K. Schlenga, G. Hechtfischer, R. Kleiner, W. Walkenhorst, P. Müller, H. L. Johnson, M. Veith, W. Brodkorb, and E. Steinbeiß, Phys. Rev. Lett. **76**, 4943 (1996).
[46] C. Helm, C. Preis, C. Walter, and J. Keller, Phys. Rev. B **62**, 6002 (2000).
[47] K. Schlenga, R. Kleiner, G. Hechtfischer, M. Mößle, S. Schmitt, P. Müller, C. Helm, C. Preis, F. Forsthofer, J. Keller, H. L. Johnson, M. Veith, and E. Steinbeiß, Phys. Rev. B **57**, 14518 (1998).
[48] J. C. Fenton, P. J. Thomas, G. Yang, and C. E. Gough, Appl. Phys. Lett. **80**, 2535 (2002).
[49] J. C. Fenton, G. Yang, and C. E. Gough, Physica C **388**, 341 (2003).
[50] S.-J. Kim, Y. I. Latyshev, and T. Yamashita, **74**, 1156 (1999).
[51] S.-J. Kim, Y. I. Latyshev, T. Yamashita, and S. Kishida, Physica C **362**, 150 (2001).
[52] C. Bell, R. H. Hadfield, G. Burnell, D.-J. Kang, M. J. Kappers, and M. G. Blamire, Nanotechnology **14**, 630 (2003).
[53] P. A. Warburton, A. R. Kuzhakhmetov, C. Bell, G. Burnell, M. G. Blamire, H. Wu, C. R. M. Grovenor, and H. Schneidewind, IEEE Trans. Appl. Supercond. **13**, 821 (2003).
[54] H. Hilgenkamp and J. Mannhart, Rev. Mod. Phys. **74**, 485 (2002).
[55] A. J. Pauza, D. F. Moore, A. M. Campbell, A. N. Broers, and K. Char, IEEE Trans. Appl. Supercond. **5**, 3410 (1995).
[56] D.-J. Kang, N. H. Peng, R. Webb, C. Jeynes, J. H. Yun, S. H. Moon, B. Oh, G. Burnell, E. J. Tarte, D. F. Moore, and M. G. Blamire, Appl. Phys. Lett. **81**, 3600 (2002).
[57] W. Wang, M. Yamazaki, K. J. Lee, and I. Iguchi, Phys. Rev. B **60**, 4272 (1999).
[58] D. J. Van Harlingen, Rev. Mod. Phys. **67**, 515 (1995).
[59] B. Chesca, R. R. Schulz, G. Goetz, C. W. Schneider, H. Hilgenkamp, and J. Mannhart, Phys. Rev. Lett. **88**, 177003 (2002).
[60] R. Kleiner, A. S. Katz, A. G. Sun, R. Summer, D. A. Gajewski, S. H. Han, S. I. Woods, E. Dantsker, B. Chen, K. Char, M. B. Maple, R. C. Dynes, and J. Clarke, Phys. Rev. B **76**, 2161 (1996).
[61] Q. Li, Y. N. Tsay, M. Suenaga, R. A. Klemm, G. D. Ghu, and N. Koshisuka, Phys. Rev. Lett. **83**, 4160 (1999).
[62] Y. Takano, T. Hatano, A. Fukuyo, A. Ishii, S. Arisawa, M. Tachiki, and K. Togano, Supercond. Sci. Techol. **14**, 765 (2001).

[63] C. C. Tsuei and J. R. Kirtley, Rev. Mod. Phys. **72**, 969 (2000).
[64] R. A. Klemm, Physica B **329**, 1325 (2003).
[65] J. F. Annett and J. P. Wallington, Physica C **341**, 1621 (2000).

Chapter 4

Film deposition, processing & measurement

The film deposition, lithography and milling used to form micron scale tracks is discussed, as well as the method of processing in the focused ion beam used to create a planar device. This is followed by details of the measurement set-up.

4.1 Film deposition

4.1.1 Substrate preparation

All films were deposited on (100) silicon substrates with a 250 nm oxidised surface layer, unless otherwise stated. A four inch wafer was diced with diamond edged circular saw into 10×5 mm^2 chips. The wax used to glue down the wafer during cutting was removed using an ultrasound bath of chloroform, followed by further soaking and ultrasound in acetone. Prior to loading into the sputter deposition system the chips were cleaned using an airgun with acetone followed by isopropanol.

4.1.2 Sputter deposition

Sputtering uses an argon plasma to bombard a target material to produce molecular or atomic fragments. These fragments are then collected on the substrate and the thin film is built up. The sputtered atoms undergo multiple collisions with the plasma gas before reaching the substrate. In this way the pressure of a sputtering gas allows control over the kinetic energy of the sputtered atoms reaching the substrate. This in turn controls the mobility and the resulting stresses in the film.

The 'UFO' Ultra High Vacuum, (UHV), sputter deposition system described below uses d.c. planar magnetron targets. The strong permanent magnets keep the plasma near to the target. This makes the sputtering process more efficient, at the expense of preferential removal of material around a 'race-track' section of the target, (figure 4.1).

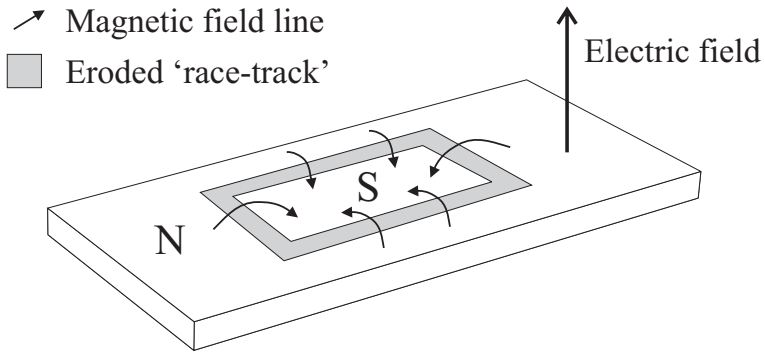

Figure 4.1: A planar d.c. magnetron, (adapted from Ohring [1]).

4.1.2.1 Growth modes

Sputtered films grown at relatively low temperatures and pressures in general have a polycrystalline microstructure and grow in columnar grains. The grain size has a strong influence on for example the coercive field of ferromagnetic films, and can also affect the T_C of superconducting films (section 8.3.2). A more in depth discussion into the factors affecting thin film growth can be found in [1] and [2]. Detailed microstructure characterisation of films grown in the 'UFO' sputtering system can be found in [3].

4.1.3 The 'UFO'

A schematic of the 'UFO' system is shown in figure 4.2. Five targets out of a choice of: Nb, Co, Cu, $Fe_{50}Mn_{50}$, $Fe_{20}Ni_{80}$ (permalloy - Py) or $Cu_{40}Ni_{60}$ could be loaded into the main chamber at a given time. The load-lock kept the main chamber at high vacuum, ensuring no contamination of the targets between depositions, and also allowed many different films to be grown in a single day. After cooling for at least three hours with liquid nitrogen, the base pressure was typically better than 3×10^{-7} Pa with oxygen partial pressure $\leq 3 \times 10^{-9}$ Pa.

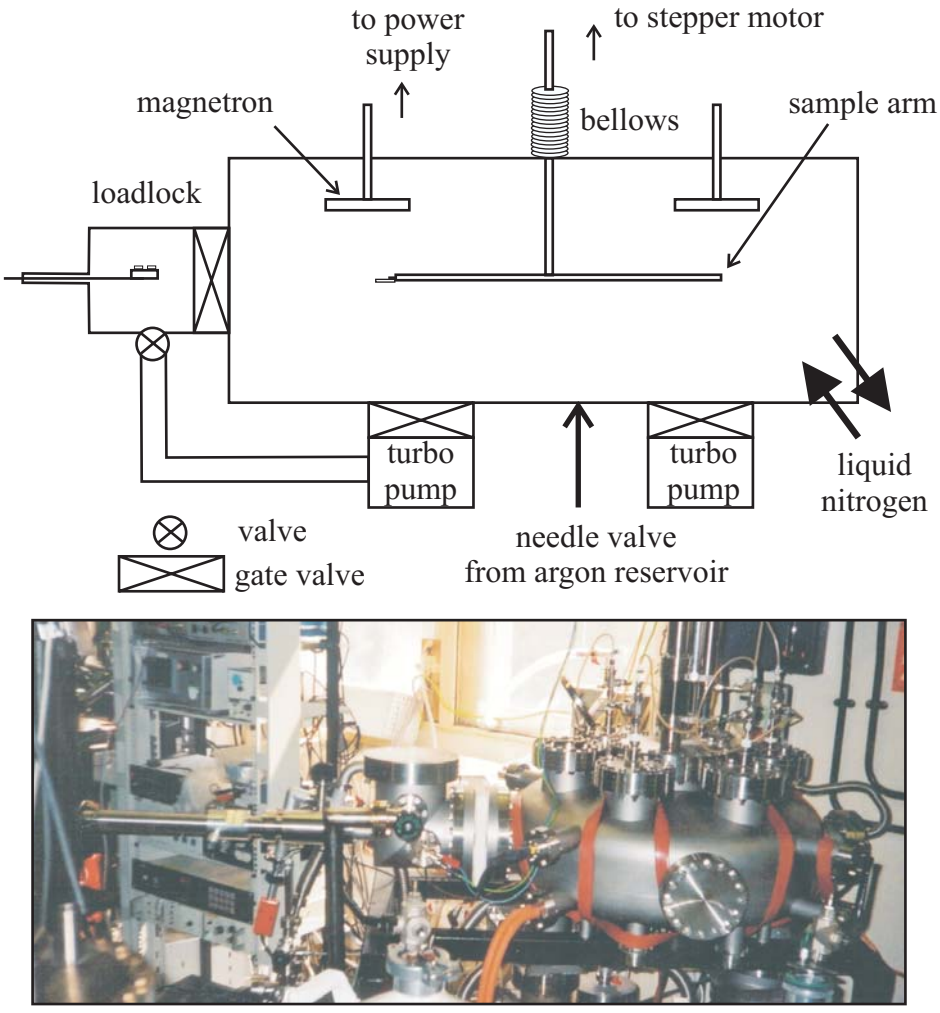

Figure 4.2: Schematic outline and photograph of the load-lock 'UFO' sputtering system.

For the sputtering, Ar gas with purity greater than 99.9999% was used. All the films grown in this system used a sputtering pressure of 0.5 Pa, which was stable to within $\pm$ 2 $\times$ 10^{-3} Pa (0.4 %) during film growth. The films grown from section 7.4.1 onwards were all grown using the 'UFO'. Earlier films were grown in similar UHV systems with sputtering pressures in the range $0.5 - 2$ Pa (depending on the material to be deposited).

The sample holder (figure 4.3) allowed an in-plane magnetic field of $\mu_0 H \sim 40$ mT to be applied to up to four 10×5 mm^2 chips during the film deposition. This induces an easy axis

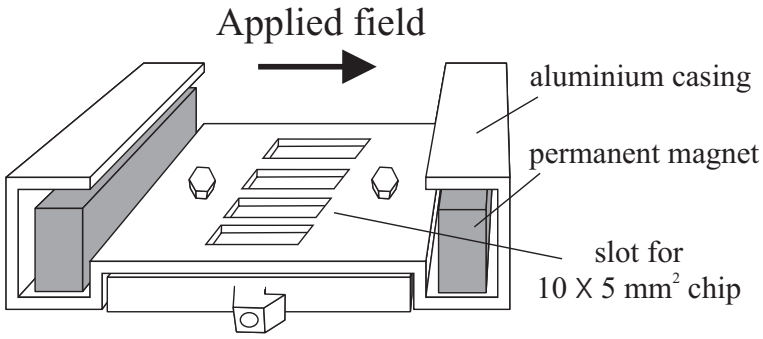

Figure 4.3: Sample holder for *in-situ* applied field used in the sputter deposition system.

(section 1.1.4) in the field direction, as can be seen in the $M(H)$ loops of a single Co layer (figure 4.4). The applied field was also used to saturate deposited ferromagnetic layers before an exchange biasing FeMn layer is grown on top, to fabricate spin valves (sections 1.2.3 and 8.4.1).

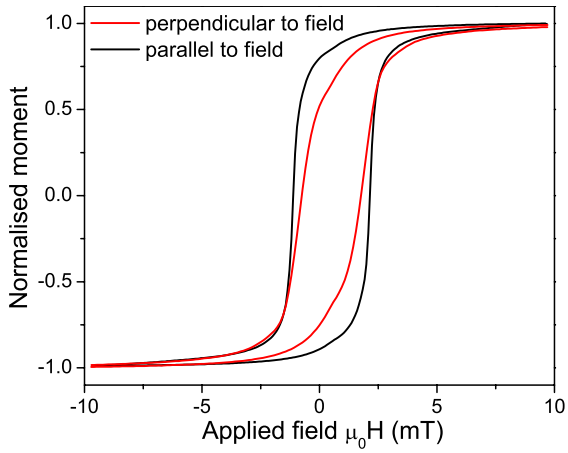

Figure 4.4: $M(H)$ loops of a 140 nm thick Co film with applied field parallel and perpendicular to the direction of the field during the deposition.

4.1.3.1 Deposition rates

Deposition rates were found using a profilometer (for the first half of the work), and an atomic force microscope (AFM) in tapping mode to measure a step height across a lift-off edge, (section 4.2.1), of height ≥ 50 nm. The deposition rate of a material on the substrate is dependent on the rate of rotation of the sample holder, the total number of rotations, the gas pressure, the substrate-target distance and linearly on the power through the magnetron. The stepper motor in the 'UFO' was used to rotate the sample holder past the targets with speeds in the range $0.05 - 1$ rpm. The angle control was better than 5° in over 100 rotations. The substrate-target distance was fixed at 90 mm. Table 4.1 shows a summary of the deposition rates for the various materials deposited in the 'UFO' system.

Target	Rate (nm / W / pass at 1 rpm)
Nb	0.0089
Cu	0.0304
Co	0.0234
$Cu_{40}Ni_{60}$	0.0167
Py	0.0187
$Fe_{50}Mn_{50}$	0.0183

Table 4.1: Deposition rates for various targets used in the 'UFO' system.

4.2 Track formation

4.2.1 Photolithography

Photolithography can be used both before and after the film deposition to produce micron scale tracks. The basic process is shown in figure 4.5. In both cases a photosensitive polymer resist is spun onto the surface of the chip. The resist is then exposed to a source of ultra-violet (UV) radiation behind a mask of the required pattern. 'Positive' resists were used in this work: the polymer chains in the regions of the resist exposed to the UV undergo a photochemical reaction and become soluble in a developer solution. The developer is used to dissolve these regions, leaving the required pattern. A pre-grown film is then patterned using ion milling, or a film deposited and 'lifted-off' (section 4.2.1.2).

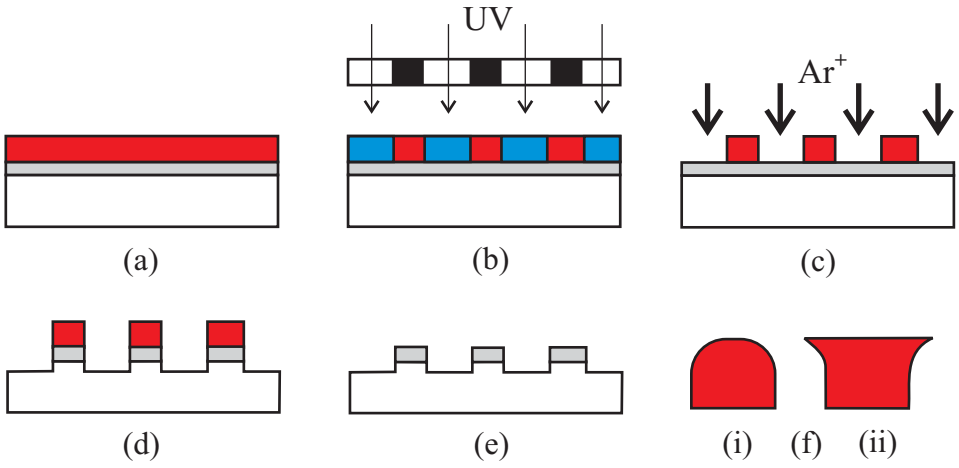

Figure 4.5: Schematic of track formation: (a) photoresist (red) spun on film (grey), (b) exposure with UV, (c) after developing, (d) after ion milling, (e) final tracks after removing photoresist, (f) exaggerated resist profile for (i) overexposed and (ii) chlorobenzene treated samples.

Practically this was done by exposing the chip in a Karl Suess mask aligner. The lithography was done in the following stages:

- After cleaning with an acetone spray, the chip was transferred to a resist spinner, and 3-4 drops of Hoechst AZ1529 resist pipetted onto it.

- Spun on a standard programme of 6000 rpm for 30 seconds giving a layer of resist of thickness ~ 2.4 μm at the centre of the chip, with a thicker 'edge-bead' around the perimeter.
- Exposure of the edge-bead (to allow close proximity to the mask for fine exposure), using a rectangular mask of dimensions slightly smaller than the chip.
- Develop in a 4:1 developer : water solution for not more than 30 seconds.
- Fine exposure in 'soft contact' mode: expose for between 9 and 10 seconds.
- Develop in a 3:2 developer : water solution again for not more than 30 seconds.

The 'Cam 39' chrome-on-glass mask designed by G. Burnell is used for the main patterning. The 'Cam 39' mask gives a track width of 4 μm at its thinnest section, (figure 4.6).

4.2.1.1 Lift-off

For so-called 'lift-off', the bare substrate is patterned before deposition, using a negative version of the ion milling mask. After the film is deposited, the metal sputtered onto the resist is removed when the resist beneath it is dissolved in acetone, leaving the required track pattern behind. The rounded resist profile, (due to scattering of the UV radiation, which is greatest near the surface of the photoresist - figure 4.5 (f)(i)), can be a problem. The film grows up the sides of these rounded resist walls, forming a continuous layer that peels off when the resist is dissolved. Large metal edges sticking up above the tracks can also be left - which is problematic for the Focused Ion Beam processing (section 5.1). Overdeveloping the photoresist will also tend to smooth out the edges of the tracks leading to the same effect. Treatment of the resist with chlorobenzene, (after UV exposure but before developing), causes an overhang in the edge profile, (figure 4.5 (f)(ii)). This prevents growth of the film over the sides. Given these added complexities, 'lift-off' was not used for the majority of this work.

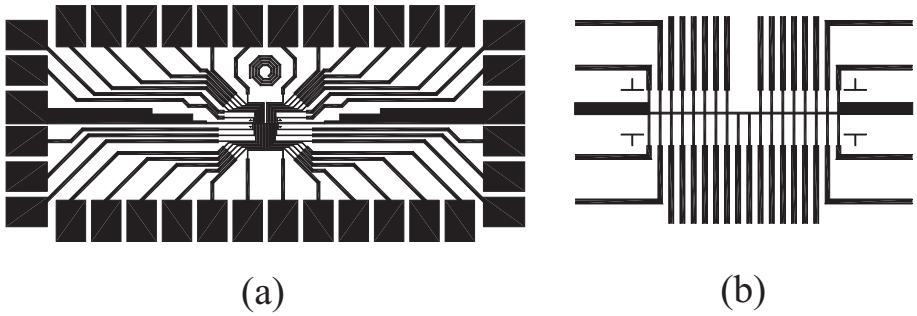

Figure 4.6: (a)'Cam 39' mask design for a 10×5 mm^2 chip used in this work, showing contact pads for wirebonding to. (b) Central detail: thinnest track widths are 4 μm.

4.2.1.2 Ion milling

Argon ions from a plasma are accelerated at the sample which mills the metallisation away. The patterned resist acts as a thick layer of protection against the bombarding ions, (and will also

mill more slowly due to the lighter mass of the carbon atoms in the polymer). Regions not covered in resist are therefore milled away, and when the resist is dissolved, the desired pattern remains in the film. For the early bilayer films (section 7.1) a large diffusion-pumped milling system was used. For the remaining of the work, a turbo-pumped system was used, which was fitted with a load-lock. This considerably reduced the pumping time to reach base pressure and also milled at a higher rate. In both cases the sample stage was water cooled, and rotated continuously to ensure uniform milling. The system base pressure was $\leq 2 \times 10^{-4}$ Pa, Ar / 2% O_2 milling pressure 4×10^{-2} Pa, with beam voltage 500 V, and beam current density 1 mA cm^{-2}.

4.3 Device fabrication

4.3.1 The Focused Ion Beam microscope

The Focused Ion Beam microscope[1] (FIB) can image samples using secondary electrons produced by the rastering ion bombardment. This is analogous to a scanning electron microscope, (SEM). Repeated scanning or dwelling over a region can create features by milling material from the surface. Many different ion sources are possible [4], but the most reliable is presently the liquid gallium source, which is used in the present work. The gallium self assembles into a sharp tip, (diameter $\sim$ 2 nm) at high electric field. From this tip Ga^+ ions are extracted. These ions pass through a series of apertures and electrostatic lenses which focus them onto the sample. An outline of the ion column is shown in figure 4.7. The working pressure in the chamber was $< 10^{-3}$ Pa, while the ion column pressure was maintained at $< 10^{-5}$ Pa.

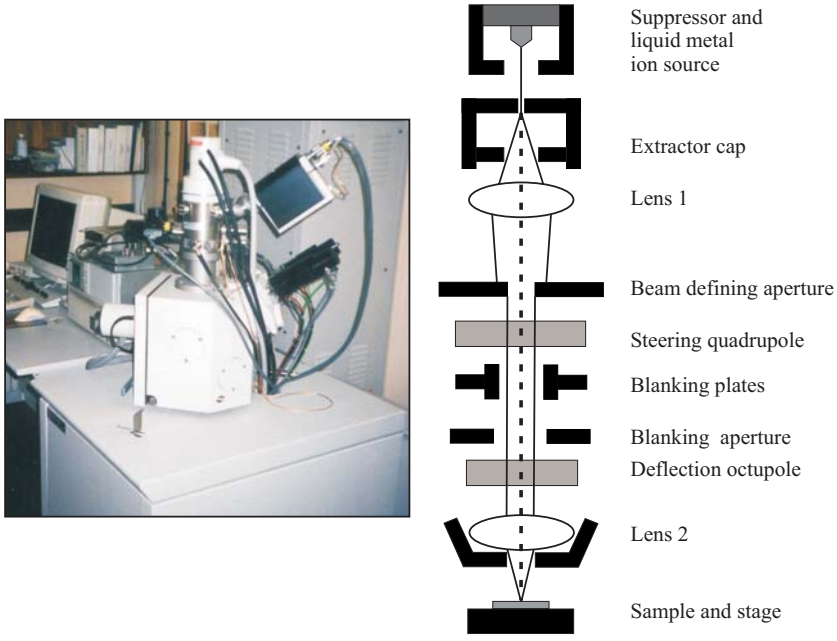

Figure 4.7: Outline and photograph of the FIB (adapted from [5]).

[1]FEI200 series FIB xP 2.25.

The impinging ions either implant themselves or mill material from the surface of the sample. Beam currents in the range 1 pA to 1 nA are available by changing the beam defining aperture. Typically the 4, 11, 70 and 150 pA beams were used in this work, (section 5.1), with a beam voltage of 30 kV. The spot size of the FIB is limited by chromatic aberration due to a distribution of ion energies. Due to this limitation the spot size increases with beam current [5]. For a 4 pA beam current the optimal spot size $\sim 10-15$ nm. The beam profile is approximately Gaussian, although deviations in the tail (several orders of magnitude lower than the beam peak) have been observed [4].

In contrast to other forms of lithography, FIB processing requires no masking with resists, post-FIB wet or dry etching, or resist removal. FIBs are being increasingly used for a range of applications, (for a recent review see [6]), including the site-specific preparation of transmission electron microscope (TEM) specimens, failure analysis in the semiconductor industry, and micromachining applications. Other applications of the FIB for optoelectronics will be discussed in section 6.4.

4.3.1.1 Platinum deposition and enhanced etch

The Ga^+ beam can be used to deposit Pt by injecting an organometallic gas containing Pt into the chamber during milling, through a needle brought close to the sample surface. Where the beam dwells the compound is broken down, the volatile organic gases escape and Pt is deposited, (although in practice there is a combination of Pt, Ga and other organic compounds [7]). The Pt deposition was used in the fabrication of Nb/Mo/Nb junctions, (figure 5.6 and section 7.2) as well as the GaN devices (section 6.4).

Iodine gas can also be injected into the chamber to produce so-called Enhanced Etch (EE). This reactive gas greatly increases the milling rate of the FIB as well as reducing the Ga damage / amorphous layer usually found, by forming volatile compounds with the milled material which is subsequently pumped out of the system ([8, 9] and section 5.2). EE was used in the fabrication of S/I/S junctions (section 7.3), but not extensively for most of the work, since the increased milling rate was unnecessary and less controlled than the normal milling. A drawback of I_2 is the formation of CuI crystals: hence EE cannot be used in the presence of Cu.

4.3.2 Planar junction fabrication

A 50 nm wide trench is cut with the FIB across a micron scale track of a Cu/Nb bilayer (figure 4.8). A variable thickness S/N/S Josephson junction is created. Some Nb is left at the bottom of the trench: it is weakened both by the proximity effect of the normal metal underlayer, and gallium poisoning / damage by the FIB. The Cu (typically 75 nm thick [10]) serves as a thermal shunt to reduce heating and hysteresis in the $I-V$ characteristic, (which is observed in the case of Nb only devices), as well as carrying some supercurrent due to the proximity effect (section 2.3).

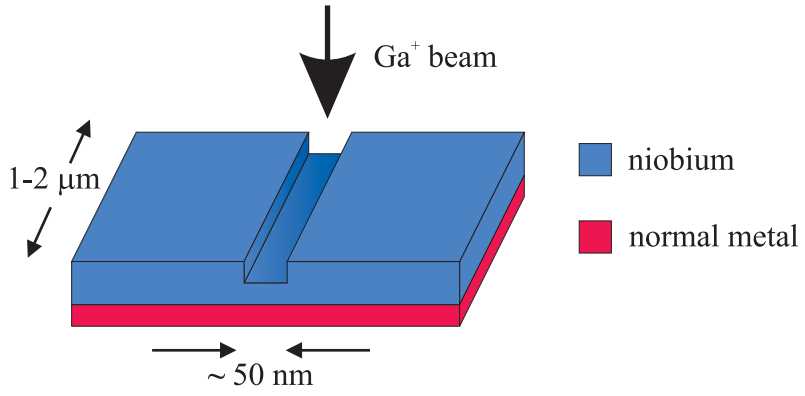

Figure 4.8: Planar junction fabrication with the FIB.

4.3.2.1 *In-situ* resistance

Early attempts to make the trench cuts reproducibly were not successful [11]. An *in-situ* resistance measurement, developed by W. Booij and A. Latif [12], was used to calibrate the depth of cut into the metal. A four probe measurement of the resistance of the track is made as the FIB mills.[2] A typical $R(t)$ obtained is shown in figure 4.9. Here the track is milled through at a measurement time $\sim$ 23 seconds. The close up of the plot shows the slight increase in resistance due to Ga implantation when an image is taken, followed by a steady increase as the track is milled through. An $R(t)$ for a Nb only sample can be converted into depth verses milling time, (for a constant beam current) by assuming a rectangular trench in series with the rest of the track, (whose resistance is constant). This can be used to calibrate cuts into a bilayer, (which was grown with the same Nb thickness as the calibration sample), assuming negligible drift in the FIB in the time between cuts. A TEM study by R. Hadfield has found that trenches with an aspect ratio of more that 2.5 cannot be reliably rectangular in shape, (caused by redeposition of the milled material on the sides of the trench) [13, 14]. Hence for a 50 nm wide trench, the Nb thickness should be $\leq$ 125 nm.

In the case of the bilayer system, the change in the resistance ΔR of the track is not simply related to the cut depth. Results have shown however that there is a correlation between ΔR and I_C, (see section 7.1 and [10]). Hence ΔR can be used to predict the junction properties. Reproducible results have been achieved as long as the FIB extraction current is maintained at 2.2 μA. Results for planar junctions with a Cu_xNi_{1-x} alloy instead of Cu as the underlayer will be discussed in section 7.1.

4.3.2.2 Applications

Since the junction length is relatively short, arrays of junctions can be cut by the FIB occupying a small distance. Applied microwaves can 'phase-lock' the individual junctions. For an array of n junctions, Shapiro steps are seen in the $I-V$ at a voltage nV_s, where V_s is the Shapiro voltage for a single junction. This technique has a potential application in voltage standards

[2] Using a Keithley 2000 DMM with LabVIEW^{TM} software written by G. Burnell.

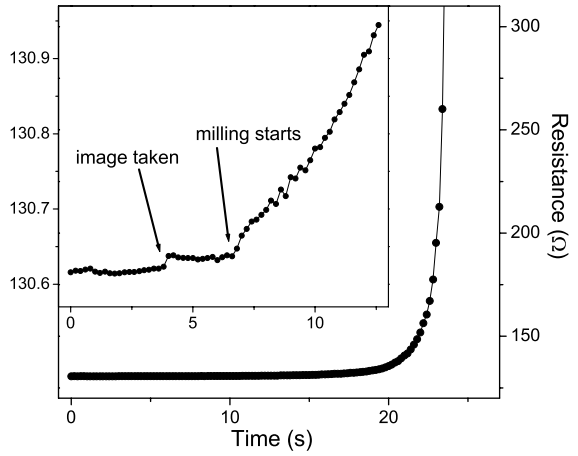

Figure 4.9: *In-situ* $R(t)$ for a calibration cut through a track with a 4 pA beam current. Inset: Detail showing the effect of imaging with the FIB.

([15] and section 6.2.1). However phase-locked arrays of FIB junctions in Cu/Nb bilayers up to only $n = 10$ have been so far demonstrated [10].

The planar FIB technique has more recently been used to produce planar junctions in MgB_2 [16], and as an initial step in the processing of metal-masked ion implanted YBCO junctions [17]. The flexibility of the FIB also allows more novel geometries to be formed: a 'Corbino' geometry has been made [13, 14]. This is formed by milling a circular trench in the track, with an electrical contact to the centre of the superconducting island. In this geometry flux can only enter the barrier in units of Φ_0, giving an interesting $I_C(H)$ response.

4.4 Measurement rigs

4.4.1 4.2 K dip probe

All electrical measurements were done with a four-point technique. Chips were secured onto a custom design copper chip carrier with silver conducting paint or carbon tape. Each section of the 'Cam 39' mask was connected to several contact pads, (figure 4.6) which could be wire-bonded to the copper pads of the chip carrier using an ultrasonic wirebonder with 25 μm diameter Al wire. Two similar dip probes were used interchangeably in this work. The measurement rigs and accompanying hardware and software were developed by G. Burnell, W. Booij, P. McBrien, R. Moseley and the author. The generic dip probe consisted of a diode thermometer, heating element, in-plane solenoid and out-of plane Helmholtz pair for applying magnetic fields, ($0 - 80$ mT at 4.2 K), and a microwave antenna ($12 - 18$ GHz). A low noise current and voltage source, (giving a typical noise level of $0.5 - 1$ μV in a 10 kHz bandwidth), applied a quasi-d.c. (~ 15 Hz) sinusoidal current output. A μ-metal shield was placed over the end of the probe to reduce stray magnetic field. Measurements involving the magnetic fields are done at 4.2 K to prevent heating of the sample by the Cu coils. The 'Dualscope' (written in LabVIEW^{TM} by G. Burnell) software was used to display and control the measurements. The set up is shown in figure 4.10.

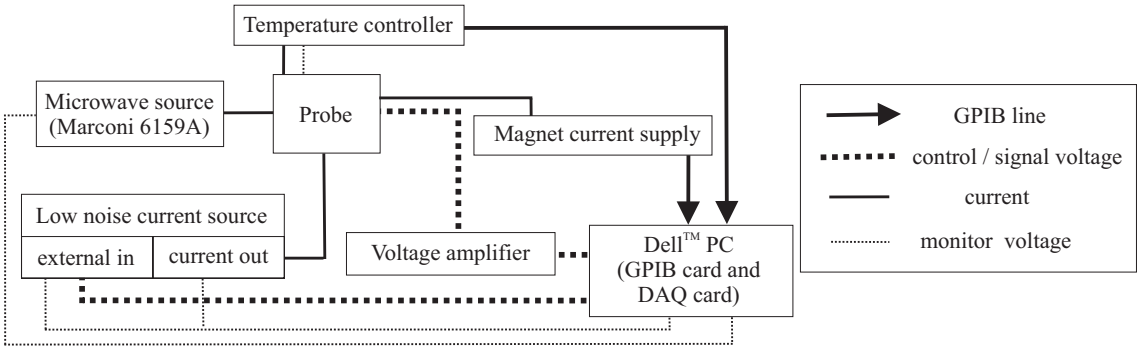

Probe	1	2	Heliox
Temperature controller	Lakeshore DRC 82C	Lakeshore 340	Oxford ITC 503
Magnet current supply	HP 6625	HP 6625	HP 6574A and Oxford IPS 120-10
DAQ card	12-bit	16-bit	12-bit

Figure 4.10: Schematic of electronics used for measurements, and table detailing the different equipment for each probe.

A lockin amplifier[3] allowed the measurement of voltage signals as low as 1 nV. A simple op-amp adder box[4] was used to combine the lockin reference oscillation, (in the range $5 - 30$ mV at 1 kHz), to a d.c. voltage output of the analogue-to-digital (AD) card, which was used to control the current source. The d.c. offset was then ramped by the software to obtain the differential resistance as a function of bias current (figure 4.11).

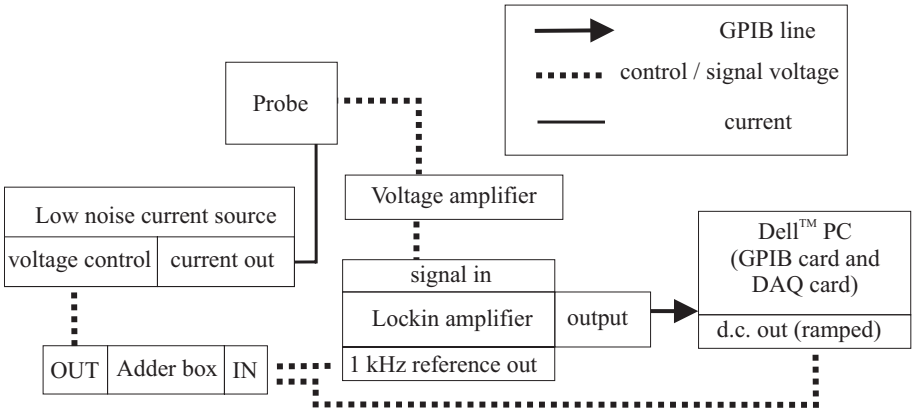

Figure 4.11: Schematic set-up for lockin amplifier measurements.

4.4.2 Oxford Instruments Heliox^{TM}

For lower temperature measurements with larger magnetic fields the closed cycle ^{3}He-based Oxford Instruments Heliox^{TM} was used. This system has a base temperature of 0.34 K with a

[3]EG & G Princeton Applied Research models 5210 and 5320L were both used.
[4]Using a Burr-Brown INA105 precision unity gain operational amplifier.

superconducting coil producing a maximum field of 2 T. The principal of operation of the ^{3}He system is shown in figure 4.12. The sample sits in a vacuum, thermally connected to the 1 K pot and ^{3}He pot. ^{4}He is drawn up through a capillary from the dewar into the 1 K pot, which is pumped on by a rotary pump. This achieves a temperature $\sim 1.2 - 1.4$ K. With the sorp at 50 K, (figure 4.12 (a)) ^{3}He is then condensed into the ^{3}He pot. The sorp is then allowed

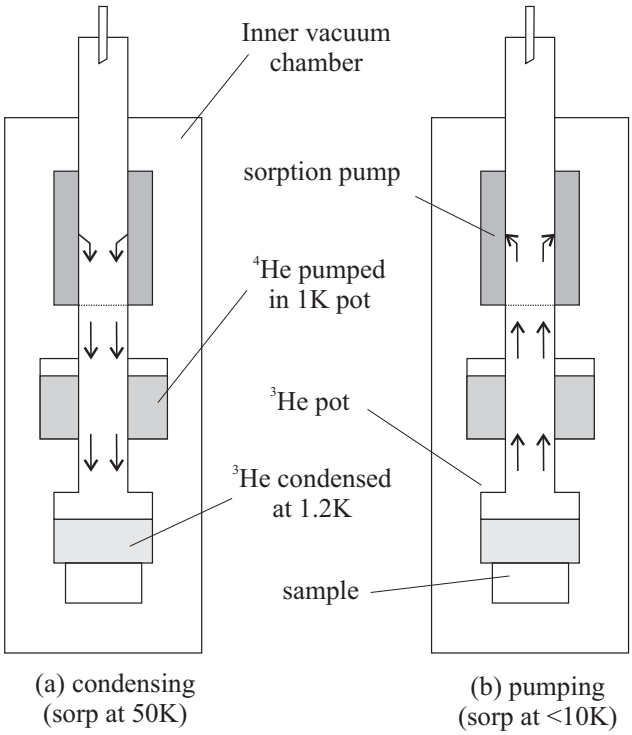

Figure 4.12: Schematic of Oxford Instruments Heliox^{TM} cooling system: (a) condensing ^{3}He, (b) pumping on ^{3}He, (taken from [18]).

to cool (figure 4.12 (b)) and pump on the condensed ^{3}He, reducing the temperature to 0.34 K. Base temperature could be maintained for several hours before the cycle had to be restarted. A drawback of the magnetic end piece of the Heliox was the extension required to place the sample in the centre of the coil. This extra length of material gave an additional unknown temperature gradient (see section 7.4.2).

4.4.3 Magnetic measurements

4.4.3.1 Magnetoresistance measurements

Resistance measurements with an in-plane field up to 330 mT, with temperature in the range 77−300 K were also possible, using a water cooled electromagnet system. The electrical measurement set-up was similar to the probes discussed above. This was used to characterise the GMR and spin-valve devices (sections 8.2 and 8.4) in the CIP configuration, (with thin Nb layers), before growing devices for CPP processing.

4.4.3.2 Vibrating sample magnetometer

All magnetic hysteresis ($M(H)$) measurements were made in a Vibrating Sample Magnetometer (VSM)[5]. Typically measurements were made on 10×5 mm^2 samples at room temperature, and could be made in and out of plane. A ^{4}He cryostat enabled measurements down to 10 K. The increased noise and the smaller sample size limit (4×4 mm^2) meant that many of the $Cu_{40}Ni_{60}$ and thin pseudo-spin-valve structures discussed in chapters 7 and 8 could not be measured at low temperatures. Quantitative measurements of the magnetic moment of samples require careful calibration: in particular given the relatively large size of the samples compared to the pick-up coils of the VSM and the calibration sample used. Hence the VSM was used primarily for measurements of the Curie temperature, coercive fields, exchange bias and qualitative shape of the $M(H)$ loops, rather than an accurate determination of the total moment of the samples.

[5]Princeton Measurements Corporation MicroMag^{TM} Model 2900.

References

[1] M. Ohring, *Materials Science of Thin Films* (Academic Press, 2002), 2nd Edition.
[2] S. A. Campbell, *The Science and Engineering of Microelectronic Fabrication* (Oxford University Press, 1996).
[3] C. W. Leung, Ph.D. Thesis, University of Cambridge (2002).
[4] J. Melngailis, J. Vac. Sci. Technol. B **5**, 469 (1987).
[5] *Focused Ion Beam Workstation Reference Guide*, FEI Company (1996).
[6] S. Reyntjens and R. Puers, J. Micromech. Microeng. **11**, 287 (2001).
[7] A. J. DeMarcoa and J. Melngailis, J. Vac. Sci. Technol. B **19**, 2543 (2001).
[8] A. Yamaguchi and T. Nishikawa, J. Vac. Sci. Technol. B **13**, 962 (1995).
[9] R. J. Young, J. R. A. Cleaver, and H. Ahmed, J. Vac. Sci. Technol. B **11**, 234 (1993).
[10] R. H. Hadfield, Ph.D. Thesis, University of Cambridge (2002).
[11] R. W. Moseley, W. E. Booij, E. J. Tarte, and M. G. Blamire, Appl. Phys. Lett. **75**, 262 (1999).
[12] A. Latif, W. E. Booij, J. H. Durrell, and M. G. Blamire, J. Vac. Sci. Technol. B **18**, 2 (2000).
[13] R. H. Hadfield, G. Burnell, D.-J. Kang, E. J. Tarte, C. Bell, and M. G. Blamire, Phys. Rev. B **67**, 144513 (2003).
[14] R. H. Hadfield, G. Burnell, P. K. Grimes, D.-J. Kang, and M. G. Blamire, Physica C **367**, 267 (2002).
[15] S. J. Benz and C. J. Burroughs, IEEE Trans. Appl. Supercond. **7**, 2434 (1997).
[16] G. Burnell, D.-J. Kang, D. A. Ansell, H. N. Lee, S. H. Moon, B. Oh, E. J. Tarte, and M. G. Blamire, Supercond. Sci. Technol. **16**, 254 (2003).
[17] D.-J. Kang, N. H. Peng, R. Webb, C. Jeynes, J. H. Yun, S. H. Moon, B. Oh, G. Burnell, E. J. Tarte, D. F. Moore, and M. G. Blamire, Appl. Phys. Lett. **81**, 3600 (2002).
[18] *Heliox^{VL} Sorption Pumped ^{3}He Insert*, Oxford Instruments (1994), Issue 3.3.

Chapter 5

Three-dimensional FIB fabrication technique

The three-dimensional focused ion beam fabrication technique used to create CPP devices is discussed. Details of this technique have been published in reference [1], which is reproduced in Appendix B.

5.1 Sandwich junction fabrication

To compliment the planar FIB technique discussed in section 4.3.2, a three-dimensional technique for creating CPP devices has been developed. This technique was used by Kim *et al* to study intrinsic *c*-axis Josephson junctions in whiskers and thin films of the HTS cuprates [2, 3]. In the present work this specific technique is extended to produce Josephson junctions in low temperature superconductor (LTS) heterostructures, giant magnetoresistive multilayers and spin valves, and other structures in which CPP transport is required.

5.1.1 Sample holder

The stage of the FIB can be rotated about an axis co-linear with main track of the 'Cam39' pattern between $\theta = 0°$ and $\theta = 45°$, where θ is the angle between the beam and the film normal. Rotation of 180° about an axis normal to the sample stage is also possible (figure 5.1). Using a custom 45° wedge holder, the two axes of rotation allow the full range of $\theta = 0°$ (figure 5.1 (a)) to $\theta = 90°$ (figure 5.1 (b)) between the beam and the sample normal to be achieved. The sample holder shown in figure 5.1 (c) was designed by D.-J. Kang, and allowed a third chip to be loaded for conventional processing at the same time. This sample holder was used for most of the work presented.

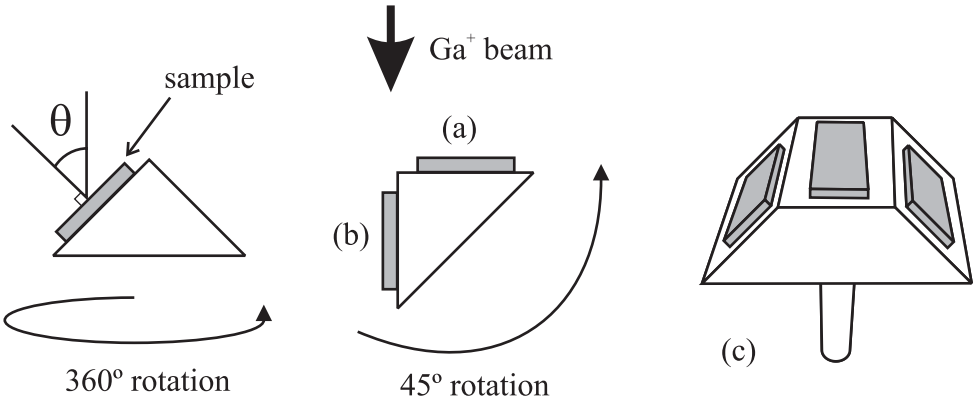

Figure 5.1: Schematic of the sample holder used in FIB, showing two axes of rotation to achieve $0° \leq \theta \leq 90°$ milling from (a) $\theta = 0°$ to (b) $\theta = 90°$. (c) A second design, for three 10×5 mm^2 chips.

5.1.2 Device fabrication procedure

The fabrication procedure is shown in figure 5.2. A film is deposited and Ar^+ milled to give 4 μm wide tracks (figure 5.2 (a)). This track is thinned to $\sim$ 700 nm from an angle of $\theta = 0°$ with a beam current of 150 pA (figure 5.2 (b)). A box of area $\sim 4 \times 2$ μm^2 typically would take between $1 - 3$ minutes to mill, depending on the material and thickness. This milling can be calibrated either by eye, (using the change of contrast in the image when the substrate is reached), or by using the stage current / end-point detection measurement, (figures 5.3 and 9.2). Figure 5.3 also shows how the milling of different layers can be distinguished: the relatively high

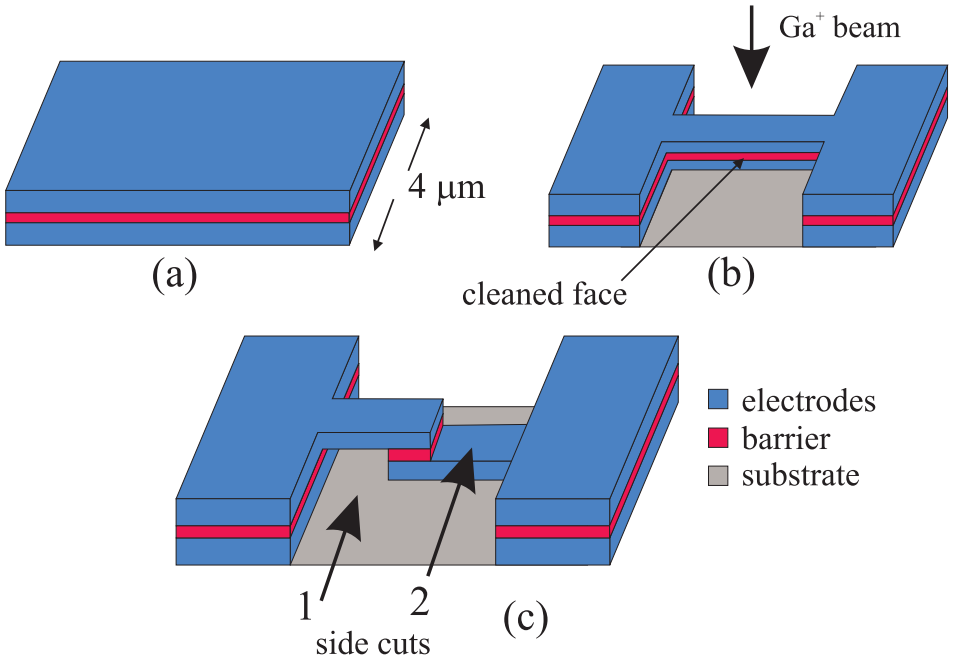

Figure 5.2: FIB procedure for device fabrication: (a) initial micron scale track (b) thinned with 150 pA beam and then cleaned (c) side cuts 1 and 2 to create the final device structure.

conductivity of the CuNi barrier giving a peak in the stage current as shown. The large drop in the stage current is seen as the SiO layer is reached. After further milling the stage current

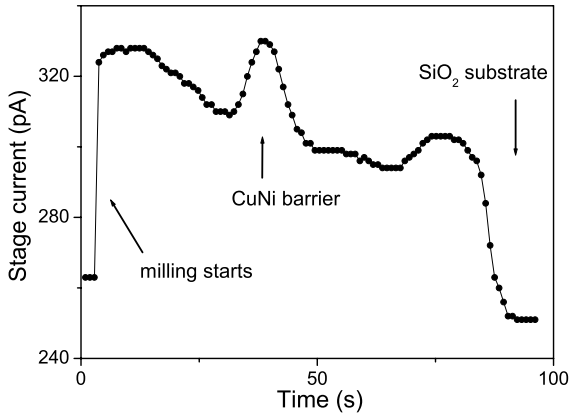

Figure 5.3: Stage current vs milling time, for a 5×2 μm^2 box milled from $\theta = 0°$ on a 200 nm Nb / 10 nm CuNi / 200 nm Nb trilayer, using a 150 pA beam current.

increases again, (figure 9.2) as the Si layer is reached, and implanted with Ga. Typically the milling was continued for a few seconds after the SiO layer is reached, to ensure that there was no possibility of shorting between the electrodes. The sidewalls of the narrowed track are then cleaned with a beam current of either 4 or 11 pA, using the standard software 'cleaning tool': which repeatedly steps in a single pixel wide line. This removes excessive gallium implantation from the larger beam size of the higher beam currents (figure 5.4), and makes the sidewalls more

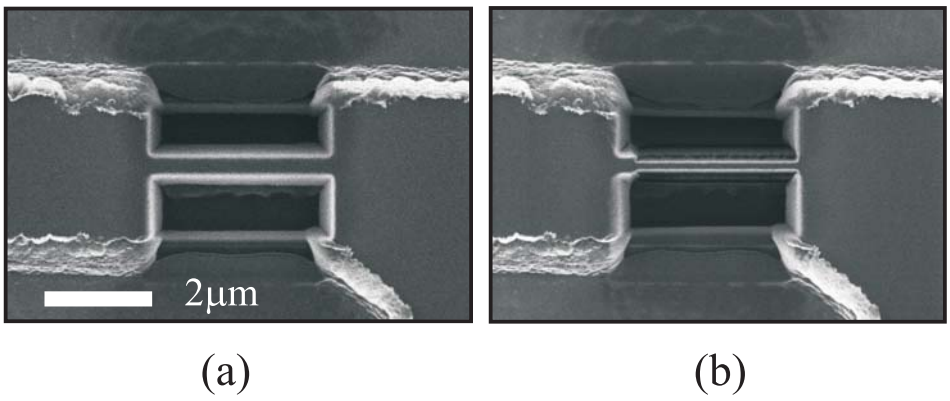

Figure 5.4: (a) Track narrowed with 150 pA showing significant bright edges due to tapering, (b) after further cleaning and narrowing with a 11 pA beam.

vertical due to the smaller spot size, (figure 5.7 (b)). The cleaning takes ~ 3 minutes per device. The track width is then ≤ 500 nm. The sample is then tilted to $\theta = 85°$, and the isolating cuts are made with a beam current of 4 or 11 pA to give the final device (figure 5.2 (c)). The two side cuts, 1 and 2, will be referred to as the 'undercut' and 'overcut' respectively. These cuts typically took between $10 - 40$ seconds depending on the dimension y and the beam current. Throughout the processing the ion beam had a dwell time per pixel of 0.1 μs and a beam spot overlap of 50%.

The side cuts in the device force the current vertically through the barrier, (or in the case of intrinsic junctions the red region in figure 5.5 has purely c-axis transport). Since the current is injected and removed from the *top* electrode, there are in fact two junctions in series: the small junction, and a much larger one (on the right hand side of figure 5.5). This second device is much larger than the central one, and will have both a much smaller resistance than the first device and such a large critical current, in the case of superconducting devices, that it can be neglected. The thickness of the device in the y direction (figure 5.5) is important - since milling

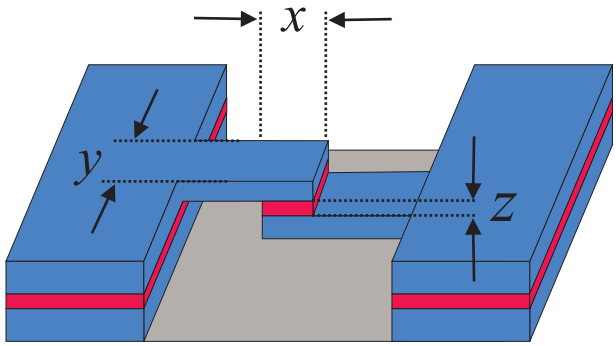

Figure 5.5: Diagram of final junction with convention for dimensions as used in this work.

cannot take place at $\theta = 90°$, due to beam distortion caused by the interaction of the Ga^+ ions and the substrate. This could be overcome by heavily overmilling into the substrate with the

Ar^+ ions, but this was not viable on the basis of the increased milling time. Simple trigonometry shows that for a y dimension of 500 nm, milling from one side at an angle of $\theta = 85°$ introduces at least an error of $\Delta z = 500$ nm $\times$ tan5° ~ 44 nm. For the heterostructure films, where the top and bottom electrodes must be isolated from one another, the overcut and undercut must therefore mill into the top and bottom electrodes by at least 50 nm to ensure this isolation is achieved (figure 5.7 (a)).

Early devices had deposited Pt on the track before milling, to provide mechanical support and thermal heat sinking of the Nb above the undercut (figure 5.6 (a)). It was found for the Nb superconducting devices that so long as $d_{\mathrm{Nb}} \geq 150$ nm, a current of several mA could be supported at 4.2 K (sections 6.2.3 and 7.2), and the Pt was an unnecessary addition and hence not used for later devices (figure 5.6 (b)). The Pt technique was required for the GaN devices (section 6.4.3), which were measured at room temperature.

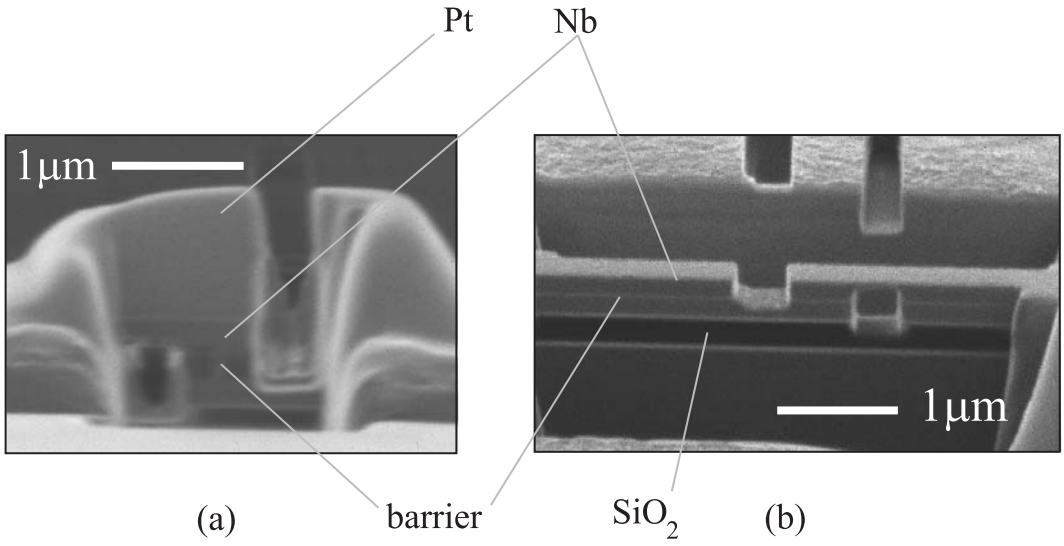

Figure 5.6: (a) FIB image of an early Nb/Mo/Nb device from $\theta = 85°$ with Pt deposited over the device, (b) a later Nb/CuNi/Nb device from $\theta = 65°$ without Pt, the CuNi barrier can be seen as thin brighter line.

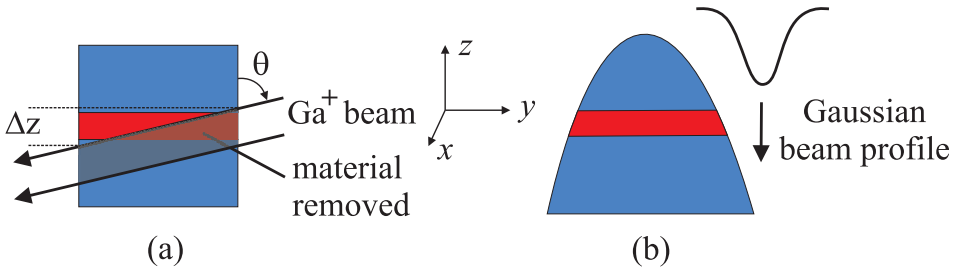

Figure 5.7: Exaggerated side views of (a) milling from an angle $\theta < 90°$, (b) rounded and tapering profile due to Gaussian beam profile, (see also figure 5.8).

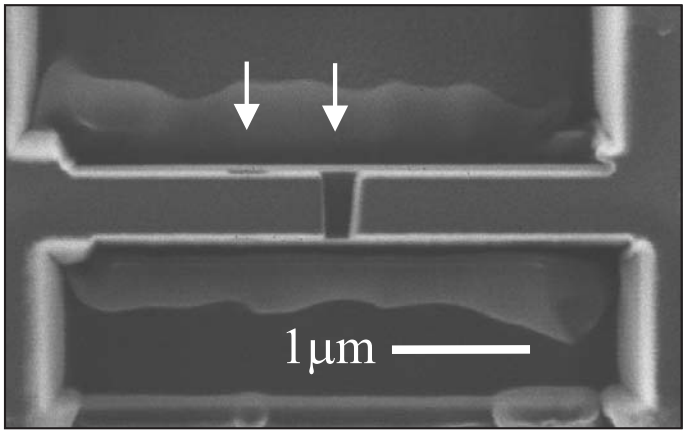

Figure 5.8: FIB image of a final device from $\theta = 0°$. The undercut and overcut are marked with white arrows. The tapering due to the aspect ratio and Gaussian beam profile of the overcut is clear.

5.2 Limitations of the FIB technique

The device dimensions are typically in the range $500 - 5000$ nm in the x-direction and $200 - 700$ nm in the y-direction (figure 5.5). The minimum achievable device area is of the order of 100 $\times$ 100 nm^2 for controllable milling. Beam drift during milling, and the beam profile (figures 5.7(b) and 5.8), prevent smaller features being reliably cut. Smaller dimensions are possible in a more uncontrolled manner. The Gaussian beam profile rounding of the top of the device does not give vertical sides to the devices, (figure 5.7 (b)). This is a problem with TEM preparation where parallel side walls are crucial, and can be overcome by slightly tilting the sample by $\pm$ $1° - 4°$ away from $\theta = 0°$ [4] when cleaning the sidewalls. In the present case however this is not such an important factor, since the top edges of the device act as an electrode, and rounding is not important. This effect serves only to slightly increase the error of the x and y dimensions of the junctions - which is of the order of $30 - 50$ nm.

FIB processing inevitably leads to Ga implantation. Potential poisoning / damage / amorphous layer formation due to this Ga implantation must also be considered. Table 5.1 shows stopping and straggling distances of Ga^+ ions calculated for a variety of elements, (the longitudinal straggle is the standard deviation of the distribution of distances about the mean stopping distance). Much work has been carried out concerning the effect of Ga^+ damage, in particular magnetic materials. Ga^+ implantation is known to cause swelling and amorphous layer formation before removal of material by sputtering begins [8]. For more complex crystal structures, for example the HTS, the implantation is anisotropic, and has been determined to be 60 nm in the c-axis of Bi-2201 and Bi-2212 [9]. This implantation will not be the same in the $a - b$ planes due to the different lattice spacing. This is known as 'channelling', and is also observed as contrast between different crystallographic orientations in a polycrystalline sample (see figure 9.4).

How the magnetic properties of thin films change when they are patterned down to nanoscale features of varying aspect ratio and shape is of course critical technologically. The MR obtained

Element	Stopping distance (nm)	Longitudinal straggling (nm)	Lateral straggling (nm)
Mo	9.9	6.4	4.6
Pt	6.8	6.1	4.7
Au	7.5	6.8	5.3
Nb	11.3	7	5.1
Fe	10	4.9	3.6
Si	25.7	8.7	6.7
Al	22.6	7.5	5.8
Ag	10.1	7	5
Pb	12.9	11.8	9.1
Cu	9.5	5	3.7

Table 5.1: Stopping distances and straggling lengths for 30 kV Ga^+ ions in various materials. (Taken from [5], after [6, 7])

in small and narrow shapes, is expected to be enhanced, (section 1.2.7). For the present geometry the devices are relatively long and thin. Kaminsky *et al* [10] found that direct Ga implantation can modify thin films of Py, reducing the coercivity even to the extent that the ferromagnetism at room temperature can be destroyed. Ozkaya *et al* [11] found an increased coercive field in implanted Py, which they attribute to magnetostrictive stresses induced in the film, as well as a slight change in the composition of the NiFe. Katine *et al* [12] claimed an effective 'dead' layer of magnetic material $\sim$ 100 nm with FIB trimming of spin-valve sensors. Xiong *et al* [13] and Roshchin *et al* [14] however have both made similar studies (with Py and Fe respectively), and found that objects in soft magnetic materials as small 100 nm can be fabricated with no significant effect on the magnetic properties. It has also been shown that even moderate, ($\sim$150 °C) temperatures can drastically alter the GMR in the case of the 1^{st} and 2^{nd} AF peaks in Co/Cu multilayers [15]. The FIB is known to increase the temperature locally when milling material. This is mainly an important effect in insulators where the thermal conductivity is lower, and for larger beam currents [16], so it is not considered as an issue in this work.

Many of the above cases try to quantify the doses of Ga implanted in the films using simply the value of It/eA, where I is the beam current applied for a time t over an area A, (e is the electronic charge). Doses of the order of 10^{16} ions / cm^2 are required before significant removal of material begins [8, 11]. The doses in the present case are difficult to quantify since the majority of the material is removed and the implantation is due to the tails of the beam profile. It is expected that much of the milling at $\theta = 0°$ damages only to the top layer of the electrode, with only a relatively small lateral straggle affecting the more critical barrier region. When milling at $\theta = 85°$ the barrier is affected more directly, (since there is no material above to shield it), but the milling rate is increased at this angle, and the doses received are therefore smaller [8], (although it is stressed again that all of the above damage / Ga dose is due only to the tails of the Gaussian beam).

As shall be seen, although the penetration distance of the Ga^+ into various materials may be different, it is the material-dependent *effect* of the Ga that is more crucial: for example the

Tl-2212 devices (section 6.1.5.1) show intrinsic S/I/S junctions - implying that the resputtered / amorphous regions are still insulating and the Ga damage only becomes important for the smaller devices, whereas AlO_x in LTS S/I/S junctions would seem to suffer more profoundly (section 7.3.3).

References

[1] C. Bell, R. H. Hadfield, G. Burnell, D.-J. Kang, M. J. Kappers, and M. G. Blamire, Nanotechnology **14**, 630 (2003).

[2] S.-J. Kim, Y. I. Latyshev, and T. Yamashita, **74**, 1156 (1999).

[3] S.-J. Kim, Y. I. Latyshev, T. Yamashita, and S. Kishida, Physica C **362**, 150 (2001).

[4] R. M. Langford and A. K. Petford-Long, J. Vac. Sci. Technol. A **19**, 2186 (2001).

[5] R. W. Moseley, Ph.D. Thesis, University of Cambridge (2000).

[6] J. Ziegler, J. Biersack, and U. Littmark, *The Stopping and Ranges of Ions in Matter* (Pergamon New York, 1985).

[7] *SRIM computer program*, available at www.srim.org.

[8] C. Lehrer, L. Frey, S. Petersen, and H. Ryssel, J. Vac. Sci. Technol. B **19**, 2533 (2001).

[9] S.-J. Kim, T. Yamashita, M. Nagao, M. Sato, and H. Maeda, Jpn. J. Appl. Phys. **41**, 4283 (2002).

[10] W. M. Kaminsky, G. A. C. Jones, N. K. Patel, W. E. Booij, M. G. Blamire, S. M. Gardiner, Y. B. Xu, and J. A. C. Bland, Appl. Phys. Lett. **78**, 1589 (2001).

[11] D. Ozkaya, R. M. Langford, W. L. Chan, and A. K. Petford-Long, J. Appl. Phys. **91**, 9937 (2002).

[12] J. A. Katine, M. K. Ho, Y. Ju, and C. T. Rettner, Appl. Phys. Lett. **83**, 401 (2003).

[13] G. Xiong, D. A. Allwood, M. D. Cooke, and R. P. Cowburn, Appl. Phys. Lett. **79**, 3461 (2001).

[14] I. V. Roshchin, J. Yu, A. D. Kent, G. W. Stupian, and M. S. Leung, IEEE Trans. Magn. **37**, 2101 (2001).

[15] J. A. Katine, A. Palanisami, and R. A. Buhrman, Appl. Phys. Lett. **74**, 1883 (1999).

[16] J. Melngailis, J. Vac. Sci. Technol. B **5**, 469 (1987).

Chapter 6

Applications to other devices

The application of the three-dimensional FIB device fabrication described in chapter 5 to various systems is presented. The fabrication and measurement of $Tl_2Ba_2CaCu_2O_8$ intrinsic Josephson junctions is discussed. A large section of this work is published in reference [1], which is reproduced in Appendix B. Nb/$MoSi_2$/Nb junctions, SQUIDs and GaN light emitting diodes are then considered.

6.1 $Tl_2Ba_2CaCu_2O_8$ intrinsic junctions

6.1.1 Introduction

An outline of the important features of the HTS was given in section 2.6, and the theory of *c*-axis intrinsic junctions was discussed in section 3.6. As was noted previously, the important aspect of figure 2.9 is the layered nature of the structure. The CuO and TlO planes (the superconducting layers), are separated by insulating layers containing Ba and Ca. The Josephson junctions formed have a total thickness of the order of 1.5 nm, with two junctions per unit cell.

6.1.2 Film growth

The Tl-2212 films were grown[1] on (001) $LaAlO_3$ substrates in a two stage process [2]:

- Amorphous precursor r.f. sputtered from Ba-Ca-Cu-O target
- *Ex-situ* anneal in a sealed crucible with a thallium source at 850 °C

For both the *c*-axis and the vicinal films (discussed in section 6.1.3), the Tl-2212 recrystallises during the annealing to grow expitaxially on the $LaAlO_3$ substrate [3]. For the *c*-axis CPP devices, a $\sim$ 300 nm thick Au or Ag/Au film was *ex-situ* sputtered onto the film to serve as a capping layer to protect against both water degradation and also Ga implantation when imaging and milling from $\theta = 0°$ in the FIB.

Ar^+ ion milling of the precursor film before thallination was also possible, however the present work contains only devices patterned on samples which were milled after thallination. The film thickness was typically 800 nm. Thicker films, although easier to process in the FIB, were found to contain regions of low contrast when viewed in the FIB, which were interpreted as either areas of a secondary phase, or voids. These made the fabrication of devices difficult. Hence most of the devices in this work were patterned on the 800 nm thick films.

6.1.3 Previous planar junctions

Previous work has been done in the planar geometry, using CIP devices patterned on 20° vicinal Tl-2212 films. In these vicinal films the *c*-axis is offset by 20° from the normal to the plane of the substrate. In this way, a CIP measurement forces the current to take a path which is a combination of $a - b$ plane and *c*-axis transport. By patterning micron scale bridges [4], or using the FIB to reduce the track width to the sub-micron scale [5, 6], the I_C of these devices was made small enough to be measurable. The film thicknesses in these cases was $\sim$ 250 nm.

6.1.4 Present work

As discussed in section 5.1, the three-dimensional FIB technique has been previously applied to create HTS intrinsic junctions in whiskers and thin films. It is interesting to note that the intrinsic S/I/S nature of the HTS does not suffer from the shorting problems found in metallic

[1] By H. Wu, Oxford University.

S/I/S junctions, (see section 7.3.3). An good explanation for this is that the resputtered material in the HTS case is some form of oxide. This is likely to be insulating, and not short out the junctions, unlike the case of the metallic junctions.

In addition to the c-axis devices fabricated by the FIB technique (figure 6.1 (a)), pseudo-vicinal devices were also fabricated. In this case triangular side cuts are made instead of the usual squares (figure 6.1 (b)). Now the current passing through the device must pass both in c-axis and $a-b$ planes, as in the CIP devices fabricated on vicinal films. Hence the drawback of lower quality of vicinal films is avoided by using a c-axis film. Such pseudo-vicinal devices showed similar behaviour of the planar CIP devices [7].

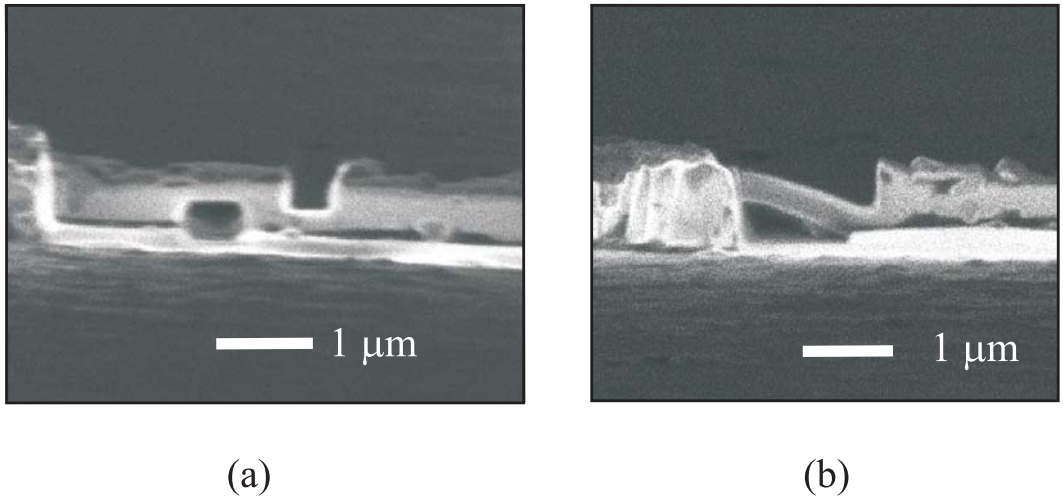

Figure 6.1: (a) Tl-2212 c-axis device (b) a pseudo-vicinal device fabricated by G. Burnell in a c-axis film using triangular side cuts. Both images were taken from $\theta = 85°$.

6.1.5 Results[2]

6.1.5.1 $I-V$s, current density scaling and resonances

A typical $I-V$ for a c-axis CPP device is shown in figure 6.2. A total of 94 ± 2 branches are present, which is consistent with the z dimension of the device as seen in the FIB, and the ~ 1.5 nm junction spacing. In the case of intrinsic junction fabrication special attention should be paid to error Δz introduced by milling at $\theta = 85°$ (figure 5.7): in the heterostructure case Δz must be taken into account in order to fully isolate the top and bottom electrodes, and ensure that current only flows through the barrier. In the intrinsic case, the milling angle means that there will an increased number of junctions in the stack compared to the z dimension measured.

The gap at $2N\Delta/e$ as indicated in figure 6.2 corresponds to a voltage of 2.44 ± 0.01 V, giving $2\Delta = 25.9 \pm 0.5$ meV. This value is consistent with previous bulk measurements [8, 9]. The R_N of the stack is 26.6 ± 0.5 kΩ, giving a single junction $I_C R_N = 5.6$ mV. This is significantly lower than the zero temperature limit of the standard BCS form for an S/I/S junction (equation

[2] All of the results presented in this section were obtained from measurements by A. Kuzhakhmetov, University College London.

3.2) of $\pi\Delta/2e \sim 20$ mV. This discrepancy has been seen elsewhere [10, 11]. The ratio of the minimum return current (the critical current when the current is reduced to zero from high bias) to the I_C is ~ 0.03. This implies a value of $\beta_C > 10^3$ [12], indicating low dissipation in the junctions. Figure 6.3 shows the scaling of I_C with junction area A. Although the linear scaling is as expected, the best fit line does not pass through the origin, implying $I_C \to 0$ for some non-zero area. The $J_C(A)$ scaling (inset figure 6.3) shows more clearly the changing properties of the stacks for $A \leq 0.5$ μm^2. This decrease may be attributed to a combination of the change in the physics of the smaller devices (due to charging effects / Coulomb blockade), as well as the increased effect of Ga damage / implantation. However both of these effects would be expected to become important at a smaller scale than observed in the present case (see discussion and references in [1]).

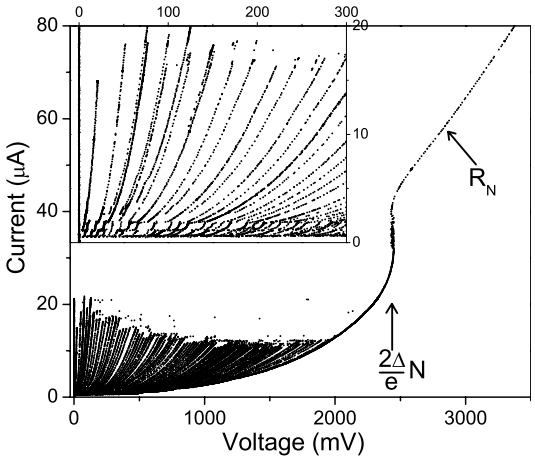

Figure 6.2: $I-V$ curve for 960×460 nm^2 area Tl-2212 stack with ~ 94 junctions in series at 4.2 K. Stack depth $z \sim 150$ nm. High bias R_N and gap for all junctions are indicated. Inset: Detail of the individual branches, sub-gap structure is evident below 2 μA.

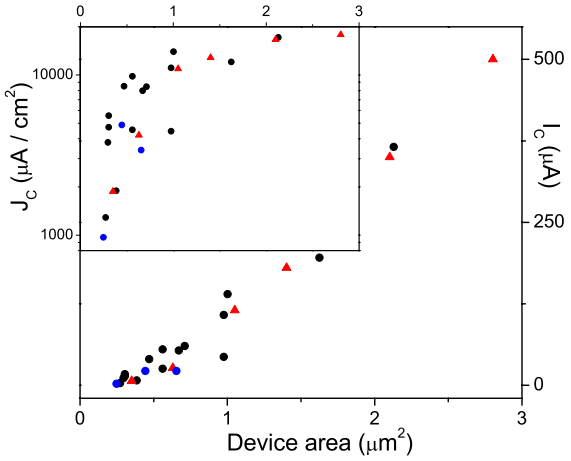

Figure 6.3: Scaling of I_C with junction area A, for Tl-2212 junctions at 4.2 K. Different coloured circles refer to different c-axis films. Triangles are vicinal CIP devices for comparison. Inset: Scaling of J_C with junction area.

Sub-gap resonances were observed in the $I-V$, as shown magnified in figure 6.4. Such features have been previously found in intrinsic junction $I-V$s of single crystals, and are thought to be a consequence of the a.c. Josephson oscillation coupling to longitudinal optical phonons in the c-axis (section 3.6). The characteristic frequency scale of the Josephson junction oscillation $I_C R_N/\Phi_0 \sim$ several THz. This corresponds to $50-100$ cm^{-1}, which is in the far infrared region. This is a similar range to phonon frequencies measured in Tl-2212 [13, 14]. The resonances are therefore consistent with the model of coupling between the Josephson oscillations and phonon modes.

6.1.5.2 *In-situ* resistance measurement

The *in-situ* resistance measurement (section 4.3.2.1) was used to try to achieve greater control over the number of junctions in a stack. After milling the undercut from $\theta = 85°$, the chip was removed from the FIB and loaded onto the *in-situ* sample holder. The overcut was then

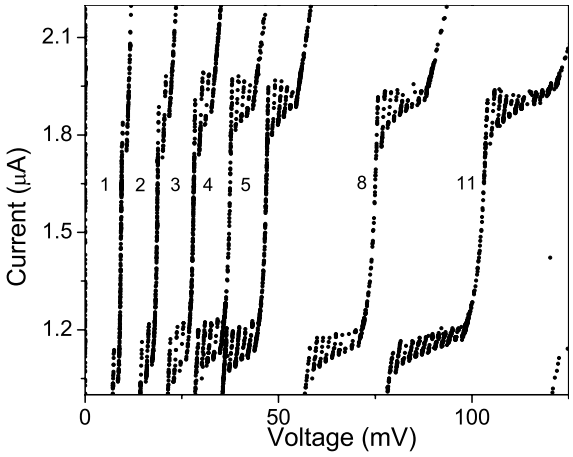

Figure 6.4: Magnified image of the inset of figure 6.2, showing some sub-gap resonances at 4.2 K. Numbers refer to the quasi-particle branch of the $I-V$, and the order of the splitting of each branch.

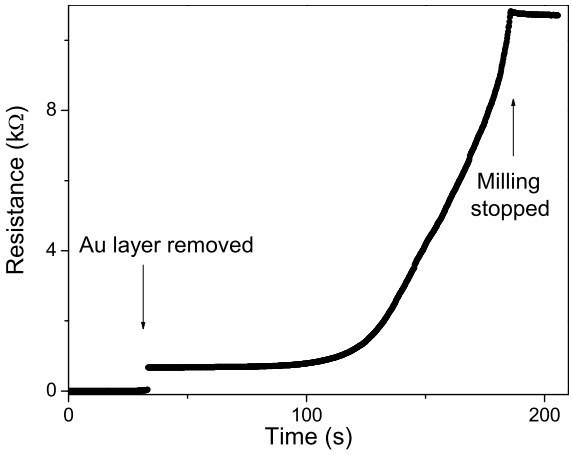

Figure 6.5: *In-situ* $R(t)$ taken while milling the overcut trench from $\theta = 0°$. Initial jump corresponds to milling through the Au capping layer.

made from $\theta = 0°$ by milling a trench in an analogous manner to the planar junction fabrication technique (section 4.3.2), while making a four point measurement of the $R(t)$. Due to the anisotropy of the resistivities in the $a-b$ and c directions of Tl-2212 in the normal state, a jump in R was expected in the $R(t)$ as soon as current was forced to flow in the c direction, i.e. $z > 0$. An increase was observed (figure 6.5), but no sudden jump was seen. The final devices fabricated by this method did not show good $I-V$ characteristics. The unreliability of the milling from $\theta = 0°$, and the smoothly varying $R(t)$ may have been associated with the roughness of the original Tl-2212 film (see figure 6.1), as well as an increased milling rate at the sides of the track due to edge effects. Both of these problems would mean that the trench did not mill uniformly, making accurate control of z difficult.

6.1.5.3 Further work: High frequency devices

FIB devices were made on c-axis films by G. Burnell using two different designs to examine the high frequency behaviour of the junctions. Single devices were made at the centre of a semi-logarithmic antenna design, to couple the device to an external THz source. A second design fabricated two devices side-by-side, to act as emitter and receiver of the THz radiation respectively. In the case of the double junctions, a single junction with y in the range $1-2$ μm was fabricated, and then cut into two from $\theta = 0°$, to give two devices each with $y \sim$ a few 100 nm. Since the initial y dimension was relatively large, the side-cuts were made using a 70 pA beam current to avoid stage drift problems associated with the longer milling times when using a lower beam current. Unfortunately, to date, neither of these designs have shown significant high frequency coupling.

6.2 Nb/$MoSi_2$/Nb junctions

6.2.1 Motivation

When an array of n Josephson junctions is phase-locked with microwave radiation of frequency f, Shapiro steps are found at a voltage nV_s, where $V_s = \frac{h}{2e}f$ is the voltage the step appears at for a single junction. This technique is used by the National Institute of Standards (NIST), among others, to produce voltage standards, since the microwave frequency can be known to a very high degree of accuracy. Currently S/I/S junctions are used [15], but S/N/S junctions are also being investigated as the next generation of standards, due to their reproducibility and stability [16].

Tens of thousands of junctions are required for a 1 V standard. To allow accurate control over the barrier widths, S/N multilayers are grown and etched into series arrays of mesa structures. Despite this technique, the junction size makes the total array area large compared to the wavelength of the microwaves. Phase-locking the junctions is then difficult. To achieve as high a density of junctions as possible the N barriers and the S spacers in the multilayer should be as thin as possible [17], while maintaining a large $I_C R_N$ product, and suitable heat dissipation of the power generated. A high resistivity barrier is attractive, since for a given required voltage, the power dissipation is reduced [18]. NIST has found that amorphous $MoSi_2$ is a good candidate for this purpose. For the thinner $MoSi_2$ barriers the J_C is prohibitively large for their micron-scale junctions. To investigate the single junction properties as the $MoSi_2$ thickness is reduced, the FIB technique was hoped to provide information on the $I_C R_N$ and J_C scaling with d_{MoSi}, as well as investigating the power dissipation properties of sub-micron junctions.

6.2.2 Film details

The films were d.c. magnetron sputtered[3] on oxidised Si, with the structure Nb(300 nm) / d_{MoSi} / Nb(300 nm), with d_{MoSi} = 15.1, 10.2, 7.9 and 5.9 nm (referred to as wafers A, B, C and D respectively). Previous studies [19] had indicated that the J_C follows the empirical form

$$J_C \sim 170 \exp\left(\frac{-d_{\mathrm{MoSi}}}{3.7}\right) \tag{6.1}$$

where d_{MoSi} is measured in nm, and J_C has units of mA/μm^2. On this basis, the devices on wafer A should have a I_C of the order 0.7 mA for a 500 × 500 nm^2 junction, increasing to 8.6 mA for wafer D. The latter being comparable to the overhanging bridge Nb I_C at 4.2 K. The x and y dimensions were therefore required to be as small as was possible to fabricate with the FIB, in order to achieve a small enough I_C. The dimensions of devices which showed Josephson junction behaviour are presented in table 6.1.

[3] By Y. Chong of NIST, Boulder, Colorado.

Wafer	x (nm)	y (nm)
A	400	700
A	250	730
A	145	250
A	195	380
A	110	270
A	200	310
B	170	220
B	180	195
B	80	120
B	230	220
B	150	340

Table 6.1: Nominal x and y dimensions of Nb/$MoSi_2$/Nb devices fabricated.

6.2.3 Results

Figure 6.6 shows the first results obtained with devices patterned on wafer A. The inset of figure 6.6 shows the $I-V$ curve at high bias. The low bias hysteresis is associated with heating in the junction, while the much larger hysteresis at high bias is the bridge I_C of the Nb above the undercut. Under 12.82 GHz microwave irradiation 14 Shapiro steps could be observed (figure 6.6). If the microwave power was chosen correctly, the I_C could be suppressed enough to make the junctions non-hysteretic to within the noise level of the measurement. As can be seen from the $I_C(H)$ (figure 6.7) the I_C is not suppressed to zero, (the $I-V$ curves confirmed that this was not an artifact of the voltage criterion used to find I_C), thus there was some non-uniformity in the junctions. Attempts to make devices on the C and D wafers were not successful. Devices

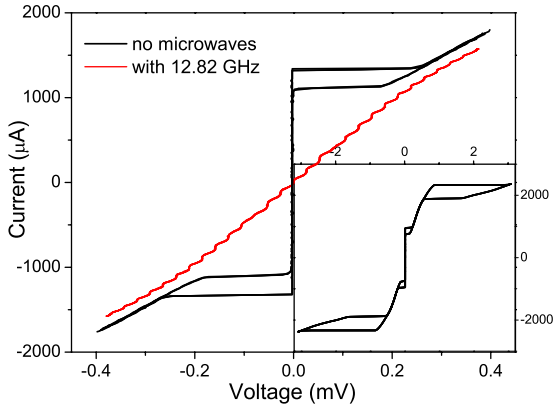

Figure 6.6: $I-V$ with and without microwave radiation of a 400×700 nm^2 Nb/$MoSi_2$/Nb device with $d_{MoSi_2} = 15.1$ nm, at 4.2 K. Inset: high bias $I-V$ showing the Nb bridge I_C.

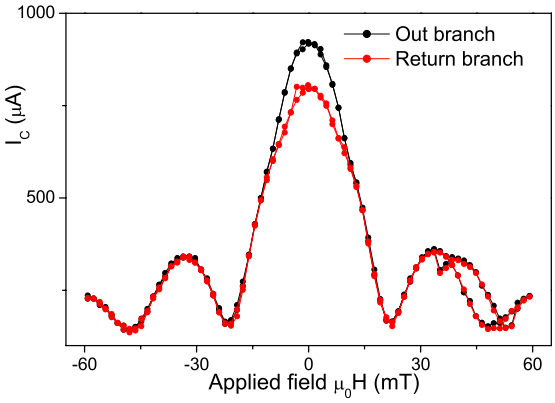

Figure 6.7: $I_C(H)$ showing the two I_Cs of the hysteretic $I-V$ for a similar sized device to that of figure 6.6 at 4.2 K. Lines are a guide to the eye.

with dimension $< 100\times100$ nm^2 were either very easily destroyed by passing too large a current, or showed resistive behaviour. As can be seen from figure 6.8, the lack of physical support and

heat sinking for such devices would limit their mechanical survival.

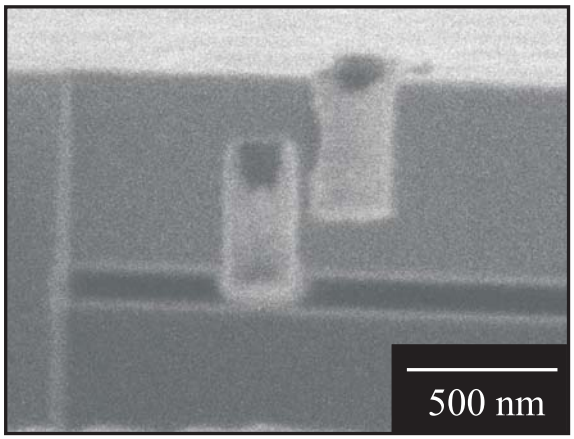

Figure 6.8: FIB image from $\theta = 85°$ of one of the smallest Nb/$MoSi_2$/Nb devices fabricated.

6.2.4 Discussion

As shown in the inset of figure 6.9, the J_C of these devices were comparable to the values predicted by equation 6.1, given the error bars associated with measuring the junction area. On the other hand, the $I_C R_N$ products of the FIB junctions were somewhat larger than the measurements made at NIST, particularly in the case of wafer B, (figure 6.9). In this case, since the junction dimensions were approaching the controllable limits of the FIB technique, a significant fraction of the device would have been Ga damaged. This may have changed the properties of the $MoSi_2$, increasing the J_C and $I_C R_N$.

From the inset of figure 6.6, the Nb bridge becomes normal at a bias current of $I_{max} = 1975$ μA, when the power dissipation $P_{max} = I_{max}^2 R_N = 1.2 \times 10^{-6}$ W. As a comparison with the

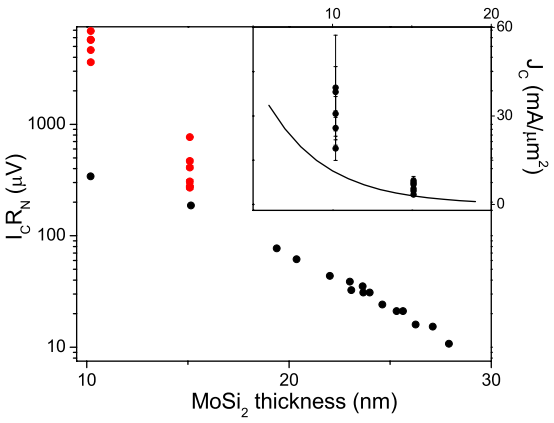

Figure 6.9: Scaling of $I_C R_N$ with barrier thickness in the present work (red) and previous micron scale junctions fabricated at NIST (black). Inset: $J_C(d_{\mathrm{MoSi}})$ for FIB devices compared equation 6.1 (line). NIST data courtesy of Y. Chong.

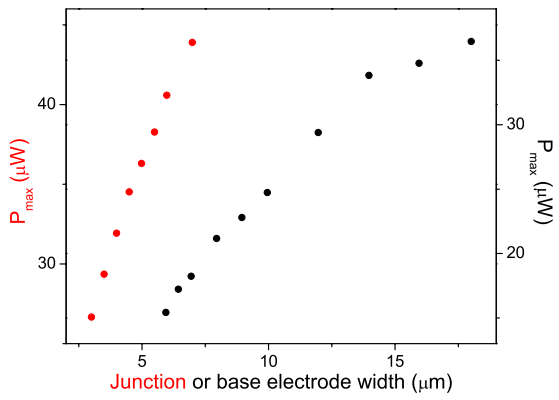

Figure 6.10: P_{max} vs electrode width (for junction width = 4 μm), and junction width (for electrode width = 16 μm), for a SiO_2 substrate. Taken from Chong *et al* [18].

NIST devices, figure 6.10 shows how the maximum power dissipation in the micron scale mesa junctions decreases with both the junction and base electrode width. This scaling is caused by the dominance of radial heat conduction to the substrate via the base electrode. The characteristic length scale over which the electrode equilibrates with the substrate, the thermal healing length ℓ_t, was found to be 2.7 μm [18]. Hence it is not possible to extrapolate these results, with the approximation of the model [18], to dimensions $< \ell_t$. In the present case, the device and one of the electrode dimensions are smaller than ℓ_t. A simple estimate of P_{max} can be made using $P_{max} = AY\Delta T$ [19]. Here $\Delta T = T - T_C = 5$ K and $Y = 1 \times 10^5$ Wm^{-2}K^{-1} is the thermal boundary conductance between the Nb and the SiO_2 substrate [18]. The base electrode area A is approximated as $y\ell_t = 0.73 \times 2.7$ μm^2. This leads to $P_{max} \sim 1$ μW, in agreement with the measured value above. For this application, the small electrode area of the FIB devices causes difficulties in removing the heat effectively. However the relatively thick Nb electrodes and thin barriers, in addition to the high $I_C R_N$ product of these films made them suitable for use in the fabrication of nanoSQUIDs, as discussed in the next section.

6.3 SQUIDs

Two junction d.c. SQUIDs can be fabricated by any reproducible junction technology. The ability to create two junctions in a relatively large loop is not surprising in itself. The results of the macroSQUID measured in section 6.3.1 were of most interest in terms of the feasibility of measuring the voltage modulation of a structure with two metallic, low $I_C R_N$ junctions. This is important in, for example, the possible measurement of π-SQUIDs (see section 9.2). On the other hand, the nanoSQUIDs discussed in section 6.3.2, are more interesting in themselves, since the possibility of creating nanoscale SQUIDs is of increasing interest for applications as detectors in the study of magnetic clusters [20]. There is increasing work concerning the fabrication of sub-micron loops by various means, (for example see [21] and references therein).

6.3.1 MacroSQUID

The SQUID design used consisted of a washer with outer dimension 2 mm and width 750 μm, directly coupled to a slit type loop with inner dimension 5 μm, as shown in figure 6.11. This design is known to have an inductance of $L = 100$ pH, and an effective magnetic area of 0.123 mm^2 [22]. For the FIB fabrication there was concern that when milling the side cuts for the second device, the Ga^+ beam would damage the first junction directly behind it. A block of Pt was deposited in the centre of the loop to prevent this from happening. Serendipitously the separation of the two tracks when viewed from $\theta = 85°$ (figure 6.12) allowed the two devices to be made without damaging one another, while at the same time the separation was not too great, so that both devices could be imaged using the depth of focus of the FIB. The Pt could therefore be removed, and both devices made without needing to re-align the chip.

The area of the pick-up loop meant that the out-of-plane magnetic field required to modulate the SQUID was relatively small. The field was applied using a few turns of wire mounted on a

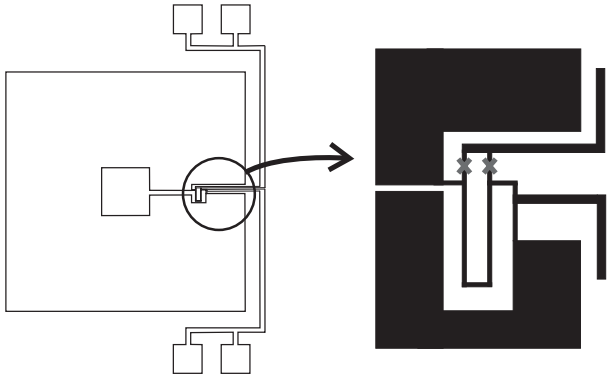

Figure 6.11: Schematic of the 2 mm washer and close-up of SQUID loop used. Junction positions are marked by crosses on the right-hand figure.

plastic screw suspended above the sample. For this reason the field calibration was not known, but can be calculated from the period of the $I_C(H)$ response, and the known effective magnetic area. The conversion factor between I_{coil} and the applied flux density is found to be 0.222 ± 0.004 nT/μA. A Nb/CuNi/Nb trilayer with $d_{\mathrm{CuNi}} \sim 8$ nm was used for the SQUID fabrication (see section 7.4.2). The I_C of the SQUID was ~ 240 μA, and the $R_N \sim 70$ mΩ. Due to the relatively low $I_C R_N$ product of these junctions, the lock-in amplifier was used to measure $\mathrm{d}V/\mathrm{d}I$ vs I as the current in the magnetic coil I_{coil} was varied. The $I_C(I_{coil})$ response is shown in figure 6.13.

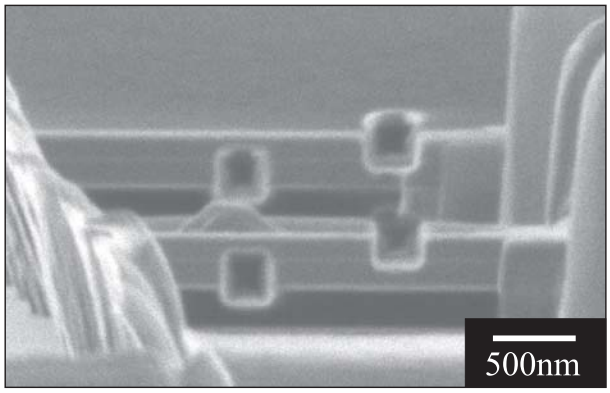

Figure 6.12: FIB image from $\theta = 85°$ showing the two devices in the SQUID loop.

The I_C was extracted directly from the $\mathrm{d}V/\mathrm{d}I$ measurement using various resistance criterions as shown. The asymmetry of the peaks is associated with the design of the SQUID mask, as well as some inevitable differences between the I_Cs of the two junctions [23]. The $\mathrm{d}V/\mathrm{d}I$ vs I curves were integrated using Simpson's rule, and the $\Delta V(I_{coil})$ extracted from the resulting $I - V$s for varying bias currents above I_C. The maximum modulation of ~ 10 nV occurs for a bias current of 253 μA ≈ 1.05 I_C. Given an inductance of 100 pH, the parameter $\beta_L \sim 36$. This is consistent with the relatively small modulation depth ΔI_C observed in figure 6.13, (see section 3.5.2).

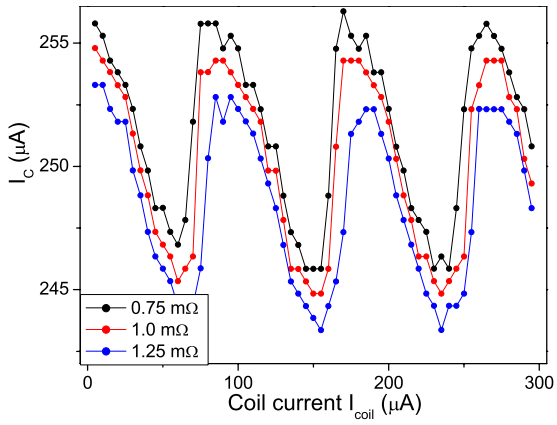

Figure 6.13: Modulation of the SQUID I_C vs I_{coil} for various resistance criterions. Lines are a guide to the eye.

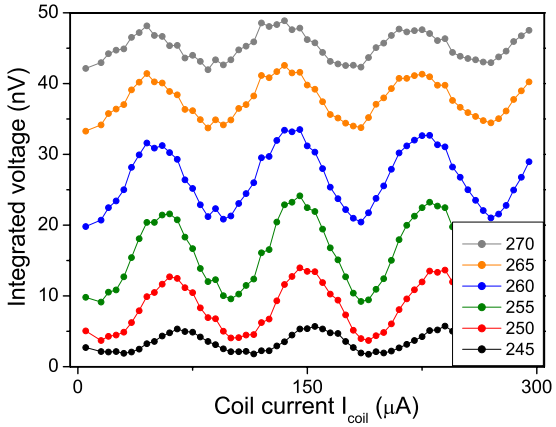

Figure 6.14: Corresponding voltage modulation for the results from figure 6.13 using various values of current bias (μA).

6.3.2 NanoSQUIDs

As Kim *et al* have previously shown [24], a SQUID with a sub-micron area loop can be created by milling a third side cut through the centre of the junction. This is shown schematically in figure 6.15. A FIB image is shown in figure 6.16. In the work of Kim *et al* the dimensions of the device were all relatively large: the Bi-2212 whisker was several microns thick, the loop x dimension was ~ 8 μm, and the junction y dimension was 1.5 μm. The SQUIDs showed a poor $I_C(H)$ modulation. In the present work smaller loop areas were fabricated.

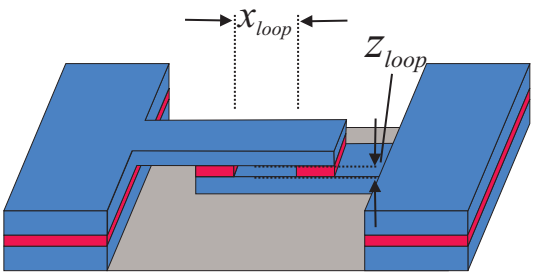

Figure 6.15: Idealised picture of the finished d.c. nanoSQUID, with loop dimensions x_{loop} and z_{loop}.

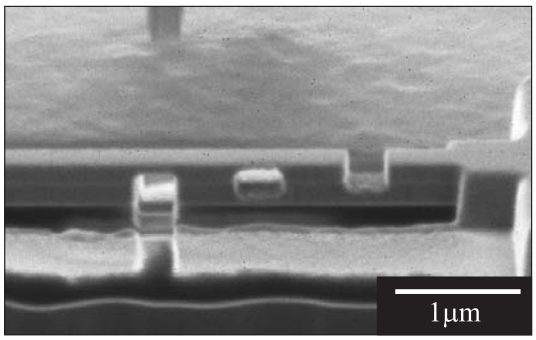

Figure 6.16: FIB image from $\theta = 65°$ of a Nb/CuNi/Nb nanoSQUID.

In section 6.3.1, not only were the junction areas $\ll$ the area of the SQUID pick-up loop, but also the applied field was out-of-plane, and therefore there was no change of the junction I_Cs due to the usual Fraunhofer modulation. For the nanoSQUIDs, the finite size of the junction with respect of the loop must be considered. In terms of the analogy with the diffraction of light, there are two δ-functions convoluted with a top hat in Fourier space. This corresponds to

a Fraunhofer single junction $I_C(H)$ *multiplied* by a cosine SQUID modulation:

$$I_C(\Phi_{ex}) = 2I_J \left| \cos\left(\frac{\pi\Phi_s}{\Phi_0}\right) \left[\frac{\sin(\pi\Phi_J/\Phi_0)}{\pi\Phi_J/\Phi_0}\right] \right| , \tag{6.2}$$

where Φ_J is the flux that passes through each of the junctions, and Φ_s is the flux linking the SQUID loop, (the junction I_Cs are assumed identical - see section 3.5.2).

6.3.2.1 CuNi barrier

The Nb / CuNi(8 nm) / Nb trilayer as used in section 6.3.1, was used to create the first nanoSQUIDs. The good contrast between the Nb and CuNi allowed good control over the positioning of the third side cut to create the loop. The $I_C(H)$ response of one device, (loop area 475 × 180 nm^2 and junction x dimensions 420 nm and 350 nm) is shown in figure 6.17. Despite the clear periodicity in the response, the $I_C(H)$ cannot be satisfactory fitted using equation 6.2, (the peaks near ±30 mT being the most obvious anomaly). This may be due in part to the additional unclear nature of the CuNi barriers themselves, and the fact that stray flux from the junctions may be feeding into the SQUID loop. Due to the size of the loop the applied fields required to modulate the SQUID are large enough to move the magnetic moment in the barrier, and change the flux in the SQUID. The other $I_C(H)$ shown in figure 6.18

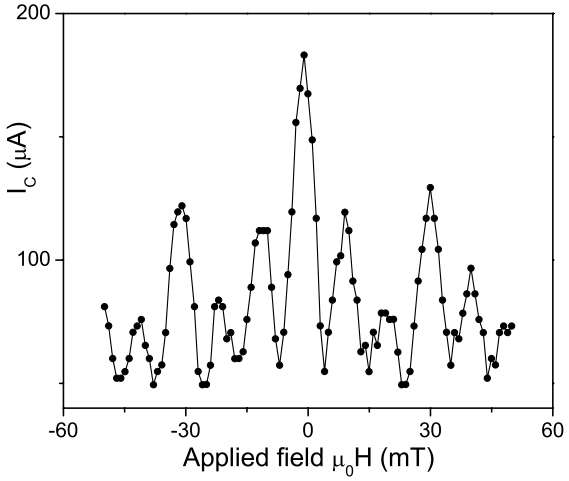

Figure 6.17: $I_C(H)$ for a Nb/CuNi/Nb nanoSQUID at 4.2 K, with $H \perp x$.

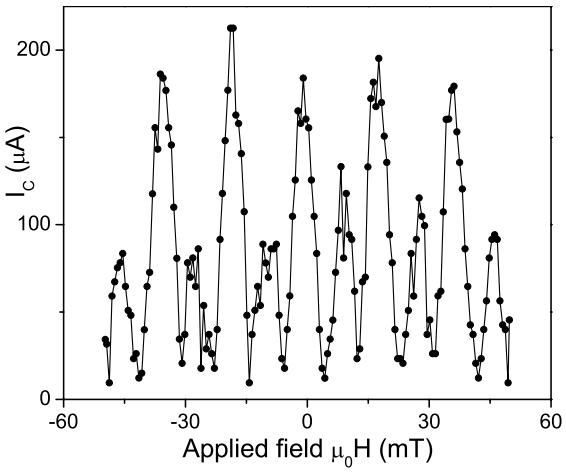

Figure 6.18: 'Beating' $I_C(H)$ for a Nb/CuNi/Nb nanoSQUID at 4.2 K, with $H \perp x$.

shows a similar periodic and distorted behaviour. In this case however, the 'beating' pattern is reminiscent of two combined SQUID modulations with different periods (see for example [25]). This may be caused by significant inhomogeneities or resputtered shorting on one or both of the single junctions. This would transform a single junction into a second SQUID, in addition to the nanoSQUID loop. This is quite possible due to the relatively small size of the SQUID loop - meaning that aspect ratio problems would tend to increase the amount of resputtering.

6.3.2.2 $MoSi_2$ barrier

To avoid the added complication of the ferromagnetic CuNi barriers, the Nb/$MoSi_2$/Nb devices discussed in section 6.2 were also used to fabricate nanoSQUIDs. The $I_C(H)$ shown in figure 6.19 was fabricated with 370×270 nm^2 loop, with $x = 220$ nm and 120 nm for the two junctions. This shows a much clearer SQUID modulation and Fraunhofer envelope function. Figure 6.20 shows the slight anti-symmetric nature of the pattern.

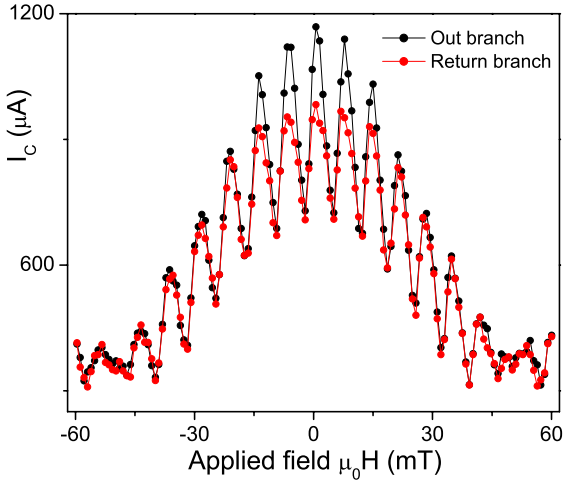

Figure 6.19: $I_C(H)$ for hysteretic $I - V$ of a Nb/$MoSi_2$/Nb nanoSQUID at 4.2 K. Applied field $H \perp x$. Lines are guides to the eye.

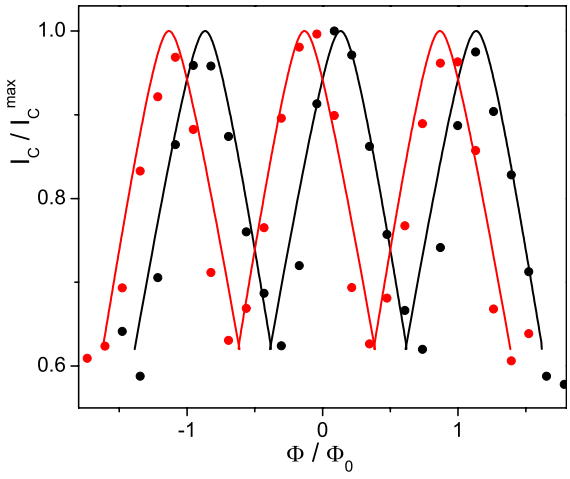

Figure 6.20: Low field $|I_C(H)|$ of figure 6.19, for both $I_C > 0$ (black) and $I_C < 0$ (red). Lines are the corresponding theoretical fits (see text).

The theoretical fit in figure 6.20 uses the most general numerical solution discussed in section 3.5.2: a non-negligible loop inductance L, and different single junction I_Cs. The two values of I_{C1} and I_{C2} are calculated using a simple potential divider:

$$I_{Ci} = \frac{x_i I_C^{\max}}{x_1 + x_2} \quad ; \quad i = 1, 2 \, . \tag{6.3}$$

x_1 and x_2 are the junction dimensions measured in the FIB. The only unknowns in the model are the inductances L_1 and L_2. The total inductance $L = L_1 + L_2$ is used as the fitting parameter to match the modulation depth of the $I_C(H)$ data. It is then important to decide how the values of L_1 and L_2 depend on the asymmetry of the device. In the limit of a large loop area compared to the single junction stacks, the difference between L_1 and L_2 due to the different values of junction dimensions x_1 and x_2 is negligible, and $L_1 = L_2$ can be assumed. When the junctions and loop are of comparable dimensions, a simple model is used, which assumes that the inductances scale in the same way as the I_Cs, leading to

$$L_i = \frac{x_i L}{x_1 + x_2} \, , \tag{6.4}$$

analogous to equation 6.3. In the case of figure 6.20, the latter limit is used. A total inductance $L = 2.6$ pH was found to fit the modulation depth of the SQUID, as shown in figure 6.20.

The values of x_1 and x_2 had to be changed to 150 nm and 180 nm (from 120 nm and 220 nm respectively), to obtain the best fit. However this variation is acceptable due to the error of the FIB measurement.

In order that many periods of the $I_C(H)$ could be measured with the copper coil of the dip probe at 4.2 K, the central loop of another SQUID was made relatively large. This device had loop dimensions of $x_{\text{loop}} = 1380$ nm and $z_{\text{loop}} = 390$ nm. The junction x values were 245 nm and 220 nm. Figure 6.21 shows the $I_C(H)$ response for an applied field $H \perp x$. The SQUID $I - V$ was hysteretic up to a field of about 25 mT, however figure 6.21 shows the out branch I_C only for clarity. A SQUID modulation with a period of 2.25 mT is observed. The re-entrance of the Fraunhofer envelope is clear. The first Fraunhofer minima is at 42 ± 1 mT. The relatively small difference between the junction dimensions (within the experimental error of the FIB measurement), is consistent with the lack of asymmetry in the $I_C(H)$, as shown in the low field detail in figure 6.22. The theoretical fits shown in figure 6.22 used $x_1 = x_2 = 230$

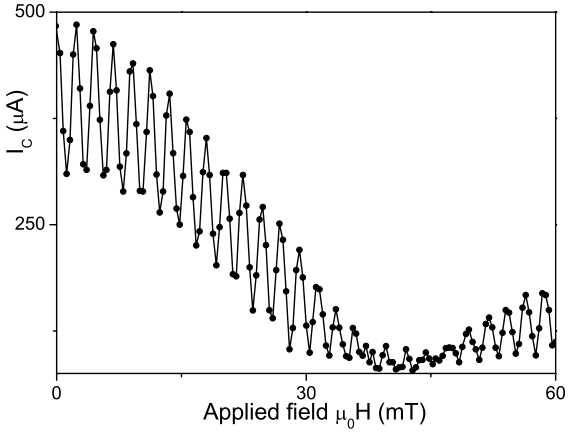

Figure 6.21: Out branch $I_C(H)$ for a Nb/$MoSI_2$/Nb nanoSQUID at 4.2 K with loop area 1380×390 nm^2. Applied field $H \perp x$. Lines are a guide to the eye.

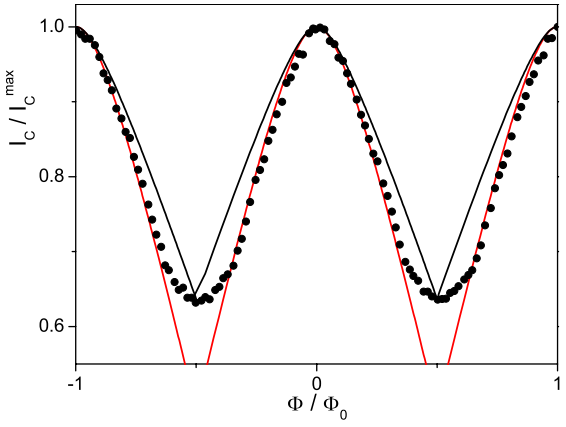

Figure 6.22: Low field $I_C(H)$ of figure 6.21 with theoretical fits for $L = 4$ pH (red) and 7 pH (black).

nm. As can be seen from the fitting, the modulation depth can be fitted using a value of $L = 7$ pH, but with poor agreement with the shape of the data. Whereas the $L = 4$ pH fit gives good agreement for $0.7 < I_C/I_C^{\max} < 1$, but predicts a smaller $I_C^{\min}$ than is observed. Given that the loop area for this device was a factor of five larger than the previously discussed nanoSQUID, which was fitted with $L = 2.6$ pH, the larger value of L for this loop would seem to be more acceptable. The model used has assumed flux quantisation, which may not be the case for the largest loop, for which the Nb above and below the SQUID loop is of the order of $100 - 150$ nm thick: in this case it may not be possible to draw an integration contour along which the supercurrent density $\mathbf{J} = 0$.

For both of the devices described above, a single value of the penetration depth $\lambda = 105 \pm 10$ nm could be used to fit both the Fraunhofer and SQUID modulation periods using equation 6.2, when the device dimensions measured in the FIB were used. This simple fit for λ also neglects the finite size of the devices, (see section 3.1.4). Using equation 3.10, a corrected value

of $\lambda = 40 \pm 5$ nm is obtained, which is consistent with other measurements (section 8.3).

By biasing the nanoSQUID of figure 6.21 at various currents, the voltage modulation against applied field was also found. This modulation using three different bias currents is shown in figure 6.23. The maximum peak-to-peak voltage modulation was ~ 24 μV.

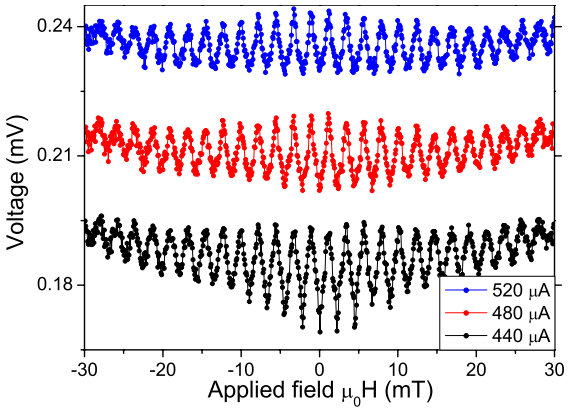

Figure 6.23: Voltage modulation as a function of applied field at different bias for $I_C(H)$ in figure 6.21.

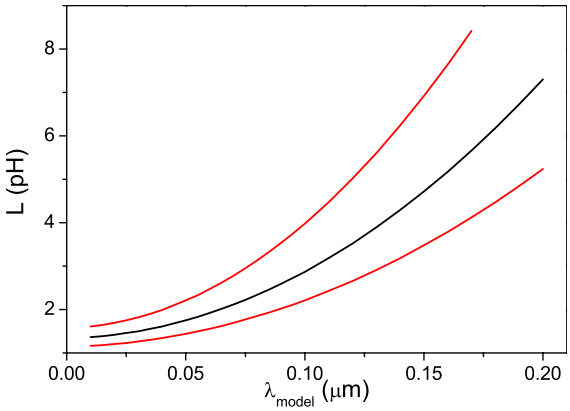

Figure 6.24: Inductance vs λ for the nanoSQUID of figure 6.21, using 3dmlsi software. Red lines above and below are extremal values assuming ± 50 nm error on each junction and loop dimension measured by the FIB.

6.3.2.3 Modelling of inductances

The 3dmlsi finite element software was used to independently find the inductance of the nanoSQUID loops discussed above [26]. The larger of the two nanoSQUIDs above was modelled. The junctions were ignored, and the whole nanoSQUID treated as a single superconducting loop. The program split the loop into triangular elements, using typically ~ 460 boundary elements, which enabled the calculations to be carried out relatively quickly.

As can be seen from figure 6.24, the calculated range of L (using a reasonable error window of the FIB dimensions) gives a lower predicted inductance than found via the $I_C(H)$ fitting, but the agreement is acceptable, given that one of the assumptions of program is that the lateral dimensions of the structures are all large compared to the film thicknesses, which is not the case in this work.

6.4 Gallium nitride LEDs

There is much interest in GaN and related materials, due to the potential uses in blue/green light emitting diodes, lasers, and solid state lighting [27]. There are many problems associated with the processing of these materials due to their inert chemical nature and strong bond energies [28]. The relatively high work function of p-type GaN:Mg also hinders the production of good Ohmic / low resistance metal wiring contacts [29, 30]. This is a drawback for spreading layer contacts above light emitting diodes.

FIBs are being increasing used in all aspects of the semiconductor industry. They have been used to implant and intermix dopants to create microelectronic and optoelectronic devices both during [31, 32] and after [33, 34] film deposition. The smoothness of mirror facets for GaN laser diodes can be improved by FIB cleaning [35, 36]. Small apertures for optical recording heads [37] have been produced. Heterostructure field effect transistor pillars as small as 20 nm have also been fabricated in bilayers of GaN/AlGaN, [38] with reasonable photoluminescence properties. The properties of generic FIB patterning of GaN have be studied in references [39, 40].

In reference to the present work, there is interest in the polarisation of light emitting devices with high aspect ratio, and dimensions $\leq$ wavelength of light, [41, 42]. The changing properties of nanoscale diodes has also been theoretically investigated [43], and the potential to investigate LED structures small enough to contain a small number, or no dislocations is also of interest [44]. With the present FIB technique submicron junction areas are obtainable. The specific contact resistance of such junctions should not be as large as an identically conventionally patterned mesa structure, due to the remaining overhanging p-type material, which is not present in the mesa structure.

6.4.1 Film preparation

A schematic cross section of the heterostructure is shown in figure 6.25 (a). The films were prepared[4] on c-plane sapphire in a close coupled showerhead metal organic chemical vapour deposition reactor at $\sim$ 13 kPa between $710 - 800$ °C. This process has been found to create high quality quantum well heterostructure films. The wavelength of the light emitted can be controlled by the temperature of the quantum well growth. A wavelength in the range $\lambda = 400 - 600$ nm is possible, with a spread of $\sim$ 2 nm over a two inch wafer [45].

For the devices fabricated, the n and p-type thicknesses were 1600 nm and 200 nm respectively, (there was also a 500 nm thick undoped GaN buffer layer beneath the n-type layer). The quantum wells structure was five repeats of a 10 nm thick InGaN/GaN bilayer. A layer of $\sim$ 200 nm thick Au, or Ni/Au was *ex-situ* sputter deposited onto the film before the broad beam Ar^+ ion milling, (as can be seen in the FIB image of a device in figure 6.25 (b)). This enabled wirebonds to be made to the chip. For the image shown in figure 6.27 however, a 20 μm wide region in the centre of the chip was not covered with Au, to allow the light produced to be easily visible from above.

6.4.2 Results

The CPP devices fabricated in the FIB were measured with a lock-in amplifier, and integrated to obtain the $I-V$ characteristic, as shown in figure 6.26. A clear diode response is observed. In contrast to the superconducting devices, it is important to note that the four-point measurement of the $I-V$ contains a series resistance due to the distance of the device from the voltage leads in the mask design (figure 4.6 (b)). A series resistance of 23.5 MΩ has been subtracted from the $I-V$ in figure 6.26. A van der Pauw measurement of an unpatterned film at 295 K gave

[4] By M. J. Kappers.

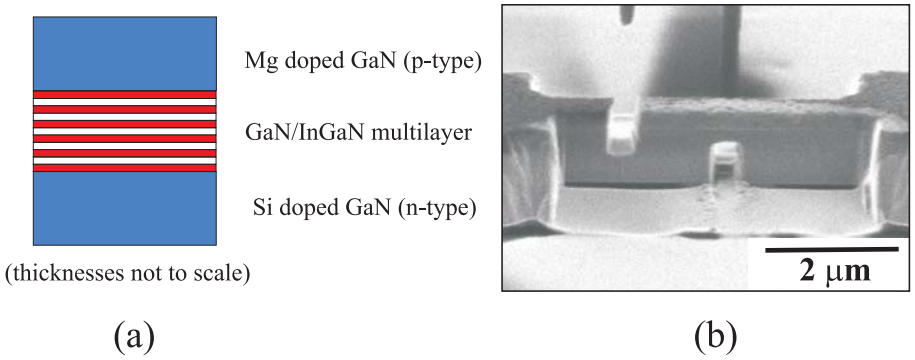

Figure 6.25: (a) GaN LED film cross section (thicknesses not to scale). (b) FIB image of GaN LED device from $\theta = 65°$. The darker surface layer is *ex-situ* deposited Au.

a value of the resistivity / thickness ratio $\rho/d \sim 2 \times 10^6$ Ω. Assuming a total film thickness of $\sim$ 1800 nm, (neglecting the undoped GaN layer), with track lateral dimensions of 25 μm and 4 μm, the resistance is calculated to be $\sim$ 12 MΩ, which is of the correct order of magnitude. When the extra resistance due to the narrowed sections around the device is estimated, it is found to be of the same order as the 12 MΩ above. The value of the linear subtraction is therefore justifiable, however without accurate modelling, it is difficult to fit the value of 23.5 MΩ perfectly. A possible solution to the problem of the series resistance would be to use the cross geometry discussed in section 9.3, but this was not attempted in these devices. When

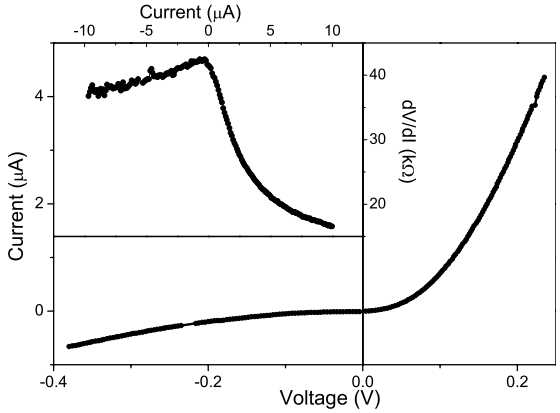

Figure 6.26: GaN $I-V$ after linear subtraction of a series resistance. Inset: Differential resistance output from the lockin amplifier.

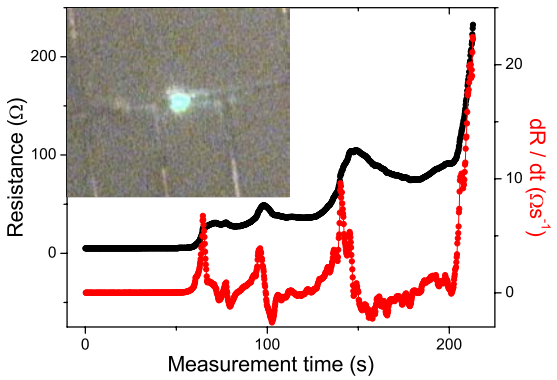

Figure 6.27: *In-situ* $R(t)$ and $\mathrm{d}R/\mathrm{d}t$ of a metal/GaN heterostructure. Inset: glowing GaN LED viewed in an optical microscope with 50 V applied.

biased at room temperature under an optical microscope a blue/green light is seen from the device area (inset figure 6.27), confirming that CPP current flow was occurring. It is clear that the FIB processing has not destroyed the quantum well structure. The relatively high resistance of the device, and the difficulties of obtaining enough light to be visible at the magnification shown meant that 50 V had to be applied to the device, (the current was of the order of several mA). The large resistance of the tracks (see above) would seem to rule out a significant voltage

drop across the quantum wells in this case, and does not explain how the light can be produced. However this argument assumes the series resistance is voltage independent. This will not be true, since significant heating will occur in the tracks, reducing the series resistance at 50 V, and increasing the voltage dropped across the quantum wells. Many devices were destroyed during the process of taking these images. Attempts were also made to try to record the spectrum of the light using an optical spectrometer. Unfortunately this was not possible due to difficulties in focusing the emitted light into the spectrometer's probe.

6.4.3 Fabrication problems

As discussed in section 5.2, the FIB processing typically requires each electrode thickness to be $\geq$ 150 nm. However in the GaN case, the different doped GaN layers and the quantum wells do not show strong contrast in the FIB. Despite knowing the layer thicknesses this did add a greater margin of error to the side cuts, particularly in the case of the thinner p-type (top) electrode. This was made worse since the devices were made relatively large (both y and $x \geq 700$ nm), in order to be visible under the optical microscope. This increase in milling time gave a larger error in the cuts due to beam and stage drift. A more conservative 500 nm thick layer would allow more margin of error to ensure that the wells are isolated. The *in-situ* resistance measurement (section 4.3.2.1) was used to calibrate the thicknesses and milling rates of the p and n-type. Figure 6.27 shows the $R(t)$ measured while a multilayer of Au/Ni/p-type GaN/quantum wells/n-type GaN/undoped GaN/sapphire was milled through with an 11 pA beam. The individual layers can be distinguished by the bumps in the $R(t)$ and peaks in the $\mathrm{d}R/\mathrm{d}t$. In this way calibrated cuts from $\theta = 0°$ could be viewed from $\theta = 85°$ to give a more accurate guide to the position of the quantum wells.

The overhanging p-type bridge was frequently destroyed by excessive current density. This problem can be reduced by using a relatively thick electrode. Metallisation above the p-type layer can also be used: this will introduce some contact resistance and also reduce the amount of light visible from above the device. As a compromise the FIB was used to deposit a block of Pt 1 μm thick, over an area $\sim 1 \times 1$ $\mu\mathrm{m}^2$ over a region of the track, before any milling had taken place. After thinning and cleaning, the undercut hole was made directly below the Pt block. This Pt provides physical support for the overhanging bridge of p-type material, as well as acting as a heat sink for Joule heating in the thinned region, but without the disadvantage of covering over the active region of light emission with metallisation. This technique was used in fabrication of the glowing device shown in the inset of figure 6.27.

References

[1] P. A. Warburton, A. R. Kuzhakhmetov, C. Bell, G. Burnell, M. G. Blamire, H. Wu, C. R. M. Grovenor, and H. Schneidewind, IEEE Trans. Appl. Supercond. **13**, 821 (2003).

[2] H. L. Dewing, B. Guttler, A. Mukherjee, I. A. Troian, L. Y. Su, J. D. O'Connor, S. M. Morley, C. R. M. Grovenor, and M. J. Goringe, Physica C **235**, 719 (1994).

[3] O. S. Chana, A. R. Kuzhakhmetov, D. M. C. Hyland, C. J. Eastell, D. Dew-Hughes, C. R. M. Grovenor, Y. Koval, M. Mößle, R. Kleiner, P. Müller, and P. A. Warburton, IEEE Trans. Appl. Supercond. **11**, 2711 (2001).

[4] O. S. Chana, A. R. Kuzhakhmetov, P. A. Warburton, D. M. C. Hyland, D. Dew-Hughes, C. R. M. Grovenor, R. J. Kinsey, G. Burnell, W. E. Booij, M. G. Blamire, R. Kleiner, and P. Müller, Appl. Phys. Lett. **76**, 3603 (2000).

[5] P. A. Warburton, O. S. Chana, A. R. Kuzhakhmetov, D. M. C. Hyland, D. Dew-Hughes, C. R. M. Grovenor, Y. Koval, and P. Müller, IEEE Trans. Appl. Supercond. **11**, 300 (2001).

[6] P. A. Warburton, A. R. Kuzhakhmetov, G. Burnell, M. G. Blamire, and H. Schneidewind, Phys. Rev. B **67**, 184513 (2003).

[7] A. R. Kuzhakhmetov, (personal communication).

[8] I. Takeuchi, J. Tsai, Y. Shimakawa, T. Manako, and Y. Kubo, Physica C **158**, 83 (1989).

[9] J. Moreland, D. S. Ginley, E. L. Venturini, and B. Morosin, Appl. Phys. Lett. **55**, 1463 (1989).

[10] S.-J. Kim, Y. I. Latyshev, and T. Yamashita, **74**, 1156 (1999).

[11] K. Schlenga, R. Kleiner, G. Hechtfischer, M. Mößle, S. Schmitt, P. Müller, C. Helm, C. Preis, F. Forsthofer, J. Keller, H. L. Johnson, M. Veith, and E. Steinbeiß, Phys. Rev. B **57**, 14518 (1998).

[12] T. van Duzer and C. W. Turner, *Principles of Superconductive Devices and Circuits, (Second Edition)* (Prentice Hall PTR, 1999).

[13] A. A. Tsvetkov, D. Dulić, D. van der Marel, A. Damascelli, G. A. Kaijushnaia, J. I. Gorina, N. N. Senturina, N. N. Kolesnikov, Z. F. Ren, J. H. Wang, A. A. Menovsky, and T. T. M. Palstra, Phys. Rev. B **60**, 13196 (1999).

[14] D. Dulić, D. van der Marel, A. A. Tsvetkov, W. N. Hardy, Z. F. Ren, J. H. Wang, and B. A. Willemsen, Phys. Rev. B **60**, R15051 (1999).

[15] C. A. Hamilton, IEEE Trans. Appl. Supercond. **7**, 3759 (1997).

[16] P. D. Dresselhaus, Y. Chong, J. H. Plantenberg, and S. P. Benz, IEEE Trans. Appl. Supercond. **13**, 930 (2003).

[17] Y. Chong, P. Dresselhaus, S. Benz, and J. Bonevich, Appl. Phys. Lett. **82**, 2467 (2003).

[18] Y. Chong, P. D. Dresselhaus, and S. P. Benz, Appl. Phys. Lett. **83**, 1794 (2003).

[19] Y. Chong, (personal communication).

[20] J. Gallop, P. W. Josephs-Franks, J. Davies, L. Hao, and J. Macfarlane, Physica C **368**, 109 (2002).

[21] V. Bouchiat, M. Faucher, C. Thirion, W. Wernsdorfer, T. Fournier, and B. Pannetier, Appl. Phys. Lett. **79**, 123 (2001).

[22] F. Kahlmann, W. E. Booij, M. G. Blamire, P. F. McBrien, N. H. Peng, C. Jeynes, E. J. Romans, C. M. Pegrum, and E. J. Tarte, IEEE Trans. Appl. Supercond. **11**, 916 (2001).
[23] G. Burnell, D.-J. Kang, D. A. Ansell, H. N. Lee, S. H. Moon, E. J. Tarte, and M. G. Blamire, Appl. Phys. Lett. **81**, 102 (2002).
[24] S.-J. Kim, J. Chen, K. Nakajima, T. Yamashita, S. Takahashi, and T. Hatano, J. Appl. Phys. **91**, 8495 (2002).
[25] V. V. Ryazanov, V. A. Oboznov, A. V. Veretennikov, and A. Y. Rusanov, Phys. Rev. B **65**, 020501(R) (2001).
[26] M. Khapaev and E. Goldobin, *3D-MLSI: The program for extraction of 3D inductances of multilayer superconductor circuits, Version 1.5* (2001).
[27] A. Žukauskas, M. S. Shur, and R. Gaska, October MRS Bulletin p. 765 (2001).
[28] S. J. Pearton, R. J. Shul, and F. Ren, MRS Internet J. Nitride Semicond. Res. **5**, 11 (2000).
[29] J.-K. Ho, C.-S. Jong, C. C. Chiu, C.-N. Huang, C.-Y. Chen, and K.-K. Shih, Appl. Phys. Lett. **74**, 1275 (1999).
[30] A. P. Zhang, B. Luo, J. W. Johnson, and F. Ren, Appl. Phys. Lett. **79**, 3636 (2001).
[31] S. Vijendran, P. J. A. Sazio, H. E. Beere, G. A. C. Jones, D. A. Ritchie, and C. E. Norman, J. Vac. Sci. Technol. B **17**, 3226 (1999).
[32] H. König, N. Mais, E. Höfling, J. P. Reithmaier, A. Forchel, H. Müssig, and H. Brugger, J. Vac. Sci. Technol. B **16**, 2562 (1998).
[33] Y. Hirayama, Appl. Phys. Lett. **61**, 1667 (1992).
[34] S. Nakata, Phy. Rev. B **46**, 13326 (1992).
[35] T. Ito, H. Ishikawa, T. Egawa, T. Jimbo, and M. Umeno, Jpn. J. Appl. Phys. Part 1 **36**, 7710 (1997).
[36] H. Katoh, T. Takeuchi, C. Anbe, R. Mizumotos, S. Yamaguchi, C. Weitzel, H. Amano, I. Akasaki, Y. Kaneko, and N. Yamado, Jpn. J. Appl. Phys. **36**, L444 (1998).
[37] F. Chen, J. Zhai, D. D. Stancil, and T. E. Schlesinger, Jpn. J. Appl. Phys. **40**, 1794 (2001).
[38] M. Kuball, M. Benyoucef, F. H. Morrissey, and C. T. Foxon, MRS Internet J. Nitride Semicond. Res. **5S1**, W12.3 (2000).
[39] I. Chyr, B. Lee, L. C. Chao, and A. J. Steckl, J. Vac. Sci. Technol. B **17**, 3063 (1999).
[40] A. J. Steckl and I. Chyr, J. Vac. Sci. Technol. B **17**, 362 (1999).
[41] J. Hu, L.-S. Li, W. Lang, L. Manna, L.-W. Wang, and A. P. Alivisatos, Science **292**, 2060 (2001).
[42] M. S. Gudiksen, L. J. Lauhon, J. Wang, D. C. Smith, and C. M. Lieber, Nature **415**, 617 (2002).
[43] G. D. J. Smit, S. Rogge, and T. M. Kalpwijk, Microelect. Eng. **64**, 429 (2002).
[44] S. Nakamura, Science **281**, 956 (1998), and references therein.
[45] E. J. Thrush, M. J. Kappers, P. Dawson, M. E. Vickers, J. Barnard, D. Graham, G. Makaronidis, F. D. G. Rayment, L. Considine, and C. J. Humphreys, J. Cryst. Growth **248**, 518 (2003), and references therein.

Chapter 7

Single barrier Josephson junctions

The results for S/F bilayer junctions, S/N/S, S/I/S, and S/F/S CPP devices are discussed. The issues related to the FIB fabrication procedure are highlighted for each case.

7.1 F/S bilayers

7.1.1 Planar junction characteristics

As described in section 4.3.2, variable thickness bridges can be formed by milling a 50 nm trench across a micron scale track of an N/S bilayer. This technique was used on a Cu_xNi_{1-x}/Nb bilayer with $d_{Nb} = 120$ nm and $d_F \sim 50$ nm. x was in the range $0 \leq x \leq 0.7$. The CuNi alloy was formed by depositing a fine multilayer of Cu/Ni with individual layer thicknesses < 1 nm. After FIB processing Josephson junction $I-V$s were obtained, which showed Shapiro steps at the appropriate voltages with applied microwaves (figure 7.1). As with the N/S case [1] the *in-situ* resistance measurement gave control over the depth of cut in the FIB: the resistance change ΔR correlated with I_C per unit width of junction, (inset figure 7.1).

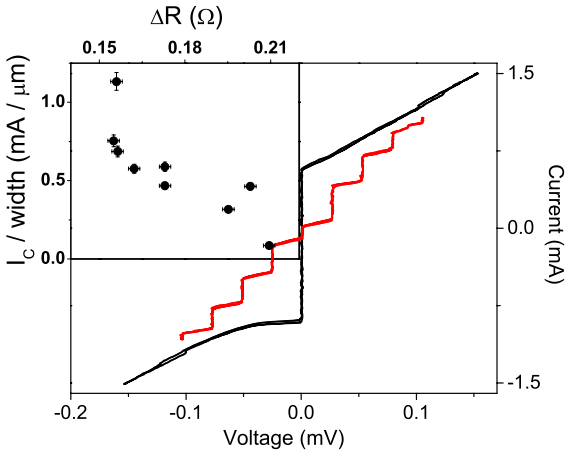

Figure 7.1: $I-V$ (black) and with 13.69 GHz microwaves (red) at 4.2 K for a Ni/Nb junction with $d_F = 50$ nm. Inset: Scaling of I_C normalised to track width with *in-situ* resistance change ΔR.

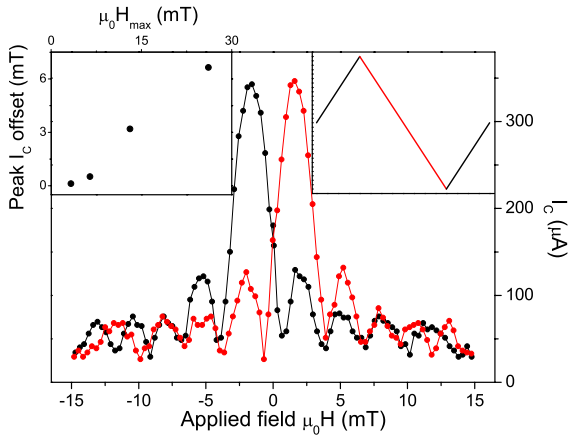

Figure 7.2: $I_C(H)$ for a Cu/Nb junction at 4.2 K. Left inset: Scaling of I_C offset with H_{max}. Right inset: Colour code for direction of field sweep.

The $I_C(H)$ (H applied perpendicular to plane), was hysteretic and in many cases heavily distorted from the ideal Fraunhofer pattern. The period of the ideal Fraunhofer is increased relative to that predicted by equation 3.8 due to the 'flux focusing' effect of the electrodes in the planar geometry [2]. The hysteresis of the $I_C(H)$ is not directly related to any flux threading the junction due to the F layer - since it is also observed in N/S bilayer junctions (figure 7.2). Such behaviour has also been seen in plane Nb tracks [3], HTS grain boundary junctions [4], and bulk samples [5]. From these other works a simple interpretation of the behaviour can be built up by examining the flux fed into the junction by screening currents set up in response to vortices near the junction. The hysteretic motion of these vortices is reflected in the $I_C(H)$ observed. The more vortices near the junction, the larger the hysteresis. Due to this, the offset of the peak I_C from zero field increases with the maximum applied field, H_{max}, (left inset of figure 7.2), as seen in other planar devices [6].

In the F/S case, the vortex entry into the track and the pinning will be strongly affected by the F layer [7]. Domain structures in the F layer may also contribute to the flux in the junction

causing non-uniform current flow, and the distorted $I_C(H)$. However no significant changes in the behaviour occurred with the composition of Cu/Ni underlayer - this is presumably since the majority of the supercurrent was carried by the remaining Nb in the trench.

7.1.2 Limits of the planar technique

The calibration of the FIB cuts showed that there was always Nb present at the bottom of the junction trenches in working devices. The junctions are not truly S/F/S. Following the discussions of section 3.2 a barrier length ≤ 20 nm is required in the dirty limit, even for weak ferromagnetic barriers. This is difficult to achieve in a 120 nm thick Nb film due to the aspect ratio of the cut. Even for thinner Nb layers the spot size of the FIB sets a more fundamental limit (section 4.3.1). The reproducibility and uniformity of the trenches is not good enough to enable control over junction widths < 50 nm. These limitations motivated the trilayer fabrication technique developed in chapter 5. The barrier thickness is then set by d_F, the film thickness, which can be controlled to < 1 nm.

7.2 Trilayer S/N/S junctions

7.2.1 Device fabrication

Trilayer Nb/Mo/Nb (S/N/S) junctions were the first junctions fabricated using the three dimensional FIB technique discussed in chapter 5. The barrier thickness was in the range 150 nm$< d_{\mathrm{Mo}} <$ 250 nm, and both S layers had $d_{\mathrm{Nb}} = 150$ nm. As previously discussed, Pt was deposited on top of these devices to serve as mechanical support for the Nb above the undercut. This was later found to be unnecessary.

7.2.2 $I-V$ characteristics

The junctions showed RSJ-like $I-V$ characteristics, and Shapiro steps when microwaves were applied, (inset figure 7.3). The $I_C R_N$ scaling with d_{Mo} (figure 7.4) shows the expected increase for thinner Mo barriers for $d_N > 150$ nm, but the thinnest samples showed a depressed $I_C R_N$. Similarly the resistivity of the Mo calculated using the high bias R_N were consistent for larger d_{Mo}, but showed more scatter for thinner barriers. A significant proportion of the error in the latter case was associated with the measurement of the junction area. An error ± 30 nm becomes very significant for the thinnest barriers, where the area was generally smaller, so that the I_C is small enough to be measurable. The anomalous values of ρ_{Mo} and $I_C R_N$ for $d_{\mathrm{Mo}} \sim 150$ nm may hint at different barrier properties for this film. This possibility was not investigated further. The quadratic behaviour of $I_C(T)$ (figure 7.3) implies 'soft' boundary conditions - i.e. the gap Δ_s near the Nb/Mo interface is suppressed from the bulk Nb value [8].

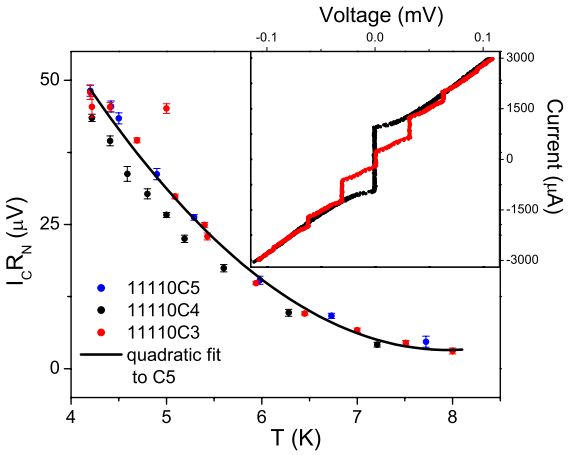

Figure 7.3: $I_C R_N(T)$ for a several devices with $d_{\mathrm{Mo}} \sim 250$ nm, with a quadratic fit to one plot. Inset: Device 11110C4 $I-V$ and with 15.21 GHz microwaves (red).

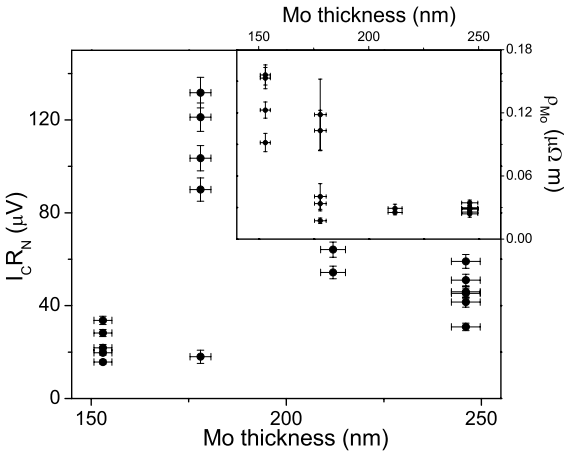

Figure 7.4: $I_C R_N(d_{\mathrm{Mo}})$ for a series of trilayer Nb/Mo/Nb devices. Inset: ρ_{Mo} vs d_{Mo} extracted from the junction R_N.

7.2.3 Behaviour with applied magnetic field

The magnetic field was applied in-plane, perpendicular to either the x and y dimensions, (see figure 5.5 for dimension convention). Since the fabrication technique requires $y < 500$ nm for the film thicknesses used, whereas the x dimension was as large as 5 μm, multiple peaks in the $I_C(H)$ were mostly observed when $H \perp x$ (figure 7.5). The agreement with the best fit Fraunhofer in figure 7.5 is good, indicating a uniform current flow. The fit used a value of $\lambda = 25 \pm 5$ nm, which is slightly smaller than that obtained via other devices. By varying the junction dimension x and measuring the position of the first minima in the $I_C(H)$ with $H \perp x$ (inset figure 7.5), a $1/x$ scaling is found, as expected. Therefore the cuts made with the FIB are actually determining the magnetic area of the junction.

The higher J_C of the thinner Mo barriers enabled junctions with dimensions longer than the Josephson penetration depth λ_J, to be fabricated. These showed more triangular $I_C(H)$ behaviour with $H \perp x$ (figure 7.6) compared to more rounded response for $H \perp y$ (inset of figure 7.6). Using a value of $\lambda = 40$ nm (section 6.3.2.2), equation 3.7 can be solved to obtain $\lambda_J = 270 \pm 55$ nm. The ratio $x/\lambda_J = 6 \pm 1$. In this case the extrapolated first minima in the $I_C(H)$ occurs at $B = 2\mu_0 J_C \lambda_J$ [9]. Using $J_C = 1.4 \pm 0.5 \times 10^{10}$ Am^{-2}, a value of $B = 9.4 \pm 2$ mT is obtained. This is in reasonable agreement to the value of 5 mT obtained from the linear fits in figure 7.6. The largest contribution to the errors in the above calculation was an estimated error of ± 40 nm in the 100 nm y dimension. Due to the difficulty of measuring such lengths in the FIB, this error may be an underestimate. The value of λ_J should therefore not be taken as accurate, although the agreement with theory is acceptable.

7.2.4 Conclusions for Mo devices

A problem of the Mo barrier was the lack of contrast with the Nb electrodes when viewed in the FIB. The cuts made in the FIB may not have sufficiently isolated the junction region in

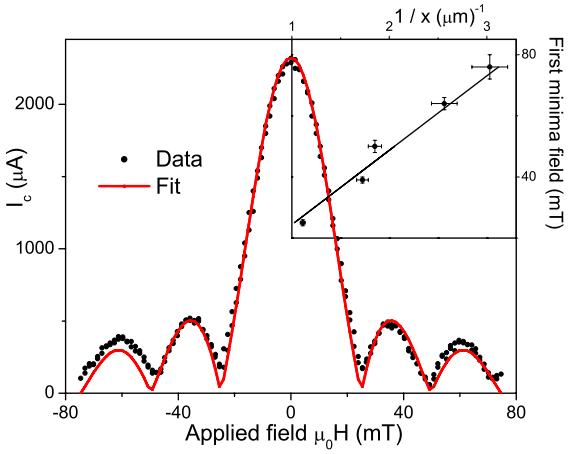

Figure 7.5: Device 11110C4 $I_C(H)$ for $H \perp x$ with $x = 890$ nm, and fit to ideal Fraunhofer, ($d_{\mathrm{Mo}} \sim 250$ nm). Inset: Position of the first minima vs junction width for several devices. Line is $1/x$ scaling.

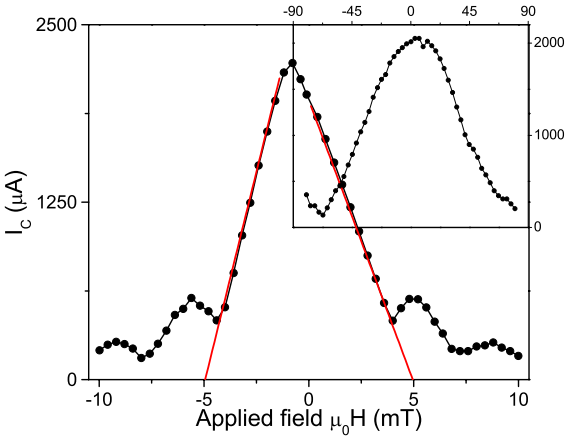

Figure 7.6: $I_C(H)$ for $d_{\mathrm{Mo}} \sim 180$ nm, with $x = 1600$ nm and $y = 100$ nm. $H \perp x$. Red lines are linear fits to the sides of the main peak. Inset: $I_C(H)$ for $H \perp y$. Black lines are a guide to the eye.

some cases. This would reduce the effective value of d_{Mo}, and explain the scatter of the $I_C R_N$ observed. In retrospect, to enable a larger error margin for the side cuts, the Nb electrodes should have been grown thicker. Also, a ~ 5 nm Cu layer for example could have been inserted at the Nb/Mo interfaces. This would not significantly change the properties of the junction, but would provide contrast for the FIB processing, to ensure the full removal of the Mo by the side cuts. Another possible problem is that the T_C of Mo may have been altered by the Ga implantation [10]: such effects have been observed with nitrogen and sulphur implantation, but the effect of Ga is unknown. This may add to the variation in the devices, but it is clear from the above results that the basic FIB technique can produce working Josephson junctions in these heterostructures.

7.3 Tunnel junctions

7.3.1 Junction deposition

The Nb/Al/AlO_x/Al/Nb junction structure was deposited in the following stages, with the Ar sputtering pressures as indicated:

- 200 nm Nb grown at 0.7 Pa
- Al with thickness in the range $5 - 20$ nm deposited at 0.7 Pa
- Oxidation: one hour at 1 kPa of pure O_2
- Pump for one hour to remove O_2
- Al with thickness in the range $5 - 20$ nm deposited at 0.96 Pa
- 200 nm Nb grown at 0.7 Pa (first ~ 5 nm at 4 Pa)

The bottom (oxidised) Al thickness will be referred to as d_{Al}. Before loading, the Al target was cleaned with a wire brush, followed by 20 minutes ultrasound in ~ 0.1 M aqueous NaOH solution to remove the oxide layer. The relatively high pressures used to grow the film immediately above the oxide layer was used to prevent damage of the barrier by the impinging atoms. This growth procedure has been used previously to form high quality S/I/S junctions [11].

7.3.2 $I-V$ characteristics

The junctions fabricated with 5 nm of Al possessed a critical current (figure 7.7). The thicker Al films showed a decrease in resistance around zero bias, (inset figure 7.8), but no measurable true supercurrent. The resistance of all of the devices increased at some 'gap' like feature, (inset of figure 7.7 and figure 7.8). The value of the 'gap' voltage as a function of T is shown in figure 7.9. A BCS theory fit to the data above 4.2 K gives $2\Delta/e = 2.68$ meV using $T_C = 9.15$ K, which is comparable to that obtained from conventionally patterned devices [11]. The 'gap' value at 4.2 K is anomalously large, and was ignored in the fitting. The reason for this anomaly is not clear.

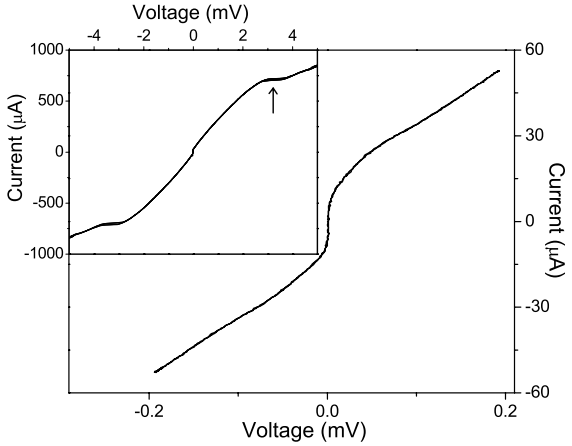

Figure 7.7: Low bias $I-V$ for a S/I/S junction at 4.2 K with $d_{\mathrm{Al}} = 5$ nm. Inset: High bias $I-V$. Arrow marks 'gap' feature.

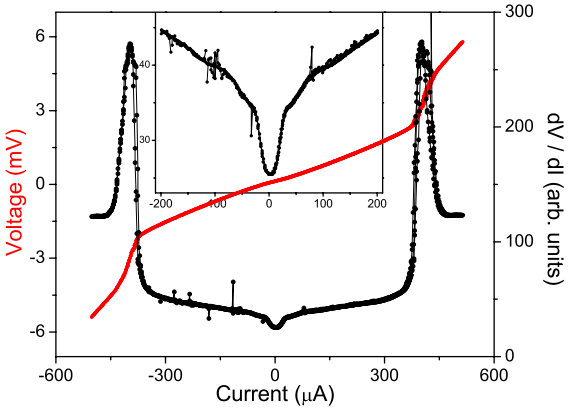

Figure 7.8: $I-V$ and $\mathrm{d}V/\mathrm{d}I$ for a S/I/S junction at 4.2 K with $d_{\mathrm{Al}} = 20$ nm. Inset: Detail of $\mathrm{d}V/\mathrm{d}I$ around zero bias.

All of the junctions showed a sub-gap resistance of the order of $1-10\ \Omega$. This resistance was close to Ohmic. The resistance in figure 7.8 is $R_S = 5.7\ \Omega$ just below the 'gap' and $R_N = 10.2\ \Omega$ just above it. The resistance area product was $R_N A \approx 1 \times 10^{-11}\ \Omega\mathrm{m}^2$. This was typical for all of the different d_{Al} values studied. No scaling of R_S/R_N with $R_N A$ was observed (figure 7.10), compared to the expected increase of R_S/R_N with $R_N A$ [12]. Scaling an $8 \times 8\ \mu\mathrm{m}^2$ junction to the dimensions of the device in figure 7.8 ($1460 \times 600\ \mathrm{nm}^2$) an $R_N A$ of the order $6 - 8 \times 10^{-10}\Omega\mathrm{m}^2$ is expected [11, 12], which is nearly two orders of magnitude larger than observed.

The 'sub-gap' $I_C(H)$ showed a strong modulation. Away from the central peak of the $I_C(H)$, the behaviour deviated from an ideal Fraunhofer pattern. This suggests an inhomogeneous current distribution. One particular possibility is the presence of metallic shorts on each edge

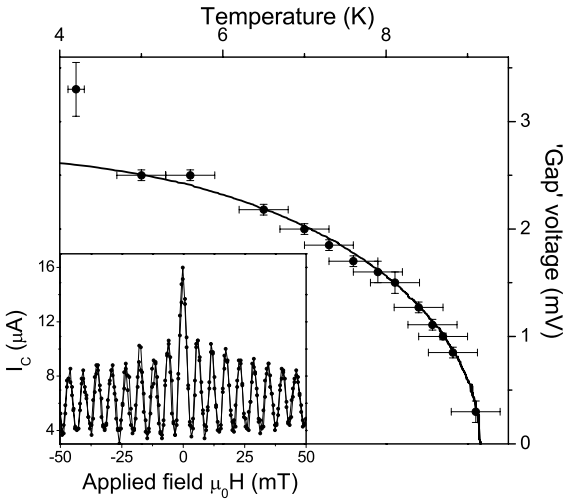

Figure 7.9: Temperature dependence of the 'gap' in the $I-V$ for a device with $d_{\mathrm{Al}} = 5$ nm. Line is a BCS theory fit with $T_C = 9.15$ K and $2\Delta/e = 2.68$ meV. Inset: Sub-gap $I_C(H)$.

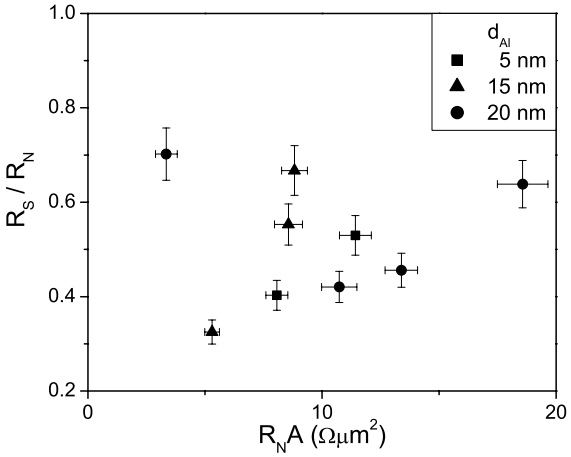

Figure 7.10: Scaling of the ratio R_S/R_N with $R_N A$ for several Al thicknesses.

of the device, with the device then acting in a similar way to a SQUID loop. In this picture the S/N/S SQUID is in *parallel* to the S/I/S junction. This does not explain why the ratio $R_S/R_N < 1$. Considering some form of series resistance does not solve this problem either. Given that the films with larger d_{Al} showed no supercurrent, the supercurrent density carried by these shorts is relatively small.

7.3.3 FIB problems

The oxide barrier in the S/I/S case is two orders of magnitude thinner than the Mo devices studied in section 7.2. The insulating barrier also has a much higher resistivity. With these considerations in mind, it is clear that metallic and/or superconducting shorts caused by re-sputtered material in the FIB are much more important in the S/I/S case compared to S/N/S. It has been previously shown that tunnel barriers patterned by standard lithography techniques can be trimmed with an FIB to reduce the barrier area [13]. This process used relatively high beam currents (1 nA followed by cleaning with 100 pA and enhanced etch). The perimeter of the trimmed barrier required anodisation afterwards to remove metallic shorts created by re-sputtering. Despite the relatively low beam currents used in the present work, this would seem to be the case here also.

Several techniques were employed to try to solve this problem. S/I/S barriers with much shorter oxidation times (10 minutes at 10 Pa) were grown, in order to reduce the barrier $R_N A$ product [14], and make it less susceptible to shorting. The aspect ratio of the side cuts was also reduced, by making y smaller, and making the cuts in two stages: first, a larger cut with an 11 pA beam, then a smaller cut was made close to the barrier with a 4 pA beam, in an effort to allow space for the resputtered material to escape from the vicinity of the barrier. Both of these techniques did not improve the $I-V$ characteristics.

7.3.3.1 Enhanced etch

The enhanced etch (EE) was also used to reduce the Ga implantation and resputtering (section 4.3.1.1). The initial thinning of the micron scale tracks could be made with an 11 pA beam: a box of $0.4 \times 5 \times 2$ μm^3 milled in about 2 minutes. This milling rate was comparable to the rate using a 70 pA beam without the EE. These cuts were not cleaned further. The EE could not be used at tilt of $\theta = 85°$ due to a physical restraint: the needle that delivers the gas approaches from an angle which is blocked by the sample holder, (from the right in figure 5.1). Hence it was not possible to make the side cuts with the EE. However devices were re-cleaned from $\theta = \pm 3°$ with the EE after the side cuts were made. There was no significant improvement in the $I-V$ characteristics using the EE. Using the EE after the milling the side cuts was problematic since the increase in the milling rate, (and therefore also the milling rate of the beam tail), significantly reduced the width of the overhanging Nb bridge.

7.3.3.2 Anodisation

An anodisation rig developed by C. Elwell and G. Burnell was used to try to post-anodise the junctions. The rig consisted of a Keithley 487 picoammeter / voltage source controlled with a LabView$^{\text{TM}}$ program[1] which recorded $I(t)$ for a constant applied V. The chip was covered in photoresist, except for a $\sim 10-20$ μm window where the anodisation was required. A current contact was made to the common bar of the chip. A droplet of buffered electrolyte solution [15, 16] was placed over the window, and the second current contact made to the top of the droplet. The experiment was monitored by measuring the decrease in $I(t)$ as the anodisation proceeded. The colour change of the surrounding Nb tracks was used to verify that anodisation had taken place [16]. However no improvement was seen in the $I-V$s. Wetting of the whole of the device might not have taken place, (in particular the holes created by the side cuts), which would explain the lack of improvement in the $I-V$s. Anodisation techniques have been recently used to create S/I/S junctions with the three dimensional FIB technique [17]. In that work the anodisation was done up to 60 V before the superconducting shorts were removed [18]. This is higher than the 17 V maximum used in the present work. It is therefore clear that the anodisation was not optimised in the present work, but that the principle can be used successfully.

The magnitude of the resistance and critical current density of the metallic shorts in these devices is important. An R_N of the order of Ohms is much larger than the typical R_N of the metallic junctions (with similar lateral dimensions), to be considered in the rest of this thesis, (of the order of tens of mΩ). Judging from the $I_C(H)$ in the inset of figure 7.9, the leakage supercurrent is < 10 μA for the thinnest d_{Al}, and even smaller for the thicker Al barriers. Both the relatively large resistivity and low supercurrent density imply a minimal effect of shorts on the metallic junctions to be discussed.

[1] Written by G. Burnell.

7.4 S/F/S junctions

7.4.1 Characterisation of $Cu_{0.4}Ni_{0.6}$ films

A $Cu_{0.4}Ni_{0.6}$ sputtering target was used to deposit all of the CuNi films in this section. The composition of the target and a thick film were measured by energy dispersive X-ray (EDX) in an SEM system[2], and were the same to within the experimental error of 1.5 %. The Curie temperature of a 300 nm thick film measured in the VSM was difficult to assign accurately (figure 7.11). This is since the $M(T)$ was measured with an applied field, which above T_M acts on the paramagnetic CuNi to give a background moment. This gives a larger apparent moment than the true value of the saturation moment M_S, of the hysteresis loop in the ferromagnetic state. The cooling rate of ~ 0.4 K/s was also relatively high, so an estimate of $T_M \sim 125 - 140$ K is taken. This is slightly lower than expected for this composition [19], but acceptable within the error margins of the composition found with the EDX.

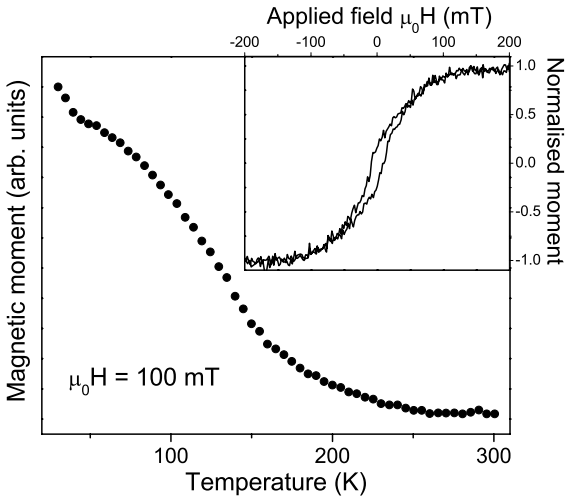

Figure 7.11: $M(T)$ measured with an applied field of $\mu_0 H$= 100 mT for a 300 nm thick CuNi film. Inset: In-plane $M(H)$ measurement at 30 K.

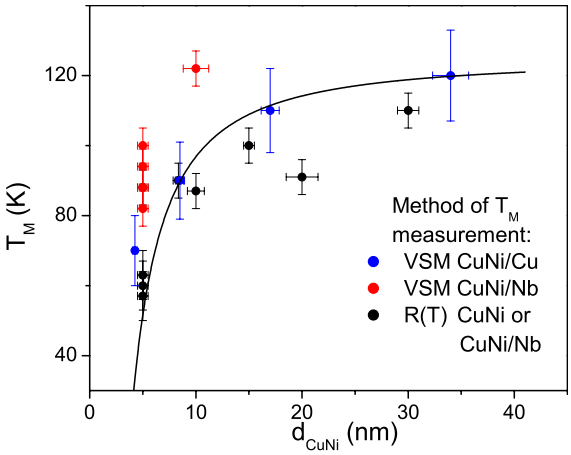

Figure 7.12: Variation of T_M with d_{CuNi} in CuNi single layers, CuNi/Nb bilayers and X/CuNi multilayers with X = Cu or Nb. Line is Ising model fit for the Cu/CuNi data assuming T_M(bulk)= 125 K (from Ruotolo *et al* [20]).

To control the value of ξ_F in the S/F/S junctions, it is important to know if T_M is changing with film thickness. The signal to noise ratio of the VSM was such that only relatively thick films ($d_F > 100$ nm) could be measured directly. Thinner layers could only be measured by growing CuNi/Cu or CuNi/Nb multilayers, with the Nb and Cu acting to decouple the CuNi layers. This requires a much larger volume of CuNi to be deposited compared to a single layer, meaning longer depositions, but also has the disadvantage that the CuNi layers are not all identical (due to the increasing roughness with thickness). T_M was therefore also found electrically by finding the peak in the dρ/dT (section 1.1.1.1). This enabled single thin films or CuNi/Nb bilayers to be characterised, (the Nb was used as a cap to prevent oxidation of the CuNi). Figure 7.12

[2] JEOL 5800 LU.

shows a range of results of T_M vs d_{CuNi} obtained for these various heterostructures, using both the $M(T)$ and $R(T)$ measurements. Although the consistency between the different films is not perfect, it is clear that T_M is decreasing for $d_F < 30$ nm.

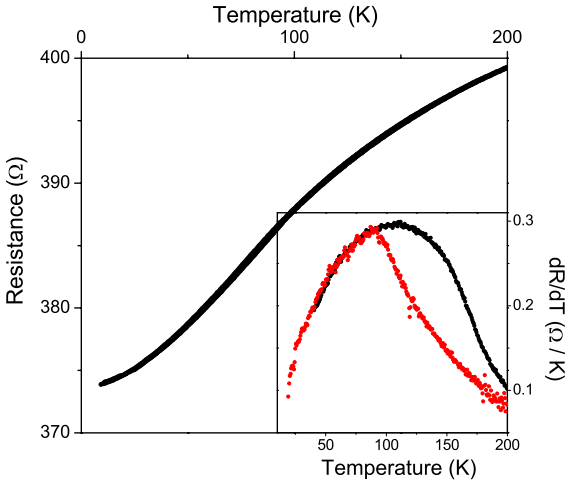

Figure 7.13: $R(T)$ for a 8 nm thick CuNi film (warming and cooling). Inset: $\mathrm{d}R/\mathrm{d}T$ for 5 nm (red) and 30 nm (black) CuNi films with 5 nm Nb cap.

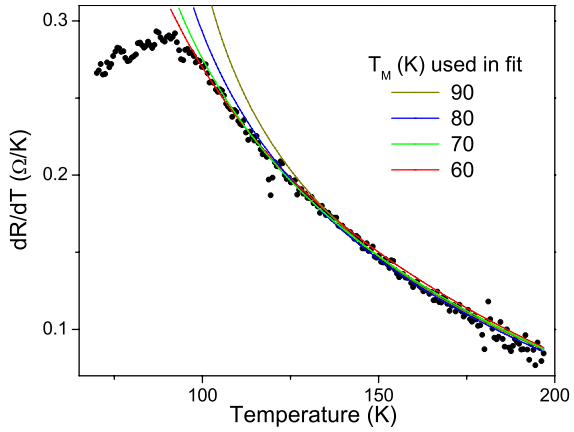

Figure 7.14: Fits to $\mathrm{d}R/\mathrm{d}T$ using $B' - A' \ln|\varepsilon|$ for various T_M with $T > T_M$, for the 5 nm thick CuNi film from the inset of figure 7.13.

For the $R(T)$ measurements a cooling / warming rate of $20 - 30$ mK/s was used (compared to ~ 100 mK/min used by Sousa *et al* [21]). $R(T)$ measurements were 'ellipse-averaged': the measured value of R was extracted from the ratio of best fit sine waves to the quasi-d.c. bias current and voltage. This was averaged until T changed by 0.3 K, or R by 0.1 %. The 0.3 K temperature window usually determined the number of $I - V$s averaged, which was typically $60 - 70$. An example of an $R(T)$ is shown in figure 7.13. The inset shows different shapes of the derivative $\mathrm{d}R/\mathrm{d}T$ of a CuNi and a CuNi/Nb film. The derivative $\mathrm{d}R/\mathrm{d}T$ was found using a parabolic fit to three consecutive points, and finding the tangent at the middle point. Taking the log of equation 1.2 gives [21]

$$\frac{1}{\rho_M}\frac{\mathrm{d}\rho}{\mathrm{d}T} = B - A\ln|\varepsilon|\,, \tag{7.1}$$

where the A and B in equation 7.1 and A' and B' in figure 7.14 are simply related via the ratio $\rho_M R(T)/\rho(T)$. The values for A and B obtained from figure 7.14 for the various T_M are summarised in table 7.1. These compare favourably to $A = 2.6 - 3.1 \times 10^{-4}$ K^{-1} obtained by Sousa *et al* in bulk $Cu_{0.3}Ni_{0.7}$ samples [21]. It is clear however that the value of T_M cannot be determined to better than 10 K in this manner, and that T_M does not occur at the same point as the maximum of $\mathrm{d}R/\mathrm{d}T$. This has been found elsewhere [21]. The blurring of the peak in $\mathrm{d}R/\mathrm{d}T$ may be due to compositional inhomogeneities and also temperature gradients in the sample. The case is worse when the fit is attempted on the other $\mathrm{d}R/\mathrm{d}T$ curve (inset figure 7.13). The further broadening in this case may be caused by a range of T_M in the relatively thick film, due to an initial 'dead' magnetic layer at the substrate/CuNi interface, and another

T_M (K)	ρ_M (Ωm)	A (K^{-1})	B (K^{-1})
90	8.06×10^{-7}	4.3×10^{-4}	1.9×10^{-4}
80	8.01×10^{-7}	4.9×10^{-4}	2.3×10^{-4}
70	7.97×10^{-7}	5.4×10^{-4}	3.0×10^{-4}
60	7.94×10^{-7}	6.2×10^{-4}	3.8×10^{-4}

Table 7.1: Values of A and B used in equation 7.1 for curves in figure 7.14.

at the CuNi/Nb interface due to alloying.

7.4.2 S/F/S junctions

Nb/CuNi/Nb trilayers were grown with d_{CuNi} thicknesses in the range $5-13$ nm. The Josephson junction $I_C R_N(d_F)$ showed a monotonically increasing $I_C R_N$ with decreasing d_F, although with considerable scatter (figure 7.15). The value of ρ_{CuNi} calculated from $R_N A/d_F$ was more consistent, (inset figure 7.15) except for the thinner barriers where again the generally smaller junction area A contained significant error due to the limitations of FIB measurements, (as in section 7.2.2). Figure 7.16 shows a good Fraunhofer $I_C(H)$ response, indicating a uniform current flow, (the $I_C R_N$ product was such that each point of the $I_C(H)$ had to be measured with the lockin amplifier). The $I_C(T)$ in this case showed a quadratic dependence near T_C, (inset figure 7.16) similar to the Nb/Mo/Nb junctions.

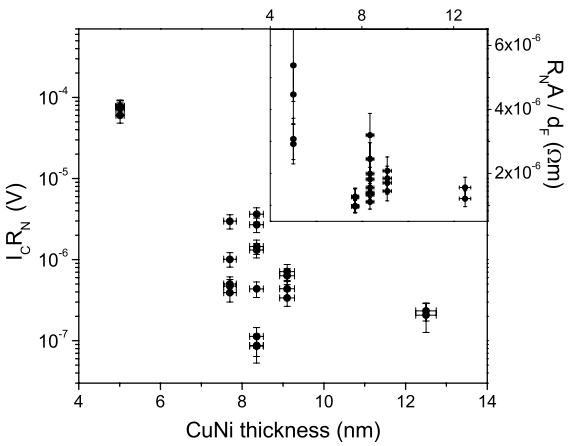

Figure 7.15: Scaling of $I_C R_N$ with d_{CuNi}. Inset: Scaling of $R_N A/d_F$ for the same devices.

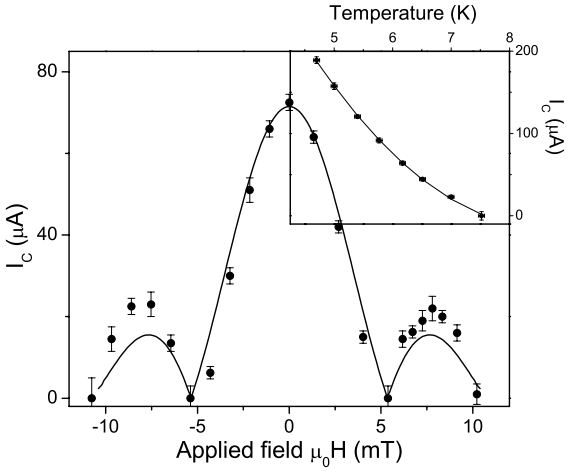

Figure 7.16: $I_C(H)$ for a 8.5 nm CuNi barrier at 4.2 K, $H \perp x$. Line is a Fraunhofer fit. Inset: $I_C(T)$ with quadratic fit.

The junction behaviour with temperature was of considerable interest: a cusp and re-entrance of the $I_C(T)$ would indicate the $0-\pi$-junction crossover. This was observed in a zero field cooled sample, as shown in figure 7.17, (the inset shows an example of a lockin amplifier measurement of the I_C). The slight kink in the $I_C(T)$ plot was an artifact due to a change in the range of the current supply, without changing the oscillation voltage of the lockin amplifier. This change slightly altered the magnitude of the signal and hence the I_C, since a resistive criterion

was used to extract I_C. In order to achieve good temperature stability the magnetic coil was not fitted onto the Heliox (section 4.4.2) for this measurement. However this prevented the measurement of $I_C(H)$, which is required to confirm that the Fraunhofer is centred on zero field. If the Fraunhofer is not centred on zero field, (due to net induction in the junction: see [22] and section 8.4.3.4) a re-entrant I_C can be produced due to the changing value of λ with T. A full $I_C(H,T)$ measurement was beyond the time constraints of the measurement. Qualitatively the $I_C(T)$ measurement can be compared to the work of Sellier [23]. This is shown in figure 7.18, and is qualitatively good. However other devices patterned on the same sample, measured at 4.2 K did not show the increasing $I_C(T)$ expected in this temperature range, (compare figures 7.16 and 7.17), but did show a Fraunhofer $I_C(H)$. This should not be too concerning since the large variation in I_C seen by Sellier in figure 7.18 was for only a 1.5 nm variation in d_F. In the case of Sellier's work, the T_M of the CuNi films was $\sim$ 23 K [24] - therefore an even stronger thickness dependence is expected in the case of the present CuNi films which have a larger T_M. It is therefore not possible to rule out small changes in the thickness or properties of the barrier, which would have a large effect on the I_C behaviour, (this point will be returned to in section 8.4.3.4).

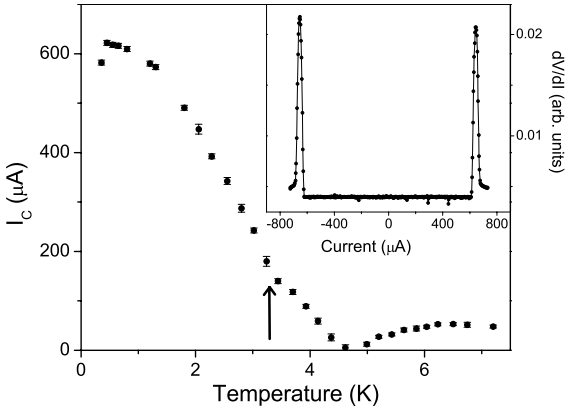

Figure 7.17: $I_C(T)$ for a Nb/CuNi/Nb device with $d_{\mathrm{CuNi}} = 8.5$ nm. Arrow marks the point where the current range was changed. Inset: $\mathrm{d}V/\mathrm{d}I$ vs current at 0.36 K.

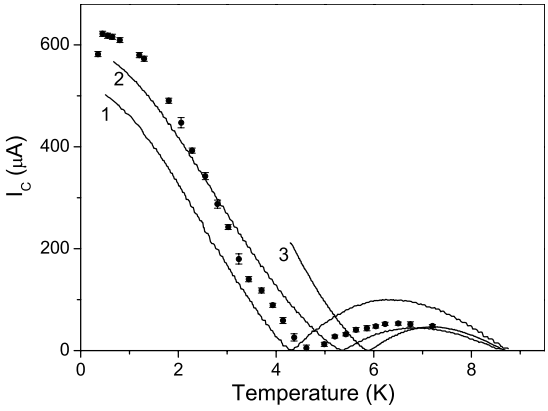

Figure 7.18: $I_C(T)$ from figure 7.17 (symbols) compared to $Cu_{0.52}Ni_{0.48}$ junctions of Sellier [23]. Curves $1-3$ had $d_F = 18, 19$ and 19.5 nm respectively. The I_C of curves 1 and 3 have been scaled by a factor of 0.5 and 3 respectively for clarity.

When a magnetic field was applied $\perp y$, several devices showed an $I_C(H)$ response which resembled a SQUID modulation, with a linear envelope. Such a response is shown in figure 7.19, and the characteristics of three devices detailed in table 7.2. From the table it is clear that the oscillation period is decreasing in proportion with the increasing y dimension. Assuming a magnetic area of $y \times (2\lambda + d_F)$, and taking $\lambda = 40$ nm (section 6.3.2.2), the predicted Fraunhofer period is then 55 mT - slightly larger than observed. The period is therefore of a similar order to the observed modulation, but clearly the shape is not a Fraunhofer. The SQUID-like appearance of the modulation may be due to inhomogeneous current flow in the device. This inhomogeneity could be caused by domain structures in the CuNi layers, but also may be associated with some damage of the CuNi barrier on the 'cleaned' faces of the device, which locally increases the

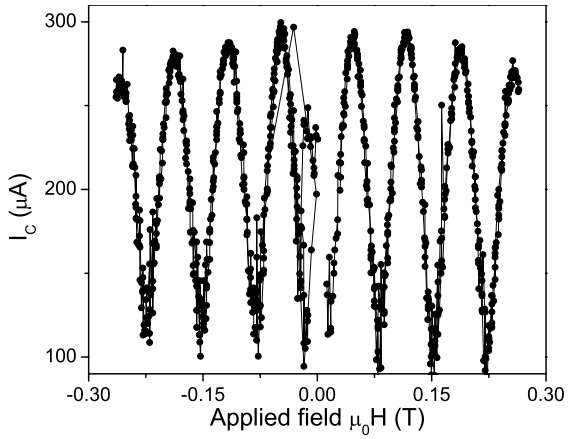

Figure 7.19: $I_C(H)$ of device b (table 7.2) at 0.34 K for $H \perp y$. Lines are a guide to the eye.

J_C. In particular for the CuNi case, any slight change in the T_M of the material due to Ga implantation for example, will strongly affect the local J_C.

Device	Nominal y (μm)	$I_C(H)$ period (mT)	Period × y (mT μm)
a	0.51	60.8	31.1
b	0.42	70.4	29.4
c	0.39	81.3	32.0

Table 7.2: Scaling of $I_C(H)$ period for $H \perp y$ with y dimension for three Nb/CuNi/Nb devices. $d_{\mathrm{CuNi}} \sim$ 9 nm.

Since the important basic results of S/F/S junctions had been previously published by Ryazanov *et al* [22, 25] and Kontos *et al* [26, 27], further detailed measurements were not made of these films, but devices with composite F layers were studied.

References

[1] R. H. Hadfield, Ph.D. Thesis, University of Cambridge (2002).
[2] P. A. Rosenthal, M. R. Beasley, K. Char, M. S. Colclough, and G. Zaharchuk, Appl. Phys. Lett. **59**, 3482 (1991).
[3] T. Aomine, E. Tanaka, S. Yamasaki, K. Tani, and A. Yonekura, J. Low Temp. Phys. **74**, 263 (1989).
[4] D. Dimos, P. Chaudhari, and J. Mannhart, Phys. Rev. B **41**, 4038 (1990).
[5] J. E. Evetts and B. A. Glowacki, Cryogenics **28**, 641 (1988).
[6] E. E. Mitchell, C. P. Foley, K.-H. Müller, and K. E. Leslie, Physica C **321**, 219 (1999).
[7] J. I. Martín, M. Vélez, A. Hoffmann, I. K. Schuller, and J. L. Vicent, Phys. Rev. Lett. **83**, 1022 (1999).
[8] K. A. Delin and A. W. Kleinsasser, Supercond. Sci. Technol. **9**, 227 (1996).
[9] T. van Duzer and C. W. Turner, *Principles of Superconductive Devices and Circuits, (Second Edition)* (Prentice Hall PTR, 1999).
[10] E. P. Harris and R. B. Laibowitz, IEEE Trans. Magn. **1**, 724 (1977), and references therein.
[11] C. A. Elwell, Ph.D. Thesis, University of Cambridge (2002).
[12] M. S. Goodchild, Z. H. Barber, and M. G. Blamire, J. Vac. Sci. Technol. A **14**, 2427 (1996).
[13] Z. H. Barber, M. G. Blamire, and N. J. Dawes, J. Vac. Sci. Technol. B **13**, 318 (1995).
[14] M. G. Blamire, R. E. Somekh, Z. H. Barber, G. W. Morris, and J. E. Evetts, J. Appl. Phys. **64**, 6396 (1988).
[15] H. Kroger, L. N. Smith, and D. W. Jillie, Appl. Phys. Lett. **39**, 280 (1981).
[16] G. Burnell, Ph.D. Thesis, University of Cambridge (1998).
[17] M. Watanabe, Y. Nakamura, and J.-S. Tsai, Appl. Phys. Lett. **84**, 410 (2004).
[18] M. Watanabe, (personal communication).
[19] S. A. Ahern, M. J. C. Martin, and W. Sucksmith, Proc. Roy. Soc. London **248**, A145 (1958).
[20] A. Ruotolo, C. Bell, C. W. Leung, and M. G. Blamire, J. Appl. Phys. (2003), (submitted).
[21] J. B. Sousa, M. R. Chaves, R. S. Pinto, and M. F. Pinheiro, J. Phys. F: Met. Phys. **2**, L83 (1972).
[22] V. V. Ryazanov, V. A. Oboznov, A. Y. Rusanov, A. V. Veretennikov, A. A. Golubov, and J. Aarts, Phys. Rev. Lett. **86**, 2427 (2001).
[23] H. Sellier, Ph.D. Thesis, Université Joseph-Fourier, Grenoble (2002).
[24] H. Sellier, C. Baraduc, F. Lefloch, and R. Calemczuk, Phys. Rev. B **68**, 054531 (2003).
[25] V. V. Ryazanov, V. A. Oboznov, A. V. Veretennikov, and A. Y. Rusanov, Phys. Rev. B **65**, 020501(R) (2001).
[26] T. Kontos, M. Aprili, J. Lesueur, and X. Grison, Phys. Rev. Lett. **86**, 304 (2001).
[27] T. Kontos, M. Aprili, J. Lesueur, F. Genêt, B. Stephanidis, and R. Boursier, Phys. Rev. Lett. **89**, 137007 (2002).

Chapter 8

Development of a spin-active Josephson junction

The development of a spin-active Josephson junction is discussed. Results for S/GMR/S, S/AF/S and S/spin-valve/S CPP devices are presented. The results of sections 8.3 have been published in reference [1]. Section 8.4 has been submitted for publication in reference [2]. These papers are reproduced in Appendix B.

8.1 Development of spin-active devices

As discussed in section 3.4.1 the S/F/I/F/S junctions allowed, in theory, the crossover from a 0 to π-junction by changing from the AF to F alignment of the magnetic layers. This would achieve a controllable π-junction. To control the F layers *in-situ* the value of H_C of the ferromagnetic layers must be considered, as well as the size of the Josephson junction. If the area of the junction is large, then the field required to move the magnetic moments around will strongly suppress the I_C due to the normal $I_C(H)$ behaviour, and wash out any effects due to the changes in the F layers. This motivates relatively small junctions, which can be achieved using the FIB technique.

Due to the problems of creating S/I/S junctions (section 7.3.3) the insulating barrier was replaced by a normal metal (Cu) barrier. Both the GMR, S/[F/N]$_n$S, system and the spin-valve (SV) structure S/AF/F/N/F/S were investigated. In the SV case, the AF pinning layer has the advantage that identical F layers can be grown ensuring correct cancellation of the net moment in the AF configuration, and the $M(H)$ loop has *uni-directional* anisotropy. This is beneficial since any uni-directional asymmetry in the $I_C(H)$ would stand out above the normal Fraunhofer suppression which is symmetric or anti-symmetric in H.

8.2 S/GMR/S structures

8.2.1 Film details

Nb/(Cu/Co)$_{10}$/Nb films with $d_{\mathrm{Nb}} = 5$ nm and 150 nm were both grown to measure the CIP and CPP GMR. The CIP films, without thicker Nb layers, could be grown and measured relatively quickly, (no patterning was required), and were used to find the correct Cu thickness for the GMR anti-parallel coupling. CPP device heterostructures with the same thickness of Cu were then grown. The Co and Cu thicknesses were ~ 2 nm and 1 nm respectively. This value of d_{Cu} is near the 1$^{\mathrm{st}}$ AF peak (section 1.2.1). The $M(H)$ loops (figure 1.14) did not show ideal AF alignment. This is expected for a relatively small number of Co layers given that the 'edge' Co layers do not couple fully with the other layers. The thicker Nb underlayer for the CPP devices increased H_C relative to the CIP film as expected.

8.2.2 MR measurements

A total of six CPP devices were measured at 4.2 K. With the maximum applied field at 4.2 K these devices showed MR $= 100\times(R_{\mathrm{max}} - R_{\mathrm{min}})/R_{\mathrm{max}}$ in the range $5 - 9$ % . As can be seen from figure 8.1, the MR was not saturated at the maximum applied field of $\mu_0 H = 80$ mT. There was no scaling of MR with area, or junction dimension. However it is difficult to draw any conclusions from this variation without being able to saturate the magnetic moments, since H_S may vary between samples. Most of these devices were destroyed by an electrical discharge, and could not be characterised in the Heliox. The CIP film and remaining CPP devices were measured in the Heliox at 0.34 K to enable a large enough magnetic field to be applied to

saturate the ferromagnetic layers. The MR measurement shown in figure 8.2 was carried out on a CPP device which had dimensions $x = 800$ nm and $y = 300$ nm. An MR of $\sim 13.0 \pm 0.2$ % was

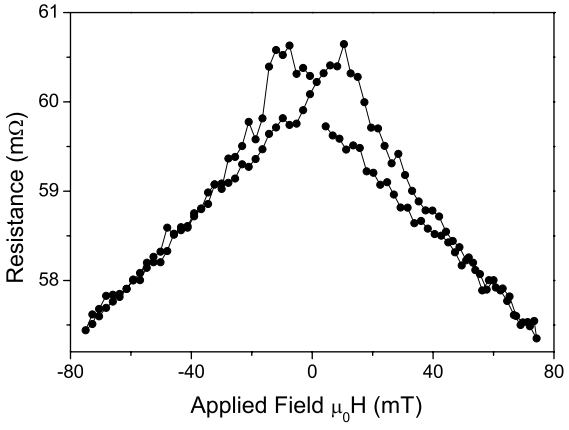

Figure 8.1: In-plane $R(H)$ at 4.2 K for a 800 × 300 nm^2 CPP device Nb/(Cu/Co)$_{10}$/Nb device. Line is a guide to the eye.

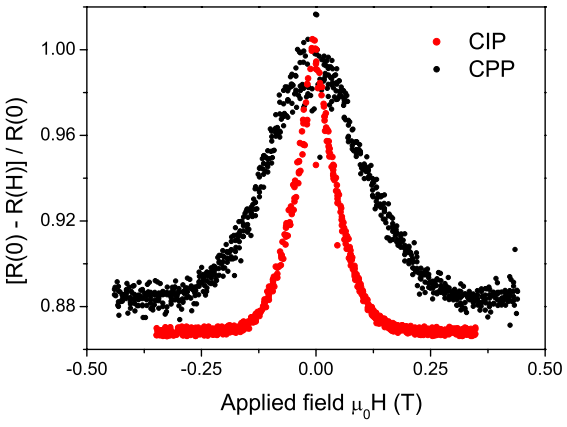

Figure 8.2: In-plane $R(H)$ at 0.34 K for a CIP plane film and a CPP device, (same device as figure 8.1).

obtained at 0.34 K for the CIP device and 11.5 ± 0.7 % for the CPP device. The CPP device would be expected to have a larger MR. The increased roughness of the thicker Nb underlayer in the CPP case means that the degree of parallel alignment is increased due to 'orange peel' coupling between the F layers, and the MR reduced due to this effect. The low field hysteresis - visible in the 4.2 K $R(H)$ data (figure 8.1), also indicates imperfect AF coupling between the layers.

8.2.3 Discussion

From section 1.2.4 the two resistor model can be used to examine the values of RA and MR obtained in these GMR devices. Table 8.1 shows various values of resistivity and interface resistance at 4.2 K. In the third section of table 8.1 the values of $\rho_F^{\uparrow\downarrow}$ are found using the relation $\rho_F^{\uparrow(\downarrow)} = 2\rho_F^*(1-(+)\beta)$. Similarly $R_{F/N}^{\uparrow(\downarrow)} = 2R_{F/N}^*(1-(+)\gamma)$. Where β and γ are the bulk and interface spin asymmetry coefficients [3]. For the Nb/(Cu/Co)$_{10}$/Nb case, in the anti-parallel (AF) configuration, considering the 'up' spin:

$$\begin{aligned} AR^{\mathrm{AF}\uparrow} = \; & 2AR_{\mathrm{Nb/Co}} + 2AR_{\mathrm{Nb/Cu}} + 9AR^{\uparrow}_{\mathrm{Co/Cu}} + 10AR^{\downarrow}_{\mathrm{Co/Cu}} \\ & +10\times 2\rho_{\mathrm{Cu}}d_{\mathrm{Cu}} + 5\rho^{\uparrow}_{\mathrm{Co}}d_{\mathrm{Co}} + 5\rho^{\downarrow}_{\mathrm{Co}}d_{\mathrm{Co}}\,. \end{aligned} \tag{8.1}$$

It is assumed that the Co layer at the Nb/Co interface is 'up' spin for both configurations, (this does not affect the results). In a similar way to section 1.2.4 the values of $AR^{\mathrm{AF}\downarrow}$, $AR^{\mathrm{F}\uparrow}$ and $AR^{\mathrm{F}\downarrow}$ can be found, and hence AR and $A\Delta R$. This calculation gives $AR^{AF} = 2.56\pm0.09\times10^{-14}$ Ωm^2 and $AR^F = 1.61 \pm 0.04 \times 10^{-14}$ Ωm^2, giving an MR = 37.2 ± 0.6 %. The predicted MR is larger than found, even at 0.34 K, but the AR^{AF} product compares favourably to the experimental value of $1.44 \pm 0.25 \times 10^{-14}$ Ωm^2.

Importantly the GMR effect is not destroyed by the FIB processing. It would also have been possible to increase the total Co thickness and number of repeats to obtain a much larger % MR. However, a key point of the thinner Co layers is that a Josephson current (due to resputtered Nb shorting the barrier) was *not* obtained. By considering thinner Co layers a Josephson GMR device may be possible, but the drawback of needing the Heliox for every measurement motivated the examination of spin valves, which have a lower H_C and H_S, and could therefore be measured with smaller applied fields in the dip probes.

Property	Value	Error	Units
$2AR_{\mathrm{Nb/FeMn}}$ $^{(a)}$	2.0×10^{-15}	1.2×10^{-15}	$\Omega\mathrm{m}^2$
$2AR_{\mathrm{Nb/Cu}}$ $^{(b)}$	2.2×10^{-15}	3.0×10^{-16}	$\Omega\mathrm{m}^2$
$2AR_{\mathrm{Nb/Co}}$	6.1×10^{-15}	5.0×10^{-16}	$\Omega\mathrm{m}^2$
$2AR_{\mathrm{Nb/Py}}$	7.0×10^{-15}	1.5×10^{-15}	$\Omega\mathrm{m}^2$
$2AR^*_{\mathrm{Co/Cu}}$	1.05×10^{-15}	5.0×10^{-17}	$\Omega\mathrm{m}^2$
$2AR^*_{\mathrm{Py/Cu}}$	1.0×10^{-15}	8.0×10^{-17}	$\Omega\mathrm{m}^2$
ρ^*_{Co}	7.6×10^{-8}	5.0×10^{-9}	$\Omega\mathrm{m}$
ρ^*_{Py}	1.64×10^{-7}	2.0×10^{-8}	$\Omega\mathrm{m}$
ρ_{Cu}	4.5×10^{-9}	5.0×10^{-10}	$\Omega\mathrm{m}$
β_{Co}	4.6×10^{-1}	8×10^{-2}	-
γ_{Co}	7.5×10^{-1}	5×10^{-2}	-
β_{Py}	5.0×10^{-1}	1.6×10^{-1}	-
γ_{Py}	8.1×10^{-1}	1.2×10^{-1}	-
$\rho^{\uparrow}_{\mathrm{Co}}$	1.04×10^{-7}	1.94×10^{-8}	$\Omega\mathrm{m}$
$\rho^{\downarrow}_{\mathrm{Co}}$	2.81×10^{-7}	5.23×10^{-8}	$\Omega\mathrm{m}$
$\rho^{\uparrow}_{\mathrm{Py}}$	2.19×10^{-7}	7.49×10^{-8}	$\Omega\mathrm{m}$
$\rho^{\downarrow}_{\mathrm{Py}}$	6.56×10^{-7}	2.25×10^{-7}	$\Omega\mathrm{m}$
$AR^{\uparrow}_{\mathrm{Co/Cu}}$	5.25×10^{-16}	4.3×10^{-17}	$\Omega\mathrm{m}^2$
$AR^{\downarrow}_{\mathrm{Co/Cu}}$	3.68×10^{-15}	3.01×10^{-16}	$\Omega\mathrm{m}^2$
$AR^{\uparrow}_{\mathrm{Py/Cu}}$	3.8×10^{-16}	6.4×10^{-17}	$\Omega\mathrm{m}^2$
$AR^{\downarrow}_{\mathrm{Py/Cu}}$	3.62×10^{-15}	6.09×10^{-16}	$\Omega\mathrm{m}^2$

Table 8.1: Values used to calculate AR, taken from measurements at 4.2 K by Yang *et al* [4], (a) Bass *et al* [5] and (b) Park *et al* [6].

8.3 S/AF/S

When considering the development of a spin-valve junction (S/AF/F/N/F/S), (section 8.1) it is important to understand the S/AF/S system. In this section the results of T_C measurements on AF/S bilayers are also presented, and compared to the results obtained from S/AF/S Josephson junctions.

8.3.1 Experimental details

For all samples containing FeMn, a 5 nm underlayer of Cu was grown, in order to achieve the required f.c.c. AF γ-FeMn phase [7]. Nb/Cu/FeMn/Nb structures were grown for Josephson junctions with FeMn thickness d_{FeMn}, in the range $2-6$ nm, with both Nb thicknesses 150 nm. For the bilayer measurements Cu/FeMn/Nb films were grown. Devices with $I_C R_N > 1$ μV were characterised by directly measuring the $I-V$. For samples with $I_C R_N < 1$ μV, $\mathrm{d}V/\mathrm{d}I$ was measured with the lock-in amplifier. T_C measurements were made on unpatterned 10×5 mm^2 films. The rate of cooling was $< 10^{-2}$ K/s near T_C, and the ellipse averaging parameters (section 7.4.1) were 0.1 % change for R, and 0.02 K for T near T_C.

8.3.2 T_C measurements of Cu/FeMn/Nb films

The film T_Cs were measured while independently varying the S and AF thicknesses, as shown in figures 8.3 and 8.4 respectively. The $R(T)$ curves showed a transition width of the order of 0.1 K, and the T_C was defined as the midpoint of the transition. An absolute error of 0.05 K was found by measuring the T_C of a thick Nb film, and repeated T_C measurements showed a relative error of ~ 0.05 K. For thicknesses of FeMn < 1 nm a broadened transition (~ 0.2 K) was observed (figure 8.5). This was presumably associated with large percentage variation of the film thickness over the substrate. As can be seen in figure 8.5, the T_C could be claimed to oscillate in this regime, but given the possible variation in thickness, and the small number of thicknesses measured, the data is simply not consistent in this thickness regime. Any possible non-monotonic behaviour in T_C could only be reliably found in this regime by using a single sample with continuously varying FeMn thickness, where T_C could be found at many different points. Such a sample would not be so affected by run-to-run variation in the deposition rates, which would be important in this thickness regime.

As shown in figure 8.3, for a constant $d_{\mathrm{FeMn}} = 6.5$ nm, with varying Nb thickness, a suppression of T_C was observed relative to the plain Nb film. In figure 8.3 the final point with $T_C < 4.2$ K was measured in the Heliox, with a different calibration and thermal environment, hence the relative error in T_C is larger.

For a constant Nb thickness of 25 nm the T_C of the film drops dramatically as soon as the thinnest layer of FeMn is grown underneath (figure 8.4). The two points at $d_{AF} = 0$ in figure 8.4 are for Nb only and a Cu/Nb bilayer respectively. Since ξ_N in Cu is relatively large, only a small decrease of the T_C of the Nb is expected, as was seen. The strong suppression of T_C with the FeMn layer, and the saturation of the suppression above only a few nm of material implies

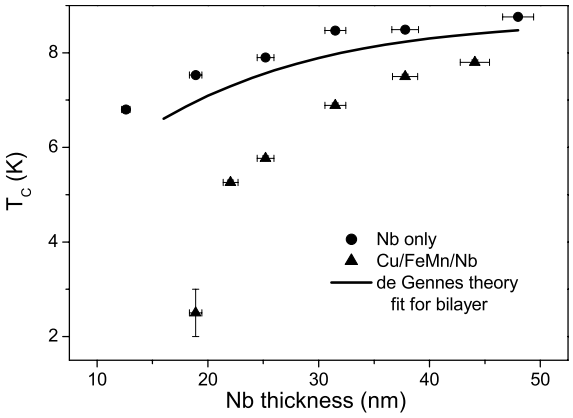

Figure 8.3: Variation of T_C vs Nb thickness for a constant FeMn thickness of 6.5 nm, (triangles), compared to plain Nb films (circles). Fit to triangles is de Gennes' theory.

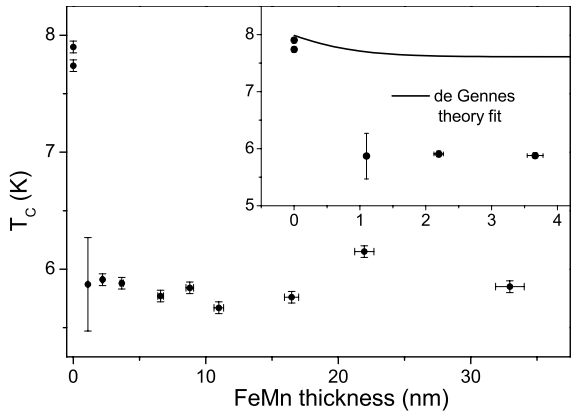

Figure 8.4: Variation of T_C vs FeMn thickness for a constant Nb thickness of 25 nm. Inset: Detail for thinner films, with de Gennes' theory fit.

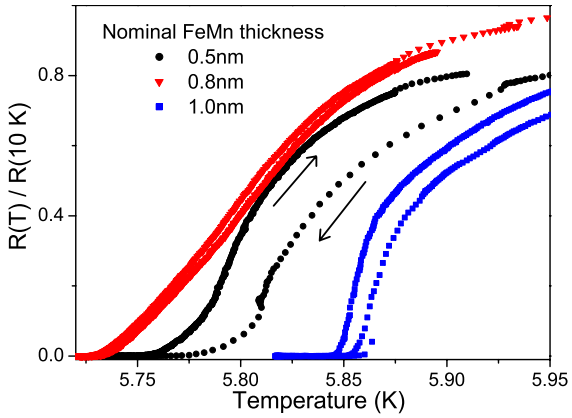

Figure 8.5: Variation of $R(T)$ behaviour for the thinnest FeMn thicknesses in the Cu/FeMn/Nb bilayers, both cooling and warming. $R(T)$ has been normalised to $R(10\ \mathrm{K})$ for clarity. Broadened transitions for thinnest layers is clear. Arrows for the 0.5 nm sample indicate warming and cooling.

a short coherence length, ξ_{AF} of the order of $1-2$ nm in the FeMn.

As can be seen from figures 8.3 and 8.6, in this thickness regime the Nb only film T_C is also decreasing. For a correct comparison with the Cu/FeMn/Nb films therefore, measurements on plain Nb films of decreasing thickness were also made. The reduction of T_C in the plain Nb films can be attributed to a combination of grain size and resistivity effects, as well as an inverse proximity effect due to the NbO layer on the surface, and a 'dead' initial layer during growth [8]. The correlation between T_C and resistance ratio R(295 K)/R(10 K), (RRR) shown in figure 8.6 is associated with the increasing grain size with d_{Nb}, (which increases the mean free path), and is consistent with previous studies [9].

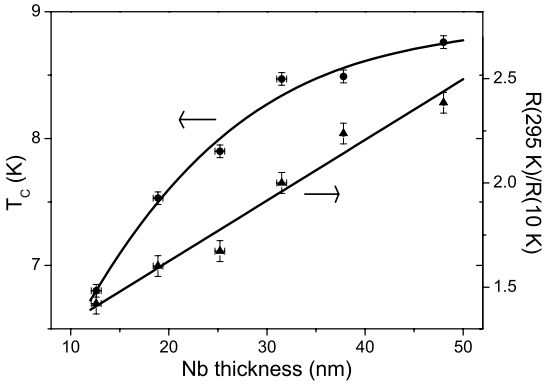

Figure 8.6: T_C and RRR variation vs thickness for Nb only films. Lines are the best fit cubic and linear curves for T_C and RRR respectively.

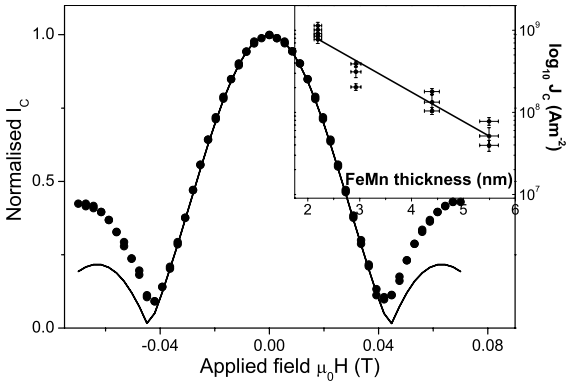

Figure 8.7: Normalised $I_C(H)$. Line is a best-fit Fraunhofer pattern. Inset: J_C vs d_{FeMn} for junctions at 4.2 K. Line is a best fit exponential $\exp(-2d_{AF}/\xi_{AF})$ with $\xi_{AF} = 2.4$ nm.

8.3.3 Josephson junctions

The Josephson junctions showed resistively shunted junction (RSJ), $I-V$ characteristics, with I_C in the range 10 μA $-$ 1.2 mA, and R_N $6-60$ mΩ. The re-entrant $I_C(H)$ in figure 8.7 shows the presence of a Josephson current through the FeMn, although an ideal Fraunhofer pattern was not obtained. In this case the modulation is normalised to zero field critical current $I_C = 500$ μA. The junction dimension perpendicular to the direction of the applied field was ~ 600 nm and the total barrier thickness, (Cu and FeMn) was 7 nm. Correcting for the finite thickness of the Nb electrodes (section 3.1.4), the Fraunhofer fit gives $\lambda = 40$ nm. This compares well to the values obtained in section 6.3.2.2 from the nanoSQUIDs. The lack of suppression of I_C to zero is an artifact of the voltage criterion used: the I_C was suppressed to zero to within the 1 μV noise level of the measurement in this case. The Josephson penetration depth is estimated for the thinnest case ($d_{AF} \sim 3$ nm and $J_C \sim 1\times10^9$ Am^{-2}) to be $\lambda_J \sim 2$ μm. The largest junction dimension for that thickness was 1.2 μm, so the junctions were close to the long junction limit only for the largest junction with the thinnest barriers.

The inset of figure 8.7 shows the variation of J_C with d_{FeMn}. Fitting $J_C \propto \exp(-2d_{AF}/\xi_{AF})$ (section 3.3) to the inset of figure 8.7, the characteristic decay length $\xi_{AF} = 2.4$ nm is found. The errors in $J_C(d_{AF})$ consist of measurement error of the sub-micron junction area, as well as scatter due to variation of d_{AF} over the area of the chip. There may also be additional variation due to domain structures in the AF, and spin compensation at the interfaces which are spatially inhomogeneous. All devices for a given film thickness are patterned on the same 10 $\times$ 5 mm^2 chip, hence interface transparency and contamination should be comparable for a given d_{AF}.

8.3.4 Discussion

From section 2.5, if FeMn is considered as a band antiferromagnet, ξ_{AF} in the dirty limit is given by:

$$\xi_{AF} = \left[\frac{2\hbar D}{E_{Ex}}\right]^{\frac{1}{2}} \tag{8.2}$$

where $D = \frac{1}{3}v_F\ell$ and $E_{Ex} \sim k_B T_N$ the exchange coupling between the AF spins. T_N in this case is in the range $450 - 490$ K [10]. In the case of FeMn, because it is a highly disordered alloy system, a short mean free path ℓ, of the order of 1 nm or less is expected [11]. A reasonable value of ξ_{AF} using equation 8.2 with $v_F = 2 \times 10^6$ ms^{-1} (both Fe and Mn have $v_F \sim 2 \times 10^6$ ms^{-1} [12]) is of the order of $4 - 5$ nm. This estimate is in agreement with the value from the trilayer junctions, and much shorter than the corresponding coherence length in a normal metal. Further information can be gained from the measurement of the coherence length. From equation 8.2 using $T_N = 450$ K, and $\xi_{AF} = 2.4$ nm from section 8.3.3, the diffusion constant D is found to be 1.7×10^{-4} m^{2}s^{-1}.

Given D the DoS at the Fermi level can be found using the Einstein relation $\sigma = 2e^2\mathcal{N}(\epsilon_F)D$ [13]. For this calculation the value of σ_{FeMn} is required. This was found using a series of Cu(5 nm)/FeMn/Nb(6 nm) films grown for differing FeMn thicknesses (the Nb is to prevent oxidation of the FeMn). Assuming a simple parallel resistor model, plotting the ratio of total thickness and resistivity against FeMn thickness should give a straight line with gradient equal to the conductivity of the FeMn. σ_{FeMn} was found to be 8.4×10^5 $(\Omega\mathrm{m})^{-1}$, from the linear fit in figure 8.8. The DoS at the Fermi level, $\mathcal{N}(\epsilon_F)$, in FeMn is found to be 9.6×10^{46} states J^{-1}m^{-3}. Nakamura *et al* calculated an average DoS of 0.5 states / eV / atom [14]. Using a unit cell dimension of $a = 0.36$ nm, (calculated from data in [15]) this becomes 2.4×10^{47} states J^{-1}m^{-3}, so the comparison is reasonable.

For parallel resistors, the intercept of figure 8.8 is given by $\sigma_{\mathrm{Nb}}d_{\mathrm{Nb}} + \sigma_{\mathrm{Cu}}d_{\mathrm{Cu}}$. Using the value of σ_{Nb} (see below) this intercept is predicted to be of the order of 0.16 Ω. The smaller observed value is associated with additional interface resistance, and the NbO surface layer, which would be significant for $d_{\mathrm{Nb}} = 6$ nm, which both reduce the effective value of σ_{Nb}. This intercept is also consistent with a higher value of σ_{FeMn} obtained from the junction R_N values: which contains an additional $30 - 50$ % component to R_N due to the Nb/FeMn to the interface resistance, (see table 8.1).

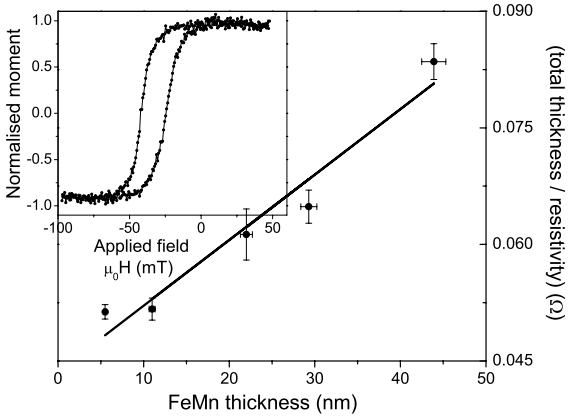

Figure 8.8: Linear fit to find σ_{FeMn} using different thicknesses of FeMn in a Cu/FeMn/Nb trilayer at 295 K. Inset: Hysteresis loop of a Nb/Cu/FeMn/Co/Nb trilayer after annealing at 0.2 T from 200 °C for 30 minutes.

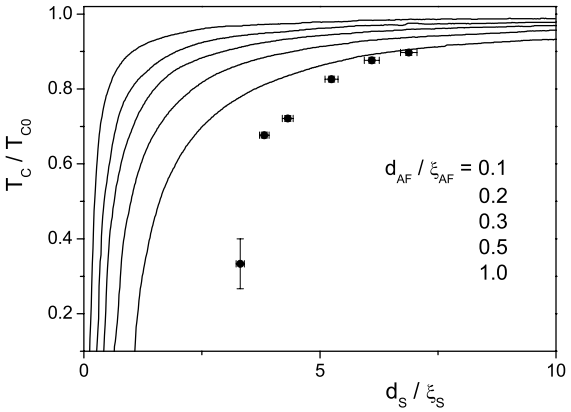

Figure 8.9: Reduced temperature vs d_S/ξ_S for various ratios of d_{AF}/ξ_{AF}, taken from Krivruchko [16]. Symbols are the present data for Cu/FeMn/Nb samples.

Equation 2.20 was used to fit the T_C data: all of the required values can be found from the results above. From the trilayer junctions $\xi_{AF} = 2.4$ nm. The thicknesses d_S and d_{AF} are known for a given film. To find ξ_S in the dirty limit $\xi_S = 0.855(\xi_0 \ell)^{\frac{1}{2}}$ is used with $\xi_0 \approx \hbar v_F / k_B T_0$. Substituting using the free electron form $D = \frac{1}{3} v_F \ell = \sigma k_B^2 \pi^2 / 3e^2 \gamma$, [17, 18] gives

$$\xi_S = \left[\frac{\pi \hbar k_B \sigma}{6 e^2 \gamma T_0} \right]^{\frac{1}{2}} . \tag{8.3}$$

Here the electronic specific heat capacity $\gamma = 720$ Jm^{-3}K^{-2}, [19] and $T_0 = 9.25$ K - the bulk T_C of Nb. From a van der Pauw measurement at 295 K, $\sigma_{\mathrm{Nb}} = 2.7 \times 10^7$ $(\Omega \mathrm{m})^{-1}$ for these films. A linear fit was used to follow the variation of RRR value with d_{Nb} (figure 8.6). For a given thickness of Nb $\sigma_{\mathrm{Nb}}(10\ \mathrm{K})$ was calculated using the RRR linear fit and ξ_S found using equation 8.3. ξ_S was found to be of the order of 6 nm.

The plain Nb transition temperature T_{CS} was similarly followed using the empirical cubic fit to the T_C (figure 8.6). Finally from $\sigma = 2e^2 \mathcal{N}(\epsilon_F) D$ the ratio $D_{AF} \mathcal{N}_{AF}(\epsilon_F) / D_S \mathcal{N}_S(\epsilon_F)$ is identical to $\sigma_{\mathrm{FeMn}} / \sigma_{\mathrm{Nb}} = 0.031$. Equation (2.20) was then solved numerically[1] to obtain T_C.

For varying Nb thickness, the fit with no adjustable parameters is shown as a solid line in figure 8.3. This is clearly not a good fit to the data. For the case of varying FeMn thickness, as can be seen from figure 8.4, the theoretical fit saturates for $d_{AF} \geq 2.5$ nm. This saturation would be expected for a coherence length of that order, however the saturation value of T_C is much higher than found experimentally. The additional variation of T_C for $d_{\mathrm{FeMn}} > 10$ nm is not expected from equation (2.20). This may be due to a different phase of FeMn being produced in films thicker than 20 nm [7]. The model of Krivoruchko [16] used a Green's function formulation of the Usadel equations, (in the dirty limit). Using the parameter $\eta = \xi_{AF} \sigma_S / \xi_S \sigma_{AF} = 10$, the family of reduced temperature vs d_S / ξ_S curves for various d_{AF} / ξ_{AF} was calculated (figure 8.9). T_{C0} is the saturation value of T_C for large d_S. In the present case $\eta \approx 13$ and $d_{AF} / \xi_{AF} = 2.7$. Although an exact comparison of the data with the fit is therefore not possible, the qualitative features of the model would seem to be in better agreement with the data than the de Gennes' theory fit.

A Nb(150 nm)/Cu(5 nm)/FeMn(4.5 nm)/Co(2 nm)/Nb(150 nm) structure was also grown as a reference to check the AF nature of the FeMn with the Nb/Cu underlayer. The $M(H)$ loop showed that there was some exchange bias associated with the applied field during deposition. The relatively weak nature of this ($\mu_0 H_{bias} \sim 15$ mT) implies that there are many misaligned domains in the Co being pinned by the AF. This was due to the F layer being grown after the AF layer, unlike the usual case where the F layer is saturated by the applied field before the AF is grown. The film was annealed in a field of 0.2 T at 200 °C for 30 minutes, and field cooled.[2] After annealing the exchange bias was measured as $\mu_0 H_{bias} \sim 33.5$ mT (inset of figure 8.8). This shows that the FeMn is an AF in this thickness regime, as expected. In this regime the magnitude of the exchange bias and also T_N is changing with d_{FeMn} [20]. It has been assumed

[1] Using Mathematica® 3.0.

[2] This was done by M. Ali, University of Leeds.

above that at 4.2 K, ($T \ll T_N$), there is no variation of the exchange coupling energy between the spins in the FeMn, leading to a constant value of ξ_{AF}. If this was not the case, a stronger decay of J_C vs d_{FeMn} would be observed (if ξ_{AF} was decreasing for increasing d_{FeMn} in equation 3.17), than the exponential seen. Hence it would seem valid to take a constant value of ξ_{AF} in this thickness range.

Many models of exchange bias in magnetic films use compensation of spins at the interface as a crucial parameter. Indeed the true structure of the present device might be S/N/F/AF/F/S: where the F layers are uncompensated AF spins. A full theoretical description of these bilayers and junctions may enable additional information concerning the nature of thin films of γ-FeMn to be gained, as well as provide a quantitative fit to the measurements of the Josephson junctions.

8.4 S/spin-valve/S

8.4.1 Development of spin-valve devices

As discussed in section 8.1, the uni-directional asymmetry of the $M(H)$ response of the spin-valve (SV) structure AF/F/N/F is a useful signature to look for in the $I_C(H)$ response of a S/spin-valve/S Josephson junction. From section 8.3 however, J_C is strongly reduced by the AF layer. To obtain as large a J_C as possible, a thin FeMn layer is required. However, when the AF thickness is reduced, H_{bias} decreases such that the $M(H)$ loop no longer has uni-directional asymmetry (figure 8.10). Using FeMn with CuNi to raise the J_C also adds the complexity of

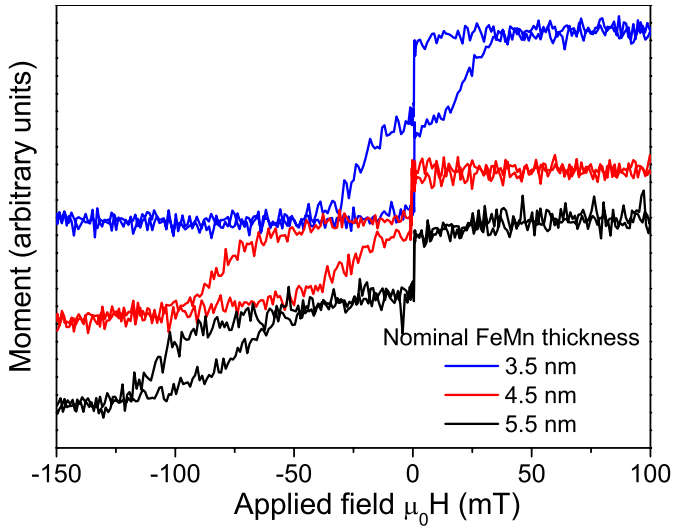

Figure 8.10: In-plane $M(H)$ loops at 300 K, showing the effect of FeMn thickness on a Nb/Py/Nb/Py/FeMn/Nb spin valve. Curves are offset vertically for clarity.

requiring field cooling from T_M to produce exchange bias, which was not straight forward in the dip probes, and not possible in the Heliox above 50 K. The physics of a system with $T_M < T_N$ is also not clear [21]. It would be possible to use a CuNi/Py/FeMn structure, as used by Gu *et al* [22] in F/S/F structures (section 2.4.3). In this case the FeMn/Py exchange bias is set at

room temperature, and the CuNi follows the magnetisation of the Py below T_M, and is hence also exchange biased. In the case of the CPP Josephson junctions however, the additional Py decreases the J_C further.

The pseudo-spin-valve structure (PSV) structure with no AF layer avoids the reduction of J_C, at the expense of requiring two F layers with different H_C to obtain an anti-parallel configuration. There is also no uni-directional asymmetry in the $M(H)$ loop. Results for Nb/CuNi/Cu/Co/Nb and Nb/Py/Cu/Co/Nb structures barriers are presented in sections 8.4.2 and 8.4.3.

8.4.2 Co/Cu/CuNi junctions

A Nb/CuNi/Cu/Co/Nb structure was grown with nominal thickness of 4, 4 and 2 nm for the CuNi, Cu and Co respectively. $d_{\mathrm{Nb}} = 5$ nm for the CIP measurements, and 150 nm for CPP measurements. These films did not show a double switch in the $M(H)$ loops to within the level

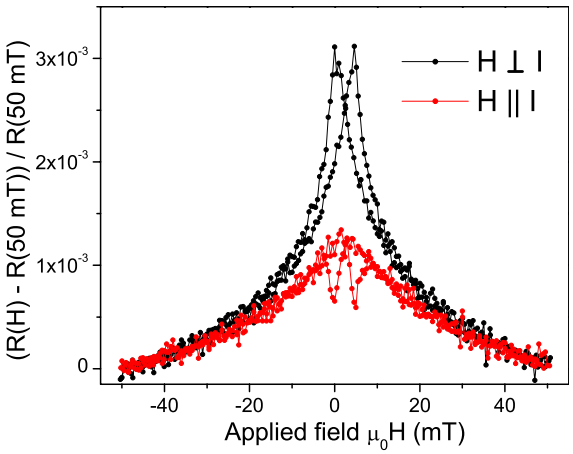

Figure 8.11: CIP $R(H)$ for CuNi/Cu/Co device at 77 K, with H applied parallel and perpendicular to I.

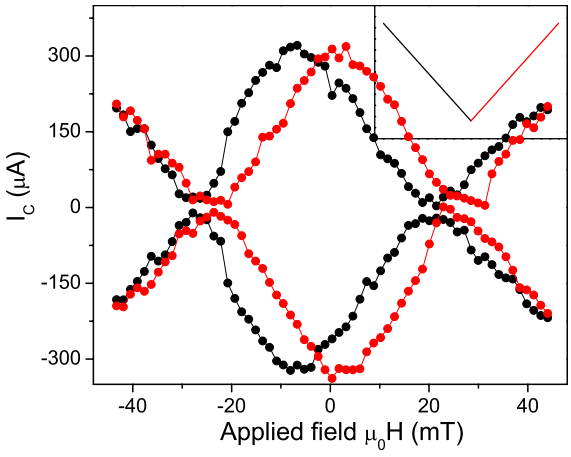

Figure 8.12: $I_C(H)$ for CuNi/Cu/Co device at 0.36 K, with $H \perp y$. Device dimensions $x = 1600$ nm, $y = 420$ nm. Inset: Direction of field sweep.

of the noise of the VSM when measured at 30 K. CIP $R(H)$ measurements at 77 K showed an MR dominated by anisotropic magnetoresistance (figure 8.11), due to the effect of the field on the current [23]. This may be due to the relative low T_M for such a CuNi thickness (figure 7.12), meaning that the CuNi magnetisation was relatively weak at 77 K. CPP devices showed a Josephson current, with $J_C \sim 5 \times 10^8$ Am^{-2} at 0.36 K. The $I_C(H)$ (figure 8.12) was hysteretic in the same sense as an $R(H)$ measurement (i.e. the peak in I_C is seen at a small positive field after saturating in a negative field). The lack of clear spin-valve behaviour in the $M(H)$ loop, and the difficulty of characterising such devices with the VSM encouraged the study of the Py/Cu/Co devices in the next section, which were possible to characterise in the VSM at room temperature.

8.4.3 Py/Cu/Co junctions

8.4.3.1 Experimental details

The Nb thicknesses were 180 nm and Cu spacer thickness was 8 nm, (to avoid significant 'orange peel' magnetostatic coupling between the ferromagnetic layers - section 1.2.6). The Co and Py layers which showed a Josephson current were 1 ± 0.2 nm and 1.6 ± 0.2 nm respectively. For

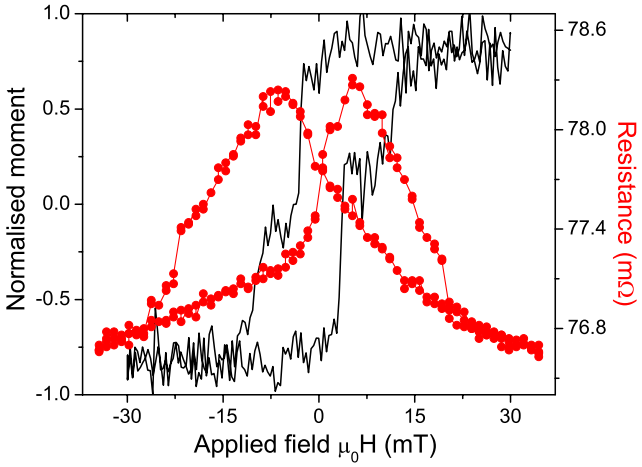

Figure 8.13: Comparison of $M(H)$ loop at 30 K for a film with relatively thick F layers (2 nm Co and 3.2 nm Py), with a $R(H)$ measurement at 4.2 K. MR $\sim$ 2% in this case.

the $I_C(H)$ and $R(H)$ measurements the $I-V$ was directly measured. The $R(H)$ measurements used a bias current of $2-3$ mA. Current induced switching of the F layers is not present since the current density is $\sim 1 \times 10^{10}$ Am^{-2} which is a few orders of magnitude lower than required [24]. The magnetic field was applied in-plane $\perp y$. As seen in the relatively thick device in figure 8.13, the peaks in the $R(H)$ of a device and the switches in the moment of a $M(H)$ measurement of a 4×4 mm^2 film are consistent with one another as expected. This device showed no measurable Josephson current at 4.2 K. For the thinner F layers, figures 8.14 and 8.15 show the two different behaviours of $R(H)$. The sudden jumps in figure 8.15 compared to the smooth variation of R in figure 8.14 can be explained by sudden switches of a small number of domains in the barrier, which would represent a significant fraction of the total resistance of a device with relatively small area. The crossover from smooth to sharp $R(H)$ switching took place as the junction area A was reduced below ~ 0.45 μm^2, but was not strongly dependent on the device aspect ratio x/y. The double switching behaviour has been seen elsewhere [25], and is likely to be associated with different domain structures being present during the switching. In both cases, despite the different $R(H)$ behaviour, MR = ($R_{\max}$-$R_{\min}$) / $R_{\max}$ of the order of 0.5 % was obtained. For all of the $R(H)$ measurements made, the MR was in the range $0.47-0.79$ %, with the majority of devices in the range 0.55 ± 0.05 %. The MR is consistent with the reduced F layer thickness [26], which results in a weaker degree of spin polarisation of the current. The $I_C(H)$ was not a Fraunhofer and was hysteretic in the same sense as the MR measurements (inset of figure 8.16), and the CuNi/Cu/Co junctions (section 8.4.2). In the inset of figure 8.16 the junction dimension

in the direction perpendicular to the field was 320 nm.

To avoid the complexity of the $I_C(H)$ measurements, which is a combination of the Fraunhofer modulation and the PSV response, the 'zero field' I_C was also measured. These measurements were done using the following method:

- Saturating field applied of ± 30 mT
- $\mp H_{set}$ applied in the opposite direction
- Field reduced to zero
- I_C measured with lock-in amplifier

In this way, the I_C of different remanent states of the PSV could be measured. Of particular interest was the parallel and anti-parallel remanent state I_Cs. In the following figures, the zero field I_C is the average of the absolute values of the positive and negative I_Cs.

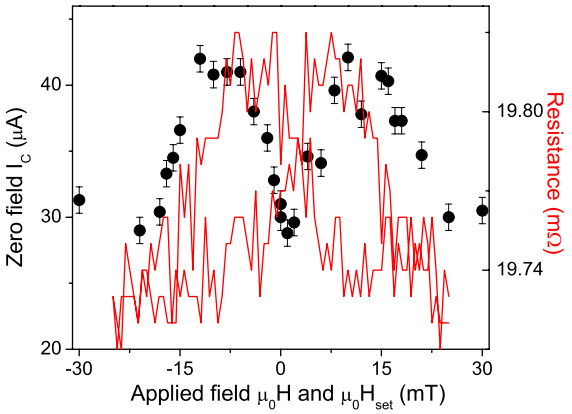

Figure 8.14: Smooth variation of the zero field I_C compared to $R(H)$. Junction size was 950 × 570 nm^2.

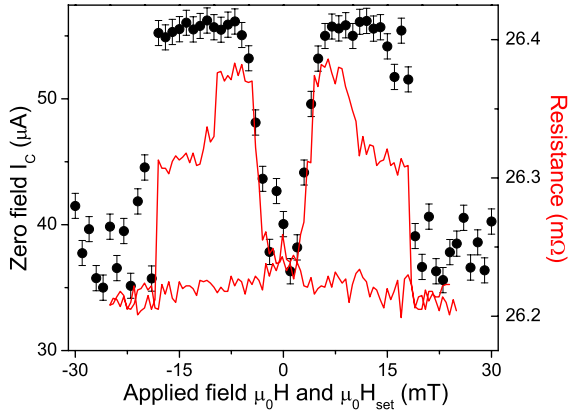

Figure 8.15: Sudden jump of zero field I_C compared to $R(H)$. Junction was 600 × 730 nm^2.

8.4.3.2 Results

The symbols in figures 8.14 and 8.15 show the zero field I_C vs H_{set}. The correlation between I_C and $R(H)$ is striking. For a total of six devices, the zero field I_C vs H_{set} was measured for the full range of $|\mu_0 H_{set}| \leq 30$ mT. Four of these devices had $\Delta I_C = (I_C^{\max}\text{-}I_C^{\min}) \ / \ I_C^{\max} = 30 \pm 2$ %. Extremal values of 17 % and 45 % were obtained for the other two devices. There was no noticeable scaling of ΔI_C with junction dimension, area or aspect ratio. The zero field $I_C(T)$ monotonically decreased with T, with parabolic behaviour as $I_C \to 0$, (figure 8.16). When normalised to the I_C at 4.2 K, both the demagnetised and saturated remanent states showed very similar behaviour. If the temperature dependencies were significantly different, it might be possible to show that the average coherence length of the PSV was changed in the two cases. The lack of any difference between these measurements does not preclude this possibility: the quadratic behaviour can be attributed to a dominance of the T dependence of

the superconducting gap near T_C, which may mask any variation in the coherence length. More investigation of the temperature dependence below 4.2 K is required, where the value of the gap is saturated.

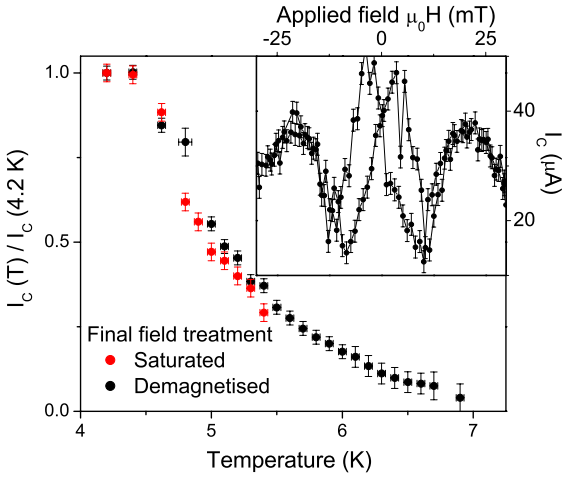

Figure 8.16: $I_C(T)$ normalised to $I_C(4.2\text{ K})$ for a 320×780 nm^2 device. Inset: Hysteretic $I_C(H)$.

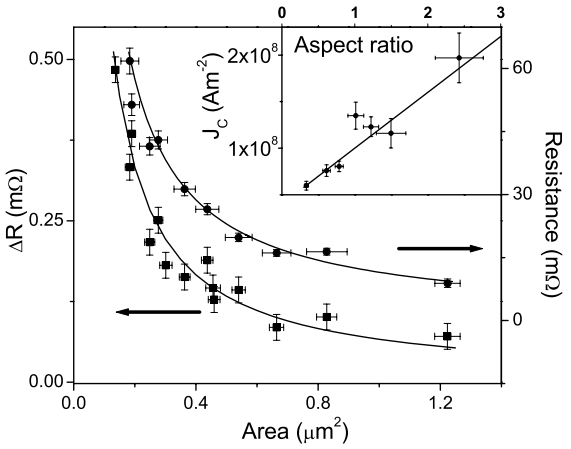

Figure 8.17: Scaling of R and ΔR with A, lines are best fit to $1/A$ power law. Inset: Scaling of J_C with aspect ratio x/y.

The junction R_N is the same as the value of the $R(H)$ measurements, and will be referred to as simply R. The I_CR was in the range 0.8 to 2 μV. The I_CR for a given thickness of barrier should be constant. Despite the apparent large difference in the shape of the $R(H)$, the I_CR was the same to within a factor of approximately two, which is reasonable if 0.1 nm variation of barrier thickness over the chip is allowed, and a coherence length of 1 nm assumed. Given that Co and Py are strong ferromagnets, a small J_C is expected, despite the thin barrier thicknesses. For the Co junctions of Sürgers *et al* [27], where the barrier thickness was 5 nm, J_C at 2.1 K was $\sim 1 \times 10^7$ Am^{-2}. Assuming $J_C \propto \exp(-d/\xi_F)$ with $\xi_F \approx 1$ nm, a thickness 2 nm gives $J_C \sim 2 \times 10^7$ Am^{-2}, for those devices. Although the comparison is crude, the present experimental values (at 4.2 K, not 2.1 K) in the range $0.5 - 1.2 \times 10^8$ Am^{-2} are somewhat larger than this. In the case of reference [27] however, the films were e-beam evaporated at room temperature, and no base pressure of the system was given. The films may therefore not be of comparable structure or quality.

For the present devices, J_C was constant to within a factor of two over the range of areas, but showed an interesting scaling with device aspect ratio x/y (inset of figure 8.17). This scaling is not understood at present, but may be associated with a local increase in J_C due to Ga damage of the 'cleaned' faces of the device parallel to the x dimension. The value of I_C and the $R(H)$ behaviour with thermal cycling was not perfectly reproducible, although the magnitude of the peak I_C in figures 8.18 and 8.19 - two different cools - is the same to within experimental error. The same qualitative behaviour was observed for each device for different measurements. This difference between separate measurements is possibly due to different magnetic configurations 'frozen in' when cooled.

The comparison between figures 8.15 and 8.18 is of considerable interest. The first sudden

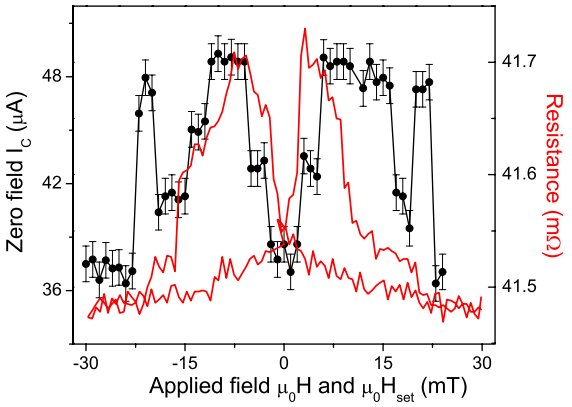

Figure 8.18: $R(H)$ and zero field I_C, with $H \perp y$. Dimensions were $x = 320$ nm, $y = 780$ nm.

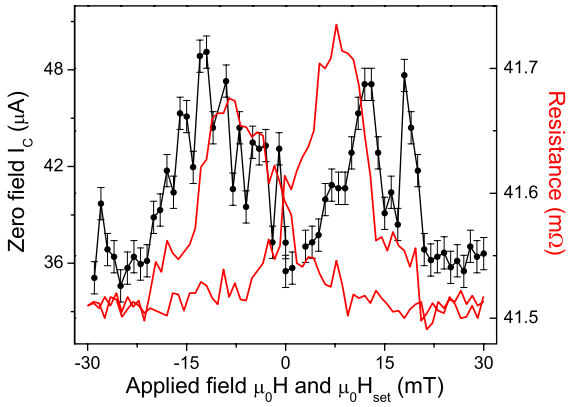

Figure 8.19: $R(H)$ and zero field I_C, with $H \parallel y$. Dimensions as figure 8.18.

switch of $R(H)$ in figure 8.15 is not accompanied by a change in the zero field I_C. This may be attributed to a metastable state not present at zero field. This could not be confirmed by measuring minor MR loops since the device was destroyed. Independently of this point, most of the PSV devices, such as figures 8.14 and 8.15 showed a decrease (increase) of zero field I_C with decreasing (increasing) MR. However in the case of figure 8.18 (and more weakly figure 8.19), the zero field I_C shows a sudden increase near a 'shoulder' of the MR loop, just before R decreases to the saturation value. As can be seen from the difference between figures 8.18 and 8.19, further investigation into the dependence of this 're-entrant' I_C effect on applied field orientation and device dimension is required

8.4.3.3 Numerical analysis of MR

Both R and the change in R, ΔR, were inversely proportional to the device area A (figure 8.17), as would be expected for constant F thicknesses in a simple two resistor model, (see below). $A\Delta R$ was in the range $5.4 - 8.7 \times 10^{-17}$ Ωm^2, and $AR = 1.1 \pm 0.2 \times 10^{-14}$ Ωm^2. The theoretical $A\Delta R$ and AR products can be found (sections 1.2.2 and 8.2.3). The resistance area product in for example the AF configuration for the up spin electron can be written as

$$\begin{aligned} AR^{\mathrm{AF}\uparrow} = \; & 2AR_{\mathrm{Nb/Co}} + 2AR_{\mathrm{Nb/Py}} + AR^{\uparrow}_{\mathrm{Co/Cu}} + AR^{\downarrow}_{\mathrm{Py/Cu}} \\ & + 2\rho_{\mathrm{Cu}} d_{\mathrm{Cu}} + \rho^{\uparrow}_{\mathrm{Co}} d_{\mathrm{Co}} + \rho^{\downarrow}_{\mathrm{Py}} d_{\mathrm{Py}}. \end{aligned} \tag{8.4}$$

In the present case the thicknesses d of the layers of Cu, Co and Py are 8, 1 and 1.6 nm respectively. Inserting these into equation 8.4 with the values from table 8.1, $AR^{\mathrm{AF}} = 9.0 \pm 1.2 \times 10^{-14}$ Ωm^2 and $AR^{\mathrm{F}} = 8.6 \pm 1.2 \times 10^{-14}$ Ωm^2 are obtained. The model gives $A\Delta R = 0.3 \pm 1.6 \times 10^{-15}$ Ωm^2. The uncertainty of the parameters of Yang *et al* was therefore too large to predict the MR of these devices. The contributions of the surface scattering can be compared to the bulk terms. For example in the $AR^{\mathrm{AF}\uparrow}$ in equation 8.4 the surface contributes 1.7×10^{-14} Ωm^2, but only 9.4×10^{-16} Ωm^2 for the bulk. As expected for such relatively thin layers, the interface scattering dominates the MR.

8.4.3.4 Modelling the junction behaviour

With this device geometry stray flux from the PSV contained in the electrodes is present (figure 5.5). However given the strong correlation between I_C and R for the two very different types of $R(H)$ behaviour, and that R is determined solely by magnetic structure of the barrier, it should be concluded that the effect of stray field from the electrodes is not important in directly determining I_C, (although the stray field can act as an applied field and change the moments in the device). A more quantitative argument can be used [28]: modelling the electrode fringe field as a line source, the flux density $B = \mu_0 M_S d_F / 2\pi r$, where r is the distance from the end of the track. The saturation magnetisation $M_S = 1.42 \times 10^6$ Am^{-1} for Co. Considering the barrier as simply a 2 nm thick Co film, for $r = 500$ nm, $B \sim 1$ mT. This flux density, while not insignificant, is not large compared to H_C, and will cause only blurring of any sharp transitions in the $R(H)$ or $I_C(H_{set})$ response. The strong correlation between the MR and zero field I_C would also seem to rule out the presence of pinholes in the individual F layers, which would allow some Josephson current to pass through only one F layer. The relatively thick Cu spacer, and good wetting of the Cu on the Py layer makes the possibility of pinholes which pass through the whole PSV very unlikely.

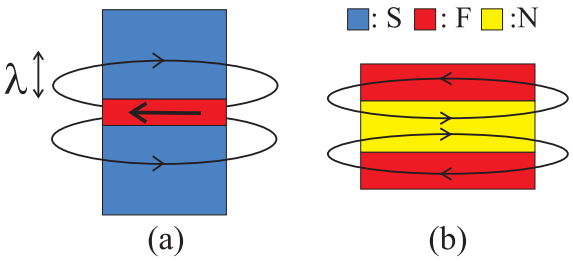

Figure 8.20: Schematic of the 'return flux' of the net magnetisation (a) penetrating the Nb electrodes over a depth λ, (b) through the N spacer in the spin-valve.

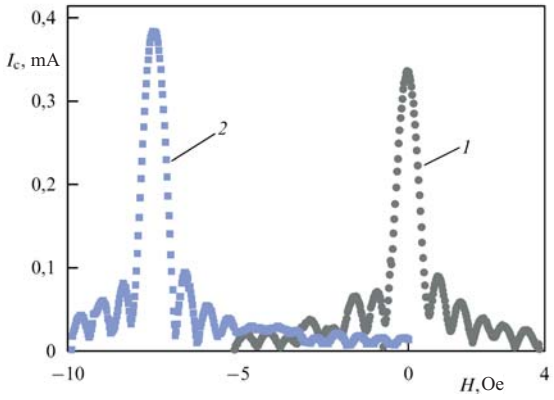

Figure 8.21: $I_C(H)$ curves (1) before and (2) after magnetisation above T_C, by field cooling through T_M. Taken from Ryazanov [29].

The magnetic induction from the barrier itself must also be considered. Using a simplistic model, in the worst case, if it is assumed that all of the moment present in the barrier passes into the junction, perpendicular to the dimension x, then the flux in the junction is $\Phi = x d_F \mu_0 M_S$. For $x = 0.5$ μm, $\Phi \sim 0.8\Phi_0$. This can explain the suppression of I_C, but not the lack of scaling of ΔI_C with the dimension x, and also neglects the 'return flux' in the opposite direction, which can penetrate the S electrode up to a depth of λ and reduce the net flux Φ threading the junction, (figure 8.20 (a)). With the PSV barrier, in contrast to the single ferromagnetic layer junctions, the return flux can also pass through the Cu spacer, again reducing the net flux through the junction, (figure 8.20 (b)). Net magnetic induction has been shown to shift the $I_C(H)$ pattern away from zero field and reduce the zero field I_C (figure 8.21). Devices demagnetised both

above and below T_C ($T = 10$ K for the 'above T_C' case) showed an increase of R above $R_{\max}$ as expected [30] (figure 8.22), but no increase in zero field I_C above $I_C^{\max}$ (figure 8.23). It would seem therefore that stray induction does not strongly influence these devices.

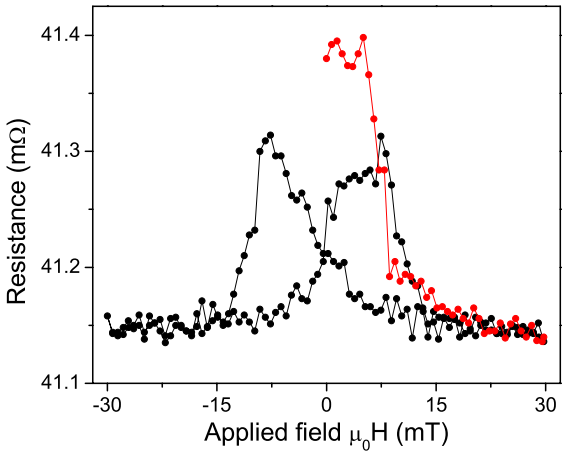

Figure 8.22: Initial $R(H)$ at 4.2 K after demagnetising at 10 K (red), with normal measurement afterwards (black). Device and field direction is same as figure 8.18. Lines are a guide to the eye.

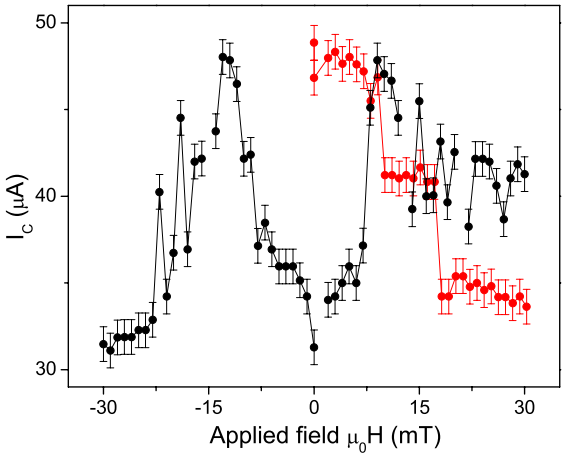

Figure 8.23: Initial zero field I_C at 4.2 K after demagnetising at 10 K (red), with normal measurement afterwards (black). Device and field direction is same as figure 8.18. Lines are a guide to the eye.

It is important to note that most of the S/F/S junctions in the literature are tens of microns across. To quote Ryazanov *et al* [31] "the averaging of a small-scale structure of magnetic domains in the F layer resulting in highly uniform current flow". This is *not* the case for sub-micron junctions where there will be a relatively small number of domains present. Such junctions have not been investigated in detail in the literature. The $I_C(H)$ shown in figure 8.21 was measured after field cooling through T_M. Once the net induction was set, the fact that the Fraunhofer period $\Delta B \ll H_C$ (for a 50×50 μm^2 junction), meant that the F layer was not affected by measuring $I_C(H)$. This is *not* the present limit: here $\Delta B \sim H_C$, so care should be taken when considering figure 8.21 in the case of sub-micron junctions.

If it is possible to rule out the effects of net induction in and around the barrier, it is then necessary to gain some qualitative understanding of reason for the correlation of the I_C and MR. Most of the models of S/F/X/F/S junctions discussed in section 3.4.1, were in the limit of $\Delta \rightarrow H_{Ex}$ and unsuitable to be applied directly to the present case. The possible sub-gap Andreev transport or triplet pairing in domain walls (sections 2.4.1 and 2.4.3.1), is quite speculative at this stage. Therefore a simple model of 'phase-unwinding' is used to give some qualitative picture in this case. Using a similar analysis to section 2.4, the phase of a Cooper pair increases with the distance x inside the F layer: $\Delta\phi = Qx$, (Q is the Cooper pair centre of mass momentum). On passing into the second F layer with opposite magnetisation, the Cooper pair would begin to unwind the phase built up, (in the limiting case this must be true, since the system is the same as an antiferromagnetic Josephson junction - section 2.5 - which showed no π transition since there was no complex term in the coherence length which changed the phase of the wavefunction). The change in the zero field I_C between the parallel and anti-

parallel remanent configurations can therefore be considered as a transition, (in the ideal case of complete phase unwinding), from an oscillating order parameter, to a monotonically decaying case. This is shown schematically in figure 8.24.

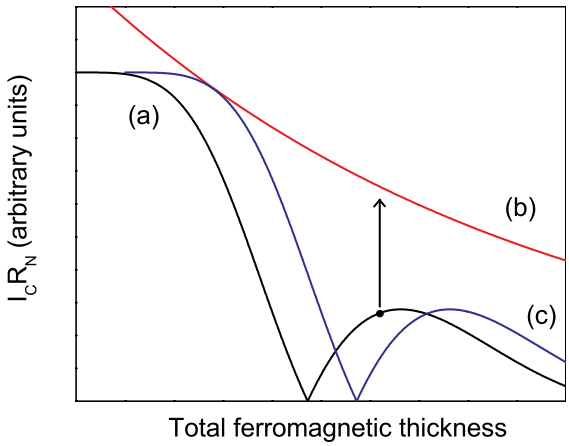

Figure 8.24: Simple schematic model of the change in $I_C R_N$ (marked with arrow) when switching from (a) parallel alignment of the PSV (oscillating order parameter) to (b) a monotonically decaying order parameter, (no π transition), assuming perfect 'phase-unwinding' in the second F layer, or (c) incomplete phase-unwinding. Relative magnitudes of curves (a)-(c) are for illustration only.

Importantly, the PSV was grown with d_{Co} and d_{Py} such that the magnetic *moments* cancel in the anti-parallel state. From equation 1.8, $E_{Ex} = H_{Ex} M_S$. It is the exchange splitting E_{Ex} which determines Q, and hence the rate of phase-winding with distance. Moment cancellation is therefore not the same as complete phase-unwinding. This interpretation can be verified by examining the variation of ΔI_C with both the total F thickness $d_{\mathrm{Co}} + d_{\mathrm{Py}}$, while also changing d_{Co} and d_{Py} individually, (see section 9.2). The possibility of incomplete phase-unwinding may also give some intuitive picture of the re-entrant I_C in figure 8.18, if the ferromagnetic thicknesses are such that a transition from curves (a)→(b)→(c) is possible in figure 8.24.

References

[1] C. Bell, E. J. Tarte, G. Burnell, C. W. Leung, D.-J.Kang, and M. G. Blamire, Phys. Rev. B **68**, 144517 (2003).

[2] C. Bell, G. Burnell, C. W. Leung, E. J. Tarte, D.-J.Kang, and M. G. Blamire, Appl. Phys. Lett. (submitted).

[3] T. Valet and A. Fert, Phys. Rev. B **48**, 7099 (1993).

[4] Q. Yang, P. Holody, R. Loloee, L. L. Henry, W. P. Pratt Jr., P. A. Schroeder, and J. Bass, Phys. Rev. B **51**, 3226 (1995).

[5] J. Bass and W. P. Pratt Jr., J. Magn. Magn. Mater. **200**, 274 (1999).

[6] W. Park, D. V. Baxter, S. Steenwyk, I. Moraru, W. P. Pratt Jr., and J. Bass, Phys. Rev. B **62**, 1178 (2000).

[7] C. Tsang, N. Heiman, and K. Lee, J. Appl. Phys. **52**, 2471 (1981).

[8] M. S. M. Minhaj, S. Meepagala, J. T. Chen, and L. E. Wenger, Phys. Rev. B **49**, 15235 (1994).

[9] A. Andreone, A. Cassinese, M. Iavarone, R. Vaglio, I. I. Kulik, and V. Palmieri, Phys. Rev. B **52**, 4473 (1995).

[10] J. Nogués and I. K. Schuller, J. Magn. Magn. Mater. **192**, 203 (1999).

[11] P. L. Rossiter, *The Electrical Resistivity of Metals and Alloys* (Cambridge University Press, 1991).

[12] C. Kittel, *Introduction to Solid State Physics* (Wiley & Sons Inc., 1996).

[13] N. W. Ashcroft and N. D. Mermin, *Solid State Physics* (Holt-Saunders, 1976).

[14] K. Nakamura, T. Ito, and A. J. Freeman, Phys. Rev. B **67**, 014405 (2003).

[15] G. Choe, A. Tsoukatos, and S. Gupta, IEEE Trans. Magn. **34**, 867 (1998).

[16] V. N. Krivoruchko, Zh. Éksp. Teor. Fiz **111**, 547 (1997), [JETP **84**, 300 (1997)].

[17] M. Hübener, D. Tikhonov, I. A. Garifullin, K. Westerholt, and H. Zabel, J. Phys.: Condens. Matter **14**, 8687 (2002).

[18] A. B. Pippard, Proc. Roy. Soc. London **A216**, 547 (1953).

[19] C. Poole, *Handbook of Superconductivity* (Academic Press, 2000).

[20] R. Jungblut, R. Coehoorn, M. T. Johnson, J. aan de Stegge, and A. Reinders, J. Appl. Phys. **75**, 6659 (1994).

[21] M. G. Blamire, *et al* (unpublished).

[22] J. Y. Gu, C.-Y. You, J. S. Jiang, J. Pearson, Y. B. Bazaliy, and S. D. Bader, Phys. Rev. Lett. **89**, 267001 (2002).

[23] M. Ziese and M. J. Thornton, eds., *Spin Electronics* (Springer-Verlag, 2001).

[24] F. J. Albert, N. C. Emley, E. B. Myers, D. C. Ralph, and R. A. Buhrman, Phys. Rev. Lett. **89**, 226802 (2002).

[25] L. Kong, Q. Pan, B. Cui, M. Li, and S. Y. Chou, J. Appl. Phys. **85**, 5492 (1999).

[26] R. D. Slater, J. A. Caballero, R. Loloee, and W. P. Pratt Jr., J. Appl. Phys. **90**, 5242 (2001).

[27] C. Sürgers, T. Hoss, C. Schönenburger, and C. Strunk, J. Magn. Magn. Mater. **240**, 598

(2002).
[28] T. W. Clinton and M. Johnson, J. Appl. Phys. **85**, 1637 (1999).
[29] V. V. Ryazanov, Usp. Fiz. Nauk **169**, 920 (1999), [Phys. Usp. **42** 825 (1999)].
[30] W. P. Pratt Jr., S.-F. Lee, J. M. Slaughter, R. Loloee, P. A. Schroeder, and J. Bass, Phys. Rev. Lett. **66**, 3060 (1991).
[31] V. V. Ryazanov, A. V. Veretennikov, V. A. Oboznov, A. Y. Rusanov, A. A. Golubov, and J. Aarts, Usp. Fiz. Nauk **171**, 81 (2001).

Chapter 9

Further work

9.1 S/F superlattices

Much of the literature discussed in section 2.4.2 concentrated on measuring the transition temperature or critical field of S/F multilayers. The latter was used to measure two-dimensional to three-dimensional crossover in the behaviour of the superconducting layers as the ferromagnetic thickness was increased. There was no discussion in these works of Josephson coupling in the intermediate regime. Despite the recent work on S/F/S junctions by an increasing number of groups, there is no work published measuring the CPP J_C in S/F superlattices. Studies of such structures have recently begun with work by A. Ruotolo *et al* [1], using $Nb/Cu_{0.4}Ni_{0.6}$ superlattices. In this work the FIB can be used in two ways. Micron scale tracks can be thinned to reduce the CIP I_C, and the $I_C(H)$ measured in an analogous manner to the S/F bilayer devices measured by R. J. Kinsey (see [2] and section 2.4.3). The *same* structure can then milled from $\theta = 85°$ to create a CPP device, and the same measurements repeated. The combination of CIP and CPP measurements will give more insight into the transport properties of such heterostructures.

As can be seen from the FIB image in figure 9.1, the contrast in the FIB allows the individual Nb and CuNi layers to be distinguished for relatively thick layers ($d_{Nb} = 20$ nm and $d_{CuNi} = 17$ nm in this case). When the side cuts are made, the number of Nb and CuNi layers in the CPP stack can be easily counted. For thinner multilayers, the FIB stage current can be used to calibrate cuts from $\theta = 0°$. As shown in figure 9.2, the oscillations of the stage current are clear as the beam mills through a total of 15 Nb/CuNi bilayer repeats, ($d_{Nb} = 20$ nm and $d_{CuNi} = 8.5$ nm). The increase in the stage current at time ~ 160 s indicates the removal of the SiO_2 layer, and Ga implantation in the Si substrate. Unlike the attempts to calibrate the number of Tl-2212 intrinsic junctions by milling from $\theta = 0°$ and using the *in-situ* resistance (section 6.1.5.2), in this case the cut from $\theta = 0°$ can be made before the undercut, and therefore before the thinning of the track. In this way, the edge effects which made the previous work unsuccessful are significantly reduced.

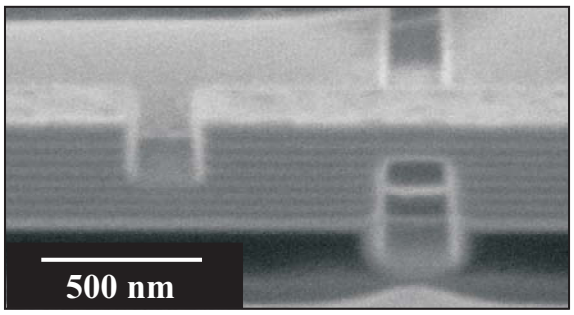

Figure 9.1: View from $\theta = 65°$ of a $(Nb/CuNi)_7$ multilayer grown by A. Ruotolo.

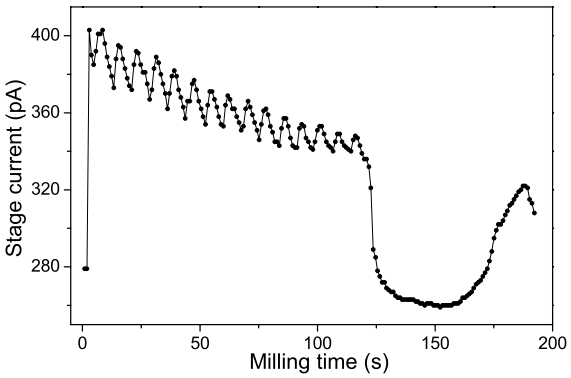

Figure 9.2: Stage current during milling of a $\sim 3 \times 1$ μm^2 box with 150 pA beam through a $CuNi/(Nb/CuNi)_{15}$ multilayer from $\theta = 0°$.

9.2 Spin-valve Josephson junctions

If the Co and Py barriers used for the devices in section 8.4 are replaced by weaker ferromagnetic layers, (e.g. Cu_xNi_{1-x} or Pd_xNi_{1-x}) then for $T < 4.2$ K a much larger J_C may be obtained. These current densities may be large enough for the Josephson current to produce spin torque effects [3], (current induced switching of the magnetic moments in the spin-valve). These current induced switches have been observed only with 'normal' currents using Cu electrodes (see below). Oscillations of the magnetic moments in such experiments have also been recently measured, with the frequency of the dynamics in the microwave region [4]. There is a clear possibility of coupling these dynamics with the a.c. Josephson current, which is in the same frequency regime.

For more direct applications, it would be important to show that the spin-valve Josephson junctions can be formed into π-junctions in the parallel state, and can be switched between the 0 and π states by changing from the parallel to the anti-parallel configuration of the spin-valve. Initially this could be investigated by examining the behaviour of ΔI_C with ferromagnetic thickness, (see section 8.4.3.4). In addition to this, the fabrication of a controllable SQUID would be an important step. In this case, only one of the two junctions in a d.c. SQUID is switched into the π state. The $I_C(H)$ response of such a $(0, \pi)$-SQUID possesses a minimum at $H = 0$, in contrast to the maximum obtained for $(0, 0)$ and (π, π)-SQUIDs. Such a controllable SQUID would be a magnetic version of the voltage controlled design using normal metal junctions [5].

It is important to remember at this stage that the FIB junctions are in fact two junctions in series, (section 5.1.2). Although the larger second junction is negligible in most cases, it is not for *phase sensitive* measurements. Assuming it was possible to arrange one of the two smaller junctions to be in a different state to the other, the phase difference of the larger junctions must also be considered. This problem can be solved simply by cutting the two FIB junctions in an

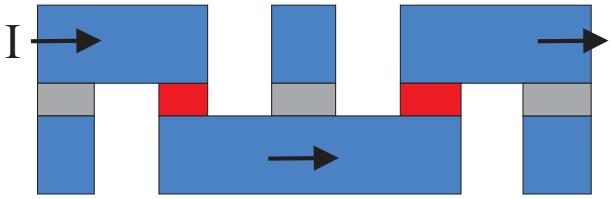

Figure 9.3: Schematic of an 'unwrapped' SQUID, showing the two sets of FIB side cuts. Current flows only through the two red junctions as indicated.

anti-symmetric way, as shown in figure 9.3. In this way the two larger junctions are shorted out and do not affect the measurement. This geometry is the same as that used in section 6.3.1. To put the two junctions into different states (one parallel, one anti-parallel), it may be possible to pass relatively large control currents in lines running close to one of the junctions. The magnetic field of this current could be used, in addition to the applied field, to switch one of the devices. Another possibility would be to exploit the shape anisotropy of the magnetic layers, and cut the two devices with different shapes / aspect ratios, such that the devices react differently for a given direction of in-plane field.

9.3 Other spin-valve devices

Following the work with Nb electrodes, C. W. Leung has shown that CPP spin valve devices can be measured up to room temperature with copper electrodes, (figure 9.4 (a)). The Cu electrodes are used in preference to superconducting materials in most of the recent work investigating current induced switching in Cu/Co nanopillars (for example see [4, 6] and references therein). This is due to the relatively high current densities required ($\sim 1 \times 10^{12}$ Am^{-2}), which are in excess of the J_C of Nb at 4.2 K. To be able to achieve these current densities, the spin-torque devices typically have lateral dimensions of 10s to 100s of nm. Early results obtained by C. W. Leung suggest that the device dimensions obtainable in the FIB are small enough that current induced switching of magnetic layers can be observed [7].

In these devices the series resistance due to the Cu leads can decrease the observed MR. To avoid this problem, the devices can be made at a junction of four tracks [8]. Four side cuts in the FIB can then be made to form a Kelvin bridge, which enables a four point measurement to be made of the CPP region alone, (figure 9.4 (b)).

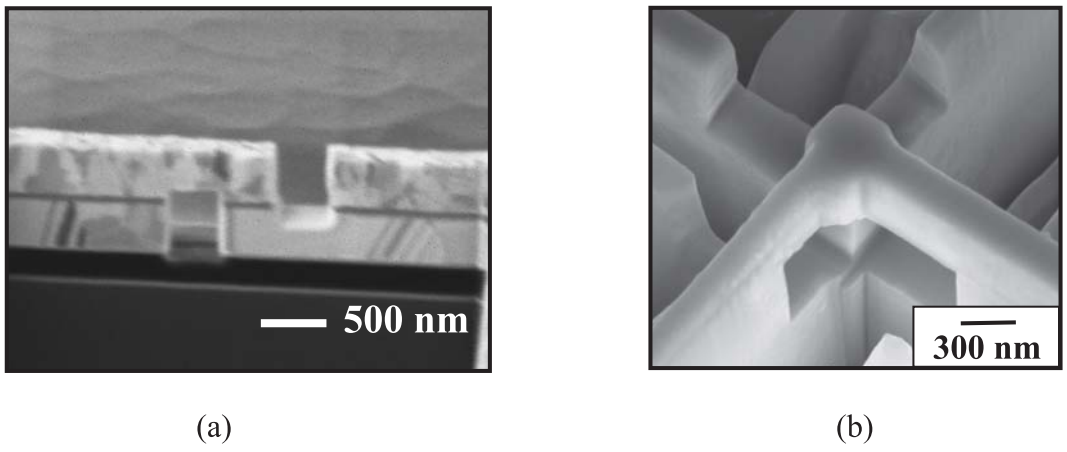

Figure 9.4: (a) FIB image of a Cu/spin-valve/Cu device from $\theta = 65°$, showing the contrast due to channelling of the Ga^+ ions in different grain orientations in the Cu. (b) SEM image from $\theta \sim 35°$, of a Kelvin bridge structure using four FIB side cuts. Images courtesy of C. W. Leung.

The flexibility of the FIB allows the further possibility of milling a hole through the device from $\theta = 0°$, (figure 9.5 (b)). Such a structure has been predicted to be useful as a potential memory element [9]. It also shows interesting current induced switching behaviour [10]. Applying this idea to the superconducting devices, much work has be done on the vortex dynamics of such structures ('annular' Josephson junctions), particularly in the S/I/S (underdamped) limit [11, 12]. The FIB allows the opportunity to extend this micron scale work to annular junctions in the sub-micron regime.

9.3.1 TEM imaging and *in-situ* biasing

It was noted in section 4.3.1 that the FIB is frequently used to prepare samples for Transmission Electron Microscopy (TEM). These samples are simply the present device structure, without

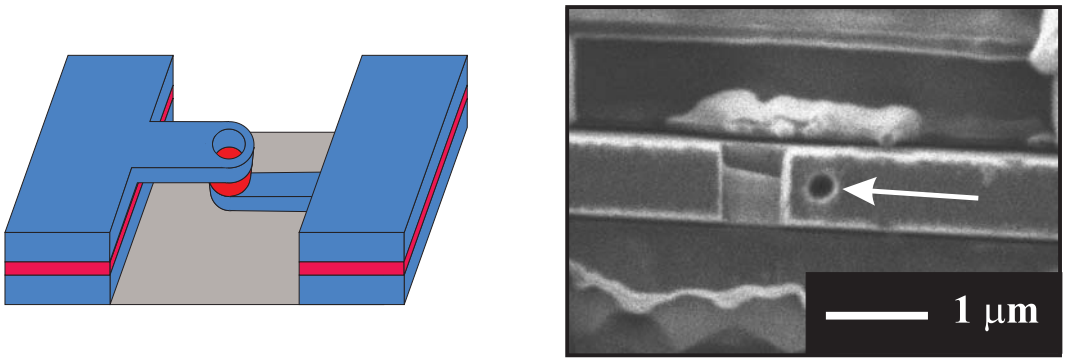

(a) (b)

Figure 9.5: (a) Schematic of an idealised junction with central hole through active barrier region. (b) FIB image from $\theta = 0°$ showing the $\sim$ 300 nm diameter hole (marked with arrow) milled through the final device.

the side cut holes. Lorentz TEM and electron holography can be used to qualitatively and quantitatively image magnetic moments in such samples [13]. Combining this with the possibility of *in-situ* current biased measurements [14, 15], and the current-induced switching discussed above, there is the opportunity to image the two states before and after the current-induced switching of the spin-valve. This geometry would compliment previous TEM imaging of spin-valve structures from $\theta = 0°$ [16].

References

[1] A. Ruotolo, *et al* (unpublished).
[2] R. J. Kinsey, Ph.D. Thesis, University of Cambridge (2002).
[3] X. Waintal and P. W. Brouwer, Phys. Rev. B **65**, 054407 (2002).
[4] S. I. Kiselev, J. C. Sankey, I. N. Krivorotov, N. C. Emley, R. J. Schoelkopf, R. A. Buhrman, and D. C. Ralph, Nature **425**, 380 (2003).
[5] J. J. A. Baselmans, B. J. van Wees, and T. M. Klapwijk, Appl. Phys. Lett. **79**, 2940 (2001).
[6] J. A. Katine, F. J. Albert, and R. A. Buhrman, Appl. Phys. Lett. **76**, 354 (2000).
[7] C. W. Leung, *et al* (unpublished).
[8] C. W. Leung, C. Bell, G. Burnell, and M. G. Blamire, Nanotechnology (2003), (submitted).
[9] J.-G. Zhu, Y. Zheng, and G. A. Prinz, J. Appl. Phys. **87**, 6668 (2000).
[10] K. Bussmann, G. A. Prinz, R. Bass, and J.-G. Zhu, Appl. Phys. Lett. **78**, 2029 (2001).
[11] A. V. Ustinov, Appl. Phys. Lett. **80**, 3153 (2002).
[12] A. Franz, A. Wallraff, and A. V. Ustinov, Phys. Rev. B **62**, 119 (2000).
[13] R. E. Dunin-Borkowski, M. R. McCartney, B. Kardynal, S. S. P. Parkin, M. R. Scheinfein, and D. J. Smith, J. Microscopy **200**, 187 (2000).
[14] A. C. Twitchett, Ph.D. Thesis, University of Cambridge (2003).
[15] A. C. Twitchett, R. E. Dunin-Borkowski, and P. A. Midgley, Phys. Rev. Lett. **88**, 238302 (2002).
[16] X. Portier, A. K. Petford-Long, T. C. Anthony, and J. A. Brug, J. Appl. Phys. **85**, 4120 (1999).

Appendix A

Conferences attended & publications

A.1 Poster presentations

IOP 'Superconductivity and Magnetism' meeting, Manchester, 2003
SET for Britain, Nanotechnology evening reception, House of Commons, 17th March 2003
IOP Superconductivity annual meeting, Cambridge University, January 2003
CMMP 7th-11th April, Brighton, 2002
IOP Superconductivity annual meeting, Cambridge University, January 2002
IOP 'Mesoscopic phenomena in superconductivity' meeting, Manchester University, 2001
IOP Superconductivity annual meeting, Birmingham University, 2001

A.2 Talks

IRC in Superconductivity seminar, University of Cambridge, 27th November 2003
Advances in Focused Ion Beam Microscopy, University of Cambridge, 4th April 2003
American Physical Society Meeting, Austin, Texas, USA, 3rd - 7th March 2003
ESF π-shift workshop, Sant Feliu de Guixols, Spain, 6th-8th November 2002

A.3 Other conferences attended

Advances in Focused Ion Beam Microscopy, Oxford 2001
SQUID 2001, Stenungsbaden, Sweden

A.4 Publications

C. W. Leung, C. Bell, G. Burnell, M. G. Blamire, (submitted to Nanotechnology)
In situ fabrication of cross-bridge Kelvin resistor by focused ion beam microscopy

A. Ruotolo, C. Bell, C. W. Leung and M. G. Blamire, (submitted to J. Appl. Phys.)
Perpendicular magnetic anisotropy and structural properties of NiCu/Cu multilayers

José Prieto, Bas B. van Aken, Gavin Burnell, Chris Bell, Jan E. Evetts and Mark G. Blamire
Transport properties of sharp antiferromagnetic boundaries in Gd/Fe multilayers
Phys. Rev. B, (in press)

C. Bell, G. Burnell, C. W. Leung, E. J. Tarte, D.-J. Kang, M. G. Blamire
Controllable Josephson current through a pseudo-spin-valve structure
Appl. Phys. Lett. **84**, 1153 (2004)

G. Testa, A. Monaco, E. Sarnelli, A. D'Agostino, D.-J. Kang, E. J. Tarte, S. H. Mennema, C. Bell, and M. G. Blamire
Submicron $YBa_2Cu_3O_{7-x}$ bicrystal grain boundary junctions by focused ion beam
Supercond. Sci. Technol. **17**, 287 (2004)

C. Bell, E. J. Tarte, G. Burnell, C. W. Leung, D.-J. Kang, and M. G. Blamire
Proximity and Josephson effects in superconductor - antiferromagnetic Nb / γ-$Fe_{50}Mn_{50}$ heterostructures, Phys. Rev. B **68**, 144517 (2003)

P. A. Warburton, A. R. Kuzhakhmetov, C. Bell, G. Burnell, M. G. Blamire, H. Wu, C. R. M. Grovenor and H. Schneidewind
Sub-Micron Thin Film Intrinsic Josephson Junctions
IEEE Trans. Appl. Supercond. **13**, 821 (2003)

C. Bell, G. Burnell, D.-J.Kang, R. H. Hadfield, M. J. Kappers, and M. G. Blamire
Fabrication of nanoscale heterostructure devices with a focused ion beam microscope
Nanotechnology, **14**, 630 (2003)

Robert H. Hadfield, Gavin Burnell, Dae-Joon Kang, Christopher Bell, and Mark G. Blamire
Corbino Geometry Josephson Junction, Phys. Rev. B **67**, 144513 (2003)

Gavin Burnell, Robert H. Hadfield, Christopher Bell, Dae-Joon Kang and Mark G. Blamire
Nanoscale superconductor-normal metal-superconductor junctions fabricated by focused ion beam
Physica C, **372-376**, 14 (2002)

Appendix B

Published papers

In following pages copies of the papers published or submitted for publication as a direct result of the work carried out in this thesis are reproduced.